UNIVERSITAT DE BARCELONA

Numerical modeling of transient multiphase thermo–mechanical problems: Application to the oceanic lithosphere

Sergio Zlotnik

Departament de Geodinàmica i Geofísica
Facultat de Geologia
Universitat de Barcelona

Group of Dynamic of the Lithosphere (GDL)
Instituto de Ciencias de la Tierra "Jaume Almera"
Consejo Superior de Investigaciones Científicas (CSIC)

Numerical modeling of transient multiphase thermo–mechanical problems: Application to the oceanic lithosphere

Memoria presentada por Sergio Zlotnik al Departament de Geodinàmica i Geofísica de la Universitat de Barcelona para optar al grado de Doctor

Directores:
Manel Fernández Ortiga Pedro Díez Mejía Jaume Vergés Masip

Tutor:
Alejandro Marcuello

Barcelona, 2008

Acknowledgments

In doing this work, I owe much to my advisors Manel Fernández, Pedro Díez and Jaume Vergés. Their support and confidence were crucial during all these years.

I also want to thank to Giorgio Ranalli, Vlad Manea and especially to Juan Carlos Afonso for all discussions and useful advices they gave me. I have learn a lot from they.

Thanks also for all the members of the Geodynamic Group at the Institute Jaume Almera and all the members of the LaCaN group at Technical University of Cataluya. All were very kind and helpful.

My greatest gratitude to my parents and brothers, who have always supported me through all these years and specially to Sandra who gives me the strength to finish all this work.

This project was financially supported by Ministerio de Educación y Ciencia, Grants DPI2007-62395, SAGAS CTM2005-08071-C03-03/MAR; the Spanish Team Consolider-Ingenio 2010 nrCSD2006-00041; WestMed (REN2002-11230-E-MAR; 01-LEC-EMA22F, ESF Eurocores -EUROMARGINS) and by StatoilHydro research center, Bergen, Norway.

Presentation of the Thesis

This PhD Thesis was elaborated within the framework of a collaborative project between the Group of Dynamics of the Lithosphere (GDL) at the Institute of Earth Sciences "Jaume Almera" of the CSIC and the Laboratori de Càlcul Numèric (LaCàN) at the Universitat Politècnica de Catalunya. The aim of the research project, developed between 2004 and 2008, was the design and implementation of a new numerical code able to simulate accurately geodynamic problems. As a result of this Thesis five original papers have been written:

1. Numerical modeling of tectonic plates subduction using X–FEM. S. Zlotnik, P. Díez, M. Fernández and J. Vergés. Computer Methods in Applied Mechanics and Engineering, 196, 2007. 4283–4293.

2. Modeling gravitational instabilities: Slab break–off and Rayleigh–Taylor diapirism. S. Zlotnik, M. Fernández, P. Díez and J. Vergés. Submitted to Pure and Applied Geophysics, 2007.

3. Assembling sparse matrices in MATLAB. S. Zlotnik and P. Díez. Submitted to Communications in Numerical Methods in Engineering, 2007.

4. Small–scale gravitational instabilities under the oceans: Implications for the evolution of oceanic lithosphere and its expression in geophysical observables. S. Zlotnik, J. C. Afonso, P. Díez and M. Fernández. Submitted to Philosophical Magazine, 2008.

5. Hierarchical X–FEM for n–phase flow ($n > 2$). S. Zlotnik and P. Díez. Submitted to Computer Methods in Applied Mechanics and Engineering, 2008.

Two different disciplines are present in this Thesis: applied mathematics and geophysics. Geophysicist and mathematicians (or engineers) both may be interested in some topics covered here. While writing this memoir we have keep in mind this possible bimodal audience, trying always to help the reader of the "other" discipline. In chapters dealing with geophysics (2, 5 and 6) some basic geophysical concepts are introduced for the engineer reader. In Chapters 3 and 4, some standard numerical procedures are detailed to be followed by geophysicists.

The terminology of each discipline may also lead to confusion, for example geophysicists call *convergence rate* to the relative velocity between tectonic plates and does not refer to the approximation properties of any particular numerical scheme, as used in mathematics. In order to avoid misinterpretations, some definitions are included through this text.

Contents

List of Figures

List of Tables

List of Algorithms

Chapter 1

Introduction

1.1 Plate Tectonics

Plate tectonics is a framework in which the outermost layer of the Earth, the lithosphere, is divided into plates moving one respect to another. The ocean floor is the active part of the system: oceanic plates are continuously created at mid–ocean ridges, where adjacent plates move apart in a process called seafloor spreading. As the adjacent plates diverge, hot mantle rocks ascend to fill the gap, the material cools, becomes rigid and creates new plate area. The complementary process of plate consumption occurs at ocean trenches, where an oceanic plate bends and descends into the Earth's interior. The oceanic plate creation process counterbalance the plate consumption to keep the surface area of the Earth constant. The ocean floor is therefore created at mid–ocean ridges and moves away while it cools and thickens until eventually being subducted.

Plate tectonics provides a framework to understand most major geological and geophysical observations. For example, the location of volcanic arcs and deep earthquakes is related with subduction zones. Mid–ocean ridges produce shallow earthquakes and continuous volcanism, which generates the oceanic crust. Ocean floor topography, heat flow data and geoid anomalies are related with the movement and aging of the oceanic lithosphere. Major tectonic deformation around the globe is concentrated in the boundaries between plates. Plate Tectonic theory is successful in accounting for all these observables. Nevertheless it is a purely qualitative theory and, therefore, it requires a physical support to quantify and demonstrate the dynamical feasibility of the processes. The dynamics of the Earth and of the processes described by Plate Tectonics is still not completely understood.

Major questions remain regarding the dynamics of the lithosphere and the mantle, for example: what are the causes of the flattening of the oceanfloor

topography in lithospheres older than 70 Ma. What controls the deformation regime of the backarcs in subductions zones? Which variables control the angle of the slab in subduction zones? How is subduction initiated? These questions, among many others, are currently active subjects of research.

Different approaches are used to gain insight on the mantle and lithosphere. Firstly, indirect measurements like geological observations and geochemical signatures from volcanism, together with geophysical data such as heat flow, topography and gravity anomalies give information about the present state and about the active processes acting on the Earth. Secondly, laboratory experiments provides valuable information about the properties of rocks such as density, thermal conductivity or viscosity, etc. Thirdly, seismic waves give first hand information about the interior of the Earth. Seismic studies and seismic tomographies allow for locate major features inside the Earth; information about material properties, phase transitions and degree of melting can be obtained from seismic data.

Nevertheless, most geological and geophysical data provide information about one moment in time, but do not give much insight into the dynamics of the processes. Therefore, numerical models are a powerful tool to gain some insight on geodynamic processes. In this work we use numerical models to study some aspects of the dynamic of the oceanic lithosphere.

1.2 Numerical Models

The complex physical models describing the Earth dynamics require advanced numerical methods to find solutions to the governing partial differential equations. The combination of mantle convection with mobile, dynamically evolving plates has been a challenge problem since the 1980s (Cohen, 2005). In many ways the problem is more computationally challenging today than it appeared to be in the 1980s mainly because of complexities introduced by rheology. The constitutive behavior of rocks is strongly dependent on temperature, pressure, stress and composition. Strong gradients in temperature, compositional boundaries (e.g. between the crust and mantle), and the tendency of deformation localization resulting from the constitutive non–linearity, all produce sharp changes in the material properties over small scales relative to the dominant scale of the system (Moresi et al., 2007). Complex rheological behavior includes plasticity (e.g. Tackley, 1998, 2000; Bercovici, 2003), grain–size dependent viscosity (e.g. Solomatov, 2001) or the effect of water on rheology (e.g. van Keken et al., 2002; Arcay et al., 2005; Abers et al., 2006).

Computational geodynamic models are in constant evolution. Numerical

techniques in one hand and physical equations including new and more accurate physical processes on the other hand, both are continuously improved leading to more realistic models. The first generation of geodynamic codes solved two dimensional, single–material problems, e.g. the early versions of TERRA (Baumgardner, 1985), ConMan (King et al., 1990), MC3D (Gable et al., 1991) and CitCom (Moresi and Solomatov, 1995; Moresi and Gurnis, 1996). Multiphase codes appeared after year 2000. Some examples are Stag3D (Tackley and Xie, 2003) which use finite volumes to solve the equations in a 3D spherical coordinates and I2VIS (Gerya and Yuen, 2003) using finite differences in a 2D Cartesian domain. In the last few years several new 3D models were written: ACuTEMan (Kameyama, 2005), Ellipsis3D (O'Neill et al., 2006) and I2ELVIS (Gerya and Yuen, 2007) all designed to run on parallel computers. New versions of early models, specially of CitCom, are also available.

1.3 Scope of this thesis

The scope of this thesis is twofold. Its first part is devoted to the development of a numerical tool to model geodynamic problems. We aim to provide a computer code able to solve efficiently the governing physical equations, that is conservation of mass, momentum and energy. This code should be flexible enough to incorporate secondary processes that might be of special interest in geodynamics. For example, mineral phase transitions, melting processes, etc.

To evaluate the realism of the simulations by comparison with real data, the model should compute geophysical observables such as surface heat flow, topography, gravity anomalies, seismic velocities, etc.

The eXtended Finite Element Method (X–FEM) is a novel numerical technique used in engineering problems. It allows to describe multiphase problems in an Eulerian framework in a convenient manner. We want to test its efficiency when applied to geodynamic problems.

The second objective is the application of the generated tool to study the dynamics of the oceanic lithosphere.

1.4 Outline

The outline of this thesis is as follows:

Chapter 2 is devoted to the physical problem. The basic equations of the model are derived and explained in the context of the geodynamical problem. All assumed

approximations are presented. The models used to reproduce the dependence of physical properties of rocks on temperature and pressure are also described.

The numerical methodologies used to solve the physical equations are explained in Chapter 3. A detailed description of X–FEM applied to the mechanical and thermal problems is given. The coupling between equations is also explained. Finally, some academical examples are used to validate the code.

The numerical techniques presented in Chapter 3 are standard in other scientific or engineering fields. In Chapter 4 we present some original numerical ideas and some computational details of our program. In Section 4.1 an extension of the X–FEM technique to handle any number of materials is presented. In Section 4.2 an adaptive scheme to track interfaces is proposed and tested. In Section 4.3 an efficient algorithm to assemble sparse matrices is proposed.

In Chapter 5 the generated program is used to analyze the stability of the oceanic lithosphere. The development of small–scale convection and it consequences on the evolution of the lithosphere is studied. Emphasis is put in i) the influence of various rheological and thermophysical parameters on small–scale convection, and ii) its ability to reproduce geophysical observables. Predictions of seismic velocities, SHF and seafloor topography are used to ensure compatibility with current observations.

Chapter 6 presents two application of our model: firstly, a parameter study of the slab breakoff phenomenon is presented in Section 6.1. The influence of shear heating, phase transitions and rheology is studied in terms of the timing of the detachment, its isostatic response. Secondly, the relation between the slab dip and convergence velocity is systematically studied in Section 6.2. A positive correlation between these variables is found.

Chapter 7 summarizes the main conclusions from previous chapters and describes possible future work.

Chapter 2

Physical Model

The physics underling lithospheric and mantle processes is complex, it includes flow and solid materials with strongly variable properties depending on thermal state and chemical composition. Phase changes are also present, introducing sharp contrasts in properties. Partial melting produces depletion of rocks in some elements, varying its chemical composition and consequently its properties.

The base of the model presented here is composed by two coupled problems: a dynamic flow problem, governed by the Stokes equation and a heat balance problem. The coupling between equations is given by the dependency of the physical parameters (e.g. density, viscosity, etc) on the solution of the equations (e.g. temperature, pressure, velocity).

In some simple cases the governing partial differential equations can be simplified to hold ordinary differential equations or even algebraic equations. However, because of the requirement for accurate modeling of many concurrent (coupled) physical processes, numerical techniques are essential in the solution of these equations.

In this chapter the physical model is presented. The basic equations of the model are derived and explained in the context of the geodynamical problem. The assumed approximations and the empirical or theoretical models used to reproduce the dependence of physical properties of rocks on temperature and pressure are presented.

2.1 Heat problem

Thermal structure of the lithosphere exerts a first order control on its behavior. As the physical properties of the rocks —for example its density and viscosity— strongly depend on temperature, the whole mechanical behavior of the mantle and the oceanic lithosphere is controlled by its thermal state. Moreover, the temperature

contrast between the cold slab and the surrounding mantle in subduction zones, generates a density contrast that provides a major source of stress within the slab, being the primary force driving the plates (Forsyth and Uyeda, 1975). Therefore, an accurate thermal model is required.

Three different heat transfer mechanisms act within the Earth: convection, conduction and radiation. The last one becomes important at temperatures higher than approximately 1500 K. The relative importance between these heat transfer mechanisms determines three major thermal regimes in the mantle. First, there are regions of nearly adiabatic temperature gradient, where advective heat transport dominates all other transfer mechanism. This is the case of the upper mantle and transition zone, which are included in all of the models presented here. Second, there are regions where the heat transfer by conduction and advection are comparable. The oceanic lithosphere belongs to this category. Finally, in some regions conductive transfer dominates. The continental lithosphere is an example. These thermal regimes act simultaneously within the Earth.

2.1.1 Heat equation

When there exists a temperature gradient within a body, heat energy will flow from the region of high temperature to the region of low temperature. This phenomenon is known as conduction heat transfer and is described by Fourier's Law

$$\mathbf{q} = -k\nabla T \tag{2.1}$$

This equation determines the heat flux vector $\mathbf{q}$ for a given temperature profile T and thermal conductivity k. The minus sign ensures that heat flows down the temperature gradient as required by the second law of thermodynamics. It is valid to assume a isotropic conductivity k for rocks. In Section 2.8 the details on how the thermal conductivity of rocks is addressed are given.

The heat equation follows from the conservation of energy for a differential element within the body

$$\nabla \cdot \mathbf{q} = h_g - \frac{\mathrm{d}e}{\mathrm{d}t} \tag{2.2}$$

where h_g is the generated heat within the body and e is the internal energy related to the body's ability to store heat by raising its temperature by

$$\frac{\mathrm{d}e}{\mathrm{d}t} = \rho\, C_p \frac{\mathrm{d}T}{\mathrm{d}t}. \tag{2.3}$$

Replacing equations (2.1) and (2.3) into (2.2) the heat equation is obtained

$$\nabla \cdot (-k\nabla T) = h_g - \rho\, C_p \frac{\mathrm{d}T}{\mathrm{d}t} \tag{2.4}$$

where ρ is the density and C_p the heat capacity. Expressing the material derivative $\frac{\mathrm{d}T}{\mathrm{d}t}$ in terms of spatial and temporal partial derivatives as

$$\frac{\mathrm{d}T}{\mathrm{d}t} = \frac{\partial T}{\partial t} + \mathbf{u} \cdot \nabla T \tag{2.5}$$

and replacing it into equation (2.4), the complete thermal energy equation including convection and conduction results

$$\rho C_p \left(\frac{\partial T}{\partial t} + \mathbf{u} \cdot \nabla T \right) = \nabla \cdot (k\, \nabla T) + \rho f \tag{2.6}$$

where the generated heat h_g is replaced by f, the rate of internal heat per unit mass, multiplied by the density. The source term f in equation (2.6) has different contributions as described next.

2.1.2 Heat sources

The main heating mechanisms acting on the mantle are: *radiogenic heating* due to decay of radioactive isotopes, *shear heating* due to mechanical viscous dissipation, *adiabatic heating* due to adiabatic compression and decompression of materials and *latent heating* due to transformation between different mineral species. The last two heating mechanisms may produce negative values.

Radiogenic heat production. A substantial part of the heat lost through the Earth's surface originates in the interior of the Earth by the decay of the radioactive isotopes of uranium, thorium and potassium. Approximately the 80% of present heat flow can be attributed to radiogenic sources, and 20% comes from the cooling of the Earth. The present distribution of these elements within the Earth is not uniform. Partial melting at ocean ridges depletes mantle rocks of incompatible elements such as radioactive ones. These elements are concentrated in the basaltic partial melt fraction. As a result the oceanic crust (tholeiitic basalt) is enriched in these elements by about a factor of four relative to the undepleted mantle. Processes that lead to the formation of the continental crust, such as volcanism associated with subduction, further differentiate the incompatible elements. The concentration of the heat–producing elements in a typical continental rock such a granite are quite

variable, but in general they are one order of magnitude greater than in tholeiitic basalts.

Shear heating. The *shear heating* is the rate at which the work done against viscous forces is irreversibly converted into internal energy (heat). It is related to the solution of the mechanical problem, discussed in Section 2.2, as

$$f_s = \sigma_{ij}\dot{\varepsilon}_{ij} = \sigma_{xx}\dot{\varepsilon}_{xx} + \sigma_{zz}\dot{\varepsilon}_{zz} + 2\,\sigma_{xz}\dot{\varepsilon}_{xz} \tag{2.7}$$

where σ and $\dot{\varepsilon}$ are the deviatoric stress and the strain rate tensors.

Adiabatic heating. The adiabatic heating is due to the adiabatic compression and decompression of materials. It is defined in terms of temperature, velocity, thermal expansivity α and pressure p as

$$\begin{aligned} f_a &= T\alpha\,[\mathbf{u}\nabla p] \\ &= T\alpha\left[u_x\frac{\partial p}{\partial x} + u_z\frac{\partial p}{\partial z}\right]. \end{aligned} \tag{2.8}$$

Neglecting the horizontal variation in pressure and replacing the vertical pressure gradient by ρg the adiabatic heating terms reads

$$f_a \approx T\alpha\,\rho\,u_z\,g.$$

Latent heating. The mineral species are stable within a range of temperatures and pressures. While the minerals composing the rocks of the subducting lithosphere descend, the T–p conditions change and the minerals adopt their most stable phase. The kinematics of these mineralogic phase reactions may be exothermic, for example the olivine–wadsleyite transformation occurring at approximately 410 km depth in an undisturbed mantle, or may be endothermic as the wadsleyite–ringwoodite transformation occurring at 660 km depth.

All these heat contributions but the latent heat, are included in the model by means of the term f in equation (2.6). The heat produced by decay of radiogenic elements f_r, the adiabatic heat source f_a and the viscous heating term f_s are added to obtain the total rate of internal heat per unit mass $f = f_r + f_s + f_a$.

2.1.3 Thermal regime of the upper mantle and transition zone

The upper mantle and transition zone are characterized by sub solidus convective cells where advective heat transport dominates over the heat conduction (and radiation). This process tends to homogenize temperatures and it is fair to assume a near adiabatic variation of temperatures with depth. The adiabatic gradient does not imply that horizontal variation in mantle temperatures can be neglected. This gradient depends on several factors such as mantle depletion, lithospheric thickness, lithospheric composition, all having lateral variations. Moreover, some processes like subduction and mantle plumes, that tend to disturb the adiabatic temperature profile and lateral variations in temperature are expected to be up to $\pm 50\%$ of the spherical average temperature (Schubert et al., 2001). The three dimensional thermal structure of the mantle is closely related to the pattern of mantle convection. Anomalous high temperatures are associated with regions of ascending flow, such as mantle plumes, while anomalously low temperatures characterize regions with descending flow, such as subduction zones.

2.1.4 Thermal regime of the oceanic lithosphere

As oceanic plates move away from ridges, they cool from above, thicken, and become denser by thermal contraction. This cooling is reflected on the dependence of geophysical observables on the age of the plate t (McKenzie, 1967; Parsons and Sclater, 1977). For plates younger than about 70 Ma[1], both seafloor topography and surface heat flow decrease linearly with $\sqrt{t}$, consistent with predictions from the *half–space cooling* (Turcotte and Oxburgh, 1967).

For larger ages, however, this relation breaks down and the two observables decrease less rapidly, reaching almost constant values in ocean basins (Parsons and Sclater, 1977; Schroeder, 1984; Stein and Stein, 1992). Since these observables reflect the thermal structure of the lithosphere, their flattening implies a similar behavior for the isotherms within the plate. These features are included in the popular *plate model* (McKenzie, 1967), which considers the lithosphere as a cooling plate with an isothermal lower boundary. Although this model can explain the observed flattening of both seafloor topography and surface heat flow, it does not propose any particular mechanism by which the horizontal isotherm is maintained at constant depth. The thermal and mechanical evolution of the oceanic lithosphere will be addressed in

[1]A usual notation in geology is to use "Ma" to indicate age, it means "million years ago", while "My" is used for the unit of time = 10^6 years.

Chapter 5.

2.2 Mechanical flow problem

2.2.1 Upper mantle and transition zone

Despite the upper mantle is composed in more than 99% by solid rocks (not molten) its behavior at geological time scales ($> 10^4$ yr) is fluid. This solid–state deformation mechanism occurs due to the thermally activated motion of atoms associated with lattice defects such as dislocations and vacancies (Ranalli, 1995).

The mantle mechanical behavior is modeled as a quasi–static Stokes flow (Busse, 1989; Schubert et al., 2001). This model is based on the following assumptions: i) rocks are almost incompressible, ii) due to the high Prandtl number, inertia terms are neglected, iii) due to the modest Rayleigh number characterizing convection in Earth's mantle, turbulent convection is neglected. In the following section the general equation governing a fluid (Navier–Stokes equation) is presented. All the assumed approximations are then introduced and justified.

2.2.2 Rheology of oceanic lithosphere

Deformation of the whole oceanic lithosphere can be related to elastic, plastic and viscous rheological behaviors. The rigidity of the oceanic lithosphere allows it to bend when subjected to load. The elastic bending of the lithosphere under vertical loads can explain the basins around volcanic islands and the structure of ocean trenches. However there are significant deviations from a simple elastic rheology (Schubert et al., 2001).

The lithosphere at ocean trenches bends and undergoes brittle failure evidenced by extensional shallow seismicity. This failure does not propagate through the entire lithosphere and it appears to have little effect on the general flexural behavior.

The pure viscous approach has been proposed on the 1970's by Gremaecker (1977), McKenzie (1977) and Melosh and Raefsky (1980). This approach can produce the same morphology as the elastic rheology, however, viscous flexure releases at long times. In some old sedimentary basins flexural effects can be still observed. Turcotte (1979) has used this argument to discard the pure viscous rheology for oceanic lithosphere. Nevertheless, application of a pure viscous rheology may be appropriate for investigating other aspects of the oceanic lithosphere and subduction process (e.g. Zhang et al., 1985; Vassiliou and Hager, 1988; Zhong and Gurnis, 1994;

Gurnis et al., 1996). The viscous approach is adopted here, mainly for simplicity facing numerical methods.

2.2.3 Conservation of mass

In non–relativistic mechanics mass must be conserved, requiring that

$$\rho_t + \nabla \cdot (\rho \mathbf{u}) = 0 \tag{2.9}$$

where ρ is the density, ρ_t its time derivative and $\mathbf{u}$ is the velocity vector. For the special case of an incompressible fluid, the density is constant and thus equation (2.9) is simplified to

$$\nabla \cdot \mathbf{u} = 0. \tag{2.10}$$

The velocity field in an incompressible fluid is divergence free.

2.2.4 Strain rate in fluids

The velocity gradient $\nabla \mathbf{u}$ is a second–order tensor defined as

$$\nabla \mathbf{u} = \frac{\partial \mathbf{u}}{\partial x_1} + \frac{\partial \mathbf{u}}{\partial x_2} + \frac{\partial \mathbf{u}}{\partial x_3}$$

where x_i are the spacial dimensions. This tensor may be decomposed into its symmetric and skew–symmetric parts according to

$$\frac{\partial u_i}{\partial x_j} = \frac{1}{2}\left(\frac{\partial u_i}{\partial x_j} + \frac{\partial u_j}{\partial x_i}\right) + \frac{1}{2}\left(\frac{\partial u_i}{\partial x_j} - \frac{\partial u_j}{\partial x_i}\right)$$

or, in abbreviated form

$$\nabla \mathbf{u} = \nabla^s \mathbf{u} + \nabla^w \mathbf{u}.$$

The symmetric tensor $\nabla^s \mathbf{u}$ defined as $\frac{1}{2}\left(\frac{\partial u_i}{\partial x_j} + \frac{\partial u_j}{\partial x_i}\right)$ is called the *strain rate* and it is noted $\dot{\varepsilon}$. The skew–symmetric tensor defined as $\frac{1}{2}\left(\frac{\partial u_i}{\partial x_j} - \frac{\partial u_j}{\partial x_i}\right)$ is called the spin–tensor. Since strain is dimensionless, the dimension of strain rate is the inverse of time, that is, in International System, $[\mathrm{s}^{-1}]$.

2.2.5 Stresses in fluids

When a fluid is at rest, no shear stresses are present and only the normal or hydrostatic stresses are possible. In this case the stress tensor is

$$\sigma_{ij} = -p\,\delta_{ij}$$

where p is the fluid pressure defined as $p = \frac{1}{3}(\sigma_{11}+\sigma_{22}+\sigma_{33})$ and δ_{ij} is the Kronecker delta. If the fluid is in motion, the stress tensor may be divided into its *isotropic* part, present when the fluid is at rest, and the *deviatoric* part, τ, as

$$\sigma_{ij} = -p\,\delta_{ij} + \tau_{ij}.$$

The stress strain rate relation for a linear (Newtonian) fluid is given by

$$\sigma_{ij} = -p\,\delta_{ij} + \tau_{ij} = -p\,\delta_{ij} + 2\eta\dot{\varepsilon}_{ij} + \lambda\dot{\varepsilon}_{kk}\delta_{ij}$$

where η is the dynamic viscosity. Assuming incompressibility the velocity field is divergence free ($\dot{\varepsilon}_{kk} = 0$) and consequently the above relation reduces to the so-called *Stokes law*

$$\sigma_{ij} = -p\,\delta_{ij} + \tau_{ij} = -p\,\delta_{ij} + 2\eta\dot{\varepsilon}_{ij} \tag{2.11}$$

or, in matrix form

$$\boldsymbol{\sigma} = -p\,\mathbf{I} + 2\,\eta\nabla^s\mathbf{u}.$$

The viscosity is then defined as function of the deviatoric tensors as

$$\eta = \frac{\tau_{ij}}{2\,\dot{\varepsilon}'_{ij}}, \qquad i \neq j$$

where $\dot{\varepsilon}'_{ij} = \dot{\varepsilon}_{ij} - \frac{1}{3}\,\dot{\varepsilon}_{kk}\,\delta_{ij}$ is the deviatoric strain rate. The dimension of the viscosity is that of stress divided by strain rate, in International System is Pascal times second [Pa s].

2.2.6 Conservation of momentum

Derivation of the equation of motion is based on the second Newton's law, according to which mass multiplied by acceleration is equal to the sum of all the forces acting on the mass under consideration. There are two different forces acting on a fluid: mass forces and surface forces. Surface forces in a fluid (pressure and friction) act on the boundary surfaces of an elementary parcel, while volume forces do on the fluid parcel

throughout its volume. We consider gravity to be the only body force. Although Coriolis forces due to rotation of the Earth are important in the Earth's liquid outer core, they are small enough to be neglected in the Earth's mantle (Schubert et al., 2001). The centrifugal force due to rotation is included in the acceleration of gravity.

Derivation of the momentum equation can be found elsewhere, for example (Batchelor, 1967; Ranalli, 1995; Dobretsov and Kirdyashkin, 1998; Schubert et al., 2001). The general governing equation, called Navier–Stokes equation, yields

$$\rho \left(\mathbf{u}_t + (\mathbf{u} \cdot \nabla) \, \mathbf{u} \right) = \nabla \cdot \boldsymbol{\sigma} + \rho \mathbf{g} \tag{2.12}$$

where $\mathbf{u}_t$ is the time derivative of the velocity field, $\boldsymbol{\sigma}$ the stress tensor and $\mathbf{g}$ the acceleration of gravity vector. The left hand side of equation (2.12) is the product of the mass and the acceleration per unit volume in an elementary parcel. The first term of the right hand side corresponds with the divergence of the net surface forces per unit volume on the elemental parcel and, the last term is the net body force per unit volume.

The stress of equation (2.12) is replaced using the constitutive equation (2.11) that relates $\boldsymbol{\sigma}$ with the strain rate and thus with velocities. The Navier–Stokes equation becomes

$$\rho \left(\mathbf{u}_t + (\mathbf{u} \cdot \nabla) \, \mathbf{u} \right) = 2 \, \nabla \cdot (\eta \nabla^s \mathbf{u}) - \nabla p + \rho \mathbf{g}. \tag{2.13}$$

When viscosity is constant, it is usual to rewrite the first term of the right hand side of the previous equation in terms of the Laplacian of the velocity. In this case the viscosity depends on temperature, pressure and on the gradient of the velocity and thus it is not possible to restate the equation. Similarly, the dynamic pressure $\hat{p} = p/\rho$ and the kinematic viscosity $\nu = \eta/\rho$ cannot be used due to variations of density.

In the case of highly viscous fluids, like the Earth mantle, the convective term $(\mathbf{u} \cdot \nabla) \, \mathbf{u}$ is neglected because the viscous term dominates the equation (Batchelor, 1967; Busse, 1989; Donea and Huerta, 2002). For incompressible and highly viscous fluids, the resulting equation is the so-called equation of Stokes flow

$$\rho \mathbf{u}_t - 2 \, \nabla \cdot (\eta \nabla^s \mathbf{u}) + \nabla p = \rho \mathbf{g}. \tag{2.14}$$

In the case of creeping flows (very slow flows) it is usual to neglect the inertial term $\mathbf{u}_t$ of the equation (2.14). This approximation, called the *infinite Prandtl number*, is supported by the dimensional analysis presented in Section 2.5. The

infinite Prandtl number approximation of the mechanical problem eliminates all explicit time dependence from the momentum equation. This produces an elliptic equation characterized by the instantaneous transmission of information across the solution domain. Changes in buoyancy and constitutive relationships at any point in the domain have an immediate influence on all other points in the domain. The Stokes equation (2.14) including the infinite Prandtl number approximation is then stated in its steady state form

$$-2\nabla \cdot (\eta \nabla^s \mathbf{u}) + \nabla p = \rho \mathbf{g} \tag{2.15}$$

and the transient mechanical flow problem, without explicit dependence on time, evolves due to changes in density field and phases location. In this circumstances (transient problem, no explicit time dependence) the problem is called *quasi–static*.

2.3 Boussinesq approximation

The Stokes flow problem stated in Section 2.2.6 assumes incompressible materials. This assumption implies a constant density field (equations (2.9) and (2.10)). In that situation the gravitational forces $\mathbf{F} = \rho \mathbf{g}$ are constant and does not have any influence on the dynamic of the model. Ignoring density variations implies ignoring gravitational forces and thus, thermal convection. In geodynamic models this is not a valid assumption because the dependency of density on temperature generates the principal forces acting on the system. Density variations in the gravitational field result, for example, in the buoyancy forces that drive the plates. Therefore, some relaxation in the incompressibility assumption is required. To handle density variations in a consistent manner the fluid must be stated as compressible and all effects associated with compressibility must be included. In that case, to obtain distributions of velocity, temperature and pressure in space and time, equations of momentum, mass, energy (heat transfer) and state of matter have to be solved simultaneously. This procedure essentially complicates the study of thermo–gravitational flows. For this reason simplifying assumptions are made and more convenient approximations are used.

The *Boussinesq approximation* consist in neglecting the variations in density in all terms but on the body force term $\rho \mathbf{g}$ of equation (2.15). Thus, conservation of mass is used as in Section 2.2.3, assuming a constant density. The Boussinesq approximation includes changes in density due to temperature variations but neglects the dependence on pressure. When the pressure dependence is included the approximation is usually called *extended Boussinesq*.

2.4 Viscosity and the constitutive equation

The mechanical behavior of a fluid is parametrized by its viscosity. The viscosity relates the stress acting on a fluid with the strain rate. It is a measure of the resistance of a fluid to deform under shear stress. There are two approaches to understand the viscosity structure of the Earth: i) using observations such as the geoid and post glacial rebound combined with flow models and ii) studying the physical deformation of mineral in the laboratory.

The viscosity of the solid mantle was first determined based on post glacial rebound by Haskell (1937). In Scandinavia the Earth's surface is still rebounding from the load of ice during the last ice age. Assuming a viscous mantle Haskell was able to explain the present uplift of Scandinavia if the mantle has a viscosity of about 10^{20} Pa s. This viscosity value is still accepted today. Although it is an immense number (honey at room temperature has a viscosity of 10 Pa s), it predicts vigorous mantle convection on geologic time scales.

Laboratory studies indicate that viscosity of minerals such as olivine is a strong function of temperature, grain size and stress (Kirby, 1983; Ranalli, 1995; King, 1995; Hirth and Kohlstedt, 2003). The deformation of minerals under mantle conditions generally follows a power–law, where the strain rate depends on a power of the deviatoric stress. There is general agreement that two main creep mechanisms are likely responsible for most of the deformation in the mantle: diffusion creep (Herring–Navarro and Coble creep) and dislocation creep (Kirby, 1983; Ranalli, 1995). Although there are significant uncertainties associated with the extrapolation of laboratory results (performed at low pressures and high strains rates) to mantle conditions, a comparison of microstructures on experimentally and naturally deformed peridotites indicates that the same deformation mechanisms detected in laboratory take place in the mantle as well (Ranalli, 1995; Hirth and Kohlstedt, 2003). Deformation caused by dislocation creep is evidenced in lithospheric mantle samples (e.g. xenoliths, peridotitic massifs) and indirectly inferred in the shallow upper mantle from seismic anisotropy studies(see Nettles and Dziewonski (2008) for a recent review). On the other hand, diffusion creep may be dominant over dislocation creep at depths $> 250 - 300$ km, where stresses are low and pressure effects become dominant (i.e. the activation volume of diffusion creep seems to be smaller than that of dislocation creep, (Ranalli, 1995)). This change in deformation mechanisms with depth is consistent with the lack of significant anisotropy at such depths, although not conclusive (Mainprice et al., 2005).

Both deformation mechanisms are based on modifications of the atomic lattice of minerals. The diffusion creep mechanism is Newtonian, that is the stress–strain rate

relation is linear. It is due to migration of atoms and ions by movements of adjacent empty sites in the crystalline lattice. Atoms move within grains (Herring–Navarro creep) and along grain surfaces (Coble creep). The diffusion of atoms in a crystalline solid is a thermally activated process. The diffusion coefficient D is given by the relation (Ranalli, 1995)

$$D = D_0 \exp\left(-\frac{E + pV}{RT}\right) \tag{2.16}$$

The activation energy E is the energy preventing the migration of an atom into an adjacent vacancy. The activation volume V takes into account the effects of pressure in reducing the number of vacancies. The exponential temperature dependence gives the fraction of atoms that have sufficient energy to overcome the energy barrier between lattice sites and can jump into a vacancy. The diffusion creep viscosity decreases strongly with decreasing grain size.

The dislocation deformation mechanism happens when a part of the crystal is shifted with respect to the other. The surface that traces the motion is the glide surface and it is planar. This shifting does not occur instantly but the shifted part increases gradually. The line of imperfections in the crystalline lattice, bounding the front of the shifting is called *dislocation*. This mechanism can also be thermally activated at low stress levels and, again, the same exponential relation indicates the number of atoms that have sufficient energy to overcome the interatomic bonds restricting the motion of a dislocation. Dislocation creep is a non–Newtonian mechanism, meaning that the relation between stress and strain rate is non–linear, namely exponential. This mechanism does not depends on grain size.

The transition between the dislocation and diffusion creep occurs when, for a given stress, the strain rates given by the two mechanisms are equal. In general, for a given stress, the deformation mechanism with the larger strain rate, or with lower viscosity, prevails. The most abundant mineral in the upper mantle is the olivine and probably, is also the weakest. Thus its rheology is likely to be dominant and usually olivine viscosity is used as an estimate of the viscosity of the mantle (Kirby, 1983; Ranalli, 1995; Hirth and Kohlstedt, 2003).

Theoretical treatments and experimental observations demonstrate that the macroscopic creep behavior of rocks is well described using a “power–law” of the form (Ranalli, 1995; Karato and Wu, 1993; Regenauer-Lieb et al., 2006)

$$\dot{\varepsilon} = A \left(\frac{\sigma}{\nu}\right)^n d^{-m} \exp\left(-\frac{E + pV}{RT}\right) \tag{2.17}$$

where $\dot{\varepsilon} = \frac{1}{2}\dot{\varepsilon}_{ij}\dot{\varepsilon}_{ij}$ is the second invariant of the strain rate with dimension s^{-2}, σ the

deviatoric stress in Pa, ν the shear modulus, d the grain size in mm, E the activation energy in kJ mol^{-1}, V the activation volume in J MPa mol^{-1}, T the temperature in K, p the pressure in Pa, R the gas constant and A is a constant. The viscosity is defined as

$$\eta = \frac{\sigma}{2\,\dot{\varepsilon}} \tag{2.18}$$

therefore, deformation is directly related to viscosity. Replacing (2.17) into (2.18) an explicit Arrhenius expression for viscosity is obtained

$$\eta = A_D^{-1/n}\,\dot{\varepsilon}^{(1-n)/2n}\,\exp\left(\frac{E + p\,V}{nRT}\right) \tag{2.19}$$

where A_D is a constant depending on the material with units MPa^{-n} s^{-1} and n the flow law exponent. Using different parameters, this expression describes both the diffusion and dislocation creep components for mantle and crustal materials. To compute the viscosity we assume a constant material parameter $A_D = \frac{1}{2}\,A^{-1/n}\mu^{-1}\,(b/d)^{-m/n}$, including the pre-exponential factor A, the grain–size dependence, and the shear modulus. Although grain–size may change due to grain growth and dynamic recrystallization processes, its dependence on stress is not well known. Thus, we consider only constant grain sizes, $d = 3$ mm, found in diatremes and ophiolites (Schubert et al., 2001).

Viscosity parameters used in this work are taken from Karato and Wu (1993), from Hirth and Kohlstedt (2003), from Ranalli (1995) and from van Hunen et al. (2004).

Diffusion and dislocation creep act simultaneously in the mantle (Ranalli, 1995). In order to account for the effect of the two mechanisms, two different viscosities η_{diff} and η_{disl} are computed separately and then combined into an effective viscosity η_{eff}, which is computed as the harmonic mean of η_{diff} and η_{disl}

$$\frac{1}{\eta_{\text{eff}}} = \left(\frac{1}{\eta_{\text{diff}}} + \frac{1}{\eta_{\text{disl}}}\right). \tag{2.20}$$

This expression is truncated if the resulting viscosity is either greater or lower than two imposed cutoff values (usually 10^{18} to 10^{24} Pa s^{-1}).

It is worthwhile to note the strongly non–linear character of the constitutive equation. Changes in deviatoric stress by a factor of two, change the viscosity by an order of magnitude. Changes on temperature of 100 K, change the viscosity by an order of magnitude. Changes in the activation volume by a factor of two, change the viscosity below 300 km depth by two or three orders of magnitude.

2.4.1 Quasi–brittle deformation

At temperatures lower than about 700 K, the viscous rheology for solid rocks is combined with a quasi–brittle rheology to yield an effective rheology. For this purpose the Mohr–Coulomb law (e.g. Ranalli, 1995; Brace and Kohlstedt, 1980) is simplified to the yield stress criterion, σ_{yield}, and implemented by a limiting of creep viscosity, η_{creep}, as follows

$$\eta_{\text{creep}} \leq \frac{\sigma_{\text{yield}}}{2\,\dot{\varepsilon}} \tag{2.21a}$$

$$\sigma_{\text{yield}} = \big(a\,p_l + b\big)(1-\lambda) \tag{2.21b}$$

where $\lambda = p_f/p_l$ is the pore fluid pressure coefficient, i.e., the ratio between pore fluid pressure p_f, and lithostatic pressure p_l; $a = 92.85$ and $b = 0$ are empirical constants (Brace and Kohlstedt, 1980).

2.5 Dimensional analysis

Heat equation. The goal of this dimensional analysis is to evaluate the relative importance of the different terms involved in the heat equation. Namely, the importance between the convective and the conductive terms. This information is used later to choose the proper numerical algorithm to solve the equation. The obtained relations between terms is not fixed and in different situations the order of involved variables may change through time and the importance between terms inverted, as discussed in Section 2.1. Furthermore, sometimes a variable, for example the velocity, has relevant spacial variations at the same time. This generates serious numerical difficulties. Nevertheless, the main behavior of the equation corresponds with the following analysis.

Dimensional analysis of the heat equation is based on the following dimensionless variables (primes denote dimensionless values)

$$\begin{array}{rclcrcl} x' &=& x/h & & T' &=& T/\Delta T \\ t' &=& t\,\kappa/h^2 & & v' &=& v\,h/\kappa \\ f' &=& \frac{f}{\rho\,C_p}\,\frac{h^2}{\Delta T\,\kappa} & & k' &=& \frac{k}{\rho\,C_p}\,\frac{1}{\kappa} \end{array}$$

where h is the height of the domain under consideration, ΔT the maximum temperature jump in the model and κ the thermal diffusivity in $m^2 s^{-1}$. Using previous dimensionless variables the thermal equation results in (Schmeling and Marquart, 1991)

$$\frac{\partial T'}{\partial t'} + \mathbf{u}' \cdot \nabla T' = \nabla \cdot (k'\,\nabla T') + f'$$

Quantity	Value	Units
h	660	km
$\|\mathbf{u}\|$	1.6×10^{-9}	m s^{-1}
ρ	3600	kg m^{-3}
C_p	1000	J $kg^{-1}K^{-1}$
κ	10^{-6}	m^2s^{-1}
k	4	W $m^{-1}K^{-1}$
ΔT	1600	K
f	10^{-8}	W m^{-3}
g	9.8	m s^{-2}
α	5×10^{-5}	K^{-1}
η	10^{21}	Pa s

Table 2.1 – Representative upper mantle values used in the dimensionless analysis of Stokes and heat equations.

Using the characteristic values listed in Table 2.1, the following coefficients are obtained

$$\begin{aligned} k' &= 2{,}29 \\ f' &= 7{,}88{\cdot}10^{1} \\ \|\mathbf{u}'\| &= 1{,}98{\cdot}10^{3} \end{aligned}$$

The convective term $\mathbf{u}' \cdot \nabla T'$ dominates the heat equation in the upper mantle and transition zone. Because of the variable velocity distribution, the time increment at each step needs to be carefully computed to keep numerical solutions in its stable domain, see Section 3.3.2.

Stokes equation. The dimensionless form of the Stokes equation involves two variables, the *Prandtl* number characterizing the convection regime and the G coefficient defined as

$$Pr = \frac{\eta}{\kappa\rho} \qquad \text{and} \qquad G = \frac{h^3 g \rho}{\eta\kappa}.$$

The dimensionless Stokes equation reads

$$\frac{1}{Pr}\mathbf{u}_t = -\nabla P + \nabla^2 \mathbf{u} - G.$$

Using the representative values for mantle materials, the coefficients of the equation (2.5) take the values $Pr^{-1} = 3.6 \times 10^{-24}$ and $G = 1.01 \times 10^7$. The relation between former values (they differ in more than 30 orders of magnitude) supports neglecting the inertia term. Thus, the time disappears from the Stokes equation and

the problem becomes quasi–static.

Other helpful dimensionless parameter characterizing vigor of convection is the *Rayleigh* number Ra defined as

$$Ra = \frac{\alpha \, \Delta T \, \rho^2 \, g \, h^3 \, C_p}{\eta \, k}$$

Using representative values for the mantle a Rayleigh number $Ra = 4.38 \times 10^5$ is obtained. Representative values for the upper mantle are listed in Table 2.1

2.6 Mineral phase transitions

The physical properties of a rock depend on the proportions and the compositions of the mineral phases. These, in turn, depend on temperature, pressure and composition. In general, one cannot assume that the mineralogy is constant when temperature and pressure varies. In the upper mantle the most important minerals determining physical properties are olivine, ortho and clinopyroxene and aluminium–rich phases such as plagioclase, spinel and garnet. All these minerals are unstable at high pressure and therefore only exist in the upper part of the mantle. Clinopyroxene, diopside plus jadeite, may be stable to depths as great as 500 km. Olivine transforms successively to wadsleyite, a spinel–like structure, near 410 km depth and to ringwoodite, a cubic spinel, near 500 km depth. At higher pressure it transforms to perovskite plus magnesiowüstite. Orthopyroxene transforms to majorite, a garnet–like phase.

The variations in mantle properties depend, to first order, on stable mineral phases and, to second order, on the variation of temperature and pressure. In order to model densities one must know the expected equilibrium assemblage and the properties of the phases. Transformations within the mantle draw a complex diagram such as shown in Figure 2.1

To model the effect of mineral transformation into the physical properties of rocks, we simplify the diagram considering four mineral domains shown in Figure 2.1. Each domain is defined following the phases transformation of the olivine: olivine to wadsleyite at 410 km depth, wadsleyite to ringwoodite at 510 km depth and ringwoodite to magnesium perovskite+ferropericlase at 660 km depth. These mineral transformations are the most relevant in terms of density and viscosity contrasts due to the abundance of the olivine in the mantle (more than 60%). Moreover, they are the responsible of the strongest discontinuities in seismic velocities at corresponding depths.

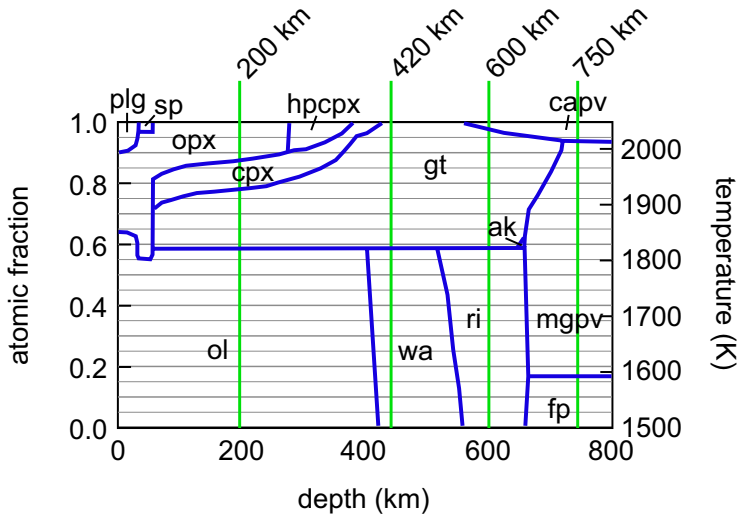

Figure 2.1 – Phase equilibria after Stixrude and Lithgow-Bertelloni (2007). Mineral species are described in Table 2.2. Mineral domains used in this work are shown in green.

Symbol	Meaning	Value used
pl	olivine	$[Mg_xFe_{1-x}]_2SiO_4$
opx	orthopyroxene	$[Mg_xFe_{1-x}]_{2-y}Al_{2y}Si_{2-y}O_6$
sp	spinel	$Mg_xFe_{1-x}Al_2O_4$
cpx	clinopyroxene	$Ca_{1-y}[Mg_xFe_{1-x}]_{1+y}Si_2O_6$
gt	Garnet	$Fe_{3x}Ca_{3y}Mg_{3(1-x+y+z/3)}Al_{2-2z}Si_{3+z}O_{12}$; $x+y+4z/3 \leq 1$
C2/c	pyroxene	$[Mg_xFe_{1-x}]_4Si_4O_{12}$
ak	akimotoite	$Mg_xFe_{1-x-y}Al_2ySi_{1-y}O_3$, $x+y \leq 1$
mgpv	perovskite	$Mg_xFe_{1-x-y}Al_2ySi_{1-y}O_3$, $x+y \leq 1$
ppv	post-perovskite	$Mg_xFe_{1-x-y}Al_2ySi_{1-y}O_3$, $x+y \leq 1$
ri	ringwoodite	$[Mg_xFe_{1-x}]_2SiO_4$
wa	wadsleyite	$[Mg_xFe_{1-x}]_2SiO_4$
wu	magnesiowüstite	$Mg_xFe_{1-x}O$
hpcpx	high pressure clinopyroxene	$Ca_{1-y}[Mg_xFe_{1-x}]_{1+y}Si_2O_6$
plg	plagioclase	$[(NaAlSi)_x(CaAl_2)_{1-x}]Si_2O_8$
fp	ferropericlase	$[Mg_xFe_{1-x}]O$
capv	calcium perovskite	$La_{1-x}Ca_xCo_{1-y}Fe_yO_3$

Table 2.2 – Solution notation and formulae. Unless otherwise noted, the compositional variables x, y, and z may vary between zero and unity.

In practice the phase transitions determining the mineral domains are characterized by a particular Clapeyron slope, which we approximate as linear functions in the temperature–pressure domain (See Figure 2.2).

Table 2.3 lists values for Clapeyron slopes reported by different authors.

The average rock properties are computed as follow: i) the volumetric fractions of the major constituent phases along a 1600 K adiabat are taken from Stixrude

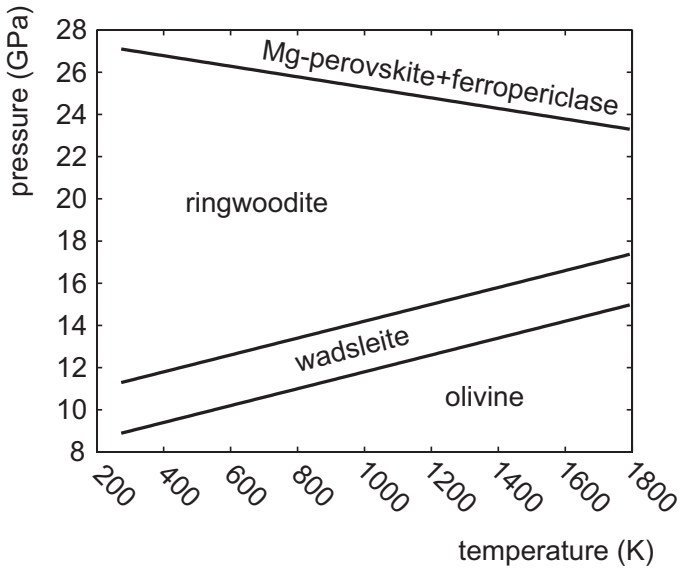

Figure 2.2 – Main domains of stable mineral species. Clapeyron curves, here approximated as straight lines, determine the equilibrium between phases.

Transition	Temperature (K)	Pressure (MPa)	Slope (MPa K^{-1})	Ref
ol to wa	1600	14200	4.0	*a*
ol to wa	1600	14200	3.6	*b*
ol to wa	1700	13500	2.5	*c*
ol to wa	1700	13500	1.5	*d*
wa to ri	1700	17000	4.0	*e*
ri to mgpv	1873	23100	-2.5	*c*
ri to mgpv	1873	23100	-3.0	*f*

Table 2.3 – References: *a* from Katsura et al. (2004), *b* from (Guest et al., 1994), *c* from Katsura and Ito (1989), *d* from Akaogi et al. (1989), *e* from Guest et al. (2004), *f* from Ito and Takahashi (1989)

and Lithgow-Bertelloni (2007) (See Table 2.4), ii) each phase is identified with only one (the most abundant) end–member (e.g. enstatite for opx, diopside for cpx, pyrope for grt), iii) experimentally derived properties of these end–members are taken from works listed in Tables 2.3 to 2.5, and finally iv) the average rock properties are computed as either the arithmetic mean of the end–members weighted by their respective volumetric proportions or with a Voigt–Reuss–Hill averaging scheme. The latter is used only when calculating the elastic moduli for seismic velocities. We acknowledge that this approach is only valid to the first–order and lack thermodynamic consistency. However, it gives values comparable to those obtained with more sophisticated methods (e.g. Stixrude and Lithgow-Bertelloni, 2005; Stixrude and Lithgow-Bertelloni, 2007) with a minimum of computational time.

Mineral	200 km	420 km	600 km	800 km
Olivine(Fo)	51.3%	0	0	0
Olivine(Fa)	5.7%	0	0	0
Orthopyroxene(Enstatite)	13.5%	0	0	0
Clinopyroxene(Diopside)	10.0%	0	0	0
Garnet (Pyrope)	19.6%	40.0%	37.5%	0
Wadsleyite	0	60.0%	0	0
Ringwoodite	0	0	60.0%	0
Ferropericlase	0	0	0	16.0%
Mg perovskite	0	0	0	78.0%
Ca perovskite	0	0	2.5%	6.0%

Table 2.4 – Stable phases at different depths used to construct the mineral domains. After Stixrude and Lithgow-Bertelloni (2007).

2.7 Thermal expansion coefficient

The thermal expansion coefficient $\alpha = V^{-1}(\partial V/\partial T)_p$, is used to express the volume change of a material due to a temperature change. It controls the variations of density as a function of temperature. The Grüneisen theory of thermal expansion (Suzuki et al., 1979) combined with the Debye model of solids (e.g. Stixrude and Bukowinski, 1990), leads to a relation between volume and temperature, based on four parameters. To fit these, accurate experimental measures of thermal expansivity are needed over a wide range of temperatures. In many cases the fitting cannot be uniquely defined, either because the accuracy of thermal expansion measurement is not sufficiently high or because the temperature range of measurement is limited. For the purpose of fitting experimental data over a specific temperature range, a polynomial expression for the thermal expansion coefficient may be used. Fei (1995) compiled a widely used data set composed by 359 fittings of 121 minerals in different conditions. He uses the expression

$$\alpha(T) = a_0 + a_1 T + a_2 T^{-2}. \tag{2.22}$$

Some newer data tables include an additional term $a_3 T^{-4}$ to improve the accuracy of the approximation (for example Schutt and Lesher (2006)). Here we use the polynomial expression 2.22 with data from Table 2.5. The data from experimentalist correspond to single mineral species. Mantle rocks are composed by aggregates of minerals, therefore the thermal expansion of each mineral specie have to be averaged to obtain the bulk thermal expansion. Here a weighted average with mineral proportions is used. For each one of the four compositions described in Section 2.6

Mineral	$a_0(\times 10^{-5})$	$a_1(\times 10^{-8})$	a_2	a_3
Forsterite[a]	2.85	1.01	-0.348	0
Fayalite[a]	2.39	1.15	-0.0518	0
Orthopyroxene[a]	2.95	0.57	0	0
Clinopyroxene[a]	2.60	1.15	0	0
Granate[a]	2.02	0.74	-0.461	0
Wasdleyite[b]	2.71	0	0	0
Ringwoodite[b]	2.37	0	0	0
Ferropericlase[d]	3.49	0.685	-0.372	0
Mg Perovskite[c]	1.86	0	0	0
Ca Perovskite[d]	3.50	0	0	0
Average at depth				
200 km	2.65	0.92	-0.2712	0
420 km	2.43	0.29	-0.1842	0
600 km	2.26	0.27	-0.1726	0
750 km	2.22	0.11	-0.0595	0

Table 2.5 – Parameters for thermal expansion formula. For single mineral species and for mantle aggregates at different depths. Parameters for the different phases were taken from: Forsterite, Fayalite, Enstatite, Diopside, Pyrope: (Afonso et al., 2007); Wadsleyite, Ringwoodite: (Akaogi et al., 1989); Ferropericlase, Ca–Perovskite: (Fei, 1995); Mg–Perovskite:(Oganov et al., 2001).

the coefficients a_0 to a_3 are calculated based on the phase equilibria from Stixrude and Lithgow-Bertelloni (2007).

The effect of pressure on the thermal expansion coefficient becomes important in thick (i.e. cold) lithospheres. Pressure dependence can be described by the AndersonGrüneisen parameter δ_T (Chopelas, 2000; Afonso et al., 2005)

$$\alpha(T,P) = \alpha(T) \left(\frac{\rho(T,P)}{\rho(T)} \right)^{\delta_T \frac{\rho(T)}{\rho(T,P)}}$$

In order to save computational time, we keep calculations of physical properties explicit (we neglect non–linear behavior). Thus, the term $\rho(T,P)/\rho(T)$ in the previous expression is approximated using the compressibility coefficient β (10^{-5} MPa^{-1}) as

$$\frac{\rho(T,P)}{\rho(T)} \approx 1 + \beta(p - p_0) \tag{2.23}$$

We have used a typical average $\delta_T = 5.5$, consistent with theoretical and experimental estimations (Chopelas, 2000; Anderson et al., 1992; Afonso et al., 2005).

2.8 Thermal conductivity

Despite thermal conductivity in single crystals is usually anisotropic, the random distribution of crystals forming a rock makes the isotropic assumption fair. The experimental measurements of the thermal conductivity and, consequently, the empirical laws derived from them, include the effect of the heat transport by black–body radiation. Thus, thermal conductivity coefficient used here accounts for both heat transfer by vibrations of adjacent atoms (conduction) and heat transfer by electromagnetic waves (radiation).

Two different options to calculate thermal conductivity as a function of temperature and pressure are tested. Firstly, an empirical formula given by Clauser and Huenges (1995). Despite this formula was formulated for approximating thermal conductivity in crustal rocks, it was extended to mantle materials in previous works (e.g. Gerya et al., 2004). The coefficients for both, crustal and mantle rock are (Gerya et al., 2004)

Oceanic crust	$[1.18 + 474/(T + 77)] \times \exp(4 \times 10^{-5} p)$
Mantle	$[0.73 + 1293/(T + 77)] \times \exp(4 \times 10^{-5} p)$

where temperature T is expressed in Kelvin units and pressure p in MPa. Resulting conductivity has units W $\mathrm{m}^{-1}\mathrm{K}^{-1}$.

The second formulation used to model thermal conductivity is that proposed by Hofmeister (1999). It based on phonon lifetimes obtained from reflectance spectra. The conductivity is calculated as

$$k(T,p) = k_{298} \left(\frac{298}{T}\right)^{a} \exp\left[-\left(4\gamma + \frac{1}{3}\right) \int_{298}^{T} \alpha(\theta)\,\mathrm{d}\theta\right] \left(1 + \frac{K_0' p}{K_0}\right) + k_{\mathrm{rad}} \quad (2.24)$$

where k_{298} is the thermal conductivity measured at ambient conditions, a is a parameter with an approximated value of 0.33 for all silicates, γ is the averaged Grüneisen parameter with values for the mantle from 1 to 1.4, K_0 is the bulk modulus with value 120 GPa, and K_0' its derivative with respect to pressure, with values between 4 and 5. The last term k_{rad} is the contribution of the radiation phenomena, approximated by the polynomial function

$$k_{\mathrm{rad}} = a + b\,T + c\,T^2 + d\,T^3 \quad (2.25)$$

where temperature T is in Kelvin, and the values of constants a to d are

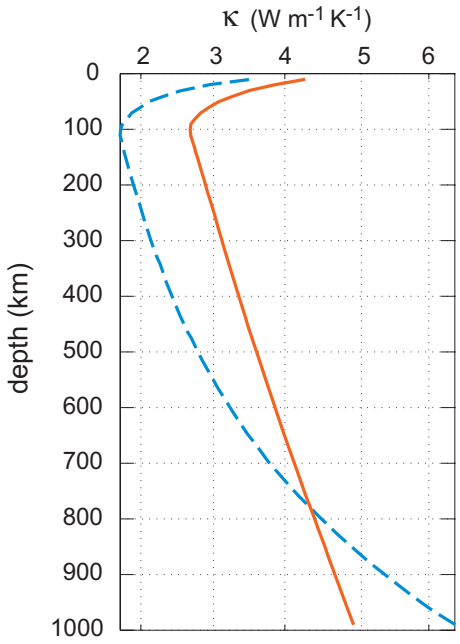

Figure 2.3 – Thermal conductivity coefficient as a function of depth. Dashed line from Clauser and Huenges (1995). Solid line from (Hofmeister, 1999).

$$
\begin{aligned}
a &= 1.753 \times 10^{-2} \\
b &= 1.0365 \times 10^{-4} \\
c &= 2.2451 \times 10^{-7} \\
d &= 3.407 \times 10^{-11}
\end{aligned}
$$

The integral of the thermal expansion coefficient in equation (2.24) is computed in practice taking into account all the mineral phase transformations described in Section 2.6. Thermal conductivity computed using both formulations is shown in Figure 2.3. Values of mantle rocks at the base of the lithosphere are underestimated by the equation of Clauser and Huenges (1995).

2.9 Density

Most of the density change in the mantle is due to hydrostatic compression. Density changes associated with temperature and pressure variations accompanying convection are small compared to the spherically averaged density of the mantle. Therefore, it is appropriate to simplify the density ρ as a function of temperature T and pressure p with respect to a reference value ρ_0 as

$$\rho(p,T) = \rho_0 \left[1 - \alpha \times (T - T_0)\right] \times \left[1 + \beta \times (p - p_0)\right] \tag{2.26}$$

where α is the thermal expansion coefficient, β the compressibility coefficient, and T_0 and p_0 are, respectively, the temperature and pressure at which the reference density ρ_0 is given. This relation becomes non–linear due to the dependency of α and β on temperature and pressure.

There are significant density variations associated with phase transitions. To account for them in our model, the reference density ρ_0 depends on the mineral phase domain.

Chapter 3

Numerical approach

The model introduced in Chapter 2 is composed of two main ingredients: a mechanical flow problem governed by the Stokes equation and a transient heat problem. Neither has a general analytical solution. In some simple cases analytical methods can be used but, in the general case, numerical techniques are required to obtain approximations of the solution.

The primary technique used in this work to approximate solutions of partial differential equations, as the Stokes and the heat equations, is the Finite Element Method (FEM). It is based on a variational or weak statement of the problem and a discretization of the variational equations. The FEM is generally attractive because it is robust, flexible in its ability to model complex geometry, algorithmically modular, and mathematically very well understood. The FEM has a long history in geodynamics, predominantly because of its ability to accurately solve problems with strong gradients (Moresi et al., 1996), but also because its geometrical flexibility; it allows for modeling spherical and cartesian domains without reformulating the equations in spherical coordinates. Adopting the FEM as the basis for the numerical solution allows dealing with material properties with steep variations (large gradients).

Another widely used technique to solve partial differential equations is the Finite Difference method (FD). Both techniques, FEM and FD, are based on a discretization (supported by a mesh) of the simulation domain. FEM uses unstructured meshes allowing for concentrating elements in the regions where more resolution is needed while leaving coarse regions where the solution is "simpler" or easier to interpolate. As the standard version of FD requires using structured meshes, it is difficult to control the resolution in different regions of the domain. Moreover, curved boundaries and boundaries not parallel to the cartesian axis are difficult to handle with DF while it is straightforward with FEM. For example, the simulations

on a spherical domain presented in Section 7 may be complex to model in a FD framework and probably they require to rewrite all equations in polar coordinates. Despite in most cases DF are used only because of reutilization of preexisting codes, there are some new developments using FD (e.g. Gerya and Yuen, 2007).

To solve the coupled model introduced in the previous chapter several techniques and algorithms are needed. These techniques complement the FEM. For example a *Padé* method is used to integrate the thermal equation trough time, a *Level Set* technique is used to track the location of the different materials, an *enrichment* technique via partition of the unity is used to allow for a solution with discontinuous gradient across the interfaces, a *Taylor–Galerkin* algorithm is used to update through time the level set functions, a basic *Picard* method is used to handle non–linearities generated by the rheologic constitutive equation, etc. In some simple models *mesh adaptivity* is used to improve accuracy and efficiency.

The mechanical flow problem described in Section 2.2 is solved by a mixed Finite Element Method with both velocity and pressure unknowns. Its multiphase character is handled by a *level set* technique. The level set approach is a computationally efficient way of tracking the different materials location. It allows for describing the interface without requiring it to conform with the mesh. A solution with discontinuous gradient on the interface described by the level set is expected. The discontinuity is generated by the jump of material properties across this interface. Here we *enrich* the finite element solution allowing for a discontinuous gradient inside the elements crossed by the level set, using a X–FEM technique. Classical finite elements cannot handle with such a solution. Moreover, the mechanical problem is non–linear due to the viscosity dependence on the velocity gradient. We found that a basic Picard method suffices to solve the non–linear problem up to the accuracy required. In Section 3.1 these techniques and their applications are described. The thermal equation is discretized in space using standard finite elements and updated through time using a Padé method as described in Section 3.2. The coupling between the mechanical and the thermal problem is handled in a staggered scheme.

This chapter is devoted to describe all the numerical methodologies used to solve the coupled transient non–linear equations. Most of the content of this chapter pertains to two original papers (Zlotnik et al., 2007a,b).

3.1 Mechanical flow problem

The numerical solution of the mechanical Stokes flow problem via mixed finite elements is described in this section. Stokes equation states the dynamical effect

of the externally applied forces and the internal forces of a fluid. The internal forces are due to the pressure and the viscosity of the fluid. A flow region $\Omega \in \Re^n$, with boundary Γ closed and sufficiently regular is considered. Then, the flow of a viscous incompressible fluid is governed by the momentum equation (2.15) introduced in Section 2.2.6

$$-2\nabla \cdot (\eta \nabla^s \mathbf{u}) + \nabla p = \rho \mathbf{g}$$

and the mass conservation equation (2.10)

$$\nabla \cdot \mathbf{u} = 0.$$

The problem must be completed with suitable boundary conditions. Typically the velocity $\mathbf{u}_\mathrm{D}$ is prescribed on a portion Γ_D of the boundary

$$\mathbf{u}(\mathbf{x}, t) = \mathbf{u}_\mathrm{D}(\mathbf{x}, t) \qquad \mathbf{x} \in \Gamma_\mathrm{D}, \quad t \in (0, T)$$

and a boundary traction $\mathbf{t}$ is imposed on the complementary portion Γ_N

$$\mathbf{n}\,\boldsymbol{\sigma}(\mathbf{x}, t) = \mathbf{t}(\mathbf{x}, t) \qquad \mathbf{x} \in \Gamma_\mathrm{N}, \quad t \in (0, T) \tag{3.1}$$

where vector $\mathbf{n}$ denotes the unit outerward normal to the boundary. The initial value of the velocity field at the initial time $t = 0$ is given in Ω

$$\mathbf{u}(\mathbf{x}, t) = \mathbf{u}_0(\mathbf{x}) \qquad \mathbf{x} \in \Omega. \tag{3.2}$$

No initial condition needs to be specified for the pressure. This is a consequence of the fact that no time derivative of pressure appears in governing equations. When velocity is imposed everywhere on the boundary Γ, pressure is only present by its gradient in the Stokes equation and thus it is determined only up to an arbitrary constant.

Some difficulties arise in the resolution of incompressible flow problems. The incompressibility condition expressed in equation (2.10) is a constraint on the velocity field which must be divergence free. Then the pressure must be considered as a variable not related to any constitutive equation. Its presence in the momentum equation has the purpose of introducing an additional degree of freedom needed to satisfy the incompressibility constraint. The role of the pressure variable is thus to adjust itself instantaneously in order to satisfy the condition of divergence free velocity. That is, the pressure is acting as a Lagrangian multiplier of the incompressibility constraint and thus there is a coupling between the velocity and

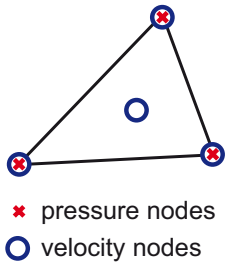

Figure 3.1 – Mini–element

the pressure unknowns (Donea and Huerta, 2002).

The variable formulation with both velocity and pressure unknowns, leads to the so-called mixed finite elements. Such methods present numerical difficulties caused by the *saddle point* nature of the resulting variational problem. The algebraic system for the nodal values of velocity and pressure in a Galerkin formulation is governed by a partitioned matrix with a null sub matrix on the diagonal. Solvability of such a system depends on a proper choice of finite element spaces for velocity and pressure interpolation. In this work the well–known mini–element is used (see Figure 3.1). This triangular element is composed by three pressure nodes at the vertices (linearly interpolated) and four velocity nodes (three linear nodes at the vertices and one central quadratic node). The mini–element satisfy the LBB compatibility condition (after Ladyzhenskaya, 1969; Babuška, 1970; Brezzi, 1974) which guarantees the solvability of the system.

An alternative to the mixed scheme is the penalty formulation. It is used in some geophysical codes, for example ConMan (King et al., 1990) and CitCom (Moresi and Solomatov, 1995). The penalty method allows for elimination of the pressure variable from the Navier–Stokes problem through a relaxation of the incompressibility condition. The problem then involves only velocities, making the penalty method computationally attractive. A numerical disadvantage is the presence of the penalty parameter λ, which may cause a loss of accuracy for excessively large values of λ, and prevent convergence to the actual solution for insufficiently large parameter. In the physical model material properties depend on pressure. Therefore, if a penalty formulation is used, the pressure is usually approximated by a linear function. This approximation neglects density variations and looses the dynamic part of the pressure.

3.1.1 Strong and weak formulations

The mixed Finite Element Method applied to a single–phase Stokes flow is next described. The multiphase character of the problem will be address in Section 3.1.2. From the numerical point of view the problem can be stated in a strong form as: given the body force field $\mathbf{g}$, the viscosity field η and the boundary conditions for velocity $\mathbf{u}_D$ in the boundary Γ_D, find the velocities $\mathbf{u}$ and the pressures p, such that

$$-2\nabla \cdot (\eta \nabla^{\mathrm{s}} \mathbf{u}) + \nabla p = \rho \mathbf{g} \qquad \text{in } \Omega \tag{3.3a}$$

$$\nabla \cdot \mathbf{u} = 0 \qquad \text{in } \Omega \tag{3.3b}$$

$$\mathbf{u} = \mathbf{u}_D \qquad \text{in } \Gamma_D \tag{3.3c}$$

$$\mathbf{n}\,\boldsymbol{\sigma} = \mathbf{t} \qquad \text{in } \Gamma_N \tag{3.3d}$$

where the symmetric gradient operator ∇^s is defined as $\nabla^s = \frac{1}{2}(\nabla + \nabla^\top)$ (see Section 2.2.4).

The formulation of the weak problem requires the following definition: a function u is square–integrable on a domain Ω if

$$\int_\Omega u^2 \, \mathrm{d}\Omega < \infty$$

and we write $u \in \mathcal{L}^2(\Omega)$. $\mathcal{H}^k(\Omega)$ is defined as the set of functions such that itself and all its derivatives up to order k are in $\mathcal{L}^2(\Omega)$.

The formulation of the weak form of the problem involves the definition of four collections of functions: the *test* functions and the *trial solution* functions, for the velocity field and for the pressure field. The space of velocity trial functions is denoted by $\mathcal{S}$. This collection of functions consists of all functions which are square–integrable, have square integrable first derivatives over the computational domain Ω and satisfy the Dirichlet boundary conditions on Γ_D defined in (3.3c). This collection is defined by

$$\mathcal{S} = \left\{ u \in \mathcal{H}^1(\Omega) \,|\, u = u_D \text{ on } \Gamma_D \right\}.$$

This space contains vector functions such that each component is in the corresponding space of scalar functions.

The test functions for velocity belong to space $\mathcal{V}$. Functions in this class have the same characteristics as those in $\mathcal{S}$, except that they are required to vanish in Γ_D

where the velocity is prescribed. The $\mathcal{V}$ space is defined by

$$\mathcal{V} = \left\{ w \in \mathcal{H}^1(\Omega) \,|\, w = 0 \text{ on } \Gamma_D \right\}.$$

Finally, we introduce a space of functions, denoted $\mathcal{Q}$, for the pressure. Since the space derivatives of pressure do not appear in the weak form of the Stokes problem, the functions in $\mathcal{Q}$ are simply required to be square integrable

$$\mathcal{Q} = \left\{ q \in \mathcal{L}^2(\Omega) \right\}.$$

This space is both the trial space and the test function space. In the case of a purely Dirichlet velocity boundary condition, the pressure is defined up to a constant, and its value must be prescribed at one point of the domain Ω.

To obtain the weak formulation of the problem, the governing equation (3.3a) is multiplied by a velocity test function $\mathbf{w} \in \mathcal{V}$ and integrated over the domain Ω. Similarly, the incompressibility condition (3.3b) is multiplied by the pressure test function $q \in \mathcal{Q}$ and integrated, obtaining

$$\int_\Omega \mathbf{w} \cdot \nabla p \, \mathrm{d}\Omega - 2 \int_\Omega \mathbf{w} \cdot \left(\nabla \cdot \left(\eta \nabla^{\mathrm{s}} \mathbf{u} \right) \right) \, \mathrm{d}\Omega = \int_\Omega \mathbf{w} \cdot \rho \mathbf{g} \, \mathrm{d}\Omega \tag{3.4a}$$

$$\int_\Omega q \left(\nabla \cdot \mathbf{u} \right) \, \mathrm{d}\Omega = 0 \tag{3.4b}$$

Integrating by parts the second term on the left hand side of equation (3.4a) results in

$$\int_\Omega \mathbf{w} \cdot \left(\nabla \cdot \left(\eta \nabla^{\mathrm{s}} \mathbf{u} \right) \right) \, \mathrm{d}\Omega = \int_\Omega \nabla \cdot \left(\mathbf{w} \cdot \eta \nabla^{\mathrm{s}} \mathbf{u} \right) \mathrm{d}\Omega - \int_\Omega \nabla \mathbf{w} : \eta \nabla^{\mathrm{s}} \mathbf{u} \, \mathrm{d}\Omega. \tag{3.5}$$

where the following notation has been introduced:

$$\nabla \mathbf{u} : \nabla \mathbf{v} = \sum_{i=1}^{m} \sum_{j=1}^{n} \frac{\partial u_i}{\partial x_j} \frac{\partial v_i}{\partial x_j}.$$

Applying the Green–Gauss divergence theorem on the first integral of the right hand side of equation (3.5) we obtain

$$\int_\Omega \nabla \cdot \left(\mathbf{w} \cdot \eta \nabla^{\mathrm{s}} \mathbf{u} \right) \mathrm{d}\Omega = \int_\Gamma \left(\mathbf{w} \cdot \eta \nabla^{\mathrm{s}} \mathbf{u} \right) \cdot \mathbf{n} \, \mathrm{d}\Gamma \tag{3.6}$$

where $\mathbf{n}$ is the outer normal vector to the boundary.

The last term of (3.5) can be written as

$$\int_\Omega \nabla \mathbf{w} : \eta \nabla^{\mathrm{s}} \mathbf{u} \, \mathrm{d}\Omega = \int_\Omega \nabla^{\mathrm{s}} \mathbf{w} : \eta \nabla^{\mathrm{s}} \mathbf{u} \, \mathrm{d}\Omega. \tag{3.7}$$

In this last step the gradient $\nabla \mathbf{w}$ is replaced by its symmetric part. The replacement is valid due to the split of the gradient $\nabla \mathbf{w}$ in its symmetric part and its skew–symmetric part as

$$\nabla \mathbf{w} = \nabla^{\mathrm{s}} \mathbf{w} + \nabla^{\mathrm{w}} \mathbf{w}. \tag{3.8}$$

As the double contraction of a skew–symmetric tensor with a symmetric tensor is zero, only the symmetric part remains and the replacement of (3.7) is justified.

Similarly, the first term of equation (3.4a), which involves the pressure gradient is integrated by parts. Applying the divergence theorem we obtain

$$\begin{aligned} \int_\Omega \mathbf{w} \cdot \nabla p \, \mathrm{d}\Omega &= \int_\Omega \nabla \cdot (\mathbf{w} p) \, \mathrm{d}\Omega - \int_\Omega p \, \nabla \cdot \mathbf{w} \, \mathrm{d}\Omega = \\ &= \cancelto{0}{\int_\Gamma \mathbf{w} p \, \mathbf{n} \, \mathrm{d}\Gamma} - \int_\Omega p \, \nabla \cdot \mathbf{w} \, \mathrm{d}\Omega. \end{aligned} \tag{3.9}$$

The integral on the boundary is zero due to the boundary conditions.

Making use of equations (3.5), (3.6), (3.7) and (3.8), the weak form of problem (3.3) becomes: given $\mathbf{g}$ and $\mathbf{u}_D$, find velocities $\mathbf{u} \in \mathcal{S}$ and pressures $p \in \mathcal{Q}$, such that for all velocity test functions $\mathbf{w} \in \mathcal{V}$ and all pressure test functions $q \in \mathcal{Q}$

$$\int_\Omega p \, \nabla \cdot \mathbf{w} \, \mathrm{d}\Omega - 2 \int_\Omega \nabla \mathbf{w}^{\mathrm{s}} : \eta \nabla^{\mathrm{s}} \mathbf{u} \, \mathrm{d}\Omega = 2 \int_\Gamma (\mathbf{w} \cdot \eta \nabla^{\mathrm{s}} \mathbf{u}) \cdot \mathbf{n} \, \mathrm{d}\Gamma + \int_\Omega \mathbf{w} \cdot \rho \mathbf{g} \, \mathrm{d}\Omega \tag{3.10a}$$

$$\int_\Omega q \nabla \cdot \mathbf{u} \, \mathrm{d}\Omega = 0 \tag{3.10b}$$

The proof of the equivalence of the strong and weak formulation can be found elsewhere, for example Hughes (2000); Zienkiewicz and Taylor (2000)

The Galerkin formulation of the Stokes problem leads to a mixed finite element method. Discretization $\mathbf{u}^h$ and p^h for velocity and pressure are introduced. The associated test functions $\mathbf{w}$ and q are also discretized as $\mathbf{w}^h$ and q^h. We denote $\mathcal{V}^h$ and $\mathcal{S}^h$ the finite dimensional subspaces of $\mathcal{V}$ and $\mathcal{S}$, and $\mathcal{Q}^h$ the finite dimensional subspace of $\mathcal{Q}$. These finite element spaces are characterized by a partition of the domain (a mesh). The computational domain Ω is partitioned into element domains Ω^e. This discretization or mesh is composed by elements and nodes.

The velocity is then formulated in terms of shape functions and associated nodal

values. We denote $\mathcal{N}$ the set of velocity nodes in the mesh. The subset $\mathcal{N}_D$ of $\mathcal{N}$ is the subset of velocity nodes corresponding to the Dirichlet boundary conditions, where the velocity is prescribed. The velocity is approximated as follows

$$\begin{aligned} \mathbf{v}^h &= \mathbf{u}^h + \mathbf{u}_D^h \\ \mathbf{u}^h &= \sum_{i \in \mathcal{N}} N_i(\mathbf{x})\, \mathbf{u}_i \\ \mathbf{u}_D^h &= \sum_{i \in \mathcal{N}_\mathcal{D}} N_i(\mathbf{x})\, \mathbf{u}_{Di} \end{aligned}$$

where N_i is the shape function associated with the node number i and $\mathbf{u}_i$ is the value of $\mathbf{u}^h$ at node i. The pressure field is interpolated using a different set of pressure nodes denoted by $\mathcal{N}_p$ and shape functions $\hat{N}_i$, as

$$p^h = \sum_{i \in \mathcal{N}_p} \hat{N}_i(\mathbf{x})\, p_i \tag{3.11}$$

where p_i is the pressure value at node i.

To complete de statement of the space discretization the technique used to track the location of the material phases is required. This technique, called level sets, is described in the next section.

3.1.2 Two–phase flow and the Level Set technique

Flow problems are naturally described in an *Eulerian* framework where the computational mesh is fixed and the fluid moves with respect to the grid. The Eulerian formulation facilitates the treatment of large distortions in the fluid motion. Its handicap is the difficulty to follow interfaces between different materials. In an Eulerian description the finite element mesh is thus fixed and the continuum moves and deforms with respect to the computational mesh. As the material flows "over" the mesh, the physical properties of one element (for example its density or viscosity) will change through time due to material advection.

Level set methods are computational techniques for tracking moving interfaces; they rely on an implicit representation of the interface. Since the introduction of the level set method by Osher and Sethian (Osher and Sethian, 1988), a large amount of bibliography on the subject has been published. See, for instance, the cited review by Sethian and Smereka (Sethian and Smereka, 2003) and the work by Osher and Fedkiw (Osher and Fedkiw, 2001). Level set methods are particularly designed for problems in multiple space dimensions in which the topology of the evolving interface changes during the course of events. This technique is commonly used in engineering

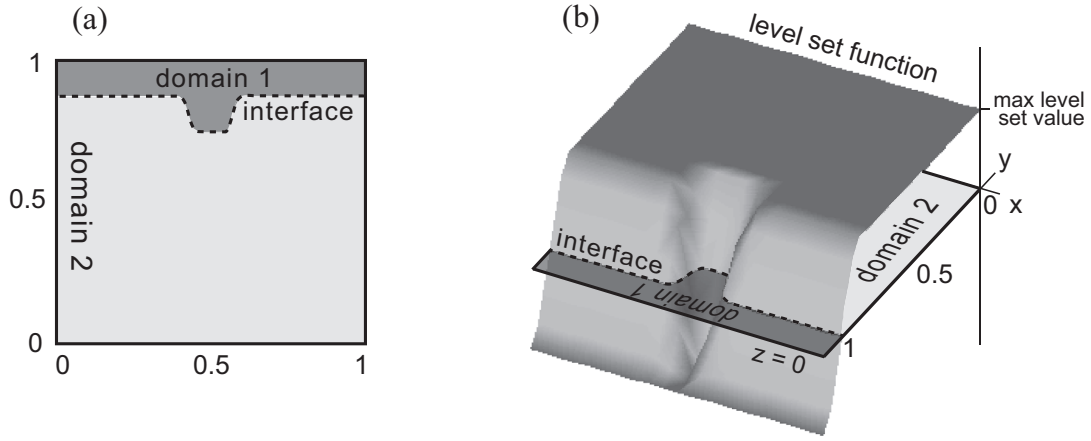

Figure 3.2 – Two material domains (a). Surface representation of the level set function ϕ (b). The sign of the function indicates the phases location.

problems to track interfaces location (e.g. Chessa and Belytschko, 2003; Moës et al., 2003) and cracks (e.g. Belytschko and Black, 1999; Stolarska et al., 2001). It is also used in computational geometry applications, in grid generations, computer vision and other applications.

The level set technique describes the location of the interface between materials by means of a function ϕ, called level set function, defined on the simulation domain. The sign of the level set function defines two geometrical domains using the following convention

$$\phi(\mathbf{x},t) = \begin{cases} > 0 & \text{for } \mathbf{x} \text{ in domain 1} \\ = 0 & \text{for } \mathbf{x} \text{ on the interface} \\ < 0 & \text{for } \mathbf{x} \text{ in domain 2} \end{cases} \tag{3.12}$$

where $\mathbf{x}$ stands for a point in the simulation domain and t is the time. The interface location is the set of points where the level set field vanishes (See Figure 3.2). The material corresponding to each point of the simulation domain is thus determined by the sign of the level set function.

Initially, ϕ is set as a signed distance to the interface. Far enough from the interface, ϕ is truncated by maximum and minimum cutoff values. The resulting level set function describes the position of the interface independently of the computational mesh.

In the practical implementation, ϕ is described (interpolated) with the finite element mesh, and therefore the resolution of the approximated interface depends on the quality of this mesh. Usually the same mesh of the mechanical problem is used to describe the level set function. This is a reasonable approach; same resolution is obtained in describing interfaces and velocities used to update these interfaces.

The level set represents interfaces which do not necessarily coincide with the element edges. Thus, the same mesh can be used throughout the entire simulation to describe the interface. Chapters 5 and 6 provide examples of simulations using the same mesh along time. Additionally, for some simple cases, we test a remeshing procedure based on the position of the interface (See Section 4.2). Mesh adaptivity allows for element concentration in the places where they are needed, while leaving coarse elements in less compromised areas. To locate phases, smaller elements close to the level set allows for an accurate description of the interface. As the level set function evolves, remeshing is needed to update the fine part of the mesh following the interface. The proposed adaptive scheme is described in Section 4.2.

The level set ϕ is a material property and consequently it is transported by the velocity. Therefore, it is updated by solving the following pure advection equation (first order hyperbolic)

$$\phi_t + \mathbf{u} \cdot \nabla \phi = 0 \tag{3.13}$$

where $\mathbf{u}$ is the velocity field computed by solving the Stokes problem (3.3) and ϕ_t the time derivative of the level set function. In this context, the velocity field is known in all the points of the domain. Thus, the level set is transported integrating equation (3.13) using an explicit time–marching scheme designed for the pure advective problem: the two–step third order Taylor Galerkin method (Selmin, 1987; Donea and Huerta, 2002). This method, described in Section 3.2.3, is straightforwardly implemented and computationally affordable. In similar situations other authors use the Hamilton–Jacobi equation to transport the interface. This is specially appropriate if the only available data is the front velocity, or if the velocity depends on the front itself, for example on its curvature. In the present situation the velocity is known everywhere as a vector and it is possible to directly integrate the pure advection problem. In general, the time evolution of the level set function is such that it does not conserve the property of being a truncated distance to the interface (as set for the initial configuration). However, as demonstrated in the examples and in Section 3.6.1, for the current application this method is sufficiently accurate and it does not require any post–process to reconstruct the distance shape.

The level set approach may describe changes in the shape (topology) of the phases. In practice, this allows the representation of detaching drops, merging bubbles, breaking sets, etc. This feature of the level set method is of great interest when used in some geophysical situations, for example to model slab breakoff, delamination, or any other process involving changes in the topology of the interface.

The description of the materials location given by the level set function is not only useful for the mechanical problem, but it is also used in solving the Eulerian

multiphase thermal equation.

Other material tracking techniques

The most popular technique used to track material phases in geophysical codes is the *markers* approach. It consists in using a number, usually large, of Lagrangian points carrying the material parameters. The properties of a point of the Eulerian framework are computed as an average of the markers close to this point. This technique was originally designed to work in a finite differences framework, where the discretization is regular and structured and thus it is trivial to identify the markers close to each node. When the mesh becomes non–structured, as with finite elements, the detection of the markers in the proximity of a node is a computationally time consuming task. To reduce the computational time most present multiphase codes run on parallel multiprocessor computers. Despite of the parallelization, the number of operations required is still high and therefore, a technique requiring less computational effort is desirable.

van Keken et al. (1997) study the material tracking problem and compare different tracking techniques to solve an Eulerian multiphase problem. They test three methods: the Lagrangian markers method (named as "tracers" in their work), a marker chain method where the interface between two materials is discretized using a series of markers and, finally, a field method where the material properties are described by a continuous field similar to temperature. They conclude that the Lagrangian marker approach is the most accurate method, alerting about the large number of markers needed. This huge number poses severe restrictions to the application of the technique to three dimensional problems. According to van Keken et al. (1997) two dimensional isoviscous materials require, at least 10 to 100 markers per element. For more realistic rheologies this ratio even increases.

Present applications of the marker technique use much more than 10 markers per element. The simulations of lithospheric structures related to subduction done by Gorczyk et al. (2006) use, in average, 1.25×10^5 markers per element. That is, an amazing grand total of 10 billion markers. With these extremely high resolutions they can track meter–size structures. Leaving aside the super–populated simulations, in most 2D models the estimation of 100 markers per element is fair.

When models move from 2D to 3D, the relationships between markers and elements become a serious restriction. To maintain the resolution used by Gorczyk et al. (2006) in a three dimensional model, 1×10^{15} markers are needed. This posses severe computational restrictions: if each marker employs only twelve bytes of memory —a minimum lower bound to store only its position— the amount of

required memory is 366 times greater than the memory of the present world biggest computer, which has 32768 giga bytes of memory.

In contrast, the level set technique has the capability to describe the location of the interface between materials using the same number of points (same mesh) utilized in the description of the mechanical problem. Therefore, when moving from 2D to 3D, the tracking of the materials does not add extra points to the nodes describing the 3D velocity. Moreover, the level set technique does not require averaging the material properties from markers to nodes, nor the temperature and pressure from nodes to markers.

3.1.3 Space discretization and enriched solutions

The space discretization of the mechanical Stokes equation (3.10) and level set update equation (3.13) is described in this section. The level set method is usually combined with an *enrichment* technique to improve the accuracy of the solution in the vicinity the interface. The combination of finite element with these two numerical techniques is called eXtended Finite Element Method (X–FEM). X–FEM is particularly suitable for multiphase problems in which the strain rate is discontinuous across the interface due to the continuity of stress and a step in the viscosity. None of the methods tested in van Keken et al. (1997) is well suited to resolve this discontinuity. Instead, it is approximated by a continuous function and effectively smeared out over a few grid elements. The enrichment technique used here adds dynamically some degrees of freedom to the mechanical solution to catch the discontinuity exactly where it is expected to happen, i.e. over the interface described by the level set.

The enrichment improves the solution near the interface described by the level set. Figure 3.3 shows how the enrichment technique modifies the solution inside multiphase elements.

The space discretization presented next includes the description of the enriched solution for the mechanical problem in a two–phase context. We have proposed an extension of the X–FEM approach to handle any number of material phases. It is presented in Section 4.1.

The mixed formulation of the Stokes problem uses different interpolations for velocity $\mathbf{u}$ and pressure p. The mini–element, shown in Figure 3.1, determines these interpolation spaces. Denoting by $\mathcal{N}_{lin}$ the indices associated with the vertex nodes and N_j, for $j \in \mathcal{N}_{lin}$, the corresponding shape functions, the interpolated pressure

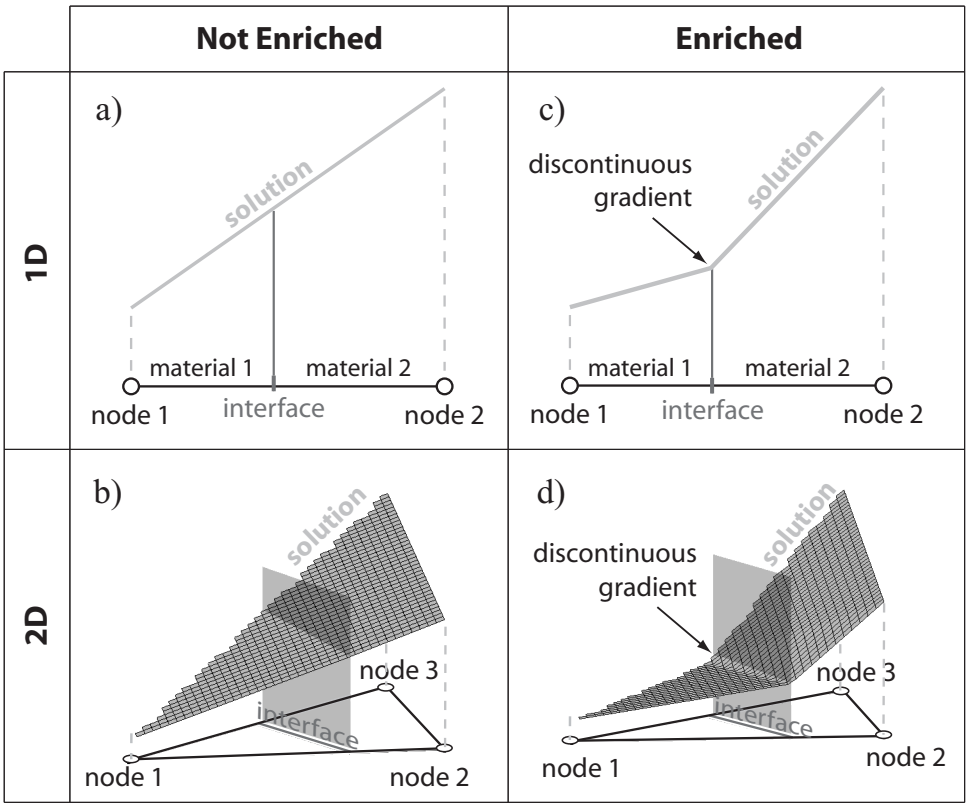

Figure 3.3 – The ability of the enriched solution to have an discontinuous gradient is illustrated. The velocity gradient (strain rate) will be discontinuous across the interface, caused by the continuity of stress and the step in the viscosity.

is

$$p(\mathbf{x},t) \simeq p_h(\mathbf{x},t) = \sum_{j \in \mathcal{N}_{lin}} N_j(\mathbf{x})\, p_j(t). \tag{3.14}$$

The interpolation of the velocity also includes the bubble degrees of freedom N_j for $j \in \mathcal{N}_{bub}$, namely

$$\mathbf{u}(\mathbf{x},t) \simeq \mathbf{u}_h(\mathbf{x},t) = \sum_{j \in \mathcal{N}_{lin} \bigcup \mathcal{N}_{bub}} N_j(\mathbf{x})\, \mathbf{u}_j(t). \tag{3.15}$$

The level set formulation is interpolated in terms of the linear degrees of freedom

$$\phi(\mathbf{x},t) \simeq \phi_h(\mathbf{x},t) = \sum_{j \in \mathcal{N}_{lin}} N_j(\mathbf{x})\, \phi_j(t). \tag{3.16}$$

In order to improve the ability of the interpolation to represent the gradient discontinuities across the interface, the interpolation of the velocity and pressure are enriched using a partition of the unity approach and a ridge function R, defined

by Moës et al. (2003) as

$$R(\mathbf{x}) = \sum_{j \in \mathcal{N}_{enr}} |\phi_j| \, N_j(\mathbf{x}) - \left| \sum_{j \in \mathcal{N}_{enr}} \phi_j \, N_j(\mathbf{x}) \right|. \tag{3.17}$$

Note that R is defined such that it is only different from zero in the elements containing part of the interface. The enrichment affects only the degrees of freedom corresponding to the vertex nodes of the elements in contact with the interface. The set of indices corresponding to such nodes is denoted as $\mathcal{N}_{enr}$. Thus enriched interpolations of velocity and pressure are expressed as

$$\mathbf{u}_h(\mathbf{x}, t) = \sum_{j \in \mathcal{N}_{lin} \bigcup \mathcal{N}_{bub}} \mathbf{u}_j(t) \, N_j(\mathbf{x}) + \sum_{j \in \mathcal{N}_{enr}} \mathbf{a}_j(t) \, M_j(\mathbf{x}) \tag{3.18}$$

and

$$p_h(\mathbf{x}, t) = \sum_{j \in \mathcal{N}_{lin}} p_j(t) \, N_j(\mathbf{x}) + \sum_{j \in \mathcal{N}_{enr}} b_j(t) \, M_j(\mathbf{x}), \tag{3.19}$$

where $\mathbf{a}_j$ and b_j are, respectively, the additional degrees of freedom for velocity and pressure and its associated interpolation function M is defined as

$$M_j(\mathbf{x}) = R(\mathbf{x}) N_j(\mathbf{x}) \tag{3.20}$$

A compact matrix expression of the interpolation of velocity and pressure is used in the following

$$\mathbf{u}_h^\top(\mathbf{x}, t) = \mathbf{N}_u \, \mathbf{U} \tag{3.21}$$

and

$$p_h(\mathbf{x}, t) = \mathbf{N}_p \, \mathbf{P} \tag{3.22}$$

where

$$\begin{aligned} \mathbf{N}_u &= [N_1, N_2, \ldots, N_{n_u}, M_1, \ldots, M_{n_e}] \\ \mathbf{U} &= [\mathbf{u}_1, \mathbf{u}_2, \ldots \mathbf{u}_{n_u}, \mathbf{a}_1, \ldots, \mathbf{a}_{n_e}]^\top \\ \mathbf{N}_p &= [N_1, N_2, \ldots, N_{n_{lin}}, M_1, \ldots, M_{n_e}] \\ \mathbf{P} &= [p_1, p_2, \ldots, p_{n_{lin}}, b_1, \ldots b_{n_e}]^\top \end{aligned}$$

where $n_u = \text{card}(\mathcal{N}_{lin} \bigcup \mathcal{N}_{bub})$, $n_{lin} = \text{card}(\mathcal{N}_{lin})$ and $n_e = \text{card}(\mathcal{N}_{enr})$. Note that the vector of unknowns $\mathbf{U}$ is defined as a $(n_u + n_e) \times 2$ array and therefore is not suitable as an entry in a linear system of equations. In order to properly write the

matrix form of the system, $\mathbf{U}$ has to be reshaped as

$$\mathbf{U}^{rs} = [u_1^x, u_1^y, u_2^x, u_2^y, \ldots, u_{n_u}^x, u_{n_u}^y, a_1^x, a_1^y, \ldots, a_{n_e}^x, a_{n_e}^y]^\top$$

which is a $2(n_u + n_e) \times 1$ vector. According to this reshape, a similar reordering has to be done in $\mathbf{N}_u$ in order to obtain an expression analogous to (3.21), namely

$$\mathbf{N}_u^{rs} = \begin{bmatrix} N_1 & 0 & N_2 & 0 & \ldots & N_{n_u} & 0 & M_1 & 0 & \ldots & M_{n_e} & 0 \\ 0 & N_1 & 0 & N_2 & \ldots & 0 & N_{n_u} & 0 & M_1 & \ldots & 0 & M_{n_e} \end{bmatrix}.$$

The size of the $\mathbf{N}_u^{rs}$ matrix is $2 \times 2(n_u + n_e)$. It is worth noting that the number of enriched nodes, n_e varies along time as the interface described by the level set is transported. Consequently, the size of $\mathbf{U}^{rs}$ and $\mathbf{N}_u^{rs}$ changes.

Problem (3.10) is discretized in space using the interpolation introduced above and the Galerkin formulation. The resulting system of algebraic equations reads

$$\mathbf{K}_u \mathbf{U}^{rs} + \mathbf{G}_u^\top \mathbf{P} = \mathbf{f}_u \tag{3.23a}$$

$$\mathbf{G}_u \mathbf{U}^{rs} = \mathbf{0} \tag{3.23b}$$

where the matrices $\mathbf{K}_u$, $\mathbf{G}_u$ and $\mathbf{f}_u$ are defined as

$$\mathbf{K}_u = \int_\Omega \mathbf{B}^\top \eta \, \mathbf{B} \, dV$$

$$\mathbf{G}_u = -\int_\Omega \mathbf{N}_p^\top \, \rho \, (\nabla \cdot \mathbf{N}_u^{rs}) \, dV$$

$$\mathbf{f}_u = \int_\Omega (\mathbf{N}_u^{rs})^\top \rho \, \mathbf{g} \, dV$$

where the gravity vector $\mathbf{g}$ used in $\mathbf{f}_u$ is the column vector in the right hand side of equation (2.15). The gradient matrix $\mathbf{B}$ is defined as

$$\mathbf{B} = [\mathbf{B}_1, \mathbf{B}_2, \ldots, \mathbf{B}_{n_u}, \tilde{\mathbf{B}}_1, \ldots, \tilde{\mathbf{B}}_{n_e}]$$

$$\mathbf{B}_i = \begin{bmatrix} \frac{\partial N_i}{\partial x_1} & 0 \\ 0 & \frac{\partial N_i}{\partial x_2} \\ \frac{\partial N_i}{\partial x_2} & \frac{\partial N_i}{\partial x_1} \end{bmatrix} \text{ and } \tilde{\mathbf{B}}_i = \begin{bmatrix} \frac{\partial M_i}{\partial x_1} & 0 \\ 0 & \frac{\partial M_i}{\partial x_2} \\ \frac{\partial M_i}{\partial x_2} & \frac{\partial M_i}{\partial x_1} \end{bmatrix}.$$

Note that the spatial derivatives of M_i contained in matrices $\tilde{\mathbf{B}}_i$, for $i = 1, \ldots, n_e$ account for the enrichment and depend on the level set ϕ. Therefore, the chain rule must be employed to evaluate those derivatives.

Equations (3.23) are compacted in the following block matrix form

$$\begin{bmatrix} \mathbf{K}_u & \mathbf{G}_u^\top \\ \mathbf{G}_u & \mathbf{0} \end{bmatrix} \begin{bmatrix} \mathbf{U}^{rs} \\ \mathbf{P} \end{bmatrix} = \begin{bmatrix} \mathbf{f}_u \\ \mathbf{0} \end{bmatrix}$$

This partitioned system can be solved with several techniques, for instance the Uzawa method (Brezzi and Fortin, 1991) was recently tested by Moresi in geophysical codes. Here we use banded solvers for sparse, square matrices or gradient bi–conjugate methods.

3.1.4 Time discretization

The mechanical problem, stated in its quasi–static version, does not requires an explicit time discretization scheme. The time variable and its derivatives are absent of the equation. Its evolution through time will be due to the thermal evolution of the model and the evolution of the phases location.

3.2 Thermal problem

The thermal problem stated in equation (2.6) involves the time derivative terms. In this case the time dependency cannot be neglected and a double discretization is needed in space and time. First we present the space discretization done in a similar way as with Stokes equation by stating a weak formulation of the problem, making a discretization of the solution on the domain and using a Galerkin formulation. Once the problem is semi–discretized in space, time is discretized by means of a Padé method.

The transient heat equation (2.6) is non–linear due to the dependency of density and thermal conductivity on temperature. As we expect only small changes in the temperature field between two consecutive steps, this equation is linearized, and the material properties are calculated based on the thermal field of the previous step.

3.2.1 Strong and weak formulations

The strong formulation of the problem is stated as follows: given a velocity field $\mathbf{u}(\mathbf{x}, t)$ in Ω, the thermal conductivity $k(\mathbf{x}, t)$, the heat source $f(\mathbf{x}, t)$, an initial temperature field $T_0(\mathbf{x})$, Dirichlet boundary conditions $T_D(\mathbf{x}, t)$ on Γ_D and Neumann

boundary conditions $h(\mathbf{x}, t)$ on Γ_N, find T such that

$$\frac{\partial T}{\partial t} + \mathbf{u} \cdot \nabla T - \nabla \cdot (k \nabla T) = f \qquad \text{in } \Omega \times [0, t_{end}], \tag{3.24a}$$

$$T(\mathbf{x}, 0) = T_0 \qquad \text{in } \Omega, \tag{3.24b}$$

$$T = T_D \qquad \text{on } \Gamma_D, \tag{3.24c}$$

$$k(\mathbf{n} \cdot \nabla T) = h \qquad \text{on } \Gamma_N. \tag{3.24d}$$

To obtain the weak formulation similar steps as with the mechanical problem are done. The test function space is defined as

$$\mathcal{V} = \left\{ w(\mathbf{x}) \in \mathcal{H}^1(\Omega) | w(\mathbf{x}) = 0 \text{ for } \mathbf{x} \in \Gamma_D \right\}.$$

The time dependency of the approximate solution T can be translated to the trial space $\mathcal{S}_t$, which varies as a function of time,

$$\mathcal{S}_t = \left\{ T | T(\mathbf{x}, t) \in \mathcal{H}^1(\Omega), t \in [0, t_{end}] \text{ and } T(\mathbf{x}, t) = T_D \text{ for } \mathbf{x} \in \Gamma_D \right\}.$$

Multiplying the heat equation by the test function w, integrating by parts and applying the divergence theorem the weak formulation of the problem is obtained: given f, T_D, h, k and T_0 such that for all $w \in \mathcal{V}$

$$\int_\Omega w\, T_t \,\mathrm{d}\Omega + \int_\Omega w(\mathbf{u} \cdot \nabla T) \,\mathrm{d}\Omega + \int_\Omega \nabla w \cdot (k \nabla T) \,\mathrm{d}\Omega = \int_\Omega w\, f \,\mathrm{d}\Omega + \int_{\Gamma_N} w\, h \,\mathrm{d}\Gamma \tag{3.25}$$

where T_t is the time derivative of temperature. The spacial discretization by means of the Galerkin formulation consists of defining two finite dimensional spaces $\mathcal{S}^h$ and $\mathcal{V}^h$ and restricts the weak form to these spaces.

3.2.2 Space discretization

The space discretization of the thermal problem (2.6) is performed using the linear interpolation, in a similar way as with pressure. The thermal conductivity is not expected to have a large jump across the interface and therefore the interpolation is not enriched, smearing out the jump. The approximation of the temperature results

$$T(\mathbf{x}, t) \simeq T^h(\mathbf{x}, t) = \sum_{i \in \mathcal{N}_{lin}} N_i(\mathbf{x})\, T_i(t) = \mathbf{N}_T\, \mathbf{T} \tag{3.26}$$

where

$$\mathbf{N}_T = [N_1, N_2, \ldots, N_{n_{lin}}]$$
$$\mathbf{T} = [T_1, T_2, \ldots, T_{n_{lin}}]^\top.$$

And the system of ordinary differential equations resulting from the spatial discretization (3.26) reads

$$\mathbf{M}_T\dot{\mathbf{T}} + \mathbf{G}_T\mathbf{T} = \mathbf{K}_T\mathbf{T} + \mathbf{f}_T \tag{3.27}$$

where the involved matrices are defined as

$$\mathbf{M}_T = \int_\Omega \mathbf{N}_T^\top \rho\, C_p\, \mathbf{N}_T \,\mathrm{d}V,$$
$$\mathbf{G}_T = \int_\Omega \rho\, C_p\, \mathbf{N}_T^\top \mathbf{u}^\top \left(\nabla \mathbf{N}_T\right) \mathrm{d}V,$$
$$\mathbf{K}_T = \int_\Omega \left(\nabla \mathbf{N}_T\right)^\top k\, \nabla \mathbf{N}_T \,\mathrm{d}V \qquad \text{and}$$
$$\mathbf{f}_T = \int_\Omega \mathbf{N}_T^\top\, q \,\mathrm{d}V.$$

3.2.3 Time discretization

The transient heat equation (2.6) is integrated upon time using a n–stage explicit Padé method. This method is easier to implement than classical Runge–Kutta methods and posses the same numerical properties (Donea and Huerta, 2002). The Padé multistage method is expressed in the following incremental form

$$T^{n+\beta_1} = T^n, \tag{3.28a}$$
$$T^{n+\beta_i} = T^n + \beta_i \Delta t\, \dot{T}^{n+\beta_{i-1}}, \qquad i = 2, \ldots, n_{tg}+1 \tag{3.28b}$$

where $\beta_1 = 0$, and $\beta_i = 1/(n_{tg} + 2 - i)$.

From the discretization (3.27) of the heat equation (2.6), each step of the explicit Padé method can be written in the matrix form

$$\mathbf{M}_T\dot{\mathbf{T}}^{n+\beta_{i-1}} = \left(\mathbf{G}_T + \mathbf{K}_T\right)\mathbf{T}^{n+\beta_{i-1}} + \mathbf{f}_T \tag{3.29a}$$
$$\mathbf{T}^{n+\beta_i} = \mathbf{T}^n + \beta_i \Delta t\, \dot{\mathbf{T}}^{n+\beta_{i-1}}. \tag{3.29b}$$

This method updates the temperature from step n to step $n+1$ computing the temperature in some intermediate points $n+\beta_i$. Same as with the TG3 integration algorithm described in Section 3.3.2, the $\mathbf{G}_T$ and $\mathbf{K}_T$ matrices depend on the velocity field $\mathbf{u}$ and, in the present implementation, a constant velocity is assumed during the time step. These matrices are assembled once in each time step and then used in each stage of the Padé method.

3.3 Level sets

The level set technique used to locate interfaces is described in Section 3.1.2. The level set function ϕ is defined in equation (3.12) and its update through time is described in equation (3.13). In the following sections the numerical approximation of these equations is described.

3.3.1 Space discretization

The level set is discretized in space using a linear interpolation

$$\phi(\mathbf{x},t) \simeq \phi^h(\mathbf{x},t) = \sum_{i\in\mathcal{N}_{lin}} N_i(\mathbf{x})\,\phi_i(t) = \mathbf{N}_T\,\Phi \tag{3.29}$$

where

$$\Phi = [\phi_1, \phi_2, \ldots, \phi_{n_{lin}}]^\top.$$

In practice the same mesh is used for the discretization of temperature, pressure and the level set function. The transport equation of the level set (3.13) is discretized using (3.29) and yields

$$\mathbf{M}_\phi\dot{\Phi} - \mathbf{G}_\phi\Phi = \mathbf{0} \tag{3.30}$$

where

$$\mathbf{M}_\phi = \int_\Omega \mathbf{N}_T^\top\,\mathbf{N}_T\,\mathrm{d}V \qquad \text{and} \tag{3.31a}$$

$$\mathbf{G}_\phi = -\int_\Omega \mathbf{N}_T^\top\mathbf{u}^\top\,(\nabla\mathbf{N}_T)\,\mathrm{d}V. \tag{3.31b}$$

3.3.2 Time discretization

The level set function is updated at each time step by the transport equation (3.13), which can be rewritten as

$$\dot{\phi} = -\mathbf{u}\cdot\nabla\phi.$$

This equation is integrated upon time using a two–step third–order Taylor–Galerkin method (2S–TG3), namely

$$\tilde{\phi}^n = \phi^n + \frac{1}{3}\,\Delta t\,\dot{\phi}^n + \alpha\,\Delta t^2\,\ddot{\phi}^n, \tag{3.32a}$$

$$\phi^{n+1} = \phi^n + \Delta t\,\dot{\phi}^n + \frac{1}{2}\,\Delta t^2\,\ddot{\tilde{\phi}}^n \tag{3.32b}$$

The α parameter takes the value $1/9$ to reproduce the phase–speed characteristics of the single–step Taylor–Galerkin scheme (Donea and Huerta, 2002). Taking into account the incompressibility equation (2.10), the second time derivative of the level set function ϕ can be expressed as

$$\ddot{\phi} = -\mathbf{u}\cdot\nabla\dot{\phi} = \mathbf{u}\cdot\nabla\left(\mathbf{u}\cdot\nabla\phi\right) = \nabla\cdot\left((\mathbf{u}\cdot\mathbf{u})\nabla\phi\right)$$

therefore, the first step of the Taylor–Galerkin algorithm is given by

$$\tilde{\phi}^n = \phi^n + \frac{1}{3}\,\Delta t\left(-u\cdot\nabla\phi^n\right) + \alpha\,\Delta t^2\,\nabla\cdot\left((\mathbf{u}\cdot\mathbf{u})\nabla\phi^n\right). \tag{3.33}$$

Using the space discretization Φ of the level set function ϕ, the first and second steps of the TG3 scheme are expressed in the following matrix forms

$$\mathbf{M}_\phi\tilde{\Phi}^n = \left[\mathbf{M}_\phi + \frac{1}{3}\,\Delta t\,\mathbf{G}_\phi + \alpha\,\Delta t^2\,\mathbf{K}_\phi\right]\Phi^n, \tag{3.34a}$$

$$\mathbf{M}_\phi\Phi^{n+1} = \left[\mathbf{M}_\phi + \Delta t\,\mathbf{G}_\phi\right]\Phi^n + \frac{1}{2}\,\Delta t^2\,\mathbf{K}_\phi\,\tilde{\Phi}^n, \tag{3.34b}$$

where $\mathbf{M}_\phi$ and $\mathbf{G}_\phi$ are defined in (3.31), and $\mathbf{K}_\phi$ comes from the discretization of the last term of (3.33)

$$\mathbf{K}_\phi = -\int_\Omega (\mathbf{u}\cdot\mathbf{u})(\nabla\mathbf{N}_T^\top\,\nabla\mathbf{N}_T)\,dV.$$

Note that $\mathbf{G}_\phi$ and $\mathbf{K}_\phi$ depend on the velocity field. In the practical implementation, the velocity field $\mathbf{u}^n$ of the n step is taken constant during the entire time step and consequently the steady (quasi–static) Stokes problem is not solved for the intermediate step $\tilde{\phi}^n$.

To keep the solution in the stability domain of the 2S–TG3 algorithm the time increment Δt must be such that the *Courant* vector (c_x, c_y) satisfy

$$c_x^2 + c_y^2 \leq 3/4 \tag{3.34}$$

where $c_x = u_x\Delta t/h_x$, $c_y = u_y\Delta t/h_y$ and h_i is the mesh size along the i–th Cartesian

direction. Thus, at most temporal steps the time increment Δt is set to satisfy

$$c_x^2 + c_y^2 = 3/4\,\theta \tag{3.35}$$

with $\theta = 0.9$. That means that at each time step each particle moves approximately nine tenths of the size of the smallest element of the mesh. Nevertheless, there are situations in which this time increment is too large: if the velocity is slowing down to zero, in order to satisfy (3.35) the time increment grows to infinite. To avoid immense time increments, the criterion (3.34) is combined with a time increment for the diffusive part of the problem

$$\Delta t_{\text{diff}} = \frac{\theta h^2}{2\kappa} \tag{3.36}$$

where κ is the thermal diffusivity and h the size of an element. This guarantees the stability of the thermal equation at very low velocities. Additionally, an absolute maximum time increment is imposed. At each step the minimum of the three time increments is used.

3.4 Coupling scheme

Mechanical and thermal problems are two ways coupled. The heat equation (2.6) involves several terms depending on the mechanical solution, that is on velocity and pressure. First, the advective term explicitly involves the velocity field. The thermal conductivity k, the density ρ and the thermal expansivity coefficient α all have a dependency on pressure. There are two heat sources directly related with the velocity field, the shear heating is calculated in terms of the strain rate (the derivative of the velocity), and the latent heat depending on the vertical velocity. In the other way, the mechanical Stokes equation (3.3a) involves density and viscosity, both highly dependent on temperature.

Our model use a staggered scheme to handle the coupling between the thermal and mechanical problems. At each time step some variables are linearized, for example the temperature, and others are iteratively solved to account for the non–linear behavior, for example the velocity.

To move the system from the step n to the following step $n + 1$, the solver uses the following scheme (Figure 3.4): first, phase locations in step $n + 1$ are calculated by integrating the level set update equation (3.13) using the explicit Padé method. Second, the thermal field in step $n + 1$ is calculated by solving the linearized heat equation (2.6) using the explicit Taylor–Galerkin algorithm. Finally, the mechanical

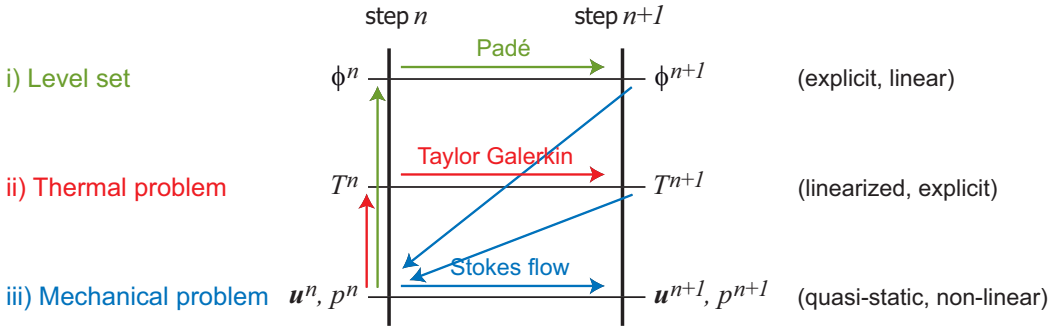

Figure 3.4 – Basic scheme of the solver. To advance one step in time the following steps are done: i) the phases are updated, ii) the temperature is calculated and iii) using the calculated locations and temperatures, the mechanical problem is solved.

Stokes problem (3.3) is solved in its quasi–static version by mean of the mixed finite elements, using the updated thermal field and phase locations. The non–linear character of the mechanical problem is solved using a basic Picard method. We found that, after the first step, only two or three iterations are usually needed to converge to the required accuracy. This fast convergence, due to the small time increments and, consequently, small changes in the solutions from step to step, makes unnecessary to implement a more complex methodology to afford nonlinearities.

3.5 Scaling of variables

The equations introduced in this chapter can be stated and solved in a dimensional or a dimensionless form. For example the dimensionless conservation of momentum equation described in Section 2.2.6 can be stated in terms of the Rayleigh number. Here we solve all the equation in its dimensional form, but using dimensionless variables. That is, the equations are solved as described in this chapter but the variables are scaled using reference values. Namely, the temperature is scaled using the largest drop in temperature in the model ΔT, the space is scaled using the height of the model h_0 and the viscosity and velocity are scaled using reference values η_0 and u_0, respectively. The scaling procedure let the values of these four variables in the range $(0, 1)$ approximately. Having these variables in a similar range reduces the condition number[1] of the matrices generated by the numerical methods described in Chapter 3. Using primes to denote scaled variables we use

$$T' = T/\Delta T, \quad x' = x/h_0, \quad \eta' = \eta/\eta_0 \quad \text{and} \quad u' = u/u_o.$$

[1]The condition number associated with a matrix gives a bound on how inaccurate the solution will be after approximate solution.

Variable	Unit	Scaling
Pressure	Pa	$p' = h_0\,\eta_0^{-1}u_0^{-1}p$
Density	kg m^{-3}	$\rho' = u_0 h_0\,\eta_0^{-1}\rho$
Mass	kg	$M' = u_0\,\eta_0^{-1}h_0^{-2}M$
Power	W	$P' = \eta_0^{-1}x_0^{-1}u_0^{-2}P$
Force	N	$F' = \eta_0^{-1}x_0^{-1}u_0^{-1}F$
Energy	J	$E' = \eta_0^{-1}x_0^{-2}u_0^{-1}E$
Thermal conductivity	W m^{-1}K^{-1}	$k' = \Delta T\,\eta_0^{-1}u_0^{-2}$
Thermal diffusivity	m^{2}s^{-1}	$d' = h_0^{-1}u_0^{-1}$
Thermal expansion	K^{-1}	$\alpha' = \Delta T\alpha$
Compressibility	Pa^{-1}	$\beta' = \eta_0 u_0 h_0^{-1}\beta$
Volumetric heat source	W m^{-3}	$H' = h_0^2\,\eta_0^{-1}u_0^{-2}H$
Specific heat capacity	J kg^{-1}K^{-1}	$C_p' = \Delta T\,u_0^{-2}C_p$
Acceleration	m s^{-2}	$a' = h_0\,u_0^{-2}a$

Table 3.1 – Scaling of physical variables

All space dimensions are scaled using the same h_0. The η_0 and u_0 coefficients are input parameters, with usual values of $\eta_0 = 10^{21}$ Pa s and $u_0 = 5$ cm yr^{-1} = 1.6×10^{-9} m s^{-1}. All other physical variables can by written in terms of these four and consequently scaled. Dimensionless quantities are listed in Table 3.1

3.6 Validation of the code

The correctness of the numerical approach described in Section 3.1 is tested here by means of some academical examples. Firstly, the ability of the level set to describe interfaces and to ensure the volume conservation is studied. Secondly, we demonstrate how the enriched interpolation improves the solution. Thirdly, a qualitative comparison of a Rayleigh–Taylor diapir against a previous model is presented. And finally, a qualitative and intuitive test is done by sinking rigid blocks into a viscous media with different viscosity contrasts.

3.6.1 Volume conservation

The goal of this example is testing the description of the phase tracking via the level set approach (see Section 3.3), the accuracy of the numerical scheme used to transport the level set (solving equation (3.13)) and the influence of the enrichment

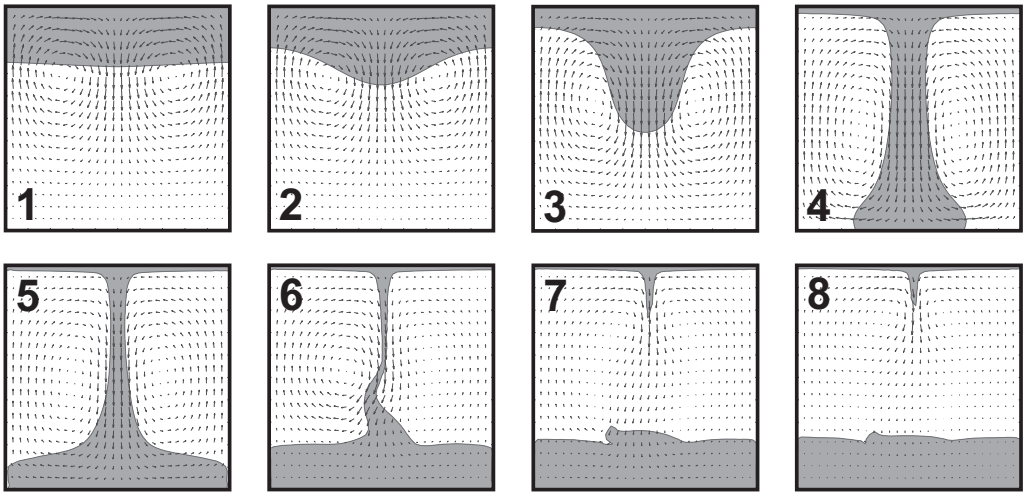

Figure 3.5 – Dense fluid falling in a square box. Evolution of the two phases.

in the numerical results. Due to the incompressibility assumption the volume of each phase has to be conserved along time. Therefore, volumetric changes in time are used to assess the accuracy of the numerical techniques.

The setup of the simulation is as follows: two immiscible fluids with different densities and viscosities lay in a square domain. Densities and viscosities are taken to be of the same order of magnitude as in a geophysical simulation, $\eta_1 = 10^{22}$ Pa s, $\rho_1 = 3300$ kg m^{-3} and $\eta_2 = 10^{20}$ Pa s, $\rho_2 = 3290$ kg m^{-3}. At the initial configuration the denser fluid is in the top of a square box. The interface has a small–amplitude perturbation to induce the instability to develop at the center of the model. The initial state and several snapshots along the evolution are shown in Figure 3.5. The evolution from step 6 looses its horizontal symmetry. This is a consequence of the unstructured mesh. Note that in this example the thermal behavior is not taken into account and the viscosity and density of each phase are assumed to be constant (linear mechanical model).

This test is performed with a series of uniformly–refined non–structured meshes. The results are displayed in Table 3.2, which shows the maximum volume variation obtained with each mesh. As expected, the finer the mesh, the better description of the level set and therefore, smaller volume variation is observed. However, even with a coarse mesh (average edges length is 0.05 of the domain side) the error produced is less than four percent.

3.6.2 Influence of the enrichment

The influence of the enrichment on the solution of the mechanical equations is addressed here. The same model as in the previous section is discretized using

Mesh	Elems	Initial vol.	Δvol	% Error
1	910	0.74	0.024	3.3
2	1432	0.74	0.020	2.7
3	2074	0.74	0.016	2.1
4	2832	0.74	0.014	1.9
5	3710	0.74	0.015	2.0
6	4706	0.74	0.014	1.8
7	5814	0.74	0.012	1.6

Table 3.2 – Volume conservation. Maximum volume variation (along time) with respect to the initial configuration for different uniform meshes.

both enriched and non–enriched interpolations. The standard interpolation (not enriched) is stated in equations (3.15) and (3.14) for velocity and pressure. The enriched interpolation is stated in equations (3.18) and (3.19).

The same material properties of the previous section are used. A reference solution is computed using the mesh displayed in Figure 3.6d, which is composed of 2074 triangular elements. Then, using a coarser mesh composed of 508 elements (see Figure 3.6c) the problem is solved with and without enrichment and both results are compared with the reference solution. The solution is analyzed at a given time that corresponds to the configuration shown in Figure 3.6c. The error is computed as the difference of the velocity solutions at a fine cloud of sample points. The global figures displayed in Table 3.3 demonstrate that the error is reduced using the enrichment both in its average and its maximum value by a factor of approximately 2.

	Enriched	Not enriched
Max. rel. error	1.212	3.783
Average rel. error	0.1462	0.3331

Table 3.3 – Comparative of errors of enriched and not enriched solutions.

The enriched solution shows smaller errors (approx. one half) when compared with the non–enriched solution (Figures 3.6a and 3.6b, respectively). The histogram of Figures 3.6, shows that the lower errors for the enriched solution occur in a much larger number of points. In addition, the larger error (up to 3.5%) are absent for the enriched solution.

This example demonstrates that, even in this simple problem, the enrichment is needed to properly capture not only the discontinuities in the derivatives of the velocity but also the values of the velocity itself.

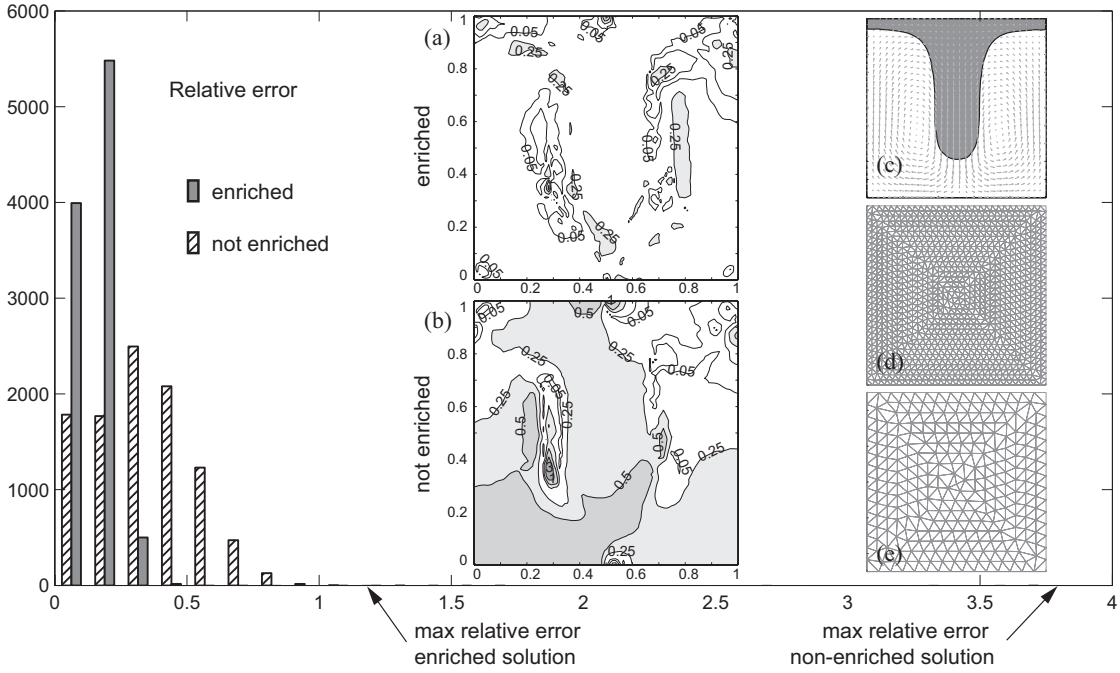

Figure 3.6 – Effect of the enrichment in the discretization error. Histogram of relative errors: number of occurrences of every error value at the sample points (left). Space distribution of relative errors for the enriched solution (a) and the not enriched solution (b). Configuration at the time analyzed (c). Finer mesh used in the reference solution (d) and coarser computational mesh (e).

3.6.3 Simple Rayleigh–Taylor instabilities

To test our mechanical solver we repeat some Rayleigh–Taylor instabilities simulations done by Schmeling and published on the web (`http://www.geophysik.uni-frankfurt.de/~schmelin/presentations/Rayleigh-Taylornew.html`). His code uses the markers technique to track material phases. Taking advantage of the horizontal symmetry of problem, only a half diapir is simulated. In Figure 3.7 the evolution of the models is shown: the left half corresponds to our result and the right half corresponds to the model of Schmeling. The physical properties and boundary conditions are shown in the figure. The qualitative comparison shows an agreement between both simulation to an first order.

3.6.4 Sinking of a hard rectangular block

According to our physical intuitions the deformation of a rigid block sinking in a viscous fluid vanish with increasing viscosity contrast. Dynamics of sinking at high viscosity contrast does not depend on the absolute value of the viscosity of the block. This test proves the accurate conservation properties of our numerical procedure in terms of preserving the geometry at large deformation and high viscosity contrast

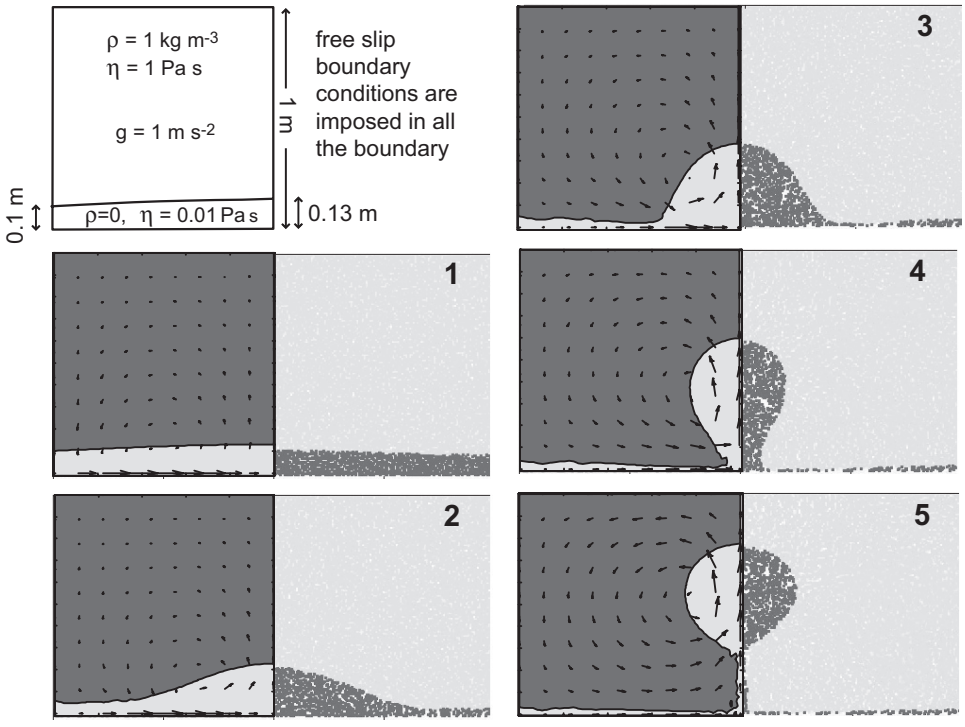

Figure 3.7 – Simple Rayleigh–Taylor instability to check the mechanical solver. Left half of each snapshot is the result of our code, right half is from Schmeling.

(1 - 10^6 Pa s) between the harder block and the softer surroundings. The results of this test are displayed in Figure 3.8. The expected qualitative behavior is obtained: as the viscosity contrast increases, the deformation of the block decreases.

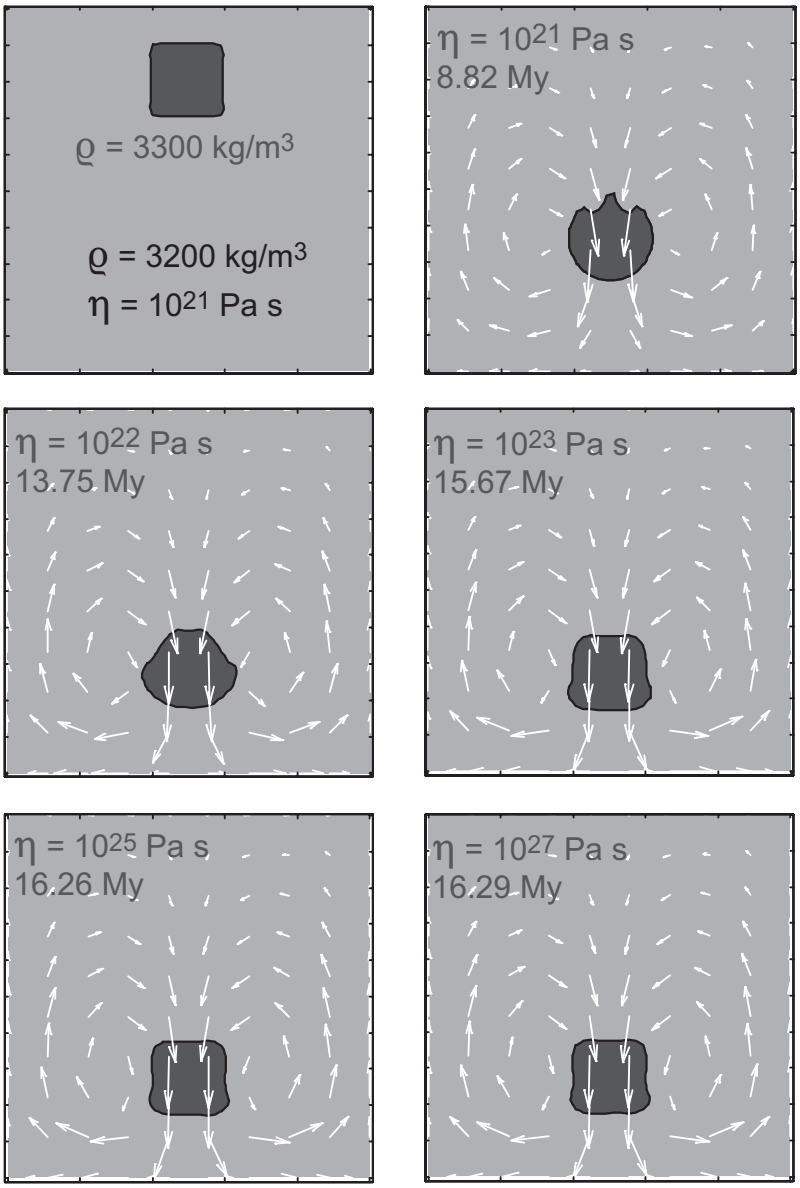

Figure 3.8 – Results of numerical experiments for the sinking of rectangular block at different viscosity contrast between the block and the surrounding soft medium. Boundary conditions: free slip at all boundaries.

Chapter 4

Advanced numerical strategies

The previous chapter describes the basic numerical techniques used to solve the coupled physical equations. Despite some of these techniques are applied for the first time in geophysical modeling, these techniques are standard in other scientific or engineering fields. In this chapter we present some original numerical ideas and some original computational details of our approach. These further numerical improvements have been developed to properly deal with some unresolved features of the model. In Section 4.1 an extension of the X–FEM technique to handle a larger number of materials is presented. The proposed approach is based on using an ordered collection of level set functions to describe the location of the phases. A level set hierarchy allows describing triple junctions avoiding overlapping or "voids" between materials. Moreover, an enriched solution accounting for several simultaneous phases inside one element is proposed. The interpolation functions corresponding to the enriched degrees of freedom require redefining the associated ridge function accounting for all the level sets. The computational implementation of this scheme involves calculating integrals in elements having several materials inside. An adaptive quadrature accounting for the interfaces locations is proposed to accurately compute these integrals. The contents of Section 4.1 are also collected in a manuscript currently submitted to Computational Methods in Applied Mechanics and Engineering (Zlotnik and Díez, 2008).

In Section 4.2 an adaptive scheme to track interfaces is proposed and tested. A simple but efficient adaptive remeshing algorithm is implemented to accurately track interfaces.

In Section 4.3 some computational aspects of the model are described. One time–consuming task in finite element–like frameworks is the assembly of sparse matrices. This is specially relevant in evolutionary processes where the matrices change and have to be computed at every time step. In this section we analyze several

factors that may influence on the efficiency of the assembly procedure. Different insertion strategies are compared using two metrics: a Cost function (the number of memory movements) and actual computing time. We propose an improved algorithm implemented in Matlab. It reduces both memory operations and computing time for all tested cases. This procedure is faster than the built-in Matlab assignment. A paper with the contents of this section has been submitted for publication to Communications in Numerical Methods in Engineering (Zlotnik and Díez, 2007).

4.1 Hierarchical X–FEM for n–phase flow

Level set methods are becoming increasingly popular for the solution of fluid problems involving moving interfaces (Sethian and Smereka, 2003). In the two–phase case, the level set methods can predict the evolution of complex interfaces including changes in topology such as deforming bubbles, break-up and coalescence, etc. This kind of flow is encountered in a wide range of industrial and natural applications.

Despite the term *multiphase* is widely used in the literature, most works using level sets for tracking material interfaces limit the number of phases to two. This restriction comes from the use of the sign of a level set function to describe the materials location. There are, however, some works handling n–phase models ($n > 2$) based on several level set functions. For example, Tan and Zabaras (2007) use the level set technique combined with features of front tracking methods to model the microstructure evolution in the solidification of multi–component alloys. In their work each component is defined by a level set function: the sign limits the solid–liquid interface. Two algorithms to simulate triple junctions where the interfaces motion depends on surface tension and bulk energies were proposed by Zhao et al. (1996) and Ruuth (1998). These works use a number of level set functions equal to the number of materials. They require adding some further restrictions to the model in order to prevent overlapping or vacuum between phases.

We propose a different approach to describe and to model n–phase flow problems based on X–FEM. We avoid the geometrical inconsistency (overlapping or voids) by introducing a hierarchy between the level sets. Moreover, the enrichment of the solution is extended to account for triple (or multiple) junctions inside an element. This allows for handling gradient discontinuities across all interfaces. In the following sections the hierarchy between level sets and the multiple–enrichment of elements are presented in the context of a n–phase flow problem. Computational considerations on how to integrate discontinuous function on elements are discussed next. Finally, in order to show the behavior of the proposed approach we present several application

examples of n–phase flow problems driven by gravitational forces in two and three dimensions .

4.1.1 Phase movement

The location of the different phases is described by a collection of level set functions. Same as in Section 3.1.2 each level set represents a material properties and it is transported by the motion of the fluid. Equation (3.13) is now used for the evolution of each one of the level sets

$$\phi_t^{(i)} + \mathbf{u} \cdot \nabla \phi^{(i)} = 0 \tag{4.1}$$

where $\mathbf{u}$ is the velocity field, solution of the Stokes problem, and $\phi^{(i)}$ is the level set number i.

4.1.2 Describing a n–phase fluid with $(n-1)$ level sets

The level set technique is widely used in two and three dimensions to track one free interface between two materials, see for example (Wagner et al., 2001; Chessa and Belytschko, 2003; Zlotnik et al., 2007a). This section is devoted to generalize this strategy to n–phase flows.

Two phases with a single level set

The location of the interface between two materials is described using a level set function $\phi^{(1)}$. The superscript $^{(1)}$ denotes the number of level set and it is useful when three or more phases have to be described. This superscript is not strictly necessary in this section, however it is used here to keep a consistent notation in the following sections. The sign of the level set $\phi^{(1)}$ describes a partition of the domain Ω into two subdomains Ω_1 and Ω_2 using the following sign convention

$$\phi^{(1)}(\mathbf{x}, t) = \begin{cases} > 0 & \text{for } \mathbf{x} \in \Omega_1 \\ = 0 & \text{for } \mathbf{x} \text{ on the interface} \\ < 0 & \text{for } \mathbf{x} \in \Omega_2 \end{cases} \tag{4.2}$$

where $\mathbf{x}$ stands for a point in Ω and t is the time. The interface is the set of points where the level set field vanishes. An example of partition is shown in Figure 4.1. Initially the level set $\phi^{(1)}$ is defined as a signed distance to the interface. Far enough from the interface, $\phi^{(1)}$ is truncated by positive and negative cutoff values.

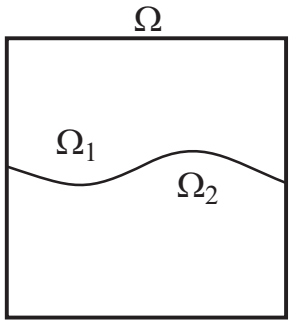

Figure 4.1 – One level set function splits the domain in two subdomains corresponding to the different phases.

Tracking more than two phases: Hierarchy of level sets

One level set allows for describing only two phases (two subdomains). To include a third subdomain Ω_3 a second level set function $\phi^{(2)}$ is needed. We propose to assign a *hierarchy* to the level set functions: the subdomain Ω_1 is determined by the first level set $\phi^{(1)}$ as

$$\phi^{(1)}(\mathbf{x},t) = \begin{cases} > 0 & \text{for } \mathbf{x} \in \Omega_1 \\ \leq 0 & \text{for } \mathbf{x} \notin \Omega_1 \end{cases} \tag{4.3}$$

The curve where the level set $\phi^{(1)}(\mathbf{x},t)$ equals zero is the interface between the first phase and the rest of the domain. That is, either the second or the third phase. The remaining part in the simulation domain ($\mathbf{x} \in \Omega \backslash \Omega_1$) is split by the second level set $\phi^{(2)}$ as

$$\text{for } \mathbf{x} \notin \Omega_1,\ \phi^{(2)}(\mathbf{x},t) = \begin{cases} > 0 & \text{for } \mathbf{x} \in \Omega_2 \\ \leq 0 & \text{for } \mathbf{x} \in \Omega_3 \end{cases} \tag{4.4}$$

determining the location of the second and third sub domains. Note that the second level set does not have any influence where the first level set is positive. We say that the first level set is "prior to" —or has upper hierarchy than— the second level set. Figure 4.2 shows the partition of the domain by two hierarchical level sets into three subdomains.

This hierarchy can be extended to the general case of n phases being tracked by $n-1$ level sets. The level set number i, $\phi^{(i)}$, defines the location of the phase i as follows

$$\text{for } \mathbf{x} \notin \bigcup_{j=1}^{i-1} \Omega_j,\ \phi^{(i)}(\mathbf{x},t) = \begin{cases} > 0 & \text{for } \mathbf{x} \in \Omega_i \\ \leq 0 & \text{for } \mathbf{x} \notin \Omega_i \end{cases} \tag{4.5}$$

for all $i = 1, \ldots, n-2$. The level set with lowest hierarchy, $\phi^{(n-1)}$, determines the

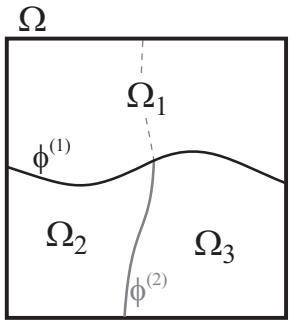

Figure 4.2 – Two hierarchical level sets describe three material sub domains. The second level set $\phi^{(2)}$ is relevant only where the first level set $\phi^{(1)}$ is negative. Dashed line represents the level set with lower hierarchy eclipsed by the first level set.

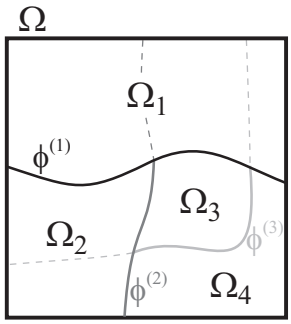

Figure 4.3 – Three hierarchical level sets allow describing four material phases. The last level set $\phi^{(3)}$ acts only where the first two level sets are negative.

location of the last two phases in the remaining space as

$$\text{for } \mathbf{x} \notin \bigcup_{j=1}^{n-2} \Omega_j,\ \phi^{(n-1)}(\mathbf{x},t) = \begin{cases} > 0 & \text{for } \mathbf{x} \in \Omega_{n-1} \\ \leq 0 & \text{for } \mathbf{x} \in \Omega_n \end{cases} \tag{4.6}$$

In this approach the positive part of the i–th level set defines the material subdomain Ω_i and the negative region have to be partitioned by the level sets with less hierarchy. Figure 4.3 illustrates a partition into four subdomains by three level sets.

Note that the interface described by a level set does not require to be simply connected, thus, assigning the right hierarchy to the level sets, any material configuration can be stated. See a more complex configuration in Figure 4.4.

A compact expression for the domains defined by the hierarchical level sets uses the McCauley brackets defined by

$$\langle \phi \rangle = 1/2\ (\phi + |\phi|)\,.$$

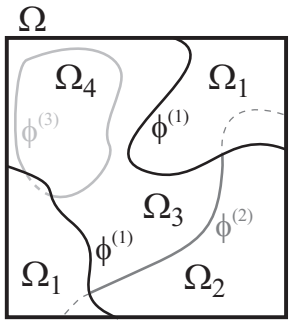

Figure 4.4 – A complex material distribution can be described with the hierarchical approach. Here, $\phi^{(1)}$ describes a disconnected interface.

Thus, the domain Ω_i reads

$$\Omega_i = \text{supp}\left\{ \langle \phi^i \rangle \prod_{j=1}^{i-1} \langle -\phi^j \rangle \right\}.$$

4.1.3 X–FEM enrichment

The interface described by a level set does not need to conform with mesh edges. That leads to multiphase elements with different materials inside. Across the interface a gradient discontinuity arises and therefore the X–FEM enriches the numerical solution in order to include gradient jumps.

The interpolation of velocity $\mathbf{u}$ on the enriched elements is composed by the standard finite element part plus an enriched part. The latter involves additional degrees of freedom $\mathbf{a}_j$ and its associated interpolation functions M_j

$$\mathbf{u}_h(\mathbf{x}, t) = \sum_{j \in \mathcal{N}} \mathbf{u}_j(t)\, N_j(\mathbf{x}) + \sum_{j \in \mathcal{N}_{enr}} \mathbf{a}_j(t)\, M_j(\mathbf{x}) \tag{4.7}$$

where $\mathcal{N}$ is the set of standard finite element velocity degrees of freedom and $\mathcal{N}_{enr}$ is the set of enriched degrees of freedom. The $\mathcal{N}_{enr}$ set evolves through time affecting the nodes located along the interface and needs to be recomputed at each time step after level set movement. The pressure field p is enriched in a similar way.

The interpolation function M_j, associated with enriched degrees of freedom, is constructed as the product of standard nodal shape functions and a ridge function denoted by R,

$$M_j = N_j R. \tag{4.8}$$

The R function is based on the level set and has a "crest" over the interface between materials. Different ridge functions have been proposed in the literature, see for example the works of Chessa and Belytschko (2003) or Moës et al. (2003). In the

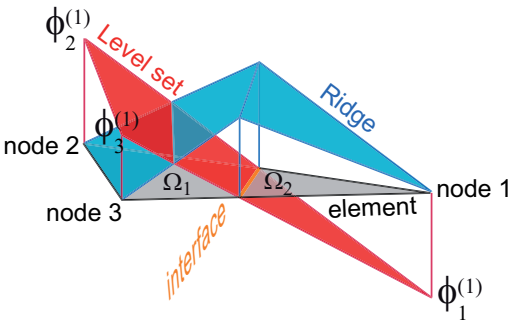

Figure 4.5 – Ridge function R based on one level set $\phi^{(1)}$.

following, a ridge function properly defined in the elements with multiple interfaces in introduced. The rationale follows the ideas proposed by Moës et al. (2003).

Two phases, one Ridge

In a two–phase simulation the single interface is described by a unique level set. The enriched elements are those which are crossed by the interface (where $\phi^{(1)}$ vanishes) and the ridge function can be constructed as (Moës et al., 2003)

$$R = \sum_{j \in \mathcal{N}_{enr}} \left| \phi_j^{(1)} \right| N_j - \left| \sum_{j \in \mathcal{N}_{enr}} \phi_j^{(1)} N_j \right| . \tag{4.9}$$

Note that this function vanishes in the element edges not crossed by the level set. Thus, the interpolation functions of enriched elements conform with those of not–enriched elements. This kind of function is depicted in Figure 4.5.

Ridge function for two level sets

The three–phase configuration requires reviewing the basic operations in the previously described approach for the two–phase flow. Firstly, the detection of enriched element has to include the level set hierarchy. Secondly, the triple junction case, where two level sets intersects one element has to be considered and properly resolved.

The detection for elements to be enriched is the following: elements have to be marked to enrich if they are crossed by the interface described by $\phi^{(1)}$ or crossed by the interface described $\phi^{(2)}$ with $\phi^{(1)}$ negative. This statement can be easily encoded in a highly vectorized Matlab function which accepts any element shape in any number of dimensions and returns if the element has to be enriched or not. See Algorithm 1.

Algorithm 1 Matlab code of the function to detect enriched elements

```
function bool = crossedByLevelSet( levelSet, tolerance )
% bool = crossedByLevelSet(levelSet, tolerance )
%
% Returns if the element has to be enriched or not
%
% INPUT
%   levelSet  Hierarchical level set field for one element
%             Each column has one level set field
%             Each row has the value of all level sets in a node
%             size( levelSet ) = [numberOfElementNodes,numberOfLevelSets]
%   tolerance Level set tolerance
%
% OUTPUT
%   bool      True if the element has to be enriched
%
if nargin < 2
   tolerance = 0;
end
C = find( (~all( levelSet <  tolerance ) & ...
           ~all( levelSet >= -tolerance )) == 1, 1 );
M = find( all( levelSet > -tolerance ) == 1, 1 );
bool = (isempty( M ) && ~isempty( C )) || ...
       (~isempty( M ) && ~isempty( C ) && C < M);
```

The ridge function in elements crossed by only the k–th level set is defined as in the previous case and denoted by $r^{(k)}$

$$r^{(k)} = \sum_{j \in \mathcal{N}_{enr}} \left| \phi_j^{(k)} \right| N_j - \left| \sum_{j \in \mathcal{N}_{enr}} \phi_j^{(k)} N_j \right| \tag{4.10}$$

where k is 1 or 2 for elements crossed by $\phi^{(1)}$ or $\phi^{(2)}$, respectively. In the elements containing only one interface the ridge function is equal to the corresponding single ridge, that is $R = r^{(k)}$.

In the triple junction case, where two interfaces meet in one element, the ridge function must account for both level sets and the hierarchy between them. In this case R is defined as

$$R = r^{(1)} + r^{(2)} C^{(1)} \tag{4.11}$$

where the cutoff function $C^{(1)}$ introduces the level set hierarchy and is defined as

$$C^{(1)}(\mathbf{x}) = \begin{cases} 1 & \text{if } \phi^{(1)} \leq 0 \\ r^{(1)}_{\text{norm}} & \text{otherwise} \end{cases} \tag{4.12}$$

Here, $r^{(1)}_{\text{norm}}$ is the normalized ridge of the level set $\phi^{(1)}$. The normalization process modifies the ridge leaving its crest with a constant value equal to one. Therefore, the cutoff function $C^{(1)}$ is continuous across the interface: $r^{(1)}_{\text{norm}} = 1$ at the interface.

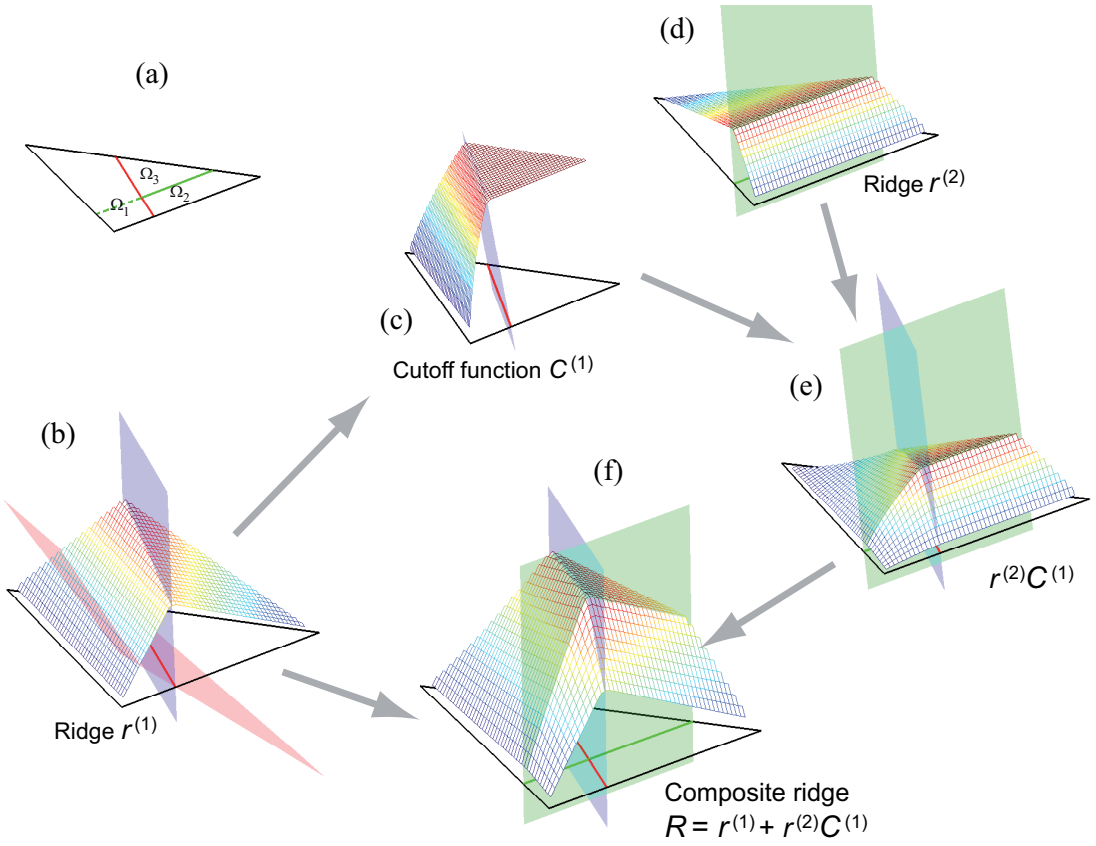

Figure 4.6 – Composite ridge based in two hierarchical level sets. Plot (a) shows the element and the location of the interfaces. The ridge $r^{(1)}$ of the first level set $\phi^{(1)}$ is shown in (b). The cutoff function $C^{(1)}$ based on the first level set is shown in (c). The ridge $r^{(2)}$ of the second level set is shown in (d). Plot (e) shows the product $r^{(2)}C^{(1)}$. Finally, (f) shows the complete composite ridge $R = r^{(1)} + r^{(2)}C^{(1)}$.

The normalized ridge function, $r^{(1)}_{\text{norm}}$, is defined as

$$r^{(1)}_{\text{norm}} = \frac{\displaystyle\sum_{j \in \mathcal{N}_{enr}} \left|\phi^{(1)}_j\right| N_j - \left|\sum_{j \in \mathcal{N}_{enr}} \phi^{(1)}_j N_j\right|}{\displaystyle\sum_{j \in \mathcal{N}_{enr}} \left|\phi^{(1)}_j\right| N_j} \tag{4.13}$$

The cutoff function $C^{(1)}$ restricts the full effect of the second ridge $r^{(2)}$ to the region where the first level set $\phi^{(1)}$ is negative. Moreover it smoothly kills the value of $r^{(2)}$ in the side of the first interface where $\phi^{(1)}$ is positive. Despite the definition (4.13) does not include the time explicitly, it inherits the time dependence of the level sets location, so $r^{(i)}$ (and consequently R) changes through time. The illustration of the proposed ridge function for an element crossed by two level sets is shown in Figure 4.6.

The elements where this multiple–enrichment has to be applied are more than

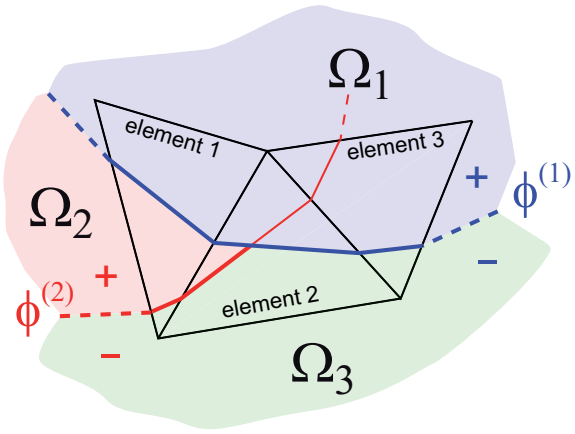

Figure 4.7 – Example of elements whose ridge must be based on both level sets. Note that the second level set, $\phi^{(2)}$, does not define an interface where the first level set $\phi^{(1)}$ is positive (element 3). Nevertheless, the ridge function in the element 3 must be constructed using both level sets to guarantee continuity.

the obvious: some of them cannot be detected at the first glance and an accurate analysis is required to avoid forgetting them. The obvious criterion is: an element is required to be multiple enriched if it is crossed by two *active* interfaces. This is not sufficient to guarantee the overall consistency (continuity) of the interpolation. This is illustrated in the following example. The elements numbered 1 and 2 in Figure 4.7 require multiple–enrichment because they have three different materials in its interior. Note that due to the hierarchy of level sets, the element number 3 has only two materials inside. Nevertheless, element number 3 must be multiple–enriched to guarantee the continuity of the interpolation functions. The multiple–enrichment of element 3 is required to guaranty the conformity with its neighbors: the left side of the element 3 matches with element 2 because both accounts for both level sets. The right side of the element is not affected by the second level set, as its ridge is zero on this edge. Finally, the ridge R on the upper side of element 3 is zero because of the ridge $r^{(1)}$, corresponding to the level set $\phi^{(1)}$, which vanishes on that side.

General case

The latter example is extended to the general case where n level sets simultaneously cross one element. The general definition of the resulting ridge is

$$R = r^{(1)} + \sum_{i=2}^{n-1} r^{(i)} C^{(i-1)} \tag{4.14}$$

Note that the ridge function $r^{(i)}$ of a level set not crossing the element is zero, thus adding all ridges $r^{(i)}$ to obtain R only accounts for pertinent level sets. The $C^{(i)}$

cutoff function defined as

$$C^{(i)}(\mathbf{x}) = \begin{cases} 1 & \text{if } \phi^{(i)}(\mathbf{x}) \leq 0 \\ r^{(i)}_{\text{norm}} & \text{otherwise} \end{cases} \tag{4.15}$$

Same as for $r^{(1)}_{\text{norm}}$, the normalized ridge $r^{(i)}_{\text{norm}}$ is the ridge $r^{(i)}$ with unitary crest, that is

$$\begin{aligned} r^{(i)}_{\text{norm}} &= \frac{\displaystyle\sum_{j\in\mathcal{N}_{enr}} \left|\phi^{(i)}_j\right| N_j - \left|\sum_{j\in\mathcal{N}_{enr}} \phi^{(i)}_j N_j\right|}{\displaystyle\sum_{j\in\mathcal{N}_{enr}} \left|\phi^{(i)}_j\right| N_j} \\ &= 1 - \frac{\displaystyle\left|\sum_{j\in\mathcal{N}_{enr}} \phi^{(i)}_j\, N_j\right|}{\displaystyle\sum_{j\in\mathcal{N}_{enr}} \left|\phi^{(i)}_j\right| N_j}. \end{aligned} \tag{4.16}$$

4.1.4 Numerical integration in multiphase elements

The X–FEM implementation requires computing integrals of discontinuous functions in elements crossed by the level set. The traditional quadrature rules, for example Gauss quadratures, are designed to integrate polynomials and regular functions that are fairly approximated by polynomials. These quadratures are not expected to show a good performance integrating discontinuous functions. To preclude the problem associated with discontinuities and to calculate the integrals accurately it is usual to split multiphase elements in single–material subdomains. In these subdomains functions are continuous and standard quadratures provide accurate results. The computational effort and algorithmic involvement of defining each integration subdomain depends on the shape of the elements and on the number of spatial dimensions involved. For example, with only one level set, triangular elements are split into one triangle and one quadrilateral or into two triangles. This geometrical splitting is coded straightforwardly based on the element geometry and the level set. The same operation for quadrilateral elements is much more cumbersome because the number of possible geometrical divisions is much higher. In particular, the splitting of a quadrilateral generates three–, four– and five–sides polygons. Further subdivisions are required to integrate on five–sided shapes with standard quadratures.

In three dimensions the number shapes generated by cutting elements by one level set increases rapidly. Tetrahedral elements crossed by a plane interface must

by split into five single–material tetrahedra. This partition of the element is much more complicated to code and computationally demanding. The element subdivision is increasingly involved if the number of phases is larger.

Using the hierarchical level set approach the elements are split in polygonal single–material subdomains with any number of sides. The general case of detecting each one of the n–side polygons is complex to code and computationally expensive. In this situation a numerical quadrature acting in the whole element (without any geometrical subdivision) is even more interesting.

The first trial is using a simple (low order) but very populated quadrature rule. Intuitively, it is clear that a large number of quadrature points should allow for integrating the discontinuity accurately. A uniformly refined overkill quadrature should be accurate enough, though ignoring the location of the interface where the discontinuity takes place. This integration method should be used only in elements crossed by several level sets. As they are expected to be only a few of such elements, the use of a costly quadrature does not affect in practice the overall computation time. This strategy is used in a triangular element crossed by one level set with a trapezoidal quadrature on a uniformly refined triangular submesh. This approach is straightforward to implement as a recursive function and thus the number of quadrature points can be increased to any desired value. Moreover, due to the simplicity of the quadrature (first order) is expected to be robust and to minimize the error in the region where the function is discontinuous. The quadrature is implemented recursively based in the split of a triangular element into four similar triangles. It is tested in the computation of an elementary matrix corresponding to the discretization of the Stokes problem. The element under consideration is affected by only one level set; the exact solution is, in that case, easily calculated by splitting the element into three triangles.

The accuracy obtained with this trapezoidal quadrature is disappointing: to obtain a relative error of 10^{-2} in all the coefficients of the elementary matrix, 8385 integration points are needed. To decrease this error to 6×10^{-3}, the number of integration points required is 33153. A larger number of integration points does not reduce the order of the relative error: using 525825 integration points still produces a relative error larger than 10^{-3}. This number of integration points exceeds the computationally acceptable. Table 4.1 displays the relative errors obtained for different levels of recursion.

We conclude that the previous integration method has to be discarded and an alternative integration procedure is required. Therefore, we propose an adaptive scheme which increases the resolution along the interfaces described by the level

sets. This adaptive quadrature is designed to optimize the location of the integration points. The resolution of the quadrature is improved along the interface using the following recursive scheme: starting from a coarse subdivision of the element into four similar triangles, we further subdivide each triangle if it contains an interface. This is illustrated in Figure 4.8, showing six levels of adaptive refinement. The Matlab implementation of the adaptive quadrature is shown in the Algorithm 2.

Algorithm 2 Matlab code of the adaptive quadrature

```
function [pip,wip] = adaptiveQuadrature( Xe, LSe, r, ppg, wpg )
%
% builds a quadrature to integrate a triangular element crossed by one or
% more hierarchical level sets. This quadrature is based on a
% quadrature defined on ppg and wpg
%
% INPUT
%   Xe  nodal coords
%   LSe nodal level set. Each column is a different level set
%   r   level of recursion
%   ppg position of quadrature points used in each sub triangle
%   wpg weight of quadrature points used in each sub triangle
%
% OUTPUT
%   pip position of integration points
%   wip weight of integration points
%
if r == 1
   N = [ppg(:,1), ppg(:,2), 1-ppg(:,1)-ppg(:,2)];
   pip = N*Xe;
   A1 = cross( [Xe(3,:) - Xe(2,:), 0], [Xe(1,:) - Xe(2,:), 0] );
   wip = A1(3) * wpg;
else
   % Six nodes
   Xn = [Xe; reshape( mean( reshape( Xe([1 2 2 3 3 1],:), 2, 6 ) ), 3, 2 )];
   % Level set in the nodes
   LSn = [LSe; reshape( mean( reshape( LSe([1 2 2 3 3 1],:), 2, ...
          53*size( LSe, 2 ) ) ), 3, size( LSe, 2 ) )];
   % Local conectivity
   ix = [1 4 6; 4 2 5; 6 5 3; 4 5 6];
   pip = [];   wip = [];
   for I = 1:4
      if crossedByLevelSet( LSn(ix(I,:),:) )
         ri = r - 1;
      else
         ri = 1;
      end
      [np,nw] = adaptiveQuadrature( Xn(ix(I,:),:), LSn(ix(I,:),:), ri, ppg, wpg );
      pip = [pip; np]; wip = [wip; nw];
   end
end
```

A simple Gaussian–type quadrature is sufficient to integrate the subdivisions not affected by the discontinuity. In the particular case of the Stokes problem (3.3) the integrated functions are polynomials of degree four at most. Thus, a seven–point gaussian quadrature of order four is selected in every single subdivision.

Using a large but reasonable amount of integration points, this adaptive quadrature drastically improves the accuracy with respect to the uniform trapezoidal

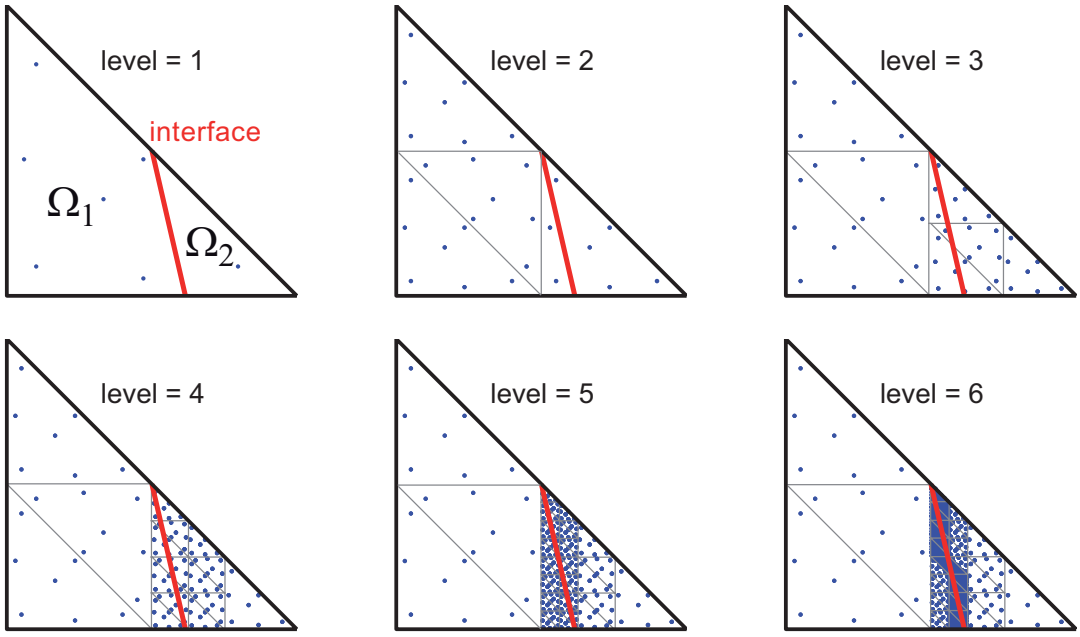

Figure 4.8 – Location of integration points in the adaptive quadrature. The number of integration points in the successively refined quadrature are 7, 29, 49, 112, 259 and 574. The accuracy obtained is shown in Table 4.1.

Trapezoidal quadrature			Adaptive quadrature		
Recursive level	Number of points	Max rel error	Recursive level	Number of points	Max rel. error
1	3	55.6	1	7	5.4
2	6	13.3	2	28	0.51
3	15	3.7	3	49	0.38
4	45	1.6	4	112	0.076
5	153	0.4	5	259	0.036
6	561	0.08	6	574	0.0047
7	2145	0.03	7	1225	0.0019
8	8385	0.01	8	2548	0.00029
9	33153	0.006	9	5215	9.65×10^{-5}
10	131841	0.0038	10	10570	1.90×10^{-5}
11	525825	0.0019	11	21301	8.71×10^{-6}

Table 4.1 – Accuracy of the uniform trapezoid and adaptive quadratures. The relative error refers to the maximum in the coefficients of the elementary matrix for the Stokes problem. The location of the interface is same as in Figure 4.8.

integration. Recall that this strategy is only needed in the elements affected by the interface. However, the computational effort to integrate the stiffness matrices in these elements is important.

An alternative integration procedure is based in the Constrained Delaunay Triangulation (or tetrahedralization, in both cases corresponding to the acronym CDT), as used for instance by Gerstenberger and Wall (2007). This idea is allowing

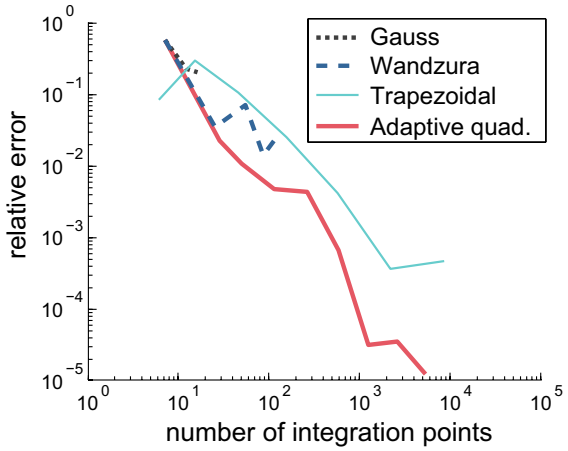

Figure 4.9 – Convergence behavior of different quadrature rules

to automatically split the element into monophasic subdomains and thus to use in each subdomain a simple quadrature. Comparing the cost of these two approaches is beyond the scope of this work.

The proposed adaptive quadrature is used in examples presented in next section providing satisfactory results.

4.1.5 Numerical examples

The strategy developed in the previous sections is tested here in some standard application examples. The n–phase X–FEM approach is used to simulate gravitational Rayleigh–Taylor instabilities in two and three dimensions. The models are composed by $n \geq 3$ immiscible materials governed by the Stokes equation (3.3). The only driving force in these models is the gravity; the density contrast makes the buoyant layers (with lower density than the overlying layers) to flow upward and the denser layers to flow downward.

Two–dimensional three–phase instabilities

The initial configuration of the following examples is given by the location of three materials, as shown in Figure 4.10. Two level sets are regarded to describe this configuration. The first level set in hierarchy is the one corresponding to the upper denser material. The second level set describes the vertical interface between the two lighter materials. Note than the vertical interface does not continue through the upper material due to the level set hierarchy. The upper layer is ten times denser than the two lower materials. The lower materials have different viscosity, thus the resulting configuration (the formed diapir) looses its vertical axis of symmetry.

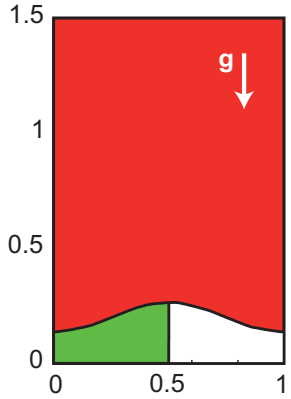

Figure 4.10 – Initial configuration composed of three materials. The upper material is denser than the other two. The viscosity of the materials for each particular simulation is indicated on the caption of Figure 4.12.

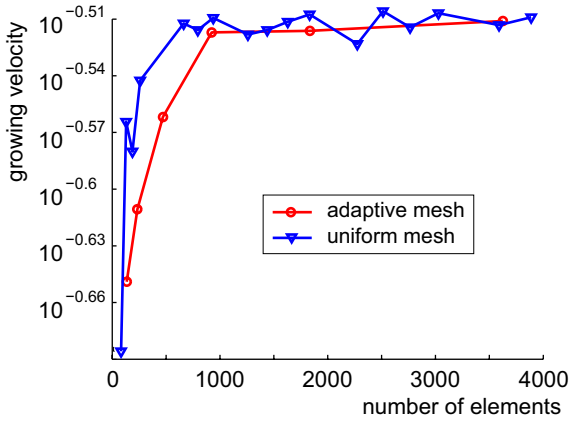

Figure 4.11 – The velocity of the growing diapir is used to check the consistency of the solution. Two series of models are shown: the triangles correspond to uniform mesh refinements, the circles correspond to adaptive mesh refinements.

Some simple configurations of two–phase Rayleigh–Taylor instabilities allow for an analytical calculation of the growing velocity. This macroscopic velocity is a meaningful quantity of interest that can be compared with analogical experiments. Nevertheless, for the three–phase case no analytical solution is available. Therefore, no direct quantitative error assessment can be performed. A numerical convergence analysis is carried out for this problem. Figure 4.11 shows the convergence of the diapir growing velocity as a function of the number of elements in the mesh. Two series of simulation are performed: one refining the mesh uniformly (marked with triangles), the other refining the mesh with an adaptive scheme near the interface (marked with circles). The adaptive scheme, described in Section 4.2, helps to converge faster and with less elements than the uniform refinement. A uniform mesh and several adaptive meshes with different refinement levels displayed in Figure 4.16.

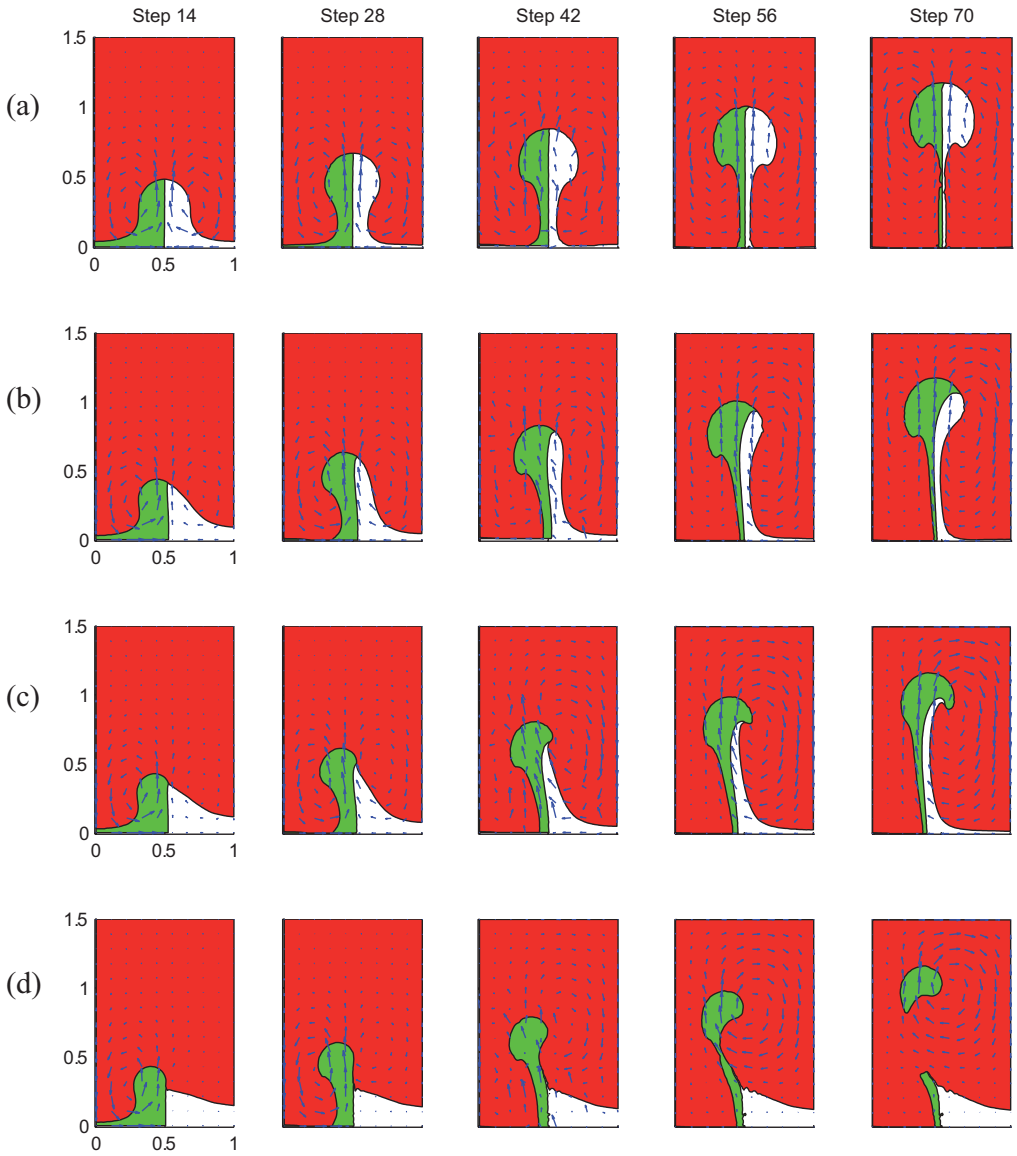

Figure 4.12 – Evolution of the 3–phase diapir. The models (a), (b), (c) and (d) differ in the viscosity of the lower right material, which is 1, 5, 10 and 100, respectively. The other two materials have viscosity $\eta = 1$. The upper denser layer has a density of 10, while the two buoyant lower materials have a density of 1.

The evolution of four models with different viscosity contrast between the two lower layers is shown in Figure 4.12. The (a) row corresponds with a model where all the materials have the same viscosity $\eta = 1$. In this conditions the two buoyant materials behave as a unique fluid and a standard symmetric diapir develops. The (b) row shows the evolution of the diapir when the viscosity of the right lower material is five times the viscosity of the left material. In this case the symmetry is lost. The evolution of the left half of the model is similar to the (a) row while the right half of

the model is controlled by the viscosity contrast between the right material and the overburden layer. The models of the (c) and (d) rows have a viscosity ratio between the two lower layers of 10 and 100, respectively. The viscous material of the last model is almost stopped and the left material develops the diapir. In this example the main pattern of generated flow changes: at early stages (1st and 2nd snapshots) the high viscosity of the right material inhibits the movement of the right half of the model and thus flow is concentrated in the left part of the domain. This configuration results in a bending of the diapir to the left. Once the material gains enough height to loose the influence of the viscous layer (last two snapshots), the main flow moves to the right half of the model because there is more space facilitating the return flow. This latter inflexion bends the diapir rightward.

The conclusion on this qualitative test, is that the results show a complex behavior corresponding with the nature of the problem analyzed.

Three–dimensional instabilities

Two examples of gravitational instabilities in 3D are presented next. Firstly, a Rayleigh–Taylor instability similar to the previous 2D example is presented. Secondly, an instability where the material phases lays horizontally is shown. In both cases the domain is a cube.

The first example involves three materials: an upper and denser phase, and two lower and buoyant fluids with a viscosity ratio of five between them. Same as in the previous case the level set $\phi^{(1)}$ (with highest hierarchy) determines the location of the upper material and has a initial sinusoidal perturbation to induce the development of the instability. The second level set represents the interface between the two lower fluids and is initially set parallel to one wall of the domain. A uniform structured mesh of 512 ($8 \times 8 \times 8$) 27–noded hexahedra is used in this simulation.

Figure 4.13 shows the location of both level sets after some time steps. In panel (a) the two level sets are shown. Due to the hierarchy, the vertical level set is only relevant below the red surface. Panel (b) shows another view of the same surfaces painted with different colors to emphasize the similarity with the 2D model. Note that the contact between colors is where the second interface (described by $\phi^{(2)}$) intersects. This 3D example is comparable to the (b) row of Figure 4.12. A snapshot of the 2D model is included in panel (c), showing the comparable asymmetric pattern developed.

The second example, involves five different materials. The physical properties are described in Table 4.2. The contacts between these materials are described by four level sets. The initial setup and two snapshots of the evolution are shown in

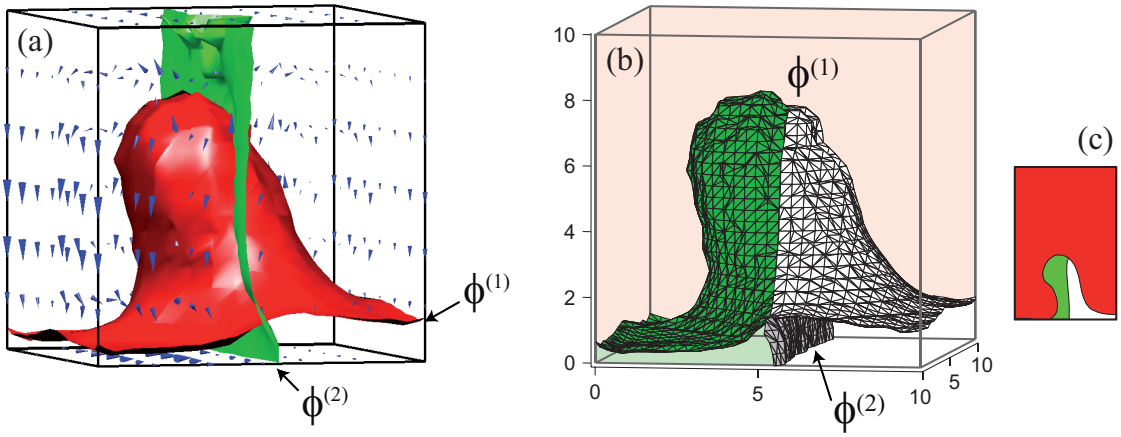

Figure 4.13 – Interfaces described by two level sets (a). The blue arrows show the velocity field. Colors in the upper surface of (b) show the contact between different materials. The generated shape corresponds to the 2D case shown in panel (c) (taken from Figure 4.12 row (b)).

Figure 4.14 panels (a), (b) and (c).

Layer	Viscosity	Density
1	1	1
2	10	100
3	10	50
4	10	25
5	10	12

Table 4.2 – Physical properties of materials for the layered 3D model. Layers are numbered bottom up.

Same as in the previous example, the lower phase is less dense than the overlying materials and a gravitational instability develops. In this case the buoyant lower material induces deformation in all the upper layers. Vertical cross–sections in the center of the model show how this deformation evolves (see Figure 4.14). A uniform non–structured mesh of 23461 four–noded tetrahedra elements is used in this simulation. The number of elements corresponds with a uniform mesh with 15 elements per side.

The examples presented in this section show how the multiphase flow evolution is resolved when i) the level sets intersects each other and triple junction occurs inside one element and ii) the level sets are parallel inside an element and are convected keeping parallelism. Both cases behave consistently.

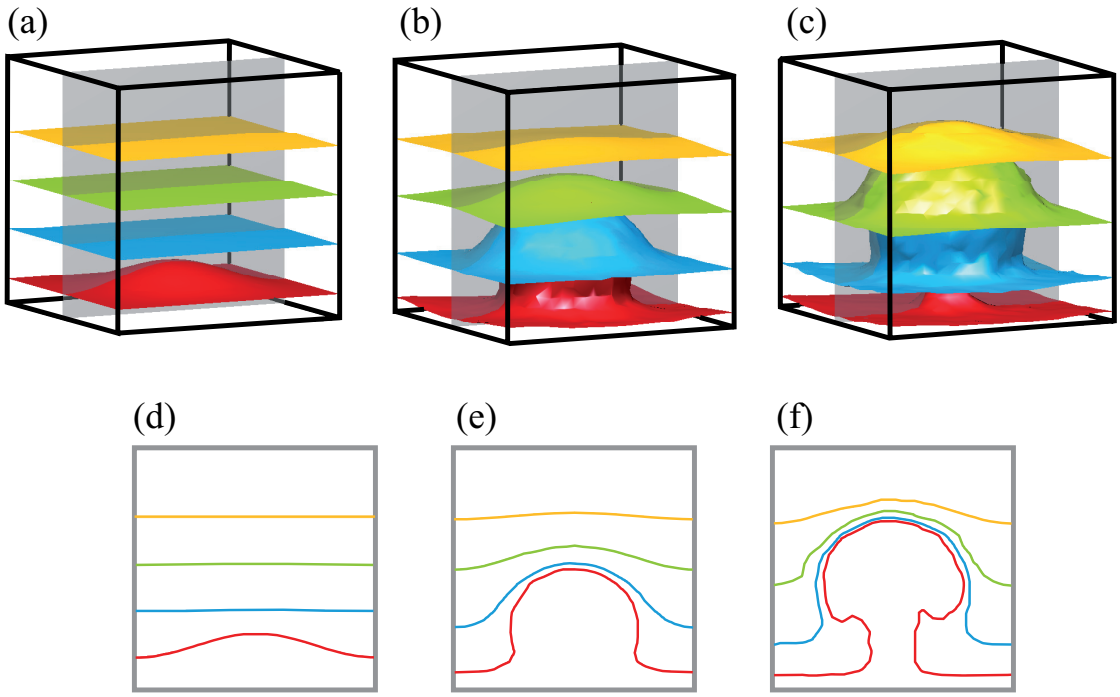

Figure 4.14 – Initial state (a) and snapshots (b) and (c) of the level set location during the evolution of the layered model. Panels (d), (e) and (f) show vertical cross–sections of the model, where the deformation of the layers is appreciated.

4.1.6 Concluding remarks

In this section the classical X–FEM is extended to handle n different materials. This approach is proposed here in the context of a n–phase flow problem but can be extended to other problems where the phases are described using level set and X–FEM. The location of the materials is described by an ordered collection of level set functions, for which a hierarchy is established. The enrichment of the solution is also restated to include cases where more than a single interface lies inside one element. To do this, a ridge function accounting for all level sets and the hierarchy between them is proposed.

A numerical study on the strategies to compute integrals in the multiphase elements is also carried out. An adaptive quadrature accounting for the interface location yields an approximation with sufficient accuracy.

The n–phase X–FEM approach is successfully applied to a multiphase flow problem in 2 and 3 dimensions, using triangular, tetrahedral and hexahedral elements.

4.2 Mesh adaptivity

The accuracy of the solution is related with the discretization of the domain[1]. In geodynamic simulations, some quantities of interest may have a much smaller size than the overall simulated domain. Additionally, these features may change its location through time. As the problem is described in a Eulerian framework, to reproduce small features accurately one must either refine the mesh in the entire region where the interesting feature moves, or adopt a dynamic scheme capable of track the feature. The first option is a static approach, the same mesh is used in the entire simulation. The second is a dynamic approach where the mesh is updated through time, only refining places where more elements are needed. The main difference between the static and the dynamic approach is the computational cost. It is theoretically possible to obtain any desired accuracy in a small region by refining the entire mesh but, in practice, the computational cost of such approach is prohibitive.

For example, Moresi et al. (1996) studied the behavior of finite element codes to solve an incompressible Stokes flow problem with variable viscosity. They conclude that the accuracy of the solution does not decrease with the global viscosity contrast across the mesh but on the ratio of viscosities associated within individual elements. In that case the contrast of viscosities can be used as a metric to measure the need of more and smaller elements.

An example of a small–scale geometric feature in geodynamic models is the oceanic crust with typical thicknesses of 7 to 10 kilometers, that is less than 0.01% of the height of the model. To describe it using level sets over a uniform mesh, the number of elements required increases the running time of a serial code to several months. A non–uniform mesh can also be used. To preserve accuracy, this mesh requires to be refined in all the places where the crust may be present during the simulation. In a slab breakoff problem, for example, this region is an important percentage of the simulation domain.

Therefore, an adaptive scheme to update the mesh dynamically is an attractive option. This procedure should detect places where more resolution is needed to increase the number of elements, while leaving the mesh coarse where the solution can be easily interpolated. As the model evolves, the dynamic scheme recalculates the mesh to adapt it to the current situation. This adaptive scheme reduces the computational cost by decreasing the number of elements. Or, in other words, it allows for more accurate models with the same computational cost by placing the

[1]The mesh

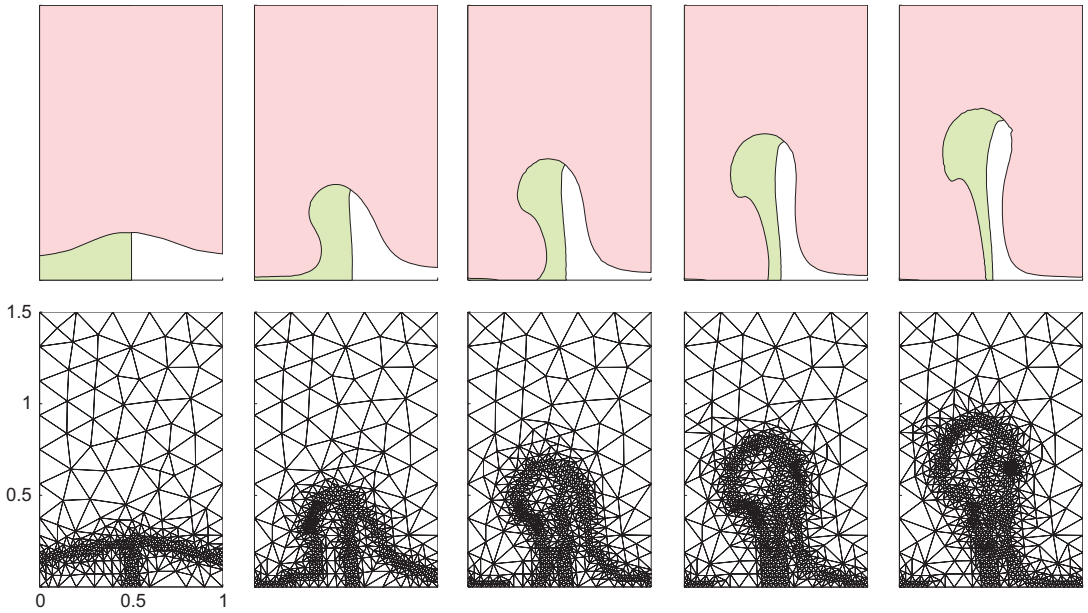

Figure 4.15 – Evolution of the adaptive mesh along time.

elements where they are required.

We developed a very simple but effective adaptive scheme to accurately track interfaces described by level sets. In that case high element density is needed close to the interfaces. Our approach uses a coarse mesh with uniform element density as a base mesh. Its enriched elements, that is, elements crossed by the level set will be refined into four smaller elements. This procedure is repeated d times. The parameter d, called the depth of the refinement, controls the final size of the elements; in the refined regions the expected average element–size is, the element–size of the base mesh divided by 4^d. The pseudo code of this scheme is shown in the Algorithm 3

Figure 4.15 shows the evolution of the mesh along time of a three–phase diapir simulation. The mesh, refined up to depth $d = 3$, closely follows the interfaces between materials defined by the hierarchical level sets. In Figure 4.16 the effect of the refinement depth from zero to five is shown.

Figure 4.17 compares the same stage of evolution of several models with increasing refinement depth. The simulations involve three different materials. Despite the second level set continues below the upper layer, it does not represents an interface because of the level set hierarchy (see Section 4.1) and, therefore, the region is not refined. The obtained description of the material locations is clearly improved as the depth of the refinement increases. The improvement does not only concern the smoothness of the interface, but also the evolution of the curve. In panels (a) and (b) of Figure 4.17 the left lower material disappear near the bottom of the model. This is not due to the size of the elements; the mesh is able to describe the

Algorithm 3 Pseudo code of the adaptive scheme

Ensure: level set field ϕ, refine depth d
1: **return** new mesh, level set supported by new mesh
2: Use the base mesh as the actual mesh
3: Pass the input level set ϕ to the actual mesh
4: **for** i = 1 to d **do**
5: $c \leftarrow 0$
6: **end for**
{Assembly}Assembly the matrix in a traditional way (using EbE– or single–insertion)
7: **for all** element e **do**
8: Find the elements to refine in the actual mesh
9: Refine actual mesh
10: Pass the input level set ϕ to the actual mesh
11: **end for**
12: Set the new mesh as the actual mesh

interface. It is related to the accuracy of the mechanical solution.

4.3 Matrix assembly

Assembling a global sparse matrix from elementary matrices is a key operation in finite element–like frameworks. Despite the great effort that has been done to optimize sparse algorithms and operations, details of how to set a sparse matrix are usually not mentioned in the literature. Nevertheless, the matrix assembly is a time consuming process which, under unfavorable conditions, can overcome the computing time of the sparse solver.

One of the scenarios where the assembly is time consuming is the solution of transient multiphase Stokes flow. In this kind of problems matrices have to be assembled in each time step and the pattern of the matrices is unknown. When partition of the unity methods are used to enrich the discretization, degrees of freedom are created and destroyed dynamically at each time step. In practice this increases dramatically the assembly time.

Matlab is a programming platform frequently used to implement finite element codes for both research and engineering practice. The reminded of this section is devoted to analyze both from the theoretical and practical viewpoint the assembly procedure in Matlab. Moreover, the best option found is provided as open code that reduces the assembly time in all the cases.

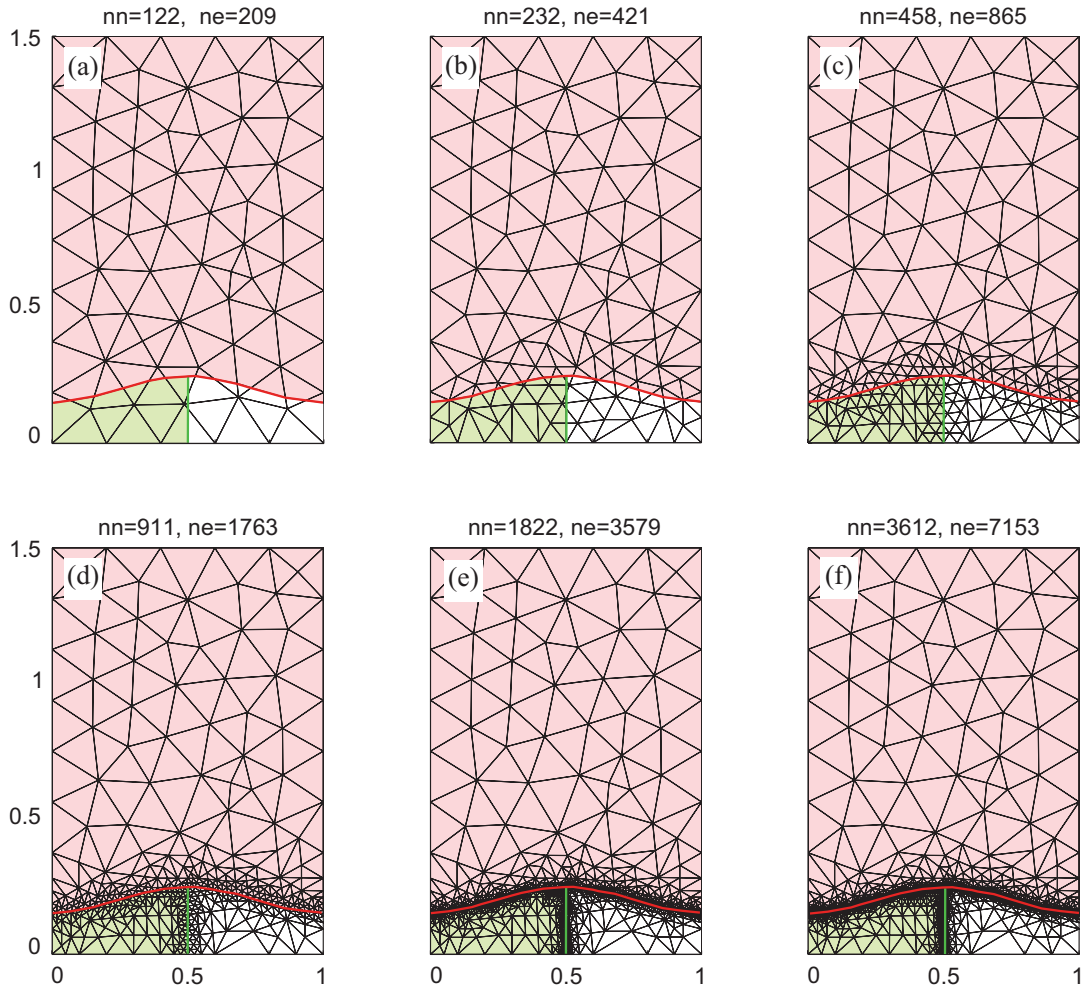

Figure 4.16 – Uniform mesh (a) and different levels of mesh refinement (b) to (f). All meshes correspond to the same moment during the evolution of different simulations. Number of nodes (nn) and number of elements (ne) are indicated for each mesh

4.3.1 Storage and creation of sparse matrices

In Matlab sparse matrices are stored in the classical Compressed Sparse Row format (CSR) (Mathworks, 2006). The CSR data structure is based in three arrays `pr`, `ir`, and `jc`. A matrix K composed of m rows and n columns, with `nnz` non–zero coefficients is stored in three arrays: 1) the real array `pr` with length `nnz` containing the non–zero values a_{ij} stored by column, 2) the integer array `ir` with length `nnz` containing the row indices of the elements of `pr` and, 3) the integer array `jc` with length $n + 1$ containing the pointers to the beginning of each row in the arrays `pr` and `ir`. The last position of `jc` contains the number `nnz`.

That means that, in CSR storage, the non–zero values a_{ij} are stored in `pr` sorted by columns. When a new value is added it has to be inserted in its corresponding place. This can lead to moving large chunks of memory if the insertion is done at

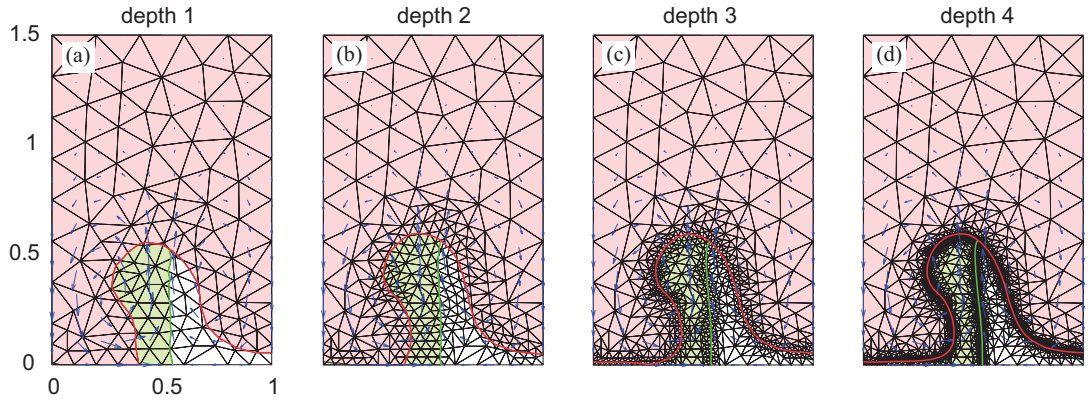

Figure 4.17 – Same stage of evolution of several model with increasing refinement depth. The improvement of the discretization affects the solution of the flow problem; in panel (a) and (b) the interface disappears at the left bottom due to the coarse resolution of the velocity field.

the beginning of the array. Despite memory operations are fast, the large number of insertions during the assembling process is time consuming.

To study the efficiency of insertions during sparse matrix assembly we define the *Cost* of an insertion in a sparse matrix as the number of coefficients moved in `pr` to add a new value. The insertion at the end of `pr` and the modification of an existing coefficient, both have Cost zero. For example, a full $n \times n$ matrix filled sequentially following the storage sorting has zero assembly Cost. If the same matrix is filled in the reverse order, the Cost would be $n^2(n^2+1)/2$.

Two different alternatives are analyzed to minimize the Cost of the assembly process: i) reduce the Cost of each insertion by node and element renumbering and, ii) group insertions to make place for several new coefficients in a unique operation.

In Sections 4.3.2 and 4.3.3 we assume that the pattern of the matrix, that is all its non–zero positions, is completely unknown before the assembling process. The case of a known, or partially known, pattern is analyzed in Section 4.3.4.

4.3.2 Influence of node numbering

The Cost of the insertion of each coefficient during assembly process depends on the order in which degrees of freedom are added to the matrix. If degrees of freedom are added in reverse order, each insertion must move all previously inserted values, maximizing the Cost of the assembly and wasting computation time. Therefore, the Cost will be highly influenced by the numbering of the mesh nodes and elements.

Node renumbering procedures have been proposed in the literature to minimize the bandwidth of a sparse matrix (e.g. Akhras, 1987; Boutora et al., 2007; Cuthill and McKee, 1969; Kaveh, 1993; Lai, 1998). A lower bandwidth implies that the

difference of numbering between related degrees of freedom is minimal. A deep analysis of different renumbering procedures is out of the scope of this work (we refer the reader, for example, to Lohner (1993)). The efficiency of different ordering algorithms in finite element models was studied by Kaveh and Behfar (1995).

The classic reverse Cuthill–McKee (RCM) algorithm is used here as a reference tool to study the influence of the node and element numbering into the Cost of the assembly procedure. The following assembly procedure in Matlab is considered,

```
for e = 1:numberOfElements
   Te = T(e,:);
   Ke = calculateElementalMatrix( e );
   K(Te,Te) = K(Te,Te) + Ke;
end
```

where `Ke` is the elementary matrix, `K` the global matrix, `T` the connectivity array and `Te` contains the global numbering of the nodes of element `e`. The Cost of this assembly procedure is evaluated for a set of meshes, with and without renumbering.

Figure 4.18 shows the Cost of each insertion during the assembly of the global matrix corresponding to an unstructured mesh of 104 linear triangular elements. The assembly Cost for renumbered and non–renumbered cases is shown. The total Cost of the assembly is the sum of all those values (the area below the curve). During assembly of the non–renumbered case of the mesh, 32606 coefficients where moved, while in the renumbered case only 4730 coefficients where moved. In this case, node and element renumbering allows reducing the Cost by a factor of seven.

Table 4.3 shows the assembly Cost for different meshes. The examples correspond to different element types (triangle/quadrangle, linear/quadratic). As expected, the node numbering has a high influence in the efficiency of the assembly process. In most cases, renumbering reduces the Cost of the assembly. Nevertheless, in two cases the RCM algorithm increases the bandwidth and the Cost (Meshes 3 and 4 in Table 4.3). This is due to the fact that these two meshes are structured and, consequently, the initial numbering of the nodes is somehow optimized. The heuristic RCM algorithm is designed for general meshes and does not account for the particular features of every concrete mesh. RCM is therefore expected to perform well for a general mesh but it is not ensuring a lower bandwidth for all meshes. In particular, this remark applies to meshes following a very special pattern as, for instance, structured meshes.

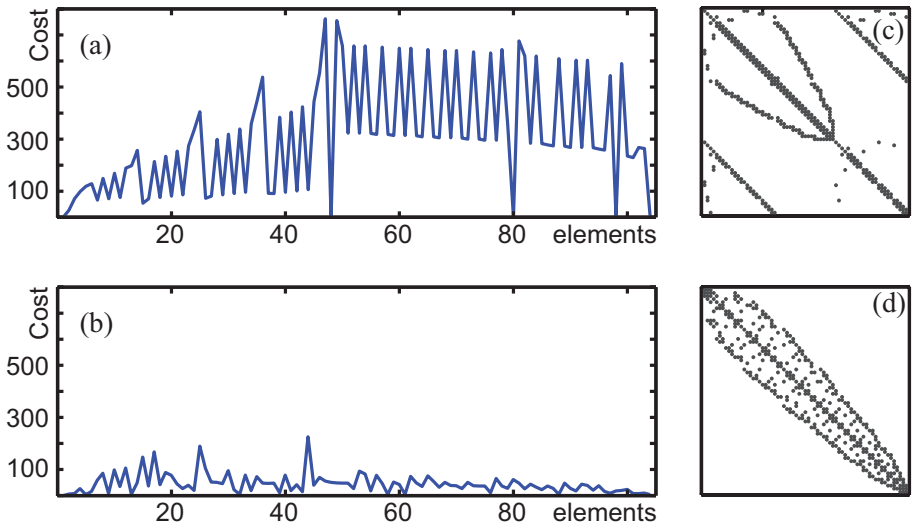

Figure 4.18 – The Cost of the insertion of each element during assembling process is shown for non–renumbered (a) and renumbered (b) cases. The total Cost is the area below the curve. The pattern of the matrices, associated with a mesh of 104 linear triangles, is shown in panels (c) and (d). Matrices have bandwidth of 65 and 14, respectively.

Mesh	Structured	Elem. shape	#Nodes	#Elem	Cost($\times 10^4$)	CostR($\times 10^4$)	Cost/CostR
1	no	△	3	104	3.2	0.4	8.0
2	no	△	3	4312	2104.7	109.9	19.15
3	yes	□	4	400	14.2	19.1	0.7
4	yes	□	9	400	670.0	945.7	0.7
5	yes	△	3	800	8.0	5.4	1.5
6	yes	△	4	800	871.7	55.3	15.7
7	yes	△	6	200	41.7	33.4	1.24

Table 4.3 – Comparative of Cost of assembly with and without renumbering for several meshes. Cost and CostR are the total assembly Cost without and with renumbering, respectively.

4.3.3 Inserting matrix components by packages

A strategy of inserting matrix components by packages consist on inserting several coefficients in the global sparse matrix in a unique high–level operation. If the location of several coefficients in the `pr` array is known, it is possible to optimize the insertion algorithm reducing the number of memory movements. In particular, we compare the single–insertion of every component and the possibility of inserting all the coefficients of every elementary matrix in a unique high level operation.

Single–insertion versus package–insertion

The two extreme grouping cases are: *single–insertion* when the position of only one coefficient is known, and *fully ordered–insertion* when the complete pattern

of the matrix is known and all coefficients (the complete matrix) are inserted in one operation. The assembling Cost using the single–insertions is the sum of each individual insertion and the Cost of the fully ordered–insertion is zero. In the later case the complete pattern of the matrix is known, thus the position of each coefficient in `pr` can be calculated in advance and no memory movements are required.

Both cases can be easily implemented in Matlab. The widely used assignment instruction using matrix–indexes

```
K(Te,Te) = K(Te,Te) + Ke
```
(4.17)

implements the single–insertion case[2]. On the other hand, the instruction `sparse(i,j,s,m,n)` implements the fully ordered–insert case. This instruction uses `i`, `j`, and `s` to generate an m–by–n sparse matrix `S` such that `S(i(k),j(k)) = s(k)`. The main drawback using `sparse` is that all elementary matrices and all indices must be stored in memory before calling the `sparse` function. The memory needed to store all elemental matrices is, in average, six times larger than `nnz` for a triangular mesh, four times for a quadrilateral mesh, 24 times for a tetrahedral mesh, and eight times for an hexahedral mesh. Therefore, this procedure can only be used if memory restrictions are not critical.

The EbE–insertion algorithm

Between these two previous extreme cases is the insertion of all the components of every elementary matrix in a unique operation. Packing the information in a element–by–element basis is a natural option in finite element context, where one element is processed at time. Additionally, the package at element level, leads to minimal changes in existing codes to include the proposed procedure.

We call element–by–element insertion, or *EbE–insertion* to the insertion of an elementary matrix in a package. The idea of the algorithm is, first locate all the positions corresponding to the inserted elements in `pr`. Some positions may correspond to already allocated positions in the global matrix. The modification of existing values is straightforward. The other positions need a modification of `pr` to create the places for the new coefficients. As several new places are created in a single operation, the movements of chunks of `pr` are reduced.

In other words, inserting every coefficient individually results in moving some

[2]The algorithm used in Matlab to implement matrix indexing is not available in Matlab documentation. However, an accurate analysis of execution times indicates that the strategy is likely based in a single–insertion and, hence, not efficient. A brief discussion is given at the end of Section 4.3.3.

components of the `pr` array several times, especially the components at the end of the array. Instead of that, we determine the space needed to insert all values in `pr`, and then, only one movement of each already allocated coefficient in `pr` is performed. Each coefficient is moved as many places as the number of new values are inserted before it, but just once.

Algorithm 4 lists the pseudo code of the EbE–insertion algorithm used to insert a elementary matrix K_e into the global matrix K at global positions T_e.

Our implementation in C language of this algorithm can be downloaded from `http://www.ija.csic.es/gt/sergioz/`. It is ready to build a Matlab external file (*mex file*) and it is designed to be used it in any Matlab program with minimal code changes: only one line of code has to be replaced (the assembly). This code has been successfully tested in Windows and Linux environments and in 32 and 64 bits processors.

Counting operations

The complexity of the insertion algorithms[3] is analyzed by counting the operations needed to insert a square element matrix of size m_e in a global square sparse matrix of size m. The worst case of the the single–insertion algorithm uses

$$\mathcal{O}\left(m_e^2\,(b+m+n_{\text{nz}})\right)$$

operations. Where b and n_{nz} are, respectively, the max bandwidth, and the number of non–zero coefficients of the global matrix. The worst case of the EbE–insertion algorithm as implemented in this work uses

$$\mathcal{O}\left(m_e^2\,b+m+n_{\text{nz}}\right)$$

operations. The average case for both algorithms modifies the term n_{nz} changing it by the average number of `pr` coefficients reallocated. This number is difficult to estimate in a general case.

Numerical tests

Analysis of the insertion Cost. To test the EbE–insertion algorithm proposed in Section 4.3.3 we compare the assembling Cost using both single– and EbE–insertion procedures. The same meshes of Section 4.3.2 are used here. For

[3]The complexity of an algorithm is the amount of resources required for its execution as a function of the size of the inputs. In this case we count the number of memory movements as a function of the size of the involved matrices.

Algorithm 4 Pseudo code of EbE–algorithm

Require: global sparse matrix K (stored in the arrays pr, ir and jc), element matrix K_e, insertion indices T_e

Ensure: updated matrix K

{Sort}sort the indices T_e and accordingly the element K_e matrix

1: sort T_e
2: sort K_e

{Find positions}find the position in K where each coefficient of K_e will be stored. Each position may be already allocated or not. If not, memory movements are needed to store the new coefficient in its corresponding place. The position of the coefficients to be inserted is stored in the *newPositions* array. The columns of the K matrix corresponding to the new positions are stored in the *columnNewPositions* array.

3: **for all** coefficient c in K_e **do**
4: p = find position of c in pr
5: **if** the position p is not already allocated **then**
6: add p to the *newPositions* list
7: add the column to the *columnNewPositions* list
8: **end if**
9: **end for**

{Fix jc}fix the jc array by increasing all values from the columns where the new coefficients are inserted to the end of the array.

10: **for** i from 1 to size($modifiedColumns$) **do**
11: increase all coefficients of jc between $modifiedColumns[i]$ and $modifiedColumns[i+1]$
12: **end for**

{Fix pr}make place in the array pr (and ir) to store the new coefficients.

13: add the size of pr to the end of *newPositions* array
14: **for** i from size(*newPositions*) to 1 step -1 **do**
15: move i places the segment of pr from $newPositions[i]-1$ to $newPositions[i-1]$
16: **end for**

{Insert}at this point all position in pr were created. Finally, the coefficients of K_e have to be inserted (or added) to their corresponding locations in pr. Only rest inserting (or adding) the coefficients of K_e in its corresponding position.

17: **for all** coefficient c in K_e **do**
18: insert c
19: **end for**

each mesh, the node numbering with minimal bandwidth has been used (the RCM renumbered version of the triangular meshes, and the non–renumbered version of the square structured meshes). Note that the worst is the node numbering, the larger is the difference between EbE– and single–insertion algorithms (favoring EbE–insertion). Therefore, using a different numbering would result in a even better performance of the EbE–insertion algorithm.

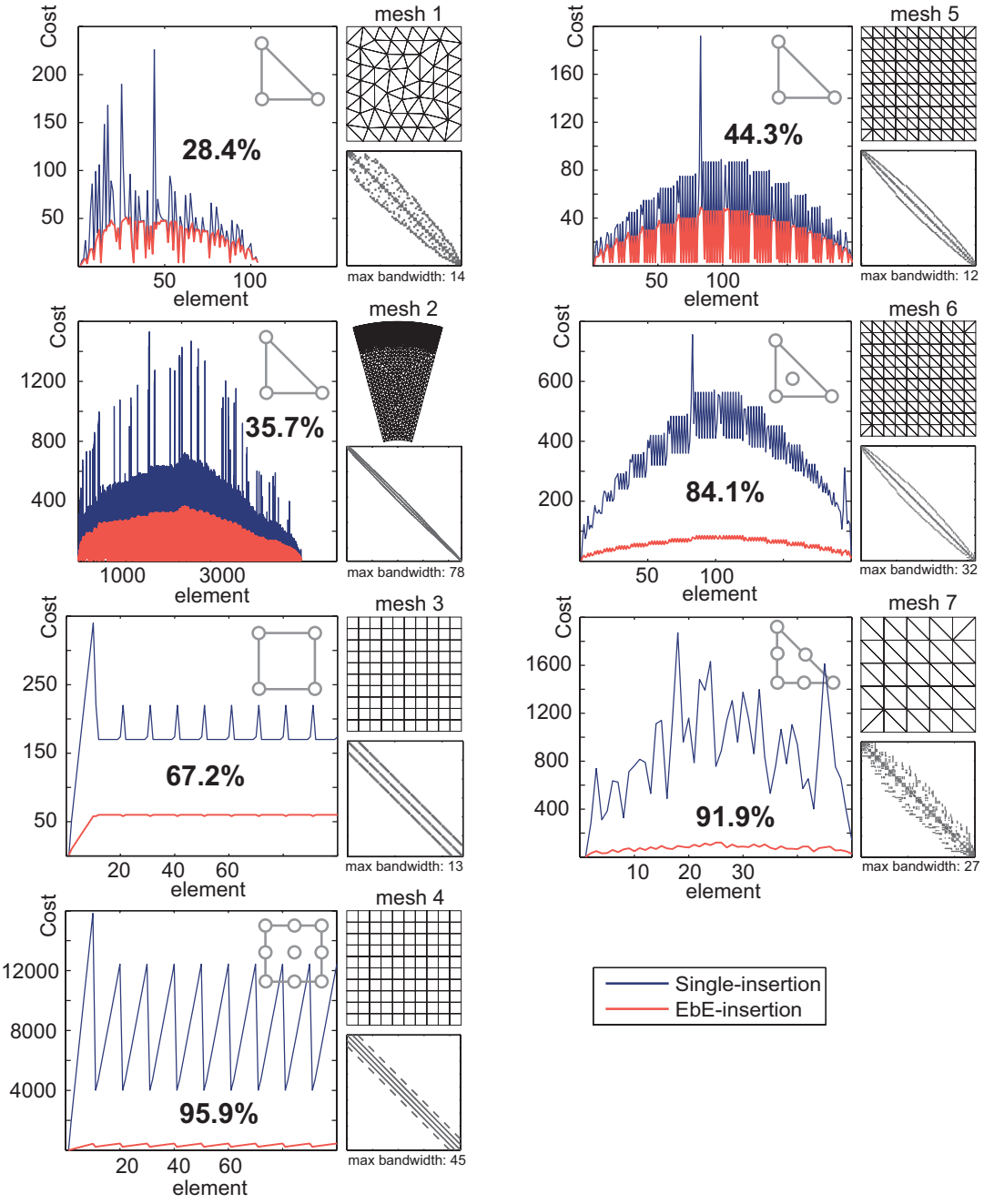

Figure 4.19 – Comparison of the assembly Cost for single– and EbE–insertion strategies for different meshes. The mesh and the pattern of the assembled matrix is shown at the right of each Cost plot. The element type is displayed inside each Cost plot. The reduction in Cost obtained using the EbE–insertion is displayed in boldface.

Figure 4.19 shows the Cost plots for both algorithms. In each panel the mesh and the pattern of the resulting matrix is also shown. As expected, the assembly using EbE–insertion has lower Cost for all the tested meshes. The improvement for high order elements is much greater than in low order elements. The reduction in Cost obtained by the EbE–insertion algorithm for second–order square elements is 95.9%

(the Cost is divided by more than 20). For the linear triangles the Cost reduction is between the 45 and 28%.

This analysis corresponds to a scalar problem, with only one degree of freedom per node. For vectorial unknowns, with more than one degree of freedom per node, the gain using EbE–insertion is even larger.

Analysis of the assembly computing time. The ultimate goal of the proposed algorithm is to reduce assembling time. The Cost, as defined in this work, is a theoretical measure that is used as an indicator but it cannot be directly related with computing time.

To study the time relation between the algorithms, a finite element global matrix is assembled and the insertion time of each elementary matrix is registered. The single–insertion is implemented with the matrix indexing Matlab assignment and the EbE–insertion is implemented in a *mex* file.

Figure 4.20 shows the measured times for several meshes. The total assembly time is the sum of all elementary insertions or, graphically, the area below the curve. The EbE–insertion algorithm reduces the computation time in all tested cases. The same behavior as with the Cost indicator is obtained: higher order elements have a larger improvement compared with simpler elements. Assembly time for mesh 3 (nine–noded quadratic squares) has been reduced in 90% compared with single–insertion time, even for a small size mesh with 400 elements.

The reduction in assembly time is more significant if the number of elements or its complexity type increases. This is confirmed comparing the results corresponding to the meshes with the same element type. See, for instance, meshes 2, 6 and 1 (composed by mini–elements) with 4300, 800 and 104 , respectively. The gain obtained using EbE strategy is however also important for simple elements. In fact, even for the simplest 2D elements, the linear triangles, the assembly time is reduced in 26%.

Since single–insertion is implemented in a Matlab built-in function and EbE–insertion is a mex file[4], the time measured can be biased by different factors like interpreter time, dynamic link library calls, etc. To fairly compare single– and EbE–insertion algorithms, a single–insertion routine was implemented in a mex file and compared with the built-in Matlab assigned function. The mex implementation is observed experimentally to be of about 10% faster than the Matlab assignment, probably due to parameter checking. The reduction percentages displayed in Figure 4.20 refer to the standard Matlab built-in function which is

[4]Matlab external file.

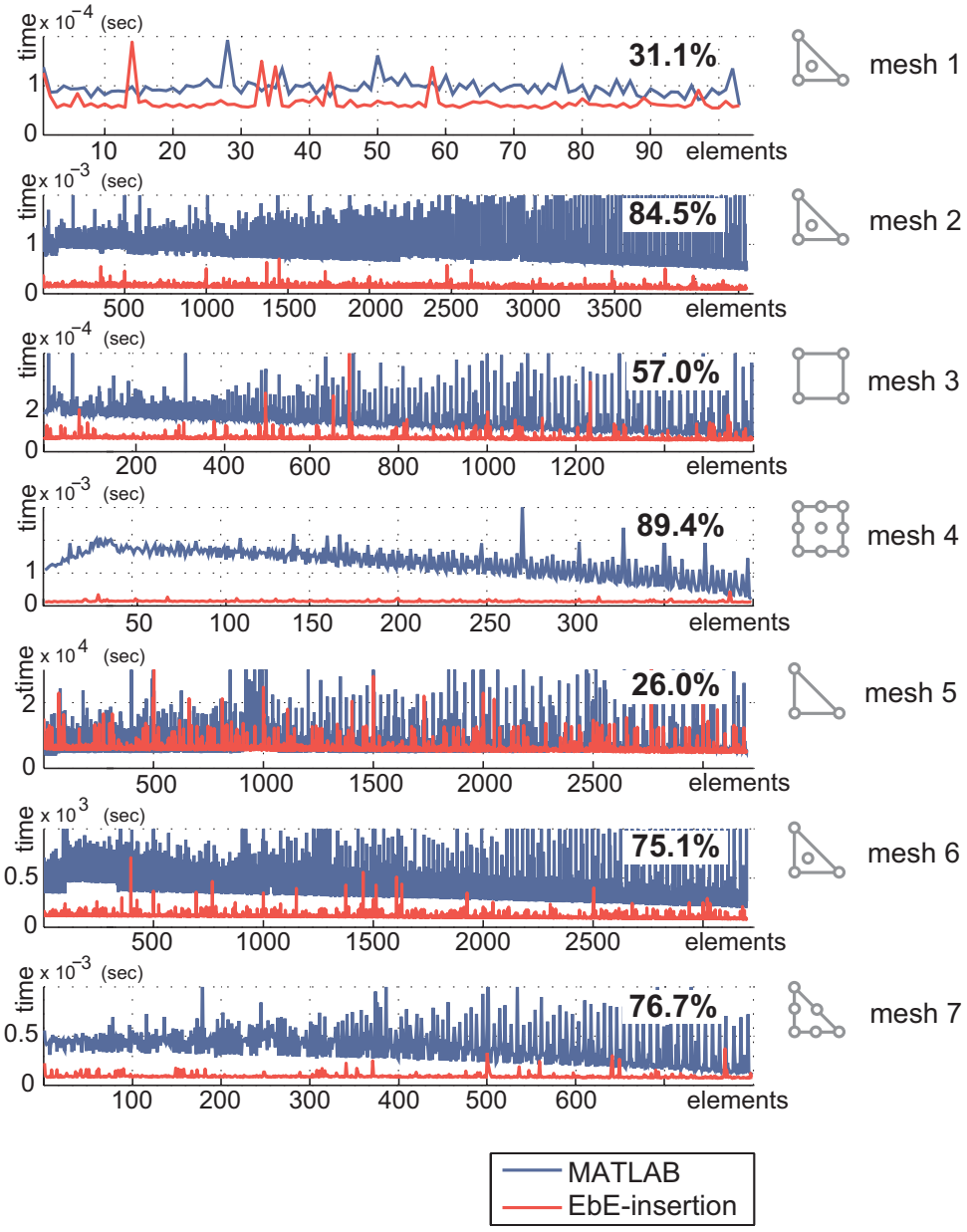

Figure 4.20 – Comparison of the computing time used to assembly a global matrix with different insertion algorithms. The time used to insert each element in the global matrix is measured. The total assembly time is the sum of all these times, that is, the area below the plotted curve. Single–insertion algorithm is implemented with the Matlab matrix assignment. EbE–insertion is coded in C and included as a Matlab external (mex) file. Same meshes as in Section 4.3.3 are used. In meshes number one and two a central bubble node is included. Element type is displayed at the right of each panel. The reduction in the global matrix assembly time obtained using the EbE–insertion is displayed in boldface.

the natural choice for a standard Matlab user. If expressed with respect to the mex implementation of the single–insertion, the gain obtained by the EbE–insertion would be slightly lower.

The fact that the relation between the built-in Matlab insertion and the mex single–insertion time is roughly a constant (it does not depend on the element order or the number of elements), indicates that the number of operations done by both algorithms are of the same order. This suggest that the Matlab assignment instruction uses this algorithm.

4.3.4 Using (previous) matrix pattern in a time marching scheme

In a time marching procedure, where matrices with similar pattern have to be assembled at each time step, the efficiency of the assembly may be improved using the pattern of the matrix at the previous step. If the pattern of the matrix completely changes from step to step, for example if a complete remesh is performed, no piece of information from previous step can be used and the situation is similar as in previous Sections. If the pattern of the matrix remains unchanged, all information on the positions of the coefficients in `pr` is available, allowing for a zero Cost assembly in all steps after the first one. An intermediate case happens when most of the pattern is fixed and only a few positions change. Examples of this case are the mesh updating methodology proposed by Knupp (2007) and the procedures adding new degrees of freedom in a partition of the unity framework (Zlotnik et al., 2007a).

A very simple algorithm, taking advantage of the information of the previous pattern can be implemented by maintaining the `ir` and `jc` vectors from the previous step and resetting the `pr` to zero. The scheme of this algorithm is summarized in the Algorithm 5. In the first step the sparse matrix K is cleared keeping the pattern in the `ir` and `jc` vectors. Note that after this step K is not a valid sparse matrix because it stores zero coefficients. The second step is a standard assembly process. All inserted coefficients will be added to existing positions in `pr`. As `pr` have been set to zero, the resulting `pr` vector is the same as starting from a empty matrix. If the pattern of the matrix is exactly the same of the previous step, all positions in `pr` will be set to its new value. If a new coefficient needs to be stored in a previously non–existent position, the insertion algorithm will generate the required place. Finally, when the assembly has been done `pr` needs to be checked to assure that no zero–coefficients remains. If there are zeros stored they have to be removed to preserve sparsity. That is done in the third step.

Note that the implementation of this strategy in an existing code is not as simple as replacing the insertion instruction (4.17), which was the case of the EbE–insertion algorithm. In fact, this strategy involves intermediate states of non–valid sparse matrices. The first step (initialization) and the third (fix sparsity) are not standard

Algorithm 5 Scheme of the pattern–reutilization algorithm

Ensure: global K matrix

{Initialization}Set all coefficients in pr to be zero and left ir and jc unchanged. Note that after this step K is not a valid sparse matrix because there are zeros stored (in fact, all stored values are zero)

1: **for all** coefficient c in pr **do**
2: $c \leftarrow 0$
3: **end for**

{Assembly}Assembly the matrix in a traditional way (using EbE– or single–insertion)

4: **for all** element e **do**
5: compute the element matrix K_e
6: insert the K_e matrix in the global matrix K
7: **end for**

{Fix sparsity}If, after assembly, some coefficient of K remains zero, remove it

8: **for all** coefficient c of K **do**
9: **if** $c = 0$ **then**
10: remove c from K
11: **end if**
12: **end for**

in Matlab. This is because they produce (the first) and fix (the third) non–acceptable sparse matrices.

The Matlab external routine provided here can also be used to perform these two operations (using the proper input options). The current implementation is only valid for matrices K with constant size (the sparsity pattern may change but the global dimensions m and n must be kept constant). The gain in computing time obtained by using this strategy in a evolutionary process has been found to be of about 10%. The outcome of the numerical experiment, with a mesh of 3200 triangular mini–elements, is shown in Figure 4.21.

4.3.5 Summary and conclusions

In this section the assembly of sparse matrices in a finite element–like framework has been analyzed. A new EbE–insertion algorithm is proposed. It reduces significantly the assembly computing time. The role of node numbering and the different insertion strategies have been tested based on a theoretical Cost indicator and computing time.

Node and element numbering is an important factor, with a high influence in the efficiency of the assembly process of sparse matrices. Algorithms designed to reduce matrix bandwidth help to reduce the assembly time in most cases. Bad node numbering considerably increases the assembly computing time, eventually

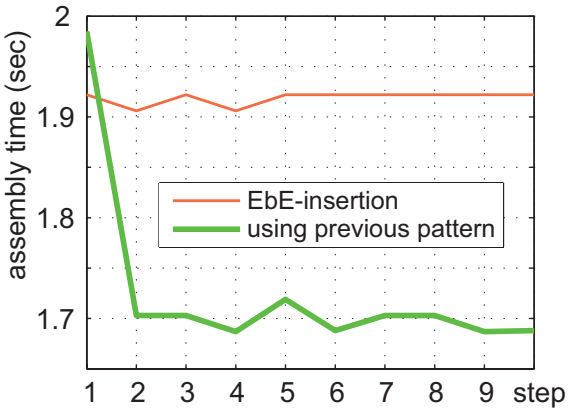

Figure 4.21 – Time of assembly a sparse global matrix in 10 consecutive time steps. Pure EbE–insertion and the algorithm taking advantage of the pattern of the matrix in the previous step are compared.

overcoming the time of solving the system.

A simple program based on grouping the insertions of a elemental matrix has been proposed and tested. This EbE–insertion strategy is natural in finite element frameworks and requires minimal changes to include it in previous Matlab codes. This program performs better than the Matlab built-in assignment. In some cases, reducing the assembly time in 90%.

In evolutionary problems, stiffness matrices must be assembled at each time step and the pattern of the previous step can be used to improve the assembly. Using this idea, the assembly time in a standard test is found to be reduced in 10%.

The implementation presented here is a C code that can be compiled to a Matlab external file (*mex file*) and straightforwardly included in any existing Matlab code.

Chapter 5

Stability of the oceanic lithosphere

Oceanic lithosphere is being continuously created at mid–ocean ridges, where adjacent plates move apart from each other in a process called seafloor spreading. As the plates diverge, hot mantle rocks ascend to fill the gap and partially melt. Upon subsequent conductive cooling, these rocks become rigid and form new oceanic lithosphere. The complementary process of plate consumption occurs along subduction zones, where plates bend and descend into the Earth's mantle. The entire process of creation, lateral displacement, and eventual subduction of oceanic lithosphere can be thought of as a large–scale convection cell, where the oceanic lithosphere represents the upper thermal boundary layer.

As oceanic plates move away from ridges, they cool from above, thicken, and become denser by thermal contraction. This cooling is reflected on the dependence of geophysical observables on the age of the plate t (McKenzie, 1967; Parsons and Sclater, 1977). For plates younger than about 70 Ma, both seafloor topography and surface heat flow (SHF) decrease linearly as $\sqrt{t}$, consistent with predictions from the *half–space cooling model* (Turcotte and Oxburgh, 1967). In this model a purely conductive cooling takes place in an infinite rigid half space.

For larger ages, however, this relation breaks down and bathymetry and heat flow decrease less rapidly, reaching almost constant values in ocean basins (Parsons and Sclater, 1977; Schroeder, 1984; Stein and Stein, 1992). Since these observables reflect the thermal structure of the lithosphere, their flattening implies a similar behavior for the isotherms within the plate. These features are included in the popular *plate model* (McKenzie, 1967), which considers the lithosphere as a cooling plate with a horizontal isothermal lower boundary. Although this model can explain the observed flattening of both seafloor topography and SHF, it does not propose any particular mechanism by which the isotherms are maintained at constant depth. In practice the plate model demands to add a basal heat to the oceanic lithosphere.

There are mainly two proposals that are aimed to explain this extra heat supplied to the lithosphere. First, the extra heating is attributed to thermal instabilities that may occur dynamically below a relatively old lithosphere (sublithospheric small–scale convection (SSC)) (Parsons and Sclater, 1977; Parsons and McKenzie, 1978; Yuen and Fleitout, 1985). In this model the material at the bottom of the lithosphere is warmed conductively by the extra heat transported by secondary convection at the bottom of the lithosphere. Deep lithospheric mantle rocks consequently become soft enough to creep but, being denser than the underlying soft upper mantle, they will plunge into it. This process prevents the lithosphere from continuous cooling as predicted by the half space cooling model. The low viscosity needed to develop the small–scale convection at the bottom of the lithosphere is justified by the dependency of the mantle viscosity on the combined effects of temperature and pressure(Yuen and Fleitout, 1985). Second, the deviations in observations are believed to be caused by convective processes associated with the deep mantle, in particular the mantle upwelling plumes (Schroeder, 1984; Davies, 1988; Morgan and Smith, 1992). This model assumes that the departure may be due to dynamic topography linked to lower mass anomalies or mantle return flows.

Small–scale convection has been studied using theoretical (e.g. Parsons and McKenzie, 1978; Yuen et al., 1981; Jaupart and Parsons, 1985), numerical (e.g. Yuen and Fleitout, 1985; van Hunen et al., 2003; Huang and Zhong, 2005; van Hunen et al., 2005; Huang et al., 2003; Korenaga and Jordan, 2004; Dumoulin et al., 2001) and analogue models (e.g. Curlet, 2001). All these studies have been focused on the general conditions for the existence of SSC, but non of them attempted a systematic exploration of the effects of all relevant physical parameters on SSC. Moreover, either seismically derived thermal structures or SHF and seafloor topography data have been used to test the reliability of the results, but no study has combined these three observables into a single consistent model. This is of particular relevance because seismic observations seem to favor half–space cooling models over plate models, while SHF and seafloor topography observations suggest the opposite.

In this chapter a systematic study on the influence of several rheological and thermo–physical parameters on SSC, its expression in geophysical observables, and its role in determining the thickness of oceanic lithosphere is presented. Predictions of seismic velocities, SHF and seafloor topography are used to ensure compatibility with current observations. In the following sections the statement of the problem and the applied numerical methods are firstly introduced; then the approach to calculate the relevant geophysical observables is described; finally, the results and their implications on the evolution of the oceanic lithosphere are discussed.

5.1 Model description

5.1.1 Governing equations

The Earth's mantle behaves as a highly viscous fluid over the long time scale ($t > 10^4$yr) (cf. Busse, 1989; Schubert et al., 2001). Since the physical properties of this fluid are strongly dependent on temperature, the physical model involves a mechanical flow problem coupled to a thermal problem. We consider an incompressible fluid in a rectangular domain. Due to the almost infinite Prandtl number of the fluid, inertial terms are neglected and the problem becomes quasi–static. The transient character of the solution is due to the evolution of the temperature field. Under the Boussinesq approximation (i.e. the effects of density variations other than in the body–force terms are neglected), the three unknowns, velocity $\mathbf{u}$, pressure p and temperature T, are determined by solving the conservation of momentum, mass, and energy equations introduced in Chapter 2. A similar approach, including the incompressible and Boussinesq assumptions, has been used in previous numerical studies of SSC (e.g. McKenzie et al., 1974; Yuen and Fleitout, 1985; Schmeling and Marquart, 1991; Huang et al., 2003; van Hunen et al., 2005, and others).

5.1.2 Constitutive equation

Convective flow in the Earth's mantle is possibly due to the high–temperature creep of mantle rocks. This solid–state deformation mechanism occurs due to the thermally activated motion of atoms associated with lattice defects such as dislocations and vacancies (cf. Ranalli, 1995). There is general agreement that two main creep mechanism are likely responsible for most of the deformation in the mantle: diffusion creep (Herring–Navarro and Coble creep) and dislocation creep (Kirby, 1983; Ranalli, 1995). Although there are significant uncertainties associated with the extrapolation of laboratory results (performed at low pressures and high strains rates) to mantle conditions, a comparison of microstructures on experimentally and naturally deformed peridotites indicates that the same deformation mechanisms detected in laboratory take place in the mantle as well (Ranalli, 1995; Hirth and Kohlstedt, 2003). Deformation caused by dislocation creep is evidenced in lithospheric mantle samples (e.g. xenoliths, peridotitic massifs) and indirectly inferred in the shallow upper mantle from seismic anisotropy studies (see Nettles and Dziewonski (2008) for a recent review). On the other hand, diffusion creep may be dominant over dislocation creep at depths $> 250 - 300$ km, where

stresses are low and pressure effects become dominant (i.e. the activation volume of diffusion creep seems to be smaller than that of dislocation creep, (Ranalli, 1995)). This change in deformation mechanism with depth is consistent with the lack of significant anisotropy at such depths, although not conclusive (Mainprice et al., 2005).

Theoretical treatments and experimental observations demonstrate that the macroscopic creep behavior of rocks is well described using a "power–law" of the form (Ranalli, 1995; Karato and Wu, 1993; Regenauer-Lieb et al., 2006)

$$\dot{\varepsilon} = A(\sigma'/\mu)^n (b/d)^m \exp\left(-\frac{E+pV}{RT}\right) \tag{5.1}$$

where d is the average grain–size, σ' the deviatoric stress, A the pre-exponential factor, μ the shear modulus, b the length of the Burgers vector, n the stress exponent, m the grain–size exponent, E the activation energy, V the activation volume, and R the gas constant (see Table 6.1). The combination of equation (5.1) with the definition of viscosity ($\eta = \frac{1}{2}\sigma'/\dot{\varepsilon}$), allows isolating an explicit expression for η in terms of T, p and $\dot{\varepsilon}$. This expression is then used to solve equation (2.15).

To compute the viscosity we assume a constant material parameter

$$A_D = \frac{1}{2} A^{-1/n} \mu^{-1} (b/d)^{-m/n},$$

including the pre-exponential factor A, the grain–size dependence, and the shear modulus. Although grain–size may change due to grain growth and dynamic recrystallization processes, its dependence on stress is not well known. Thus, we consider only constant grain sizes.

Diffusion and dislocation creep act simultaneously in the mantle (Ranalli, 1995). In order to account for the effect of the two mechanisms, two different viscosities η_{diff} and η_{disl} are computed separately and then combined into an effective viscosity η_{eff}, which is computed as the harmonic mean of η_{diff} and η_{disl}:

$$\frac{1}{\eta_{\text{eff}}} = \left(\frac{1}{\eta_{\text{diff}}} + \frac{1}{\eta_{\text{disl}}}\right). \tag{5.2}$$

This expression is truncated if the resulting viscosity is either greater or lower than two imposed cutoff values (10^{18} to 10^{24} Pa s^{-1}). The viscosity η_{diff} is computed using $n = 1$ while for η_{disl} we use $m = 0$. The values of the rest of the parameters are described in Section 5.2.

The viscosity is greatly affected by the water content of the rocks and mineralogy. Its influence on viscosity is detailed in the next section.

5.1.3 Phase transitions, mineral and chemical domains

At least four main solid–solid mineral phase transitions occur in the mantle region considered in this study: plagioclase–spinel, spinel–garnet, olivine–wadsleyite, and wadsleyite–ringwoodite. Other phase transitions (e.g. orthoenstatite to clinoenstatite) may occur within the domain, but their effect on the type of gravitational instabilities of interest are negligible. Here we consider explicitly the spinel–garnet, olivine–wadsleyite, and wadsleyite–ringwoodite phase changes, which are the most relevant in terms of density and viscosity contrasts that may exert a control on the vertical structure of SSC. Each of these phase transitions is characterized by a particular Clapeyron slope, which we approximate as linear functions in the temperature–pressure domain (See Table 2.3). To accurately reproduce the Clapeyron curve of the spinel–garnet transformation, two different linear functions are used. The olivine–wadsleyite and wadsleyite–ringwoodite transitions occur at $\sim$ 410 and 510 km depth, respectively, in a pyrolitic adiabatic mantle. The spinel–garnet transition occur between $\sim$ 40 – 80 km depth. The depth variability in the latter is due to the exothermic nature of the reaction and the rapid horizontal temperature variation in the shallow oceanic upper mantle. The spinel–garnet phase change occurs deep enough to be affected by SSC, and given its exothermic nature and associated density change (0.8 – 1.0 %, Afonso et al. (2007)), it could influence on SSC through buoyancy enhancement (cf. Schubert et al., 2001).

The phase transitions not only affects to density and thermal conductivity but also the viscosity. A viscosity increment of a factor $\sim$ 10 has been reported in the transition zone due to the wadsleyite–ringwoodite transition at $\sim$ 410 km depth (Hager and Richards, 1989).

Within the lithosphere chemical boundaries may also greatly influence the density and viscosity distributions. The oceanic lithosphere forms as the residue of partial melting beneath mid–ocean ridges, which are driven by passive upwelling. The partial melting process on the ocean ridges results in a mantle residue that is not only chemically buoyant but also dehydrated, the latter resulting in an increase of intrinsic viscosity, see Figure 5.1 . These effects of the residual layer are to compete against the development on convective instabilities. There are two important consequences of melt extraction. Firstly, the residue becomes intrinsically lees dense because the dense minerals, garnet and clinopyroxene, are exhausted and the proportion of Fe relative to Mg decreases. Secondly, the progressive dehydration of the solid residue due to the incompatible nature of H_2O during partial melting. The intersection of the mantle adiabat and the mantle solidus represents the depth at which dry melting initiates and the peridotite residue can be completely dehydrated.

Using the parameterizations of the degree of melting, F, depending on pressure taken from Afonso et al. (2008)

$$F(p) = \begin{cases} 25.23 - 16.19p & \text{if } p < 1.25 \text{ GPa} \\ 10.0 - 4.0p & \text{if } p > 1.25 \text{ GPa} \end{cases} \tag{5.3}$$

and assuming a linear decrease in water content, W, between 0 and 3% of melt,

$$W(F) = \begin{cases} 1 & \text{if } F = 0 \\ 0 & \text{if } F > 3 \\ 1 - \frac{F}{3} & \text{otherwise} \end{cases} \tag{5.4}$$

we compute the dry–wet viscosity transition within the oceanic lithosphere, shown in Figure 5.1, as a linear combination of the fully wet and fully dry cases

$$\eta_{\text{eff}} = \eta_{\text{wet}} W + \eta_{\text{dry}}(1 - W) \tag{5.5}$$

where η_{wet} is the viscosity based on diffusion and dislocation deformation mechanisms and η_{dry} is incremented in two orders of magnitude.

5.1.4 Geophysical constraints to mantle dynamics

Geophysical observables are commonly used to infer the physical state of the Earth's interior. Available data sets that help to constrain, to different extents, mantle dynamics include ocean floor topography, surface heat flux and seismic velocities. As a post–process of our simulations, we estimate these observables.

Seafloor topography. Seafloor topography is estimated assuming local isostasy (i.e. mass per unit area of a vertical column is compared with respect to a reference value taken at the ridge). Following Jarvis and Peltier (1982), we define the isostatic topography w_{iso} as

$$w_{\text{iso}} = \int_{d_{\text{com}}}^{\text{surface}} (\rho - \rho_{\text{ref}}) \, \mathrm{d}z \tag{5.6}$$

where d_{com} is a compensation depth and ρ_{ref} is the density at the reference column. Although the choice of d_{com} is somewhat arbitrary, it should be taken close to the depth of the deepest isotherm with a dominant conductive component. Isotherms significantly deflected by convection are associated with dynamic loads that are not isostatically compensated (see dynamic topography below).

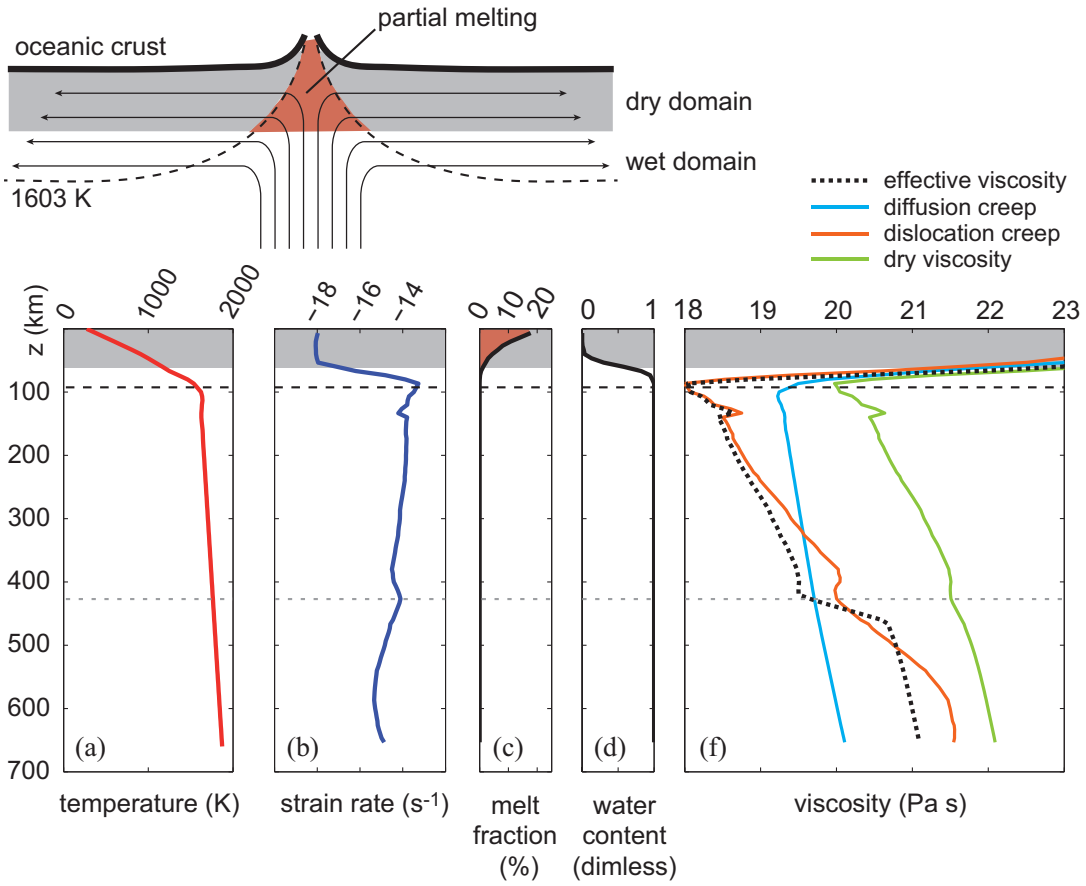

Figure 5.1 – Transition from dry to wet rheology due to dehydration produced by partial melting in the mid–ocean ridges. The thermal bottom of the lithosphere (dashed line) is determined by the 1603 K isotherm. Profiles at ~ 60 km from the ridge: (b) strain rate (log scale), (d) dimensionless water content. The effective viscosity is computed in terms of the dislocation and diffusion creep laws as an harmonic mean. At ~ 410 km depth, the wadsleyite–ringwoodite transition produces an increment in viscosity of one order of magnitude (Hager and Richards, 1989). In the dry zone within the lithosphere, the viscosity is incremented two orders of magnitude (Lee et al., 2005).

Dynamic topography. Vertical components of mantle flow may result in a modification of the surface topography. The resulting topography arising from this mechanism is known as *dynamic topography*, to distinguish it from that part of the topography resulting from the isostatic compensation of *static* loads (see above). Following McKenzie (1977), we estimate the dynamic component of topography w_{dyn} as

$$w_{\mathrm{dyn}} = \frac{\sigma_{zz}}{\rho\, g} \tag{5.7}$$

where σ_{zz} is the vertical stress component acting on the surface, ρ the density, and g the vertical component of the gravity acceleration. Convective shear stresses acting at the base of the lithosphere would also have an effect in the dynamic topography.

However, they typically represent less than 5% of the dynamic topography generated by vertical stresses and therefore they can be neglected (Marquart and Schmeling, 1989). In all our simulations the dynamic topography associated with SSC never exceeds ± 150 m. This number would be reduced by as much as 75 % if we included the elastic strength of the plate (Marquart and Schmeling, 1989).

Seismic velocities. The calculation of seismic velocities [$V_p^2\rho = K_S + 4/3G$ and $V_s^2\rho = G$] requires knowing the elastic moduli of each stable phase, the density of the bulk rock at the pressures and temperatures of interest, and estimations of anelastic attenuation. Here we compute these properties by a free energy minimization procedure (see details in Connolly, 2005) within the system CFMAS (CaO-FeO-MgO-Al_2O_3-SiO_2). These five major oxides make up more than 98% of the Earth's mantle, and therefore they constitute an excellent representation of mantle's composition. The minimization program (PerpleX) requires a thermodynamic database for pure end–members and solution models to compute the properties of stable phases (usually solid solutions of two or more end–members). The thermodynamic database used in the energy–minimization is that of Stixrude and Lithgow-Bertelloni (2007) with solution models as listed in Table 2.2 of Chapter 2.

The thermal and pressure fields necessary to calculate the seismic velocities are obtained from the thermo–mechanical simulation. This generates an unavoidable inconsistency between the density values used to calculate buoyancy forces in the thermo–mechanical problem and those used to calculate seismic properties in the energy–minimization scheme (densities from the energy–minimization are systematically greater than those from the thermo–mechanical simulation). Parallel computations indicate that this inconsistency translates into errors of $\lesssim$ 1.1 % in our calculated *absolute* seismic velocities. However, the seismic structure (i.e. spatial velocity distribution) generated by our models is not significantly affected.

Anelastic effects are computed as a function of grain size, d, oscillation period, T_o, T, p, and empirical parameters A, E, and α as Karato (1993); Afonso et al. (2008)

$$V_\theta = V_{\theta_o}(P,T)\left[1 - \zeta \cot\left(\frac{\pi\alpha}{2}\right) Q_s^{-1}(T_o,T,p,d)\right] \tag{5.8}$$

where $V_{\theta_o}(p,T)$ is the unrelaxed high frequency wave velocities at a given temperature and pressure (i.e. including anharmonic effects) and θ stands for either P–wave or S–wave velocities. The term ζ takes the values 2/9 and 1/2 for P–waves and S–waves, respectively (Afonso et al., 2008). The quality factor is represented as

$$Q_s^{-1}(T_o,T,p,d) = A\left[T_o\, d^{-1} \exp\left(\frac{-E+Vp}{RT}\right)\right]^\alpha \tag{5.9}$$

with A =750 $s^{-\alpha}$ μm^{α} , $\alpha = 0.26$, $E = 424$ kJ mol^{-1}, $V = 1.2 - 1.4 \times 10^{-5}$ m^3 mol^{-1}, and R the universal gas constant (Jackson et al., 2002; Faul and Jackson, 2005).

5.1.5 Model setup and boundary conditions

The simulation domain is a rectangular box representing a vertical plane parallel to the plate motion, see Figure 5.2a. The box is divided into approximately 13000 triangular elements representing a vertical thickness of 660 km in nature. The horizontal dimension is 7000 km wide, unless indicated otherwise. Since the oceanic crust does not play any significant role on the dynamics of SSC, it is neglected in our model. Temperature boundary conditions assume constant temperatures at the surface and at the bottom of the simulation domain and zero–flux on the domain sides. The initial internal temperature distribution follows the half–space cooling model, which is calculated in terms of the surface temperature T_{surf}, temperature at the bottom of the lithosphere T_{lith}, and thermal diffusivity κ as Schubert et al. (2001)

$$T(t,z) = (T_{\text{surf}} - T_{\text{lith}})\ \text{erfc}\left(\frac{z}{2\sqrt{\kappa\, t}}\right) + T_{\text{lith}} \tag{5.10}$$

where t is the age of the plate, z is the depth and erfc is the complementary error function. The age t is directly related to the horizontal space dimension through the plate velocity. This model gives "conductive" temperatures above a specific isotherm T_{lith}, which represents the base of the lithosphere. For temperatures below this isotherm, a linear interpolation is done between T_{lith} (here chosen = 1603 K) and the temperature at the bottom of the box, T_{bot}. The latter is chosen to be 1880 K, in accordance with results from high–pressure and high–temperature experiments on mineral phase equilibria (e.g. Katsura et al., 2004). On the laterals the normal flow is set to zero.

A constant horizontal velocity is imposed at the top of the model, everywhere but near the corners (see Figure 5.2a). Imposing a constant velocity at the top of the entire domain generates singularities in the upper corners (and nearby regions) where the strain rate reaches unrealistic high values. We avoid this undesired effects by allowing a free–slip condition in regions near both corners, which leads to the generation of a smoother corner flow. For similar reasons, we further introduce two small weak zones near the upper corners (see Figure 5.2a), as commonly done in similar studies (Huang and Zhong, 2005). The viscosity in these regions is divided by 10, 100 or 1000 depending on the model. In the other three sides of the domain free slip boundary conditions are imposed. To avoid excessive heating generation at the corners of the model, shear heating is turned off within two rectangular areas

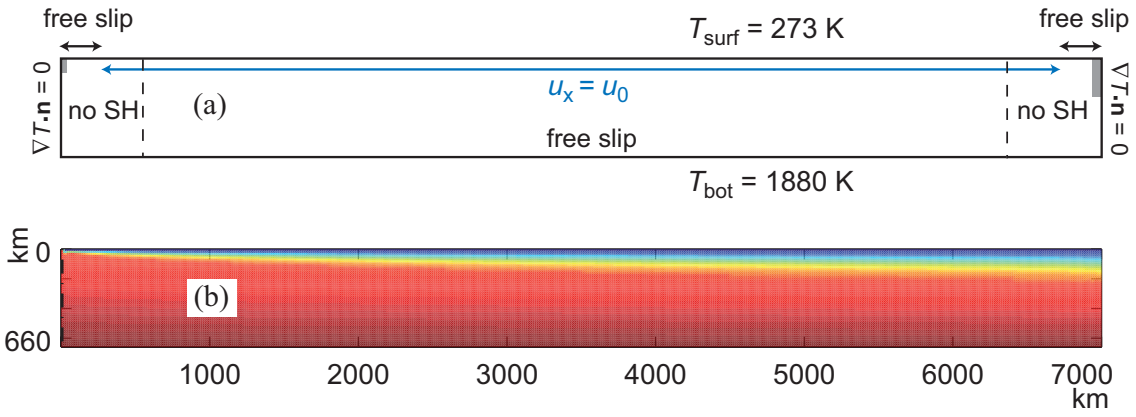

Figure 5.2 – Boundary (a) and initial (b) conditions for SSC models. The gray areas in panel (a) are the regions were viscosity is decreased. The dashed lines delimit areas where shear heating is neglected.

at the ends of the domain (see Figure 5.2a). Each rectangle represents 10% of the total domain length. Since we are interested in the generation and evolution of SSC regions well outside these regions, the neglect of shear heating within them does not affect our results and conclusions.

5.2 Results

This section is organized in two parts. In the first part the main features of SSC and its effect on the thermal structure of both lithosphere and sublithospheric mantle is described. In the second part systematical analysis of the influence of key physical parameters on the generation and evolution of SSC is presented.

5.2.1 General features of small–scale convection

In this section an illustrative model in which SSC is fully developed is presented. The imposed upper velocity is 3.5 cm yr^{-1}, comparable to absolute velocities reported for oceanic plates (Gripp and Gordon, 2002). The only internal heating term included in the energy equation is the adiabatic heating (i.e. shear heating and radiogenic heat production are set = 0). The wet to dry rheology transition is not included in this model. Instead, we assume a pure Newtonian rheology with the following parameters: activation energy $E = 120$ kJ mol^{-1}, activation volume $V = 4 \times 10^{-6}$ m^3 mol^{-1}, and pre-exponential factor $A_D = 7.6 \times 10^{-16}$ Pa^{-1} s^{-1}. Similar values have been extensively used in earlier studies on SSC (e.g. van Hunen et al., 2003; Huang and Zhong, 2005; van Hunen et al., 2005; Huang et al., 2003), allowing qualitative comparisons between these and our models. We emphasize, however, that the chosen

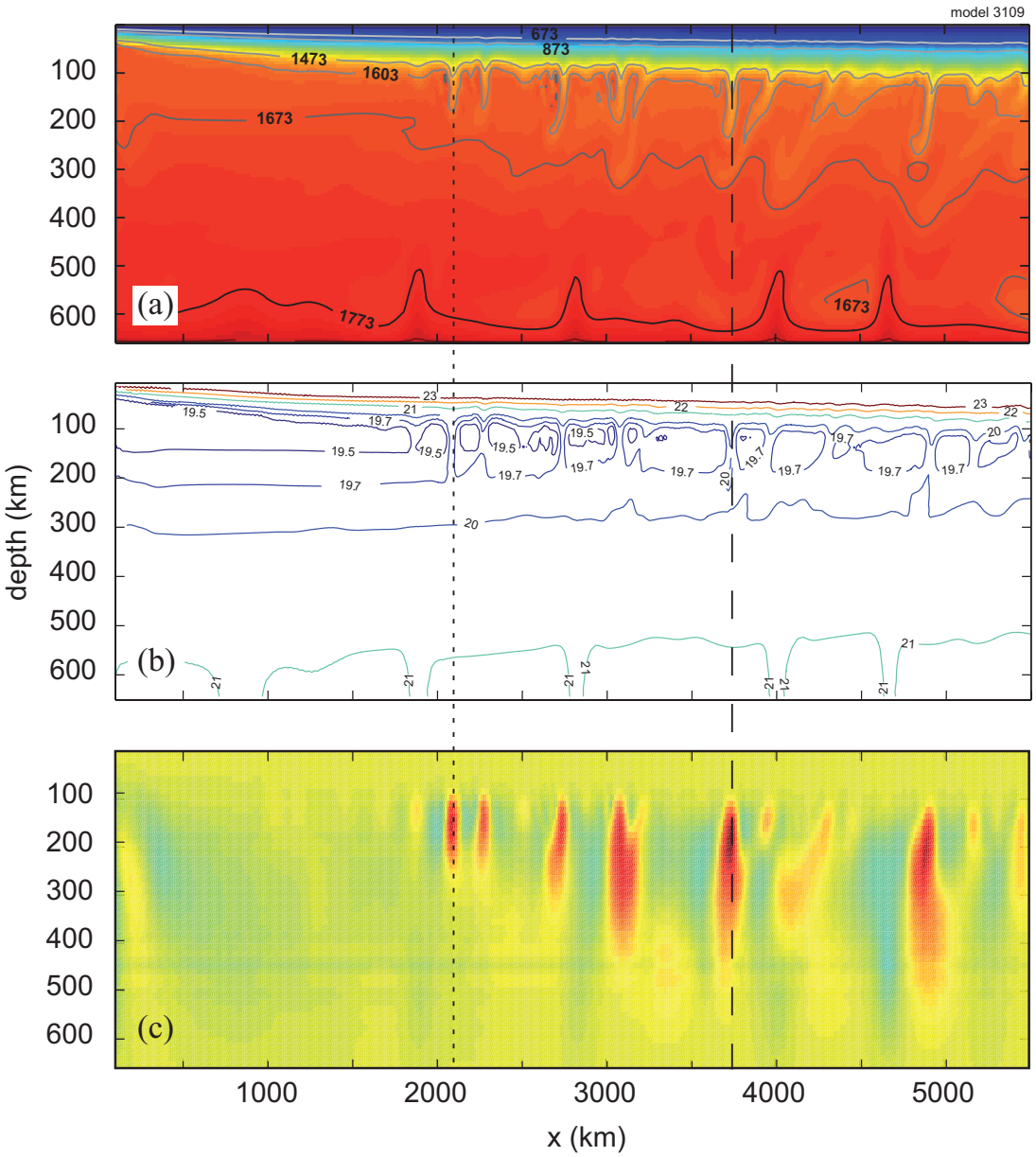

Figure 5.3 – Typical temperature (a), viscosity (b) and vertical velocity (c) when small–scale convection develops. Temperature expressed in K, viscosity in Pa s. See text for details.

activation energy and pre-exponential factor values are too low to be consistent with currently available laboratory experiments on diffusion creep (e.g. Karato and Wu, 1993; Hirth and Kohlstedt, 2003). A complete discussion on the effects of these parameters on the development and evolution of SSC is provided in the next section.

Figure 5.3a shows the resulting thermal structure after the dynamic steady–state is reached At this stage, the onset of SSC occurs at $\sim$ 2100 km from the ridge (dotted line in Figure 5.3) or when the lithosphere is $\sim$ 60 Ma old. At shorter distances (younger lithosphere), the isotherms follow closely the initial thermal structure

predicted by the half–space cooling model. The wavelength of the instabilities is of the order of 150 – 200 km throughout the entire model. Some isotherms (in Kelvin) are plotted to show the perturbing effect of SSC. The 1603 K isotherm, which is typically assumed to represent the base of the lithosphere, is completely distorted due to SSC (advection–dominated). Even the 1473 K isotherm shows an advective component, although considerably less than hotter isotherms.

The resulting viscosity structure is plotted in Figure 5.3b. In order for SSC to develop, we find that the viscosity of the upper 300 km of mantle needs to remain lower than 10^{20} Pa s, since values inhibits SSC. This value is similar to those previously reported by different authors (Korenaga, 2002; Huang and Zhong, 2005; van Hunen et al., 2005). Figure 5.3c shows the vertical component of the velocity vector. Small–scale convection produces a significant vertical flow. Maximum velocities reach values of about 6 cm yr^{-1}, which is a factor of two greater than the imposed surface velocity. Strain rate values are within the range of 10^{-14} – 10^{-15} s^{-1} between 100 and 500 km depth; the greatest values in the entire domain are always associated with SSC cells.

The dashed line, at about 3750 km, shows the correspondence of the drippings of lithospheric material with high values of viscosity and downward velocity. The viscosity is increased because cold lithospheric material is downwelled to higher pressures. No dripping instabilities are seen close to the ridge. The dotted line at about 2100 km shows the place of the onset of SSC determined by simple observation. This distance to the ridge corresponds with a 60 Ma old lithosphere.

As expected, SSC slows down the conductive cooling of the lithosphere by replacing cold mantle with hotter mantle, effectively reducing its thermal thickness when compared with predictions from the half–space cooling model. Likewise, the underlying sublithospheric mantle is cooled by the cold downwellings. We illustrate this effect in Figure 5.4. This Figure compares temperature profiles across the mantle at different simulation times, starting from the initial temperature distribution given by the half–space cooling model (red line in Figure 5.4). The profiles are located at 3000 km away from the ridge, where the plate is 85.7 My old. To remove short–wavelength temperature anomalies, the temperature is horizontally averaged in a 400 km region (from x = 2800 to 3200 km). The profiles in panel (a) clearly show that the lithosphere reaches a "steady" thermal thickness after $\sim$ 60 My of simulation time. However, a closer inspection (panel c) reveals that this steady thickness is reached after only $\sim$ 30 My of simulation time. During this time, about 50 km of unstable lithospheric material is removed, thinning the thermal thickness plate by an equal amount. This indicates that the temperature structure predicted

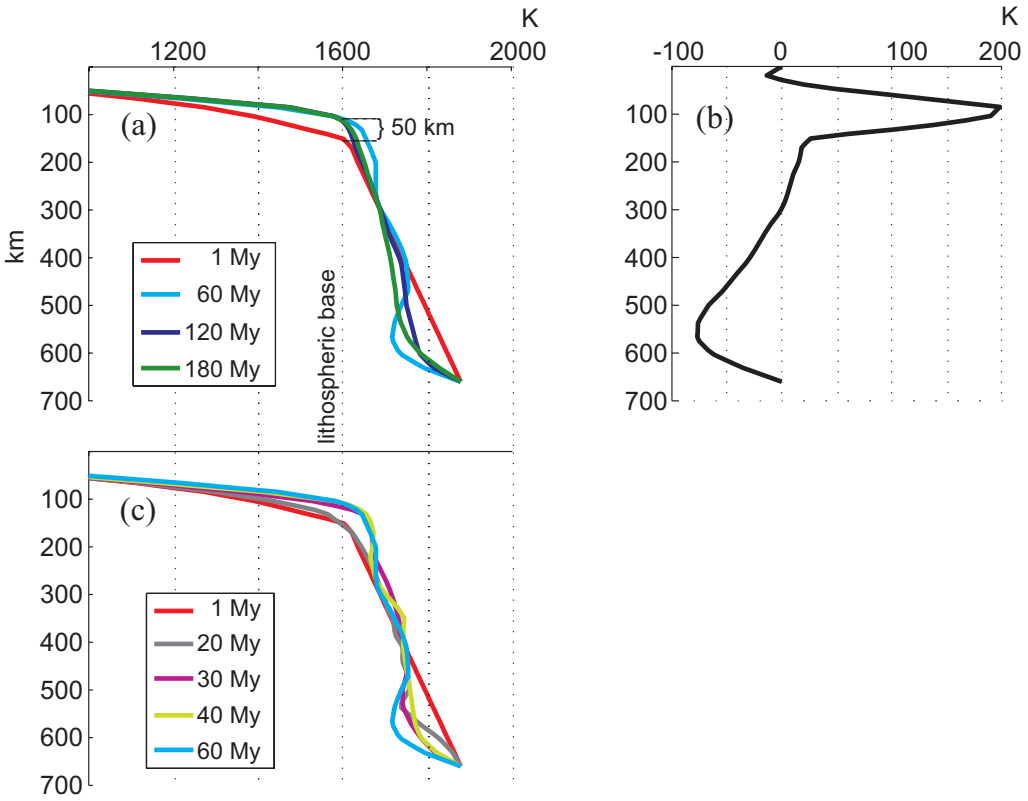

Figure 5.4 – Temporal evolution of temperature at 3000 km away from ridge. Panel (a) and (c): temperature profiles at different times. Panel (b) temperature variation between 1 and 180 My. The model includes shear heating and radiogenic heat production of 2×10^{-8}W m^{-3}

by the half–space cooling model for plates older than 65 Ma is extremely unstable in a convecting mantle characterized by the present physical parameters.

At the base of the lithosphere, temperature increases by about 200 K with respect to predictions from the half–space cooling model (see panel (b)). At depths between 200 and 400 km, the temperature variation is $< \pm$ 25 K with respect to the initial "adiabatic" profile, but this difference increases to $>$ 75 K (i.e. colder) in the transition zone. However, the latter value needs to be taken with caution, since our energy equation does not include the effect of latent heat of phase transformations (olivine–wadsleyite and wadsleyite–ringwoodite). It has been shown that the temperature increase across the transition zone along an adiabat can be as much as 100 K (Katsura et al., 2004). Therefore, if we take into account this effect, the temperature difference between our initial "adiabatic" and the final profiles is reduced to $\lesssim 10 - 20$ K. This supports our choice for the temperature at the bottom of the simulation box.

Table 5.1 – Oceanic models

Model	SH	RHP (W m^{-3})
09	no	0
14	yes	0
15	no	2.0×10^{-8}
16	yes	2.0×10^{-8}

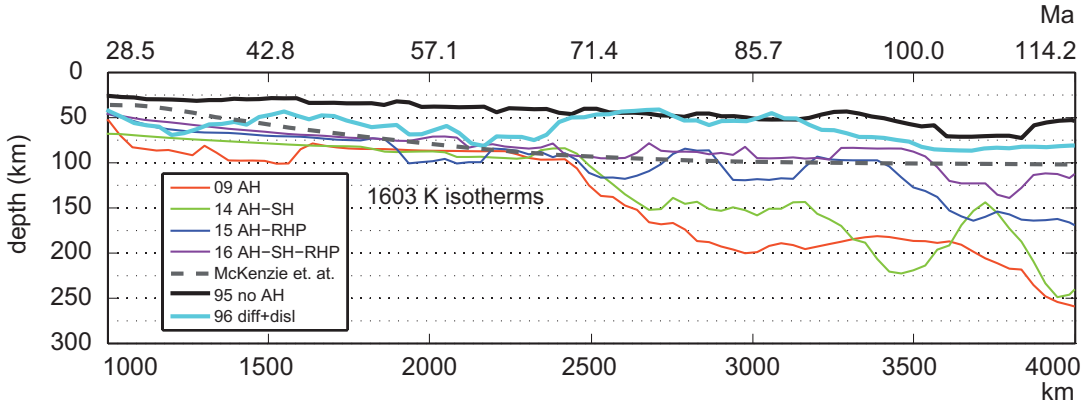

Figure 5.5 – Lithospheric base defined by the averaged 1603 K isotherm.

5.2.2 Influence of key physical parameters

Effect of shear heating and radiogenic heat production. In the following set of numerical experiments, the effects of shear heating and radioactive heat production (RHP) are tested for a model with identical rheological parameters as in the previous section. Table 5.1 lists the models and whether they include or not shear heating and RHP. The adopted RHP rate per unit mass is at the high end of estimated values for the mantle (Ranalli, 1995; Labrosse and Jaupart, 2007). Model 09 was described in the previous section and is shown in Figure 5.3. We note that SSC is active in all four models.

In order to make a meaningful comparison between our results and those from conductive plate models, we calculate the averaged depth of the 1603 K isotherm by applying a moving–average filter to the depths of the isotherms. Since the wavelength of SSC is 150 – 200 km, a window size of 250 km removes the intrinsic local variability caused by SSC without adding significant diffusion.

The averaged 1603 K isotherm, defining the bottom of the lithosphere, for the four models is shown in Figure 5.5. We find that values of shear heating associated with SSC are of the same order as the RHP (10^{-8} W m^{-3}), although some punctual values can become one order of magnitude greater. Nevertheless, as shown in Figure 5.5 the shear heating has little or no influence on the final lithospheric

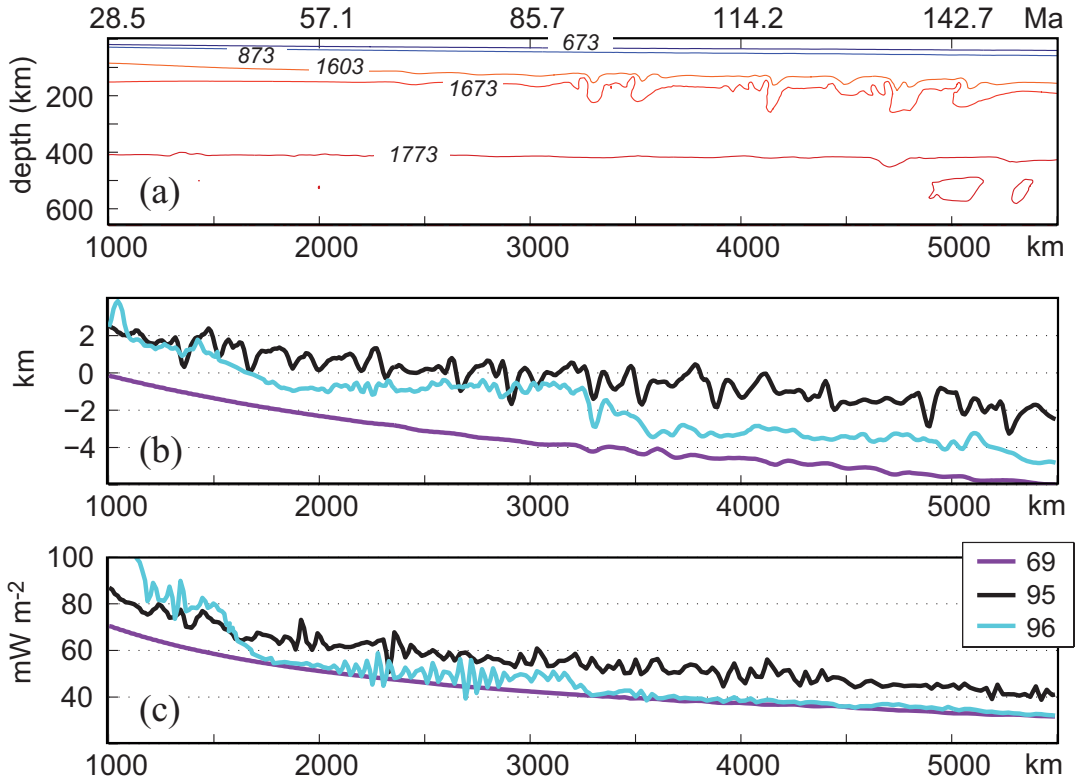

Figure 5.6 – Temperature in K (a), seafloor topography (b), and surface heat flow (c). Temperature in panel (a) corresponds to model 69 after 120 My of simulation time. Horizontal distance [km] is measured from the ridge, and the equivalent plate age [My] is included at the top.

thickness. Models 09 and 14 exhibit an average lithospheric thickness of $\sim$ 200 km in plates 100 My old. This value is well outside the ranges of all existing plate models (cf. Schubert et al., 2001), and predicts patterns of seafloor topographies and SHF that do not fit observed data satisfactorily (Figure 5.6). On the other hand, the inclusion of RHP brings the average thickness of old oceanic lithosphere to values around 125 km, closer to results from theoretical plate models (Parsons and Sclater, 1977; McKenzie et al., 2005) and combined geophysical–petrological models (Afonso et al., 2007). This result is in agreement with those from Huang and Zhong (2005).

Influence of adiabatic heating. In the absence of other sources of heat, a fluid element would undergo changes in temperature due to variations in pressure. In a convecting mantle, major changes in pressure are related to vertical motion of material. Without adiabatic heating, the density difference between downwellings and upwellings increases, enhancing SSC. We illustrate this by setting to zero the adiabatic heating term in one of our previous models (model 95 in Figure 5.5). In this case, the vigor and eroding capacity of the convective cells is dramatically increased. Average lithospheric thicknesses are now 25 to 50 km thinner than in the

case with adiabatic heating. As a result, seafloor topography and SHF data are more closely reproduced, although a continuous decrease with time is still seen in both observables (i.e. no flattening, Figure 5.6).

Adiabatic heating has been neglected in most studies addressing SSC (e.g. van Hunen et al., 2003, 2005; Huang et al., 2003; Dumoulin et al., 2001; Zaranek and Parmentier, 2004). Huang and Zhong (2005) state that adiabatic and shear heating was explicitly included in their calculations, but no assessments of their influence on SSC or on the thermal structure of the plate were provided. Our results indicate that adiabatic heating exerts a major control on the final structure of the oceanic lithosphere (Figure 5.5). Consequently, any attempt to explain its thermal structure and associated geophysical observables using thermo–mechanical models should consider this effect. In principle, this conclusion also applies to other gravitational instabilities such as lithospheric delamination and unroofing, although further studies are needed. In this context, we emphasize that it is widely accepted that the temperature increase within most of the Earth's mantle follows closely the condition of uniform entropy (i.e. adiabatic profile, cf. Schubert et al., 2001).

Influence of plate motion. A positive relation between the onset time of SSC and plate velocity has been reported in several studies (Houseman, 1983; Huang et al., 2003; van Hunen et al., 2003). Using isoviscous convection models, Houseman (1983) found a clear delay in the SSC onset when increasing plate velocity. This author suggested that sufficiently high plate motions may even preclude the development of gravitational instabilities. van Hunen et al. (2003) described a similar behavior in their 2D Newtonian simulations; on the other hand, Dumoulin et al. (2001) found no significant correlation between the onset time of the first dripping instability and plate velocity.

We have run five Newtonian models to test the role of plate velocity on the development of SSC. The parameters used in these models are those of model 16 in Table 5.1. We found a positive correlation between plate velocity and the onset of SSC. For velocities of 2, 4, 6, 8, and 10 cm yr^{-1}, the first drippings appear when the plate is 28, 43, 70, 72, and 80 My old, respectively, in agreement with the observations reported in van Hunen et al. (2003) and Houseman (1983).

Influence of rheological parameters. We run fourteen Newtonian models in which we varied the pre-exponential factor A_D and the activation energy E to test the sensitivity of SSC to these parameters. Figure 5.7 shows which models developed vigorous SSC (in green) and which ones failed to do so (red). The results suggest a quasi–linear relation between E and A_D that defines the region where SSC can be

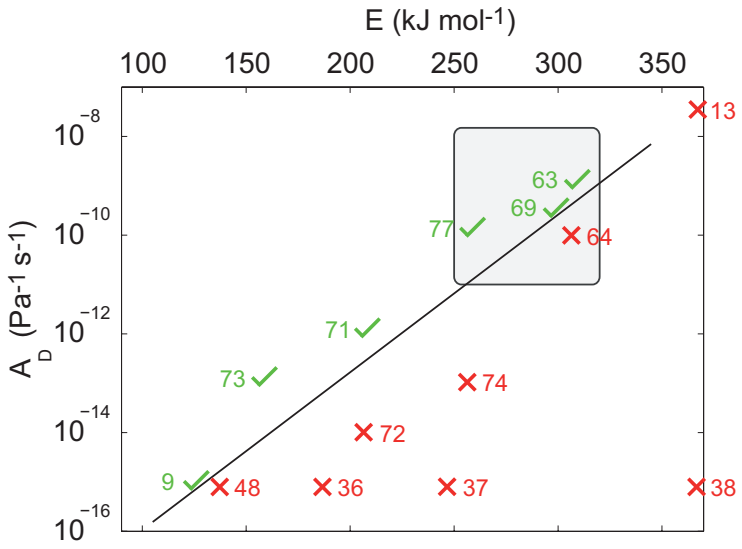

Figure 5.7 – Models varying the activation energy E and the material parameter A_D. Models marked with cross do not initiate SSC, models marked with tildes do initiate SSC. A linear relation between E and A_D defines the region where SSC is active. The gray region indicates ranges in agreement with laboratory experiments. Numbers at the side of the markers are the run number.

active. Moreover, the range of values that define this boundary seems to be rather limited (see e.g. experiments 69–64 and 9–48), indicating that the development of SSC is extremely sensitive to these parameters, and hence to viscosity. In fact, the straight line in Figure 5.7 separates the models with average upper mantle viscosities $\lesssim 10^{20}$ Pa s (green) and $> 10^{20}$ Pa s (red). This viscosity value is found to be a limit above which vigorous SSC cannot develop. When the average viscosity of the upper mantle is above this threshold, the cooling of the oceanic lithosphere follows closely the HSC model. Although some small instabilities may develop at the base of the lithosphere, they cannot evolve into well defined drippings due to the high viscosity of the mantle below. This in turn precludes any significant thermal erosion of the lithosphere. A similar result was also found by Huang et al. (2003). On the other hand, if the average viscosity of the upper mantle is below $\sim 2 \times 10^{19}$ Pa s, velocities associated with SSC reach unrealistic values (> 10 m yr^{-1}), the lithosphere is strongly eroded, and SHF and seafloor topography depart significantly from the observed values.

The shaded box in Figure 5.7 represents the range of values for E and A_D from laboratory experiments (Ranalli, 1995; Karato and Wu, 1993; Hirth and Kohlstedt, 2003). Three of our models (labeled as 63, 69, and 73) that developed SSC are well within this range. Note also that the parameters used in our previous Newtonian examples (taken from previous studies) are far from experimental results. Figure 5.6 shows the observables predicted by model 69. In this model, both elevation and SHF

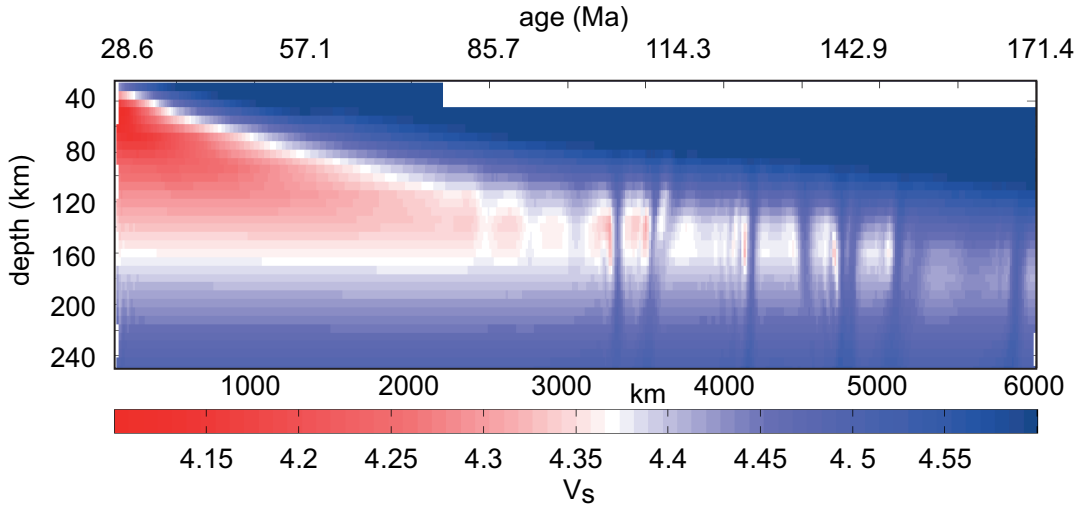

Figure 5.8 – Synthetic Vs seismic structure

increase steadily with age, in contrast to what it is observed. However, its seismic structure (Figure 5.8) resembles closely those recently obtained from tomography studies in the Pacific as well as in other oceans (compare with Figure 10 in Maggi et al. (2006) and Figure 11 in Ritzwoller et al. (2004)). Other similar models (not shown here) give identical results. This discrepancy between what is inferred from seismic data and from other observables (i.e. SHF, bathymetry) is a fundamental, yet not solved, problem in geodynamics.

To this respect, it is worth noting that van Hunen et al. (2005) recently concluded that dislocation creep (i.e. non–Newtonian rheology) is the main deformation mechanism in the upper mantle, based on a comparison between their numerical simulations and the tomography from Ritzwoller et al. (2004) in the Pacific. The lithospheric thermal structure derived by (Ritzwoller et al., 2004) shows a distinctive flattening of the isotherms (strictly, isovelocity contour lines) between 70 and 100 Ma, which these authors associate with a period of lithospheric reheating. van Hunen et al. (2005) showed that this reheating could be modeled only with non–Newtonian models, if the adopted rheological parameters are taken to be consistent with laboratory experiments. However, the unrealistic thermal structure used in the numerical simulations (see their Figure 3), as well as the neglect of activation volumes and internal heating, make their conclusions ambiguous. Moreover, Maggi et al. (2006) has recently presented a tomography for the Pacific in which no flattening of the isovelocity contours is observed. These authors pointed out that the flattening observed by Ritzwoller et al. (2004) may be an artifact due to insufficient path coverage. If this is true, and at the light of our results with Newtonian models, the argument used by van Hunen et al. (2005) favoring

dislocation over diffusion creep in the upper mantle becomes invalid.

There is, however, abundant independent evidences that point to dislocation creep as the main deformation mechanism in the upper mantle (Ranalli, 1995; Karato and Wu, 1993; Hirth and Kohlstedt, 2003). We have run experiments with combined dislocation–diffusion creep rheologies, always restricting rheological parameters to realistic ranges (i.e. within the shaded box in Figure 5.7 for diffusion creep, and $n = 3.5$, $E = 500$, $V = 17$ and $A_D = 2.42 \times 10^{-14}$ for dislocation creep), to test the potential eroding effect of dislocation creep. In our simulations, dislocation creep becomes dominant in the first 250 – 300 km (i.e. $\eta_{disl} < \eta_{diff}$) and generates an extra 20 – 50 km of erosion at the bottom of the lithosphere (Figure 5.5). Due to the greater activation volume of dislocation creep, and the small convective stresses generated below $\sim$ 250 km depth ($\lesssim$ 0.1 MPa), diffusion creep becomes dominant below this depth. Interestingly, the resulting seafloor topography and SHF exhibit wide regions where the signals become flat (Figure 5.6), but the overall fitting to observed data is still poor.

Influence of partial melting and water content at mid–ocean ridges. Water content has a large effect on the viscosity. Due to the incompatibility of water, a small degree of partial melting (3 – 5%) is enough to dehydrate mantle rocks, leading to a much more viscous residue and viscosity can be increased by 10 – 100 (Karato, 1986; Hirth and Kohlstedt, 2003; Lee et al., 2005).

This increment in viscosity due to the dehydration of rocks at oceanic ridges has a first order influence on the thermal evolution of the oceanic lithosphere. Considering a wet rheology for the upper mantle and including the transition from wet to dry rheology within the lithosphere greatly enhances the flattening effect of SSC. Lithospheric thickness, heat flow and ocean floor depth, all show an important flattening for lithospheric ages older $\sim$ 70 Ma as shown in Figure 5.9. This simulation, which includes the simple melting model described in Section 5.1.3, reproduces accurately the geophysical observables and the expected onset time of SSC.

The parameters of the melting and dehydration models are subjected to uncertainties, thus we test its influence on the evolution of the lithosphere. Two parameters, the depth at which the partial melting F starts and the percentage of melting needed to completely dehydrate a mantle peridotite, are considered. The results, in terms of viscosity profiles and lithospheric thickness is shown in Figure 5.10. We consider two extreme depths, 80 and 110 km, at which partial melting starts (Hirth and Kohlstedt, 1996). Results of these models are plotted

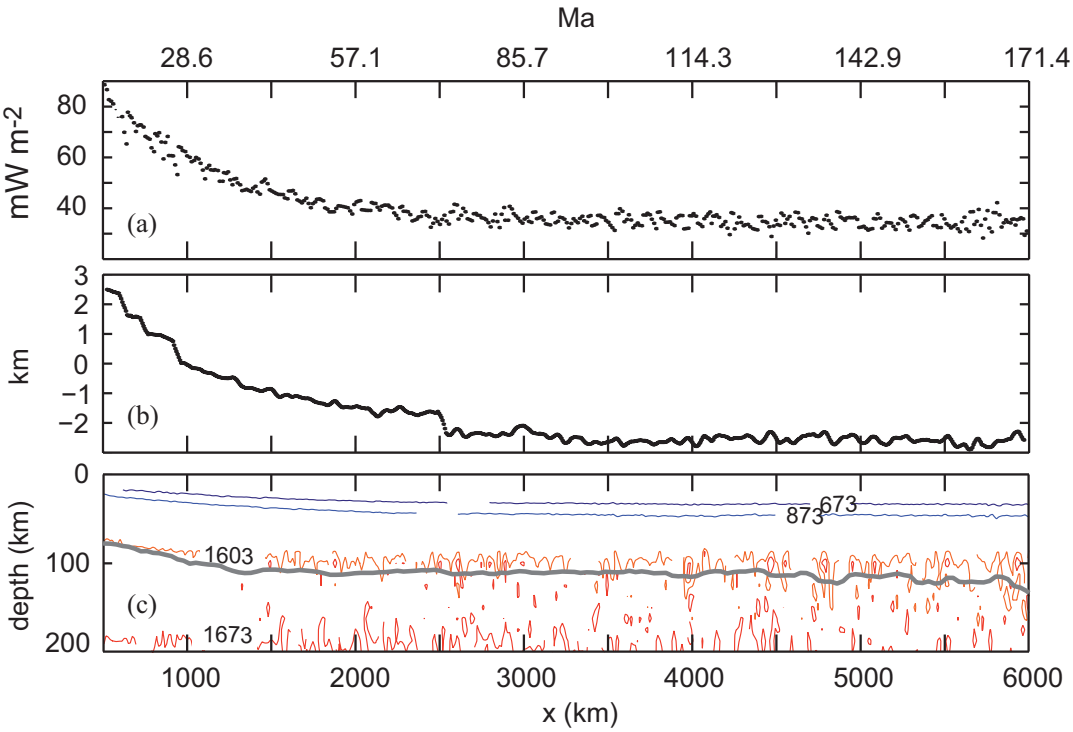

Figure 5.9 – Flattening due to the wet–dry transition at mid–ocean ridges. Heat flow (a), relative seafloor depth (b), and temperature in K (c). The thick line of panel (c) indicates the averaged lithospheric thickness defined by the 1603 K isotherm.

with dashed and solid lines respectively. The behavior of the oceanic lithosphere is greatly affected: the depth at which the viscosity jumps to values corresponding to dry peridotites is linearly controlled by the melting depth. This leads to $\sim$ 20 km of difference in the lithospheric thickness.

The depth at which the melting starts in a ridge is supposed to by a function of the rate at which ocean floor is produced. If that is the case, fast and slow ridges would produce dry domains with different thicknesses, leading to different viscosity profiles, different lithospheric thicknesses and different onset times for SSC.

Variations in the degree of melting required to completely dehydrate the mantle rocks have less influence on the evolution of the model. This is a consequence of the high derivative of the degree of melting F with respect to pressure (or depth). The profiles shown in Figure 5.11 show very similar trends when this parameter is varied from 3% to 5%.

The phase transition of the aluminium minerals, spinel to garnet, may also play a role in the stability of the oceanic lithosphere (Wood and Yuen, 1983). Because it is an exothermic reaction its effect is to reduce instabilities, avoiding the formation of SSC. The average depth at which this transition occurs is between 40 and 80 km. We tested the effect of the spinel to garnet transition at this two depths and found little

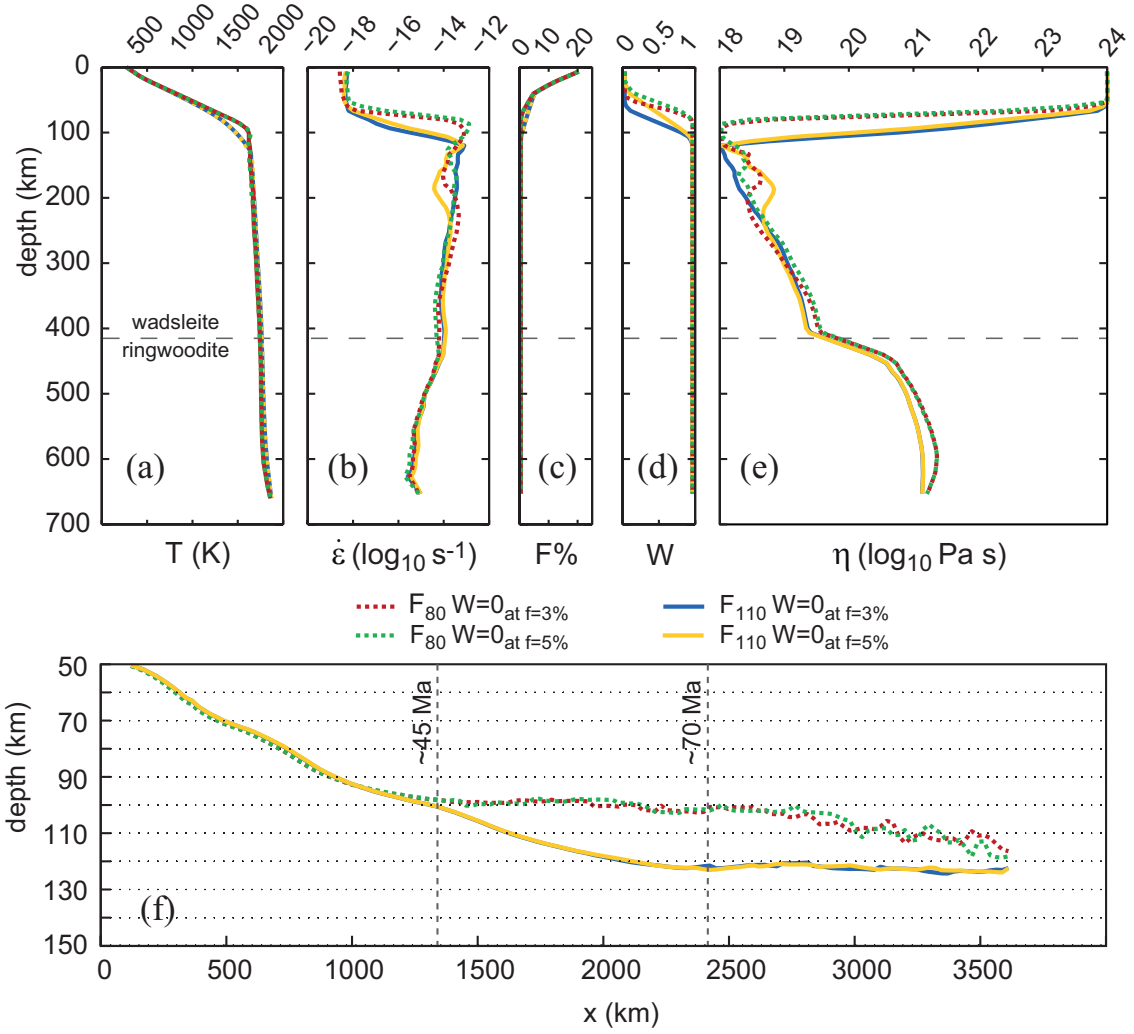

Figure 5.10 – Influence of the degree of melting, F, and dehydration, W, on viscosity profiles and lithospheric thickness. Two depths of melting initiation (80 and 110 km depth) and two dehydration percentages (rock is completely dehydrated (W=0) at $F = 3\%$ and at $F = 5\%$) are tested. Representative profiles of temperature (a), strain rate (b), melt percentage (c), water content (d), effective viscosity (e) and lithospheric thickness (f) defined by the averaged 1300 °C are shown.

or no influence on the resulting lithospheric thickness as shown in Figure 5.11. This is probably due to the small density change ($\sim 1\%$) associated with this transition.

5.3 Conclusions

We have studied the development and evolution of small–scale gravitational instabilities under the Earth's oceanic lithosphere using numerical simulations. Our results can be summarized as follow:

- The influence of three different heating terms was tested. Shear heating has

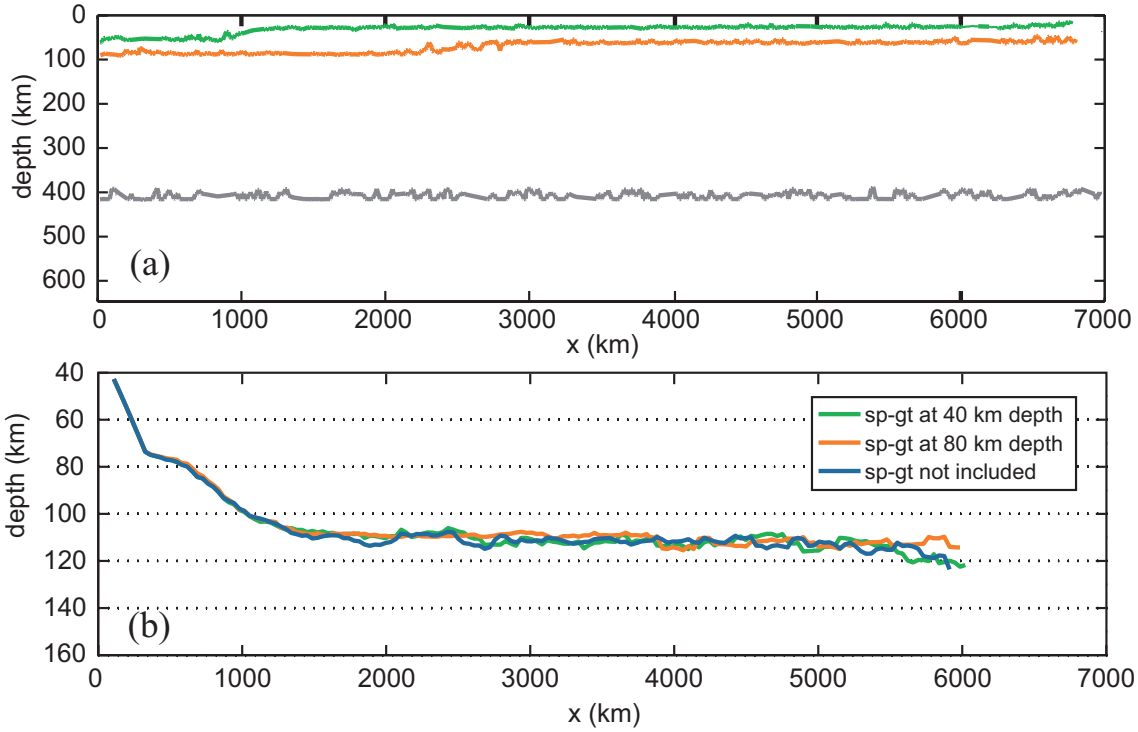

Figure 5.11 – Influence of the spinel–garnet phase change in the lithospheric thickness. Location of mineral equilibria curves (a). The wadsleyite–ringwoodite curve is the same for the three models. The effect of the spinel–garnet transition at two different depths (40 and 80 km) is tested. Panel (b) shows the average lithospheric thickness for each model.

negligible influence on the overall temperature of the model as well as on SSC. In contrast, heat from radiogenic sources increases mantle temperatures, favors the development of SSC, and reduces the average thermal thickness of the lithosphere. The inclusion of adiabatic heating reduces the temperature contrasts between ambient mantle and downwellings/upwellings. This in turn diminishes the vigor of SSC and lithospheric erosion.

- A low viscosity region below the lithosphere is needed to develop and maintain SSC. The height of this zone has to be similar to the horizontal wavelength of instabilities ($\geqslant$ 200 km). For realistic rheological parameters, the average viscosity in this region cannot be higher than $\sim 10^{20}$ Pa s.

- Small–scale convection can be generated using experimentally derived rheological parameters. Nevertheless, the activation of SSC does not always result in significant lithospheric erosion. To reduce the lithospheric thickness considerably, Newtonian models need activation energy and pre-exponential factor values that are too low in comparison with those reported in laboratory studies. In models where both diffusion and dislocation deformation mechanisms are

present, the low viscosity zone is dominated by dislocation and considerable lithospheric erosion occurs.

- A positive relation is observed between plate velocity and SSC onset time, in agreement with previous studies.
- Phase transition of aluminium minerals occurring within the lithosphere does not affect the first order evolution of the oceanic lithosphere.
- Dehydration of mantle rocks in mid–ocean ridges due to partial melting generates a lithospheric domain where dry rheology law prevails. This generates a dry–wet viscosity contrast which allows for an efficient flattening of the oceanic lithosphere in terms of its thickness, topography and heat flow.

Chapter 6

Slab breakoff and slab dip models

6.1 A numerical study of slab breakoff

Several subduction zones exhibit a clear gap in the hypocentral distribution between 100 and 300 km depth. These gaps are believed to be an expression of a mechanically decoupling of the descending slab (slab detachment or slab breakoff) relative to the subducting lithospheric plate. This interpretation is supported by seismic tomography (e.g. Fuchs et al., 1979; Xu et al., 2000), theoretical considerations (Blanckenburg and Davies, 1995), geochemical data (Astis et al., 2006), gravity modeling (Ioane and Lillie, 2004) and numerical and analogous modeling (Gerya et al., 2004; Buiter et al., 2002; Faccenna et al., 2006). Slab breakoff has been proposed in many zones around the world, for example in New Hebrides (Isacks and Molnar, 1969; Pascal et al., 1973), the Carpathians (Fuchs et al., 1979; Oncescu et al., 1984; Wortel and Spakman, 2000), the Hellenic arc (Spakman, 1988), Italy (Wortel and Spakman, 1992, 2000; Macera et al., 2008), the Alps (Blanckenburg and Davies, 1995), Iran (Molinaro et al., 2005), Indonesia (McCaffrey et al., 1985), etc.

Detachment of subducted slab is expected to cause changes in a subduction zone system which may be observed at the Earth's surface. Among the predicted surface effects are uplift (e.g. Westaway, 1993; Buiter et al., 2002; Gerya et al., 2004), a temporal change in stress regime (Meijer and Wortel, 1996), magmatism, metamorphism and rapid exhumation (Blanckenburg and Davies, 1995; Davies and von Blanckenburg, 1995).

Slab breakoff has been successfully modeled with the incorporation of complex rheologies and physical processes related to plate subduction (e.g. Yoshioka and Wortel, 1995; Davies and von Blanckenburg, 1995; Gerya et al., 2004). A common characteristic of all the models is the use of Lagrangian markers to determine the conditions under which slab detachment is produced. In this section we present a

numerical experiment to simulate the breakoff and sinking of a subducting slab by using X–FEM with a two–fold goal. On one hand, we use previous slab breakoff simulations to benchmark our numerical code and to demonstrate the capability of X–FEM to model complex geodynamic processes. On the other hand, we explore the role of shear heating, adiabatic heating, mineral phase changes and plate thickness as factors controlling the slab detachment. Rheological factors, like the maximum imposed viscosity are also studied. To be able to recognize the expressions of slab breakoff in geological observations, a knowledge of the magnitudes of the surface effects that may be expected is required. Therefore, we include a quantification of the changes in topography related with the detachment process.

6.1.1 Model setup

We consider the following setting for slab detachment: after consumption of an ocean basin subduction of oceanic lithosphere ceases. The detachment process initiates when the down–dip movement almost stops, so that extensional forces inside the slab can increase to values large enough to produce breakoff. The subducted slab sinks into the mantle due its negative buoyancy. We do not assume a zone of weakness to promote detachment or to localize necking in a particular zone.

The main gravitational forces acting on the subducting lithosphere are the negative buoyancy of the slab (slab pull), the ridge push, and the negative and positive buoyancy of the mineral phase changes from olivine to wadsleyite at 410 km depth and from wadsleyite to perovskite and magnesiowüstite at 660 km depth. In order to include these forces in our model, the density is calculated as a function of temperature and pressure as described in Section 2.9. Here we include two mineral phase transitions incorporating sharp increments in the density field. The temperature and pressure region of stable mineralogy is delimited by the Clapeyron curves of the mineral transition reactions.

It is worth noting that the ridge push force is not included in the model because the detachment process is expected to happen after cessation of active subduction. In other words, in our simulation the convergence velocity is zero.

This model involves two material phases described by a level set: the lithosphere and the underlying mantle. In our approach we have used the thermal definition of lithosphere and therefore the interface between the lithosphere and the sublithospheric mantle coincides with the initial 1300°C isotherm. Actually, the level set and the 1300°C isotherm roughly coincides during the whole evolution of the model due to the low thermal conductivity values of rocks which makes advection to be dominant over diffusion. In addition, the density ρ_0 assigned to the lithospheric

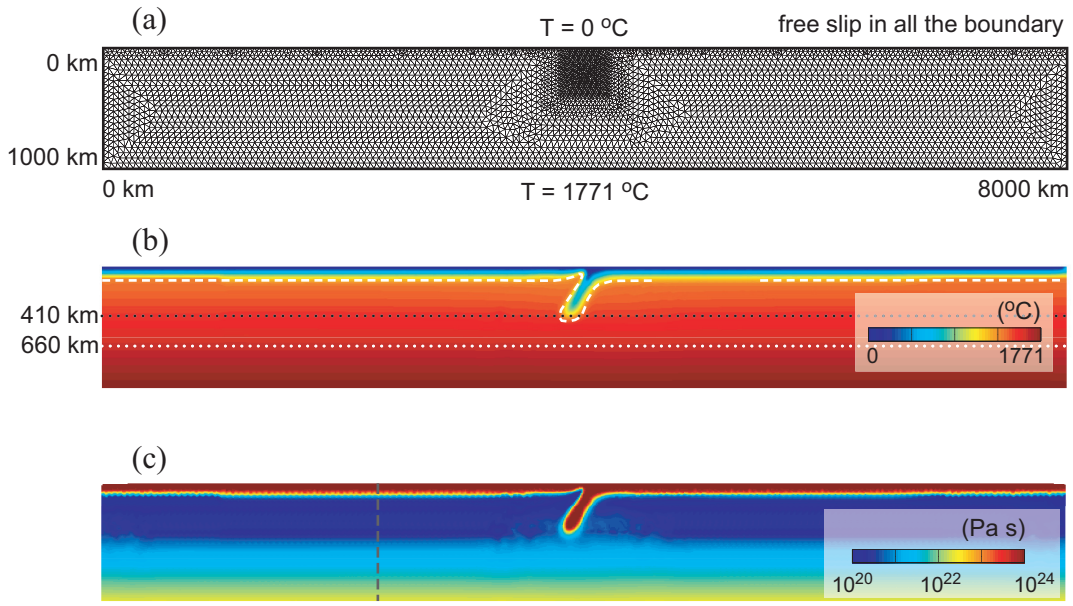

Figure 6.1 – Mesh geometry (a) used to simulate slab detachment. Initial temperature distribution (b), the dashed white line represents the level set location. Initial viscosity field (c). The vertical dashed line shows the location of profiles shown in Figure 6.2.

material is an average bulk density for the lithosphere and incorporates the lower density of crustal materials. Another configuration that might be used —and would give more accurate results— to model slab break-off, is to different materials for the crust and the mantle. We discarded this option because of the reduced thickness of the oceanic crust (usually < 10 km) which requires to greatly increase the number of elements and consequently the computation time. We consider that the chosen material configuration is a good trade off between computation time and accuracy of the model. This fact is demonstrated by the similarity between our results and those from previous numerical studies.

The initial configuration of all the models is shown in Figure 6.1b and corresponds to a subduction zone with the slab reaching a depth of 400 km. This initial thermal structure has been generated by a previous simulation where a horizontal velocity of 2.5 cm yr^{-1} is imposed on the subducting plate while the overriding plate is fixed.

Temperature structure of the subducting plate is horizontally homogeneous. Its thickness, defined by the 1300°C isotherm, is laterally uniform corresponding with a plate older than 80 Ma. During the evolution of the model the temperatures at the surface and the bottom of the model are imposed to be zero and 1771°C, respectively. Across the side walls of the model domain a null heat flux is imposed.

Assuming that the detachment process will start only after the cessation of plate convergence (Yoshioka and Wortel, 1995), the surface of the model is considered as

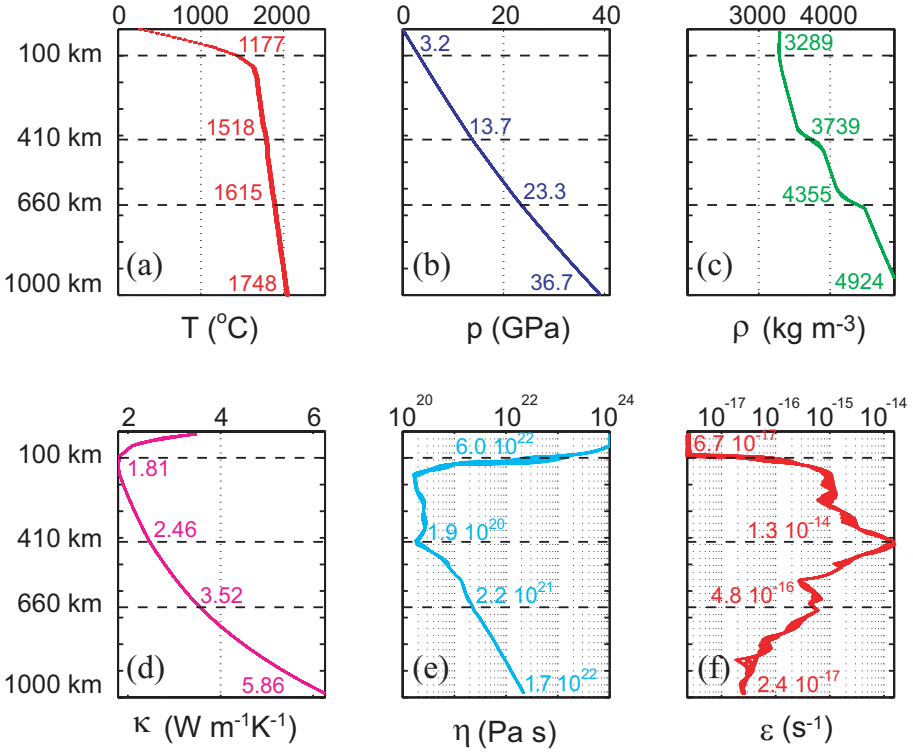

Figure 6.2 – Profiles of initial mantle properties and values at 100, 410, 660 and 1000 km depth. (a) temperature, (b) pressure, (c) density, (d) thermal conductivity, (e) viscosity, (f) strain rate. The position of the profiles is shown in Figure 6.1c.

a free surface and no horizontal velocity is imposed on it. Free slip conditions are also used in the bottom and side walls of the domain.

6.1.2 Results

In this section we study the influence of the key parameters on the slab detachment process. We generate a reference model using the parameters listed in Table 6.1. The influence of each parameter is evaluated by comparison against the reference model. The initial viscosity is shown in Figure 6.1c and profiles of mechanical and thermal properties across the whole mantle are shown in Figure 6.2.

Reference model. The evolution of the detachment process corresponding to the reference model can be followed in Figure 6.3. The first stage ($\sim$ 24 My) of the detachment process is characterized by thermal diffusion of the slab. In this period the slab increases its dip until reaching almost 90 degrees with respect to the lithosphere at the surface. The second stage of the detachment is a fast ($\sim$ 2 My) necking process where the strain is localized at depths between 150 – 200 km. The deformation is driven by the negative buoyancy of the cold slab.

Symbol	Meaning	Value used	Dimension
$\mathbf{g}$	gravity acceleration vector	(0,-9.8)	m s^{-1}
R	gas constant	8.314510	J mol^{-1} K^{-1}
T_0	reference temperature	273	K
p_0	reference pressure	0.1	MPa
ρ_{ol}	reference density	3300	kg m^{-3}
α	thermal expansion coefficient	3×10^{-5}	K^{-1}
β	compressibility coefficient	5×10^{-5}	MPa^{-1}
C_p	thermal Capacity	1200	J kg^{-1} K^{-1}
f_r	radiogenic heat production	0	W m^{-1} K^{-1}
$S_{\text{ol-wa}}$	Clapeyron slope for the 410 phase change	2.5	MPa K^{-1}
$S_{\text{wa-ri}}$	Clapeyron slope for the 660 phase change	-2.5	MPa K^{-1}
$T_{\text{ol-wa}}$	reference temperature of the 410 phase change	1700	K
$T_{\text{wa-ri}}$	reference temperature of the 660 phase change	1873	K
$p_{\text{ol-wa}}$	reference pressure of the 410 phase change	13500	MPa
$p_{\text{wa-ri}}$	reference pressure of the 660 phase change	23100	MPa
$\Delta\rho_{\text{ol-wa}}$	density increment in the 410 phase change	250	kg m^{-3}
$\Delta\rho_{\text{wa-ri}}$	density increment in the 660 phase change	250	kg m^{-3}
	Dislocation creep		
E	activation energy	540	kJ mol^{-1}
V^*	activation volume	14	J MPa^{-1} mol^{-1}
n	power law exponent	3.5	-
A	pre-exponential factor	7.6×10^{-16}	Pa^{-n} s^{-1}
	Diffusion creep		
E	activation energy	300	kJ mol^{-1}
V	activation volume	4.5	J MPa^{-1} mol^{-1}
n	power law exponent	1	-
A	pre-exponential factor	6.07×10^{-11}	Pa^{-n} s^{-1}

Table 6.1 – Parameters, notation and value

Necking concentrates extensional deformation in a narrow zone of the slab producing large stresses and shear heating (Figure 6.3, 25 My row). The slab detachment is characterized by a high strain rate and a spread shear heating all around the slab (Figure 6.3, 26 My row). Once the detachment has been produced, the slab sinks towards the bottom of the upper mantle. The shear heating controls the dynamics of the system not only during the necking, but also during the sinking of the detached slab. Moreover, the temperature increment due to the shear heating decreases the viscosity around the slab lubricating the sinking. Values of shear heating up to 3×10^{-5} W m^{-3} are obtained. This amount of heating is about three orders of magnitude larger than the radioactive heating of the mantle and are in accordance with values reported by Gerya et al. (2004).

A summary of relevant results like the maximum values of strain rate second invariant, shear heating, stress second invariant and velocity are listed in Table 6.2 together with the corresponding time and average depth at which these maximum values have been obtained.

Modifications of the surface topography are calculated as a post–process as

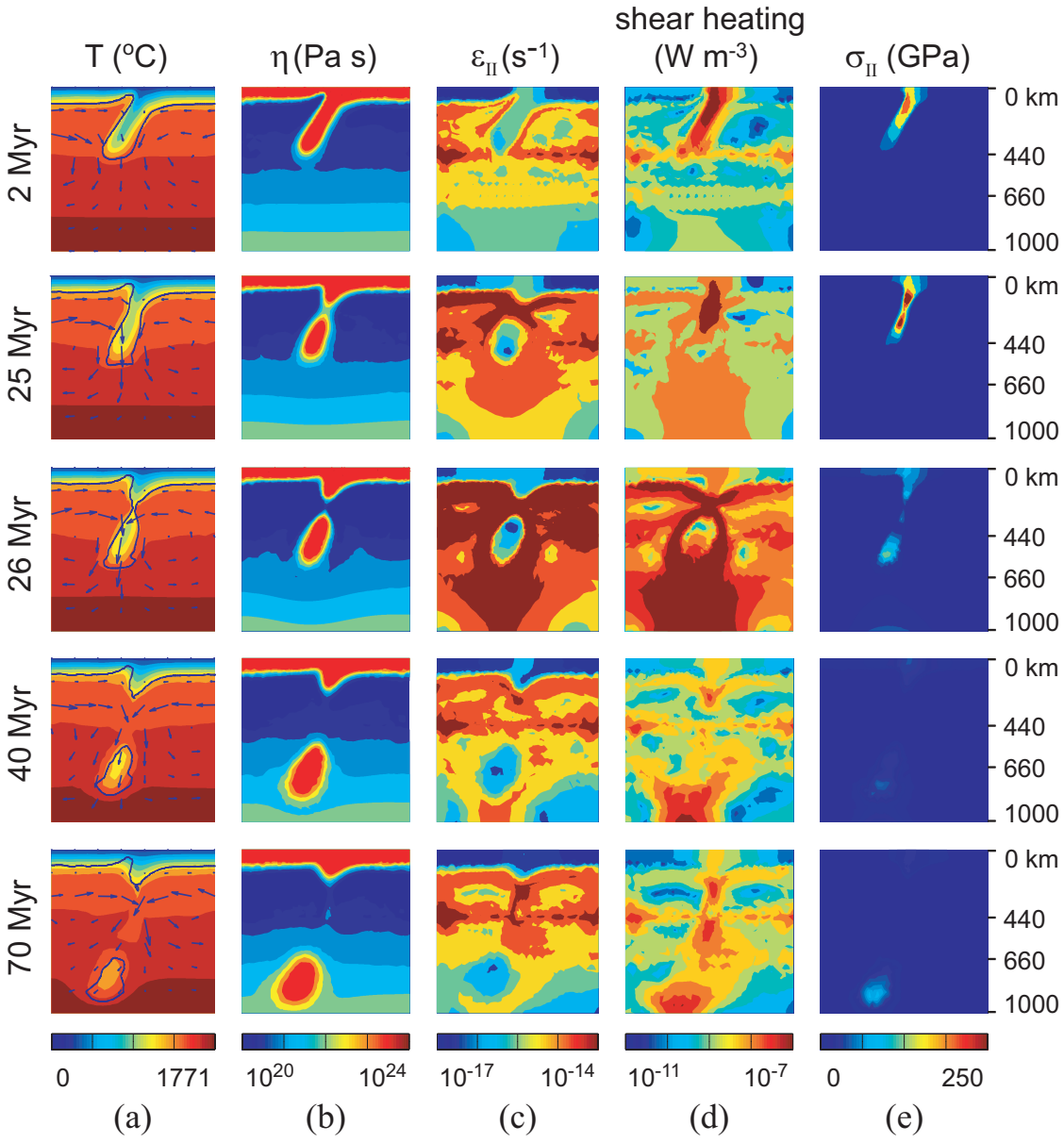

Figure 6.3 – Evolution of the detachment calculated with the reference model. (a) Temperature, velocity and level set position, (b) viscosity, (c) strain rate second invariant, (d) shear heating, (e) stress second invariant.

described in Section 5.1.4. The topography changes related with the detachment process are shown in Figure 6.4. Previous works (Buiter et al., 2002; Gerya et al., 2004) reported a period of uplift that reaches about 1.5 km after slab detaches. This uplift is mainly localized in a $\sim$ 300 km wide area within the overriding plate immediately above the detached slab. Initially the uplift area is characterized by a significant ($\sim$ 2 km) depression developed during the initial period of slab bending and thermal diffusion.

Our estimated uplift is consistent with values obtained by Gerya et al. (2004)

Model	$\dot{\varepsilon}_{II}$			Shear heating			σ_{II}			Velocity		
	max	time	depth	max	time	depth	max	time	depth	max	time	depth
	s^{-1}	My	km	Wm^{-3}	My	km	MPa	My	km	cm yr^{-1}	My	km
ref	7.6×10^{-14}	26	243	1.1×10^{-5}	26	252	423	23	158	10.1	26	400
noSH	2.4×10^{-14}	40	278	0	-	-	450	35	158	3.5	40	423
noAH	5.2×10^{-14}	25	468	1.1×10^{-5}	22	208	565	19	166	29.3	23	397
no410	3.2×10^{-14}	48	253	5.0×10^{-6}	47	224	230	38	147	4.7	48	239
no660	6.8×10^{-14}	26	219	2.4×10^{-5}	26	235	428	23	166	9.2	26	223
max η	8.2×10^{-14}	41	220	1.6×10^{-5}	41	241	456	25	130	10.86	41	400
lith70	1.3×10^{-13}	23	184	3.1×10^{-5}	23	184	273	21	107	16.8	23	383

Table 6.2 – Maximum values for the second invariant of strain rate, shear heating, second invariant of stress and velocity for each model. Second and third columns of each box are the time and depth where the maximum values are obtained. Model labels: *ref* for the reference model, *noSH* for the model without shear heating, *noAH* for the model without adiabatic heating, *no410* for the model without the 410 km depth mineral phase transition, *no660* for the model without 660 km depth mineral phase transition, *max* η for the model with increased maximum allowed viscosity and *lith70* for the model with 70 km thick lithosphere.

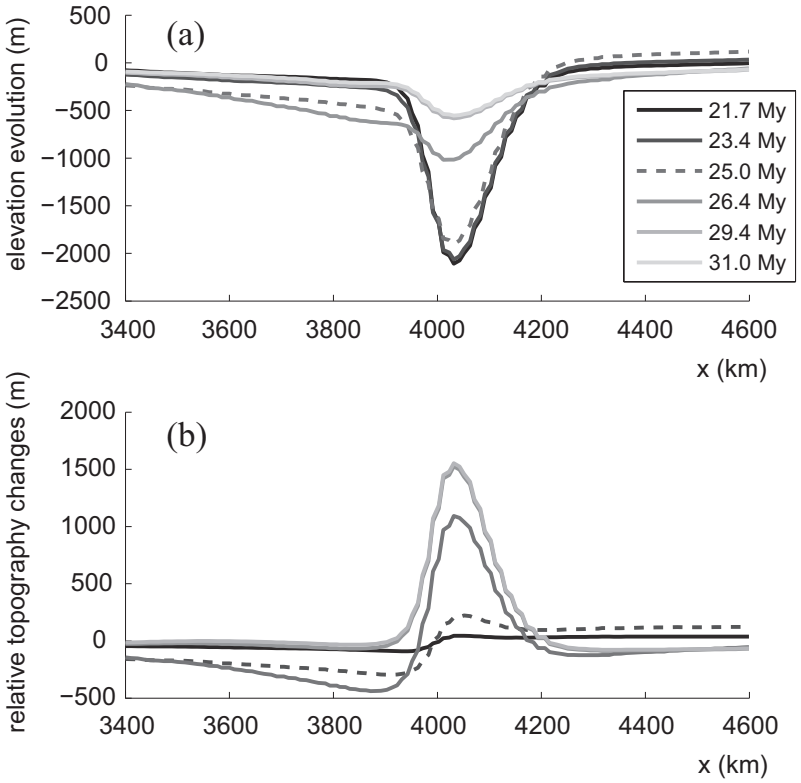

Figure 6.4 – Elevation evolution (a) and relative topography changes (b) during slab detachment. Dotted lines indicates the approx. detachment time.

but is significantly smaller than the values reported in Buiter et al. (2002) ($\sim$ 6 km). This difference is due to the different rheological models assumed. Since our model does not account for the lithospheric elasticity (our model is purely viscous), the estimated uplift values are significantly lower than those obtained using more complex rheologies. Calculated uplift rates reach values of 400 m My^{-1}.

Shear heating. Shear heating exerts a first order control on the dynamics of the detachment process. When shear heating is not considered the detachment occurs about 20 My later and the sinking velocity of the slab is about one third of the velocity obtained with the reference model. The shear heating helps in focusing the deformation in a narrow area of the slab.

Adiabatic Heating. The adiabatic heating term is important to reproduce the behavior of the mantle at great depths. Numerically it acts reducing the coupling between the mechanical and the thermal equations. As shown in Figure 6.5, the obtained mantle structure for a model without adiabatic heating greatly differs from the reference solution, even before the detachment occurs. Therefore, excluding the adiabatic heating produces that hot material from the deeper part of the model is upwelled forming large convective cells that involve the whole mantle. The mantle surrounding the slab at 200 – 300 km depth is hotter than in the reference model enhancing the thermal diffusion and accelerating the detachment process, which happens about 1 My before.

Mineral phase transitions. The role of mineral phase transitions at 410 and 660 km depth is crucial in determining the depth distribution of the mantle density. It is well known that the endothermic character of the olivine–wasleyite reaction developing at 410 km depth increases the slab pull force, and therefore helps the detachment to occur. According to this, the slab detachment may be delayed by about 20 My with respect to the reference model when the olivine–wasleyite phase transition is not considered. Moreover, the maximum stress reached is about one half of that obtained with the reference model. The role of the wasleyite–to–perovskite+magnesiowüstite exothermic transition occurring at 660 km depth is less noticeable. In the absence of this phase change, the detachment occurs at the same time and the maximum stresses and strain rates are similar to those obtained with the reference model and happen at similar times and depths. The main obvious difference is that the sinking velocity of the detached slab is not reduced when reaches the depth of 660 km since, in this case, any discontinuity is imposed at this depth.

Viscosity bounds. The effects of varying the mantle rheology have been also examined. Increasing the upper bound of the allowed viscosity to values of 10^{26} Pa s delays the breakoff by about 15 My although it is not enough to inhibit the detachment of the slab. The time at which the maximum strain rate is reached undergoes also a similar delay but the maximum stress occurs 2 My later when

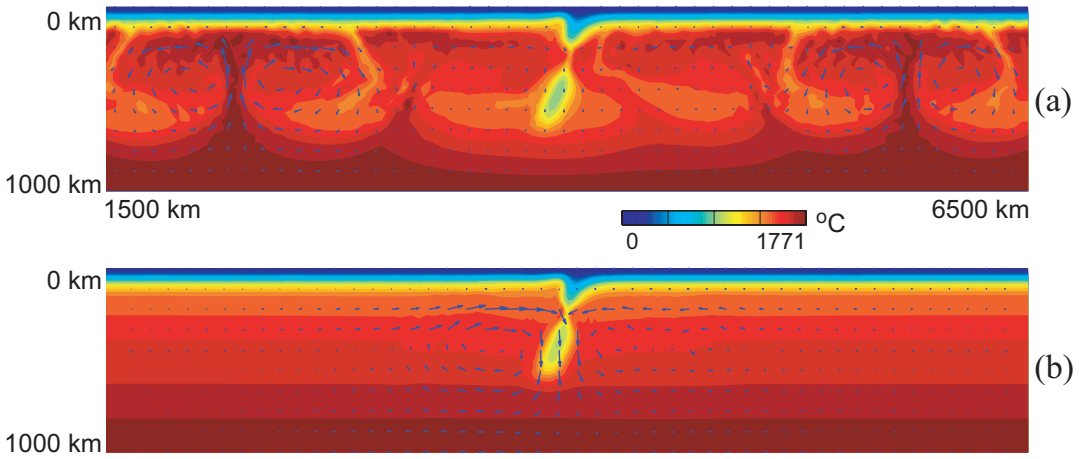

Figure 6.5 – (a) Thermal structure and velocity field at 26 My after convergence cessation obtained with a model excluding the adiabatic heating term. (b) Thermal structure and velocity field at 26 My for the reference model.

compared with the reference model. In fact, the time at which the strain rate reaches its maximum value is a good proxy of the detachment time, while the time interval during which the stress is maximum is a proxy of the necking process.

Lithospheric thickness. Finally, reducing the lithospheric thickness to 70 km (the reference lithosphere is 100 km thick) produces that the slab detaches 2 My earlier. The breakoff occurs at a depth about 60 km shallower and the magnitudes of the generated stresses are almost a half with respect to the reference model.

6.1.3 Discussion and conclusions of the slab breakoff model

In this work, we have presented a thermo–mechanical numerical study of the slab detachment process. The influence of the key parameters controlling the process have been investigated. Using realistic values of physical properties of mantle rocks, we have demonstrated the dynamic feasibility of the detachment process as caused by thermal diffusion of subducted slabs after cessation of active subduction. Some of the presented results are quantitatively similar to those found in previous studies demonstrating the correct behavior of the code.

Our results show that the slab detachment process is characterized by a period dominated by thermal diffusivity, followed by a fast slab necking and the sink of the detached slab. The adiabatic heating term, i.e. the heat exchange due to adiabatically compression or decompression of materials, plays a major role in mantle models, specially if gravitational instabilities are expected. Neglecting this term greatly enhances temperature contrasts favoring instabilities. Moreover, the

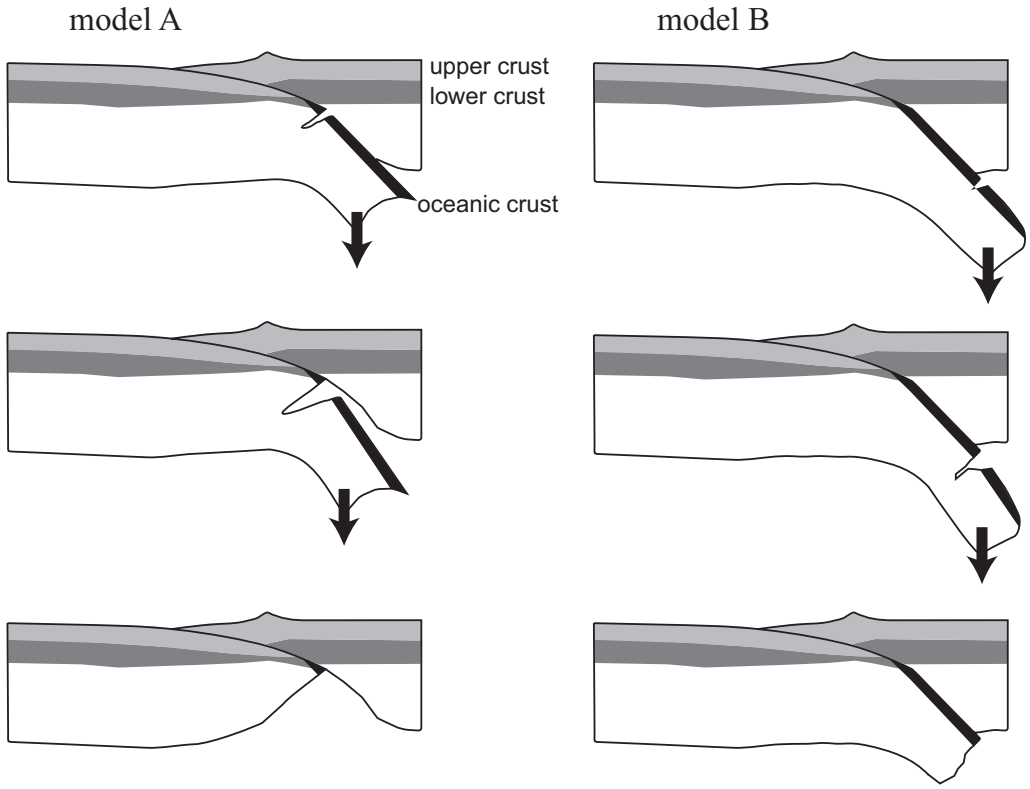

Figure 6.6 – Schematic evolution of two different detachment models. Model A shows a shallow detachment generating lithospheric thinning. Model B reproduces the results obtained in this work, which result in a increase in the lithosphere thickness.

detachment process is accelerated due to the strain–rate softening and focusing of thermal effects related to significant thermal feedback from shear heating. This feedback is also enhanced by the non–Newtonian rheology.

Mineral phase transitions act as expected although further work should include the effect of a metastable olivine wedge, which may modify the buoyancy of the slab.

Some works, for example Molinaro et al. (2005); Ioane and Lillie (2004); Schoonmaker et al. (2005), propose a slab detachment process in order to explain a locally thinned lithosphere. In these works the lithospheric thickness is usually inferred from geophysical observables (topography, gravimetry, etc). This hypothesis does not match with present dynamical simulation of slab detachment: we always observe a thickened lithosphere after detachment, as shown in Figures 6.5 and 6.3. A similar thickening is observed in the results of (Gerya et al., 2004).

To obtain a net lithosperic thinning after detachment, the lithospheric necking related to slab breackoff must occur at shallower depths. See the Figure 6.6 model A for an schematic evolution of the process.

There are clear differences between the geological implications produced by the shallow detach model A and deep detach model B. The thinned lithosphere induces

a thermal uplift not associated with the detachment but with hot mantle rocks replacing the detached material. In this thinned model the fast uplift of mantle rocks may cause decompression melting, increasing the surface heat flow and likely generating vulcanism. These effects are not expected in the model B.

Because of the innate differences between a breakoff model which reduces the thickness of the lithosphere and one which increases it, our results are not an appropriate support for a tectonic history similar to the model A of Figure 6.6.

The lithospheric thickening obtained in the simulations may be caused by the fact that our model does not explicitly includes the inter–plate fault or subduction channel. Another possible cause of differences is the absence in our model of the lower crust, which has a ductile behavior and thus may concentrate and propagate deformation quickly.

A more accurate geometry accounting for continental crust and preexisting faults may also influence the location of the detachment. The slab breakoff may preferentially take place in the transition zone between oceanic and continental crust. Bending forces should concentrated in this region due to the buoyancy of the continental crust which resists the downward pull of the slab. Additionally, this region may be already weakened by extensional fault zones which developed during the opening of the ocean.

Future directions in the modeling of slab detachment will test the influence of existence of a subduction channel and a ductile lower crust. More complicated starting geometries and thermal structures of slabs matching initiation of continental collision are also required. Other interesting parameters to study are the effects of phase transformations within the crust and the mantle (e.g. Lee et al., 2005); and the influence of slab visco–elasticity. We note that the presence of visco–elasticity in the slab bending region may potentially store an abundant amount of elastic potential energy, which can be converted into localized shear heating (K. Regenauer-Lieb, 1998).

6.2 On the relation between convergence velocity and slab dip

The correlation between different subduction parameters has been an active topic in geophysics since the acceptance of plate tectonics. Relations between geometrical parameters, for example slab dip or arc curvature and kinematic parameters as convergence velocity or trench absolute movement, are expected to give some insight on the dynamics of subduction zones.

The relation among slab dip and convergence rate was one of the first to be tested Luyendyc (1970). However, there are several competing processes with opposite trend which may influence the relation between velocity and slab dip. Some processes favor a direct relation while others predict an inverse relation.

A direct relation, the faster the plate the steeper the slab, can be explained as follows: a fast downgoing plate has no time to equilibrate thermally with the surrounding mantle. The thermal contrast leads to a density contrast which, in turn, leads to an increased negative buoyancy. It is expected that the less buoyant is the plate, the steeper is the dip of the subducted slab. In a slow downgoing slab we expect the opposite behavior: small thermal and density contrasts leading to a buoyant plate, which goes down with shallower dip.

On the other hand, an inverse relation, the faster the plate the shallower the slab, is expected based on the viscous forces of the mantle resisting the penetration of the slab. A different explanation supporting an inverse relation is that the vertical downward velocity is a constant, thus the dip is controlled by the horizontal plate velocity as sin(dip)=sinking rate/convergence rate. This relation was proposed by Luyendyc (1970) based on examination of the Tonga, Java and Kamchatka–Kurile subduction zones.

Furlong et al. (1982) relates inversely the convergence rate with the upper plate velocity. Roeder (1975) proposed that convergence rate changes may cause dip changes. However, Tovish and Schubert (1978) compared deep slab dips to convergence rate for 39 subduction zones and found little correlation between both. The analysis of Jarrard (1986) confirms these results. The statistical analysis of Lallemand and Heuret (2005) shows that slab dip does not correlate with the convergence rate and it neither does with the magnitude of slab pull, the age of subducting plate, the thermal regime of the subducted lithosphere, or the subduction polarity (east versus west).

One of the difficulties that appears in the study of the oceanic lithosphere is to find unperturbed sections. The oceanic lithosphere may show of changes in the crustal thickness, in the overlying sediment thickness, or it may be affected by mantle plumes, or may be close to a ridge or an island arc, etc. All these perturbations to the "normal" oceanic lithosphere have effects on its evolution and, consequently, on the subduction system. In this context numerical models allows for a systematic study, where the influence of a single parameter can be isolated while leaving the rest of the conditions and properties unaltered.

Here we address the relation between the subducting plate velocity and the slab dip by means of a systematic numerical study. The goal of the simulation is to

find a relationship between the convergence rate and the geometry of the subducted oceanic plate (*slab*). The geometry of the slab is parameterized by the slab dip (angle with respect to the horizontal) and the curvature at the bottom of the transition zone (660 km depth).

6.2.1 Model setup

The problem statement is illustrated in Figure 6.7. The simulation is performed to reproduce approximately 1360 km of plate convergence, that is, one plate moves 1360 km against the other. The upper plate remains fixed, thus the convergence rate is equal to the lower plate velocity. The velocity of the plates at the surface is imposed by the boundary conditions, as explained in Section 6.2.1. In order to test the influence of the velocity in the slab dip, the surface velocity is changed during each simulation. Three different realistic values for the velocity are used: low (2.5 cm yr^{-1}), moderate (5 cm yr^{-1}) and high (10 cm yr^{-1}). Each simulation uses two of these velocities. The transition from one velocity to another is either gradual or sudden.

Initial and boundary conditions

The boundary conditions for the mechanical problem (3.3) are described in Figure 6.7a. The velocity is imposed on the top of the domain. It is set to be zero on the left half and it is imposed certain horizontal velocity on the right side. At the center point between these two domains, a downward velocity (55° with the horizontal) is prescribed. A free slip condition is adopted at the bottom ($u_z = 0$, zero shear forces). Along the sides, labeled as Γ_s on Figure 6.7, periodic boundary conditions are imposed. This allows material to flow through the sides of the model in a confined domain. Finally, as a reference for the pressure field, a node on the surface is set to have null pressure (See Section 3.1). In this study the mechanical flow problem is linearized by using the velocity values of the previous step to compute the viscosities.

The model domain is a 2D, 1000 km depth and 8000 km wide rectangle. The initial thermal state corresponds to that of a 100 km thick oceanic plate subducting beneath another plate with identical features (shown in Figure 6.7b). This simple thermal state is used to avoid the influence of variations in plate thickness. The location of the material interface and the velocity field are set accordingly to this configuration. The white line corresponds to the 1573 K isotherm which is the base of the tectonic plates. During simulation this isotherm closely follows the interface

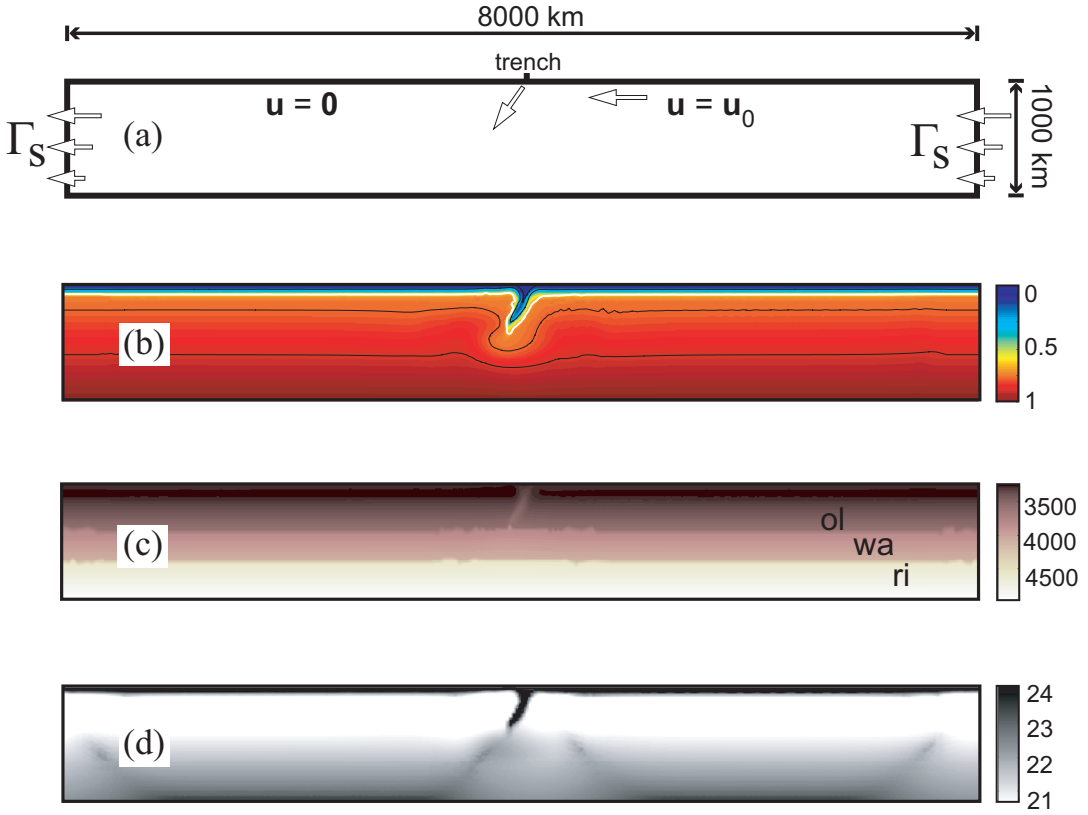

Figure 6.7 – Problem statement for the simulation of subduction: computational domain and boundary conditions (a); initial thermal state (dimensionless) (b); initial density (c) (note that two discontinuities occur at 410 and 660 km depth due to the phase transitions olivine–wasleyite–ringwoodite) and initial viscosity (d).

defined by the level set. Figure 6.7c and d are the initial density and viscosity fields, respectively. These fields are computed by a simple post–process of a static Stokes problem with the boundary conditions described above. The density accounts for the main mineral phase transitions at 410 and 660 km depth.

The boundary conditions that complete the thermal problem are of Dirichlet type at the surface and bottom of the model, and periodic at its sides. The imposed temperatures at the surface and bottom are $T_{surf} = 273$ K and $T_{bot} = 2053$ K, respectively. The lateral sides are set as periodic to be consistent with the mechanical problem.

6.2.2 Results

Observations of real subduction zones reveal that the slab dip increases gradually from the surface to a depth of 80 – 150 km. Below this depth, it remains almost constant down to the limit between the upper and the lower mantle at 660 km depth, where the slab may deflect. In our models the slab dip is computed between

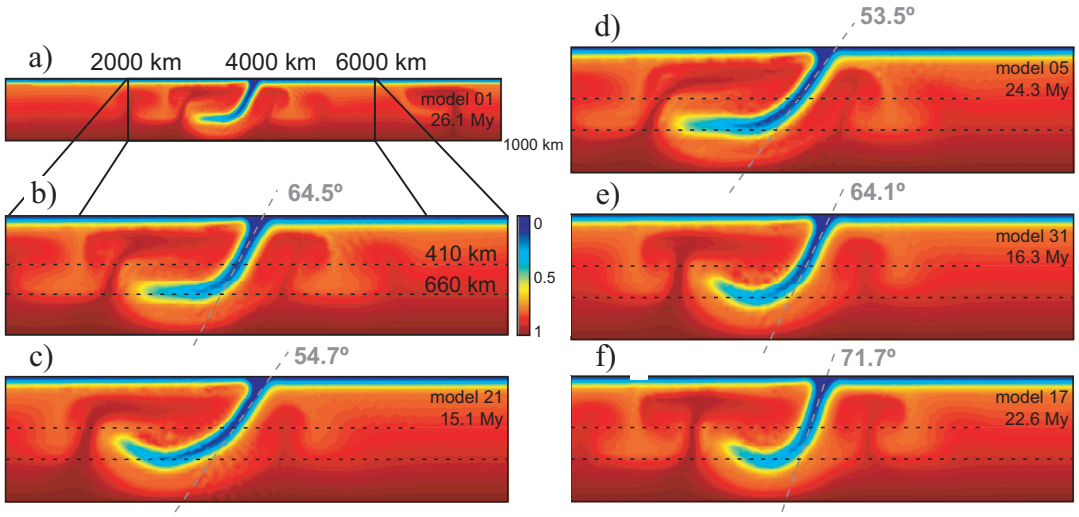

Figure 6.8 – Final temperature distributions (dimensionless) resulting in five different simulations with different convergence rates. The convergence between plates in all models is $\sim$ 1300 km Complete computational domain (a) and zoom into the zone of interest (b) to (f). The slab dip is indicated for each simulation. All models have the same shortening.

200 and 400 km depth. Ignoring the upper 200 km precludes the influence from the shallow dip, possibly biased by the surface boundary conditions. The lower 400 km limit is above the curved part of the slab caused by the deflection at 660 km.

The slab dip is computed by a linear least squares fitting of the position of the interface between the subducted lithosphere and the upper mantle. Note that this interface is described by the level set function. The slab dip is computed at many stages in each simulation. Figure 6.8 shows the final dimensionless temperature distributions for five different simulations, and the slab dip measurements. Due to the extremely low conductivity, the temperature field is a good proxy for identifying the slab geometry.

Figure 6.9 shows the results of a set of numerical simulations in terms of slab dip and convergence rate: every circle in the plot corresponds to a specific measurement in each simulation, all with different conditions. A clear correlation is found: high velocities are associated with low subduction angles. Taking into account all the velocity–dip measurements (a grand total of 412 corresponding to 39 different simulations) the correlation parameter is $R = -0.71$. The same analysis performed only with the measurements taken after a period of constant velocity (at the end of the simulation or before the velocity change, that is 61 measures) gives a correlation parameter of $R = -0.88$. If the linear regression is applied to the cases where the slab reaches the 660 km discontinuity (a grand total of 209 measures) the correlation is even better: $R = -0.93$.

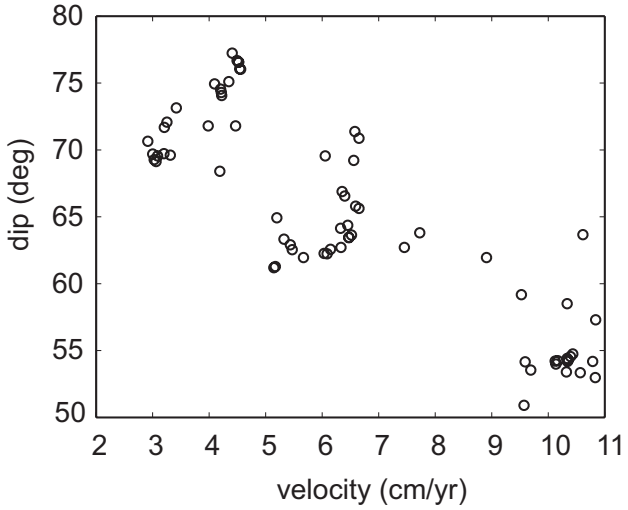

Figure 6.9 – Velocity–dip values

An analysis of the relations between plate curvature at 660 km depth and other known parameters showed no evident correlation. At the end of every simulation, the slab remains buoyant at the 660 km discontinuity. Moreover, no systematic relationship is found between the final slab geometry and the type of velocity transition (sudden or gradual) or the acceleration of the slab (positive or negative).

Figure 6.10 shows six velocity–dip paths, three corresponding to sudden velocity transitions and three to gradual transitions. It is observed that the average dip rate is 2 degrees My^{-1} for shallowing slabs and 2.7 degrees My^{-1} for steepening slabs.

The velocity–dip path for the model with a constant convergence rate of 10 cm yr^{-1} (see Figure 6.11) shows a clear increment in slab dip, until the plate is deflected at 660 km depth. Similar behavior was found in other examples.

According to the simulations, the slab dip does not depend on the length of the subducted lithosphere, nor on the thermal state of the slab (slabs of slower subduction zones have more time to adjust its temperature to the surrounding mantle). A clear dependence is found between the slab dip and the convergence rate (velocity). The smoother velocity–dip paths correspond to the gradual velocity transition models and corroborate the velocity–dip correlation.

6.2.3 Discussion and conclusions of the slab dip study

The results of the simulations performed here show a clear inverse relation between the convergence rate (or lower plate velocity) and the slab dip. This correlation is supported by velocity changes during the evolution of each model.

We interpreted that two forces are in competition to control the slab dip: the

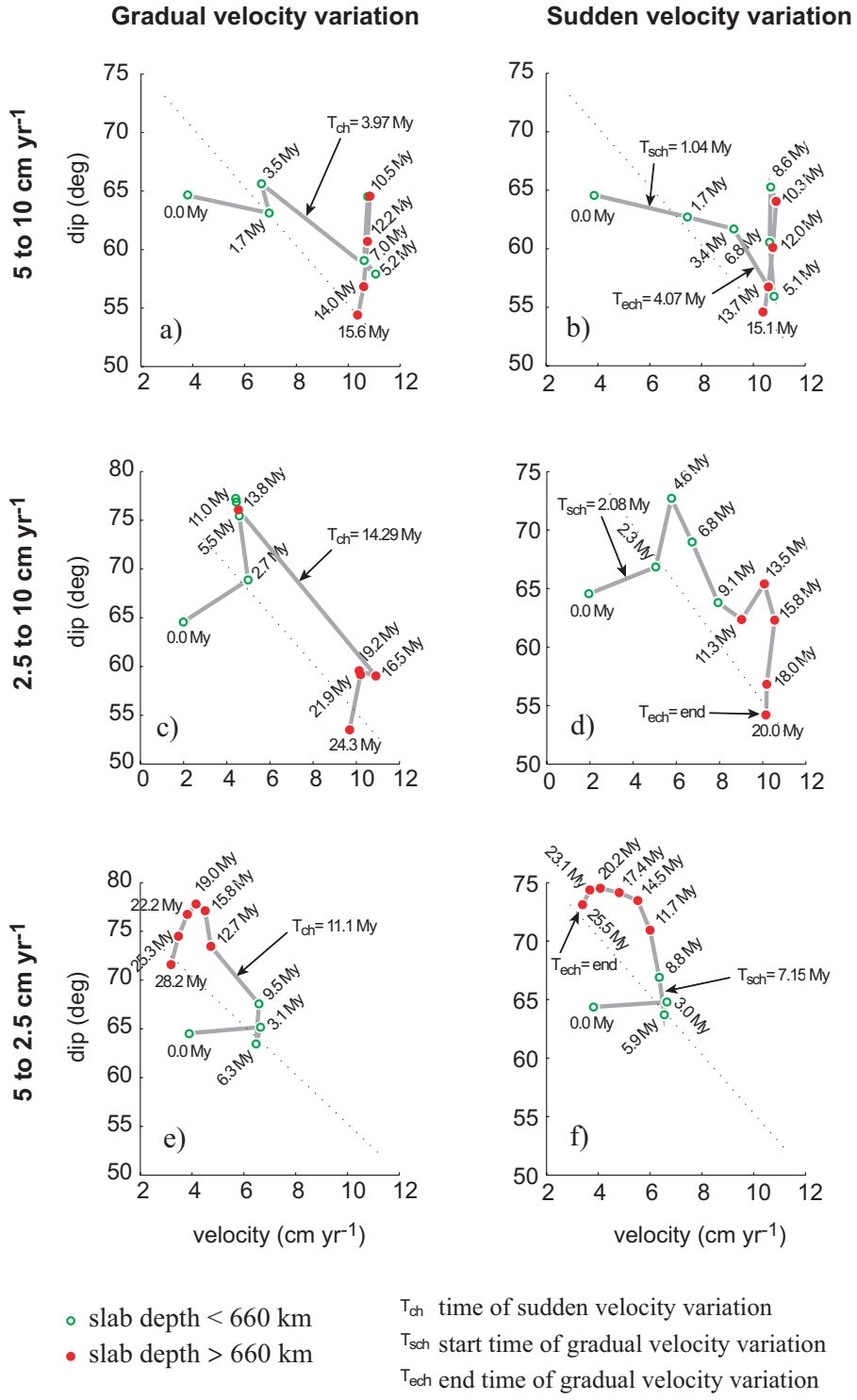

Figure 6.10 – Velocity–dip paths for six shallowing and steepening models. Black arrows indicate the times where the velocity changes. Gradual transition models have smoother paths than sudden transition models with same initial and final velocity. The dotted line is the best fit between velocity and dip for all models.

viscous force of the mantle resisting the slab penetration, which depends on the plate

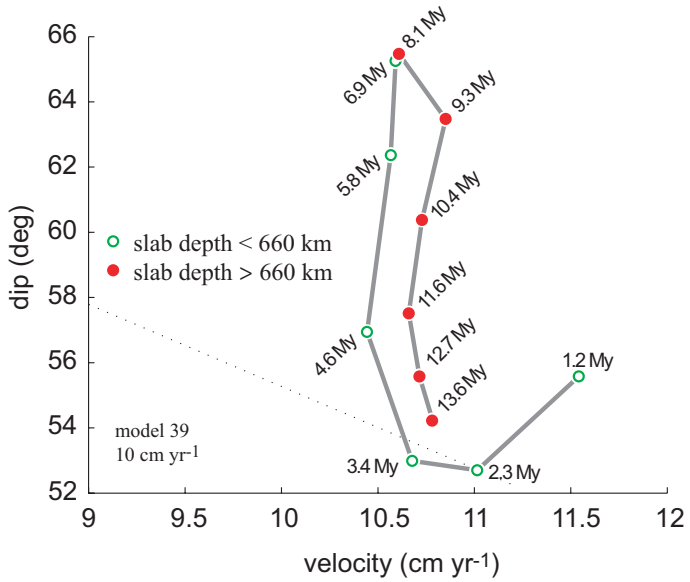

Figure 6.11 – Velocity–dip path for a constant velocity model (10 cm yr^{-1}).

velocity, and the mass excess caused by the lateral density contrast, depending on the temperature contrast between the slab and the mantle (the slab–pull force). If, as it is found in the present simulations, the velocity correlates with the slab dip, the mechanical viscous forces have a greater influence in the slab geometry than the gravitational forces. The effect of the thermal state is in this case of second order.

The relation dip–velocity in real subduction zones does not follow the linear behavior found here (Jarrard, 1986; Heuret and Lallemand, 2005; Lallemand and Heuret, 2005). The causes of this first order deviations can be diverse: the influence of more complex rheologies like visco–elastic (our result are purely viscous) acting on the subducting plate; the influence of variations in the oceanic crust thickness; the mantle wedge suction controlled by the wedge viscosity controlled, in turn by volatiles released by the subducting plate (Manea and Gurnis, 2007).

Chapter 7

Summary and conclusions

This thesis deals with the complete process of modeling the dynamic behavior of the oceanic lithosphere; we describe the physics governing the problem, its mathematical statement and the numerical approach used to solve the equations. Additionally a computational implementation of the numerical methods is provided. Moreover, the generated code is used to study different aspects of the dynamics of the oceanic lithosphere: its stability along time, the relation between convergence rate and geometry of subduction zones and the influence of key parameters on the detachment of a subducted slab. These studies may help to understand the complex geodynamic processes acting within the Earth.

Physical Model

Our transient multiphase thermo–mechanical model is based on the usual conservation equations. It accounts for complex non–linear rheologies based on diffusion and dislocation creeping mechanisms, which are likely responsible for mantle deformation. The physical properties of rocks (density, thermal conductivity, thermal expansivity, etc.) are calculated based on temperature and pressure by means of widely used and accepted theoretical or empirical formulas. The variation of the physical properties with major mineral phase transitions is also included in the model. Because of the abundance of olivine in the mantle (more than the 60%), including its successive transformations (olivine–wadsleyite–ringwoodite–perovskite+magnesiowüstite) allows to reproduce most important density and viscosity discontinuities. Adiabatic–, viscous– and radiogenic–heating terms are accounted for in the energy balance equation. These heat sources are of great importance in the simulation of gravitational instabilities as demonstrated in the application examples.

Numerical approach

We use several numerical techniques to solve the partial differential equations. The base of our approach is the eXtended Finite Element Method (X–FEM), which is used for the first time in geophysical applications. This technique, common in engineering applications, allows for describing and accurately solving multiphase problems in an Eulerian framework. The X–FEM adds two new ingredients to the standard FEM: a level set technique to locate the interface between materials and a enrichment technique to improve the accuracy of the solution across this interface. The application of level sets to geophysical problems was proposed in two almost simultaneously published works (Zlotnik et al., 2007a; Gross et al., 2007).

Most geodynamic codes use the markers technique instead of level sets. There are several differences between these techniques: Level sets successfully describe the interface between deforming materials with the same resolution as for the mechanical problem. The markers technique requires a much denser grid, penalizing computer time. If marker density is not enough, some regions of the domain may run out of markers leaving some elements without properties. On the other hand, the markers approach allows to control the accuracy of the mechanical problem and the location of the phases independently. One advantage of the level set approach is that it does not requires any averaging processes to pass data from nodes to markers and vice versa. Moreover, the X–FEM approach described here is especially well suited to use adaptive mesh refinement. This allows increasing locally accuracy of the numerical method and obtaining an accurate answer with the minimum computational cost. A very attractive advantage of level sets its straightforwardness in moving to 3D simulations: the simplicity of the coding is similar to the 2D case. Moreover, the increase in the computational cost for the 3D case is much lower than for the markers approach. These desirable properties of the level sets are demonstrated by examples using a mesh adaptive scheme and examples of three dimensional models.

Advanced numerical strategies

Further numerical improvements have been developed to properly deal with some unresolved features of our multiphase thermo–mechanical model. We have proposed and tested an original methodology to extend the X–FEM technique (usually accounting for two phases) to deal with a larger number of material phases. This is useful, for example, in detailed lithospheric models including the upper crust, the lower crust, the mantle, sediments, etc. The proposed X–FEM extension is based on a hierarchical ordering of several level set functions and an extension of

the enrichment technique. The ridge function, base of the enriched interpolation, is restated to include all the level sets and the hierarchy between them. Our method has the advantage of avoiding overlapping and void problems between materials, which exist in previous n–phase models. We also provide a computational strategy to solve efficiently the integrals that appear in the formulation of the problem.

In transient models, where the matrices change and have to be computed at every time step, the assembly of sparse matrices is a time–consuming task. We analyze several factors that may influence on the efficiency of the assembly procedure and propose an improved algorithm reducing both memory operations and computing time for all tested cases. This procedure is faster than that built-in Matlab assignment. Its use reduces the running time of our model to 60% and the assembly time to one half.

Evolution of oceanic lithosphere

The evolution of oceanic lithosphere is thought to be controlled by small–scale convection cells. These cells provide the extra heat needed to reduce the cooling of the lithosphere inferred from the seafloor depth and surface heat flow data. We present a numerical study of the evolution of the oceanic lithosphere. Emphasis is put on i) the influence of various rheological and thermo–physical parameters, always within the ranges dictated by laboratory studies, and ii) the ability to reproduce geophysical observables. We found that the water content of the lithopheric rocks, determined by the amount of partial melting at mid–ocean ridges, is possibly the responsible of the flattening of observables in old lithospheres. This dehydrated layer has been proposed by several authors as a control of the lithospheric evolution (e.g. Karato, 1986; Morgan, 1997; Lee et al., 2005) but its real influence was never tested before in dynamic codes.

We found that shear heating plays no significant role either in the onset of the instabilities or in reducing the lithospheric thickness. In contrast, radiogenic heat sources and adiabatic heating exert a major control on both the vigor of convective cells and the thermal structure of the lithosphere. It is found that either dislocation creep, diffusion creep, or a combination of these mechanisms, can generate small–scale convection with rheological parameters given by laboratory experiments.

The seismic structures predicted by our models closely resemble tomography studies from the Pacific. Nevertheless, the accuracy of present tomographies seems not to be enough to distinguish between the two competing models aiming at explain

the evolution of the oceanic lithosphere.

Slab breakoff, slab dip and 3D models

We have performed a numerical study of the breakoff of the subducted slab to study its evolution and the influence of key parameters controlling the process. Using realistic physical properties of mantle rocks, we have demonstrated the dynamic feasibility of the detachment process as caused by thermal diffusion of subducted slabs after cessation of active subduction. Our results show that the slab detachment process is characterized by a period dominated by thermal diffusivity ($\sim$ 20 My), followed by a fast slab necking ($\sim$ 2 My) and the sink of the detached slab. The adiabatic heating term plays a major role in mantle models, specially if gravitational instabilities are expected. Neglecting this term greatly enhances temperature contrasts favoring instabilities. Moreover, the detachment process is accelerated due to the strain–rate softening and focusing of thermal effects related to significant thermal feedback from shear heating. This feedback is also enhanced by the non–Newtonian rheology. Further work should include the effect of a metastable olivine wedge, which may modify the buoyancy of the slab.

The slab detachment process has been proposed in the literature to explain the thinning of the lithosphere (e.g. Molinaro et al., 2005; Ioane and Lillie, 2004; Schoonmaker et al., 2005). Our results do not support for such interpretation and neither do other geodynamic models. The causes of this differences may rely on the simplified treatment of the inter–plate fault and further work is needed to gain some insights on the process.

Finally, a possible relation between slab dip and convergence rate is studied. Our results show a clear inverse relation between the convergence rate (or lower plate velocity) and the slab dip. Nevertheless, this relation is not observed in nature. The causes of this first order deviations can be diverse: the influence of more complex rheologies like visco–elastic (our result are purely viscous) acting on the subducting plate; the influence of variations in the oceanic crust thickness; the mantle wedge suction controlled by the wedge viscosity controlled, in turn by volatiles released by the subducting plate (Manea and Gurnis, 2007), etc.

Flexibility of the developed code

Our model is designed keeping in mind that in most cases realistic geodynamic applications require accounting for the three spatial dimensions. To emphasize the

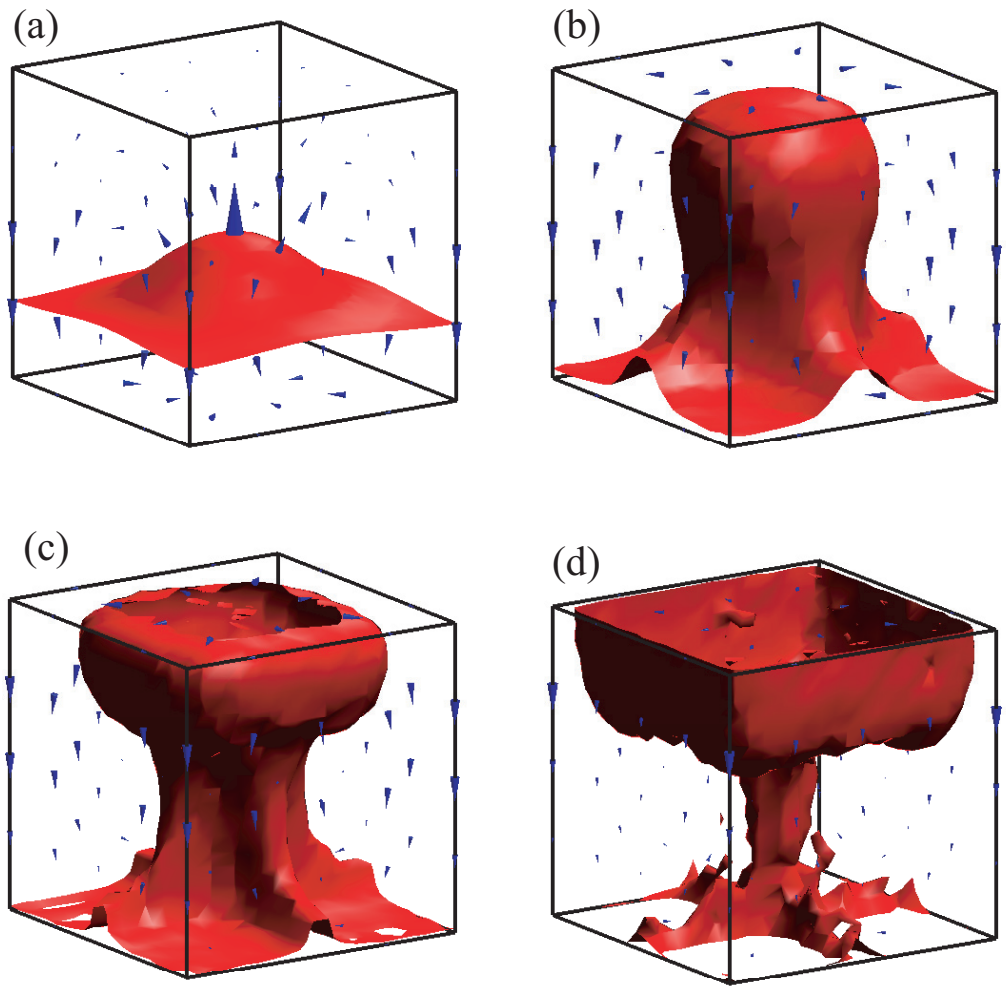

Figure 7.1 – Evolution of a Rayleigh–Taylor instability. The red surface is the interface between two materials described by the level set. The blue triangles indicate the velocity directions and magnitude. The viscosity ratio is $\eta_1/\eta_2 = 1$ and the initial lower layer thickness $h = 1/3$

abilities and flexibility of our numerical approach we show here two 3D examples. Firstly, Rayleigh–Taylor instabilities allow us to show how our model, based on the X–FEM, can be easily extended to 3D. Secondly, a global mantle model shows how geometrically complex boundary conditions can be imposed and how a spherical geometry can be used.

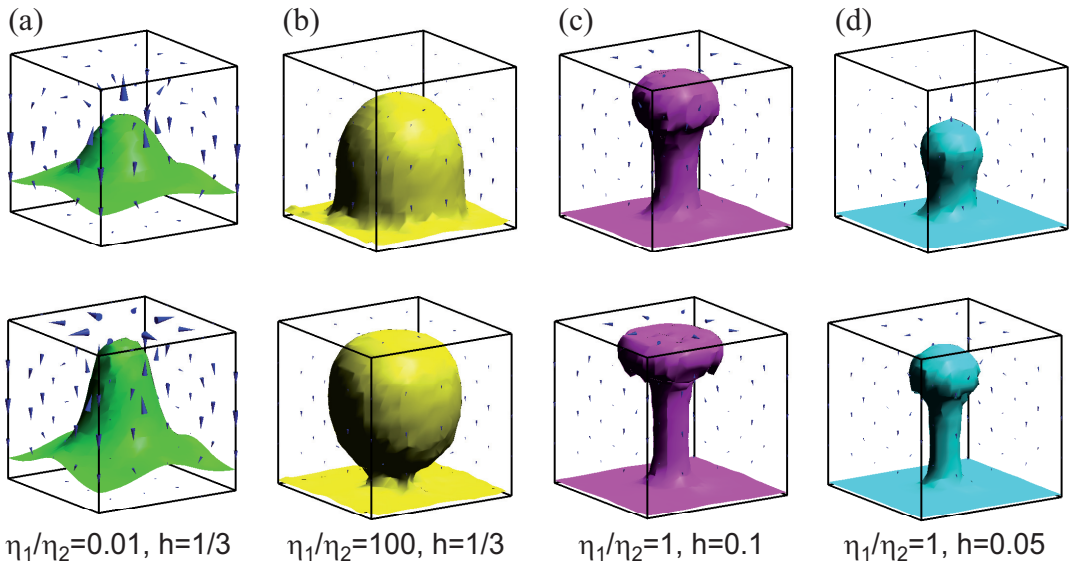

Figure 7.2 – Two snapshots of the evolution of four different Rayleigh–Taylor instabilities. The viscosity ratios and thickness h of the lower layer determines the shape of the plume.

3D Rayleigh–Taylor instabilities

In many geological and geodynamic contexts compositional differences produce gravitationally unstable configurations. In this situations a relatively light material is overlaid with a denser layer. Examples of that are salt domes, granitic batholiths, or the entrainment of a chemically distinct D" layer in the lower mantle. Some of these processes are similar to those presented in previous Sections and therefore temperature dependent. Nevertheless, for the sake of simplicity, we will only consider the compositional aspect (multiphase mechanical behavior) in order to show the capabilities of the X–FEM in 3D simulations.

Figure 7.1 shows the evolution of a Rayleigh–Taylor instability with a viscosity ratio $\eta_1/\eta_2 = 1$ and a dimensionless lower layer thickness of $1/3$. The plotted surface corresponds to the interface between the two materials described by the level set.

Figure 7.2 shows some snapshots of models with different viscosity ratios and different initial thicknesses of the lighter underlying material. In general terms, the viscosity ratio controls the size of the diapir head and the velocity at which the initial stratification overturns (Figure 7.2a and b). On the other hand, the initial thickness of the underlying layer mainly controls the velocity at which the head of the diapir rises and hence, the length of the tail.

These examples show the capability of X–FEM to reproduce the geometry of the interface evolution between two (or more) deforming materials in three dimensions.

Earth mantle model

A simplified model for the whole mantle is presented here as an example of i) a 3D mechanical model, ii) a model using spherical geometry, and iii) very complex boundary conditions. The domain is an empty sphere, representing the whole mantle, from the Moho to the core–mantle boundary. The physical properties of the material are radially averaged. We calculate a steady–state velocity field based on the present plates movement. Radial boundary conditions (normal to the inner and outer surfaces) are free slip. Tangential boundary condition in the outer surface are imposed to represent present plates velocities. The surface of the Earth is partitioned in 51 tectonic plates following Gripp and Gordon (2002). The surface velocity for each plate is computed using the Euler pole and angular velocity listed in Table 7.1

Plate	Lat.	Long.	Rot. (deg. My^{-1})	Plate	Lat.	Long.	Rot.
Africa	+59.16	-73.17	0.93	Amur	+57.65	-83.74	0.93
Antarctica	+64.31	-83.98	0.87	Altiplano	+33.64	-81.18	0.92
Arabia	+59.66	-33.19	1.16	Aegean Sea	+74.28	-87.24	0.65
Anatolia	+56.28	+8.93	1.64	Australia	+60.08	+1.74	1.07
Birds Head	+12.56	+87.96	0.30	Balmoral Reef	+45.90	-111.00	0.20
Banda Sea	+16.01	+122.44	2.13	Burma	+8.89	-75.51	2.67
Caribbean	+54.31	-79.43	0.90	Caroline	+10.13	-45.57	0.31
Cocos	+36.82	-108.63	2.00	Conway Reef	-12.63	+175.13	3.61
Easter	+28.30	+66.40	11.40	Eurasia	+61.07	-85.82	0.86
Futuna	-10.16	-178.31	4.85	Galapagos	+9.40	+79.69	5.28
India	+60.49	-30.40	1.10	Juan de Fuca	+35.00	+26.00	0.51
Juan Fernandez	+35.91	+70.17	22.52	Kermadec	+47.52	-3.12	2.83
Mariana	+43.78	+149.21	1.28	Manus	-3.04	+150.46	51.30
Maoke	+59.59	+78.88	0.89	Molucca Sea	+11.10	-56.75	4.07
North America	+48.71	-78.17	0.75	North Bismarck	-4.00	+139.00	0.33
North Andes	+58.66	-89.00	0.70	New Hebrides	+13.00	-12.00	2.70
Niuafo‘ou	+6.87	-168.87	3.25	Nazca	+55.58	-90.10	1.36
Okhotsk	+55.42	-82.86	0.84	Okinawa	+48.35	+142.41	2.85
Pacific	+0.00	+0.00	0.00	Philippine Sea	-1.20	-45.80	1.00
Rivera	+26.70	-105.20	4.69	South America	+55.00	-85.75	0.64
South Bismarck	+10.61	-32.99	8.44	Scotia	+48.63	-81.45	0.65
Shetland	+63.12	-97.08	0.86	Somalia	+58.79	-81.64	0.98
Solomon Sea	+19.53	+135.02	1.48	Sunda	+55.44	-72.95	1.10
Sandwich	-19.02	-39.64	1.84	Timor	+19.52	+112.18	1.51
Tonga	+28.81	+2.26	9.30	Woodlark	+22.13	+132.33	1.55
Yangtze	+69.07	-97.72	1.00				

Table 7.1 – Plate velocities after Gripp and Gordon (2002); location of the Euler pole and rotational velocity.

In Figure 7.3 two views of the Earth are shown. Green colors show places where the radial flux is negative (descending streams) corresponding with subduction zones. Red colors are places where the radial flux is positive (ascending streams) and are associated with mid–ocean ridges. The first view (panels a, b and c) of Figure 7.3 corresponds to South America, Nazca, Cocos, and part of the Pacific plates. In panel b, showing the radial velocity at 150 km depth, the Pacific Ridge and the subduction zone below South America are well developed. The South Atlantic Ridge can also be seen. At 300 km depth (panel c) the same features, with much

less intensity, are found. In the second view, most of the western Pacific subduction zones are well developed: Kamchatka, Japan, all zones surrounding the Philippine Sea, the Andaman–Sumatra–Java Arc, New Hebrides and Tonga. The shortening between India and Asia and the ridge between Antarctica and Australia are also well developed. All these features are, of course, induced by the surface boundary conditions.

This model shows only a steady state flow of the mantle compatible with the current plate movements. In addition to the simplified rheology, the absence of hot spots makes the obtained flow much more simpler than the real mantle. Nevertheless, a first order match of the major tectonic features of the Earth can be reproduced even with this simple model.

Future work

As shown in the previous examples the development of a full thermo–mechanical code in 3D is one of the possible future work lines. However, there are also other very interesting features to add to the model; our present approach suffers of a lack of consistency mainly due to the incompressibility approach. Despite we are dealing with solid rocks, at mantle conditions the pressure reaches values high enough to consider the rocks compressible. Moreover, the mineral phase transitions responsible of jumps in the density field also produce appreciable volumetric changes. The importance of the adiabatic heating term in our results indicates how much the rocks can be compressed.

Another interesting work line is the coupling between a dynamical model like ours, with a petrological model like PerpleX (Connolly, 2005). The petrological model calculates in a thermodynamical consistent way, the equilibrium mineral assemblage at a given temperature, pressure and composition. Using this information the physical properties of the rocks can be accurately computed accounting for solid–solutions and all mineral phase transformations.

Finally, both the 3D and the petro–dynamical models will be extremely demanding of computational power, thus requiring the use of parallelization techniques to obtain results in a reasonable amount of time. Therefore, any further improvement our of our code should contemplate running in a cluster of computers or in parallel machines.

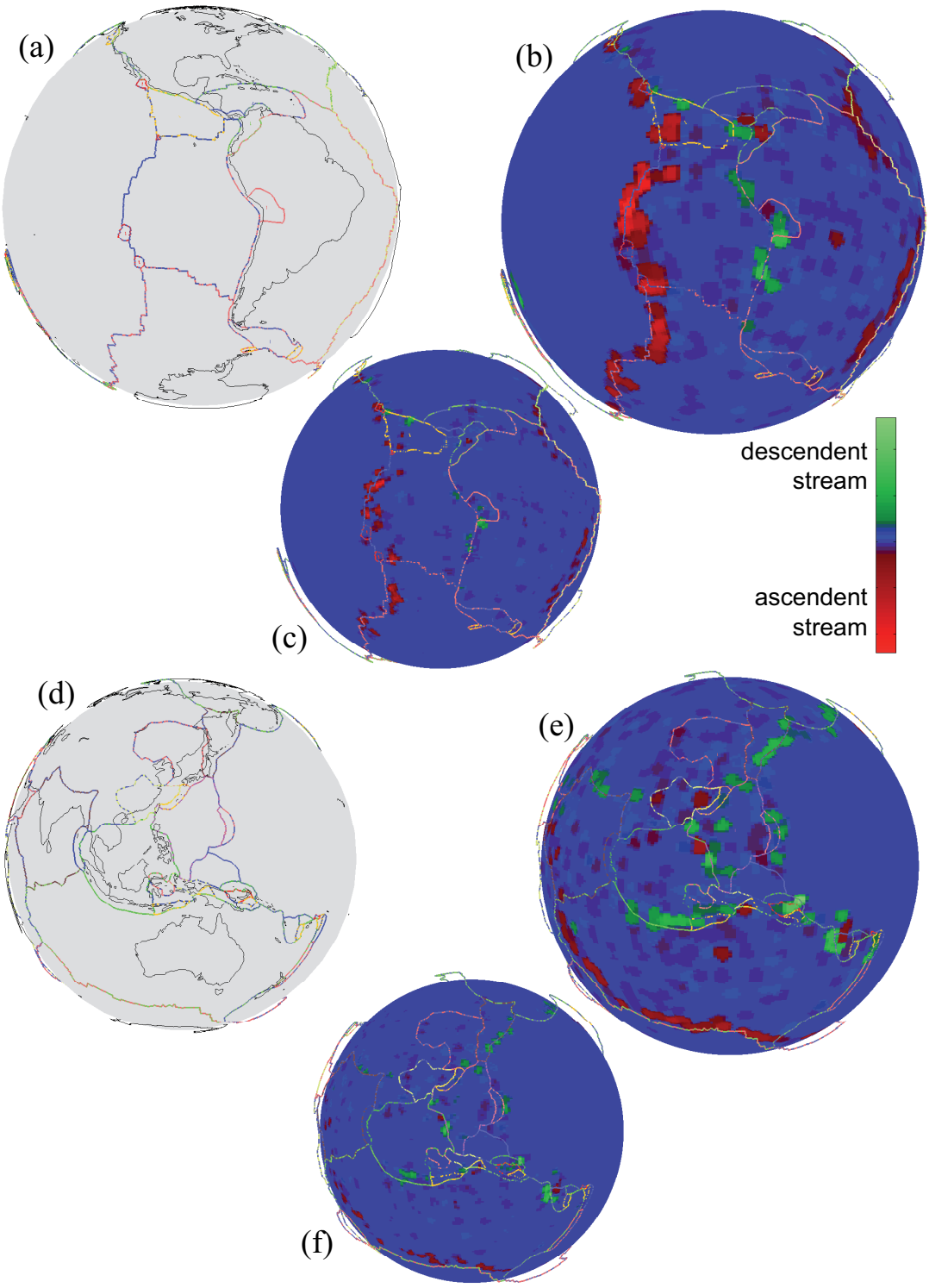

Figure 7.3 – Mantle radial velocity. The three upper globes show the plate configuration (a), radial velocity at 150 km depth (b) and radial velocity at 300 km depth (c). The three lower globes show same data as the upper globes for a different view. In (a) and (d) the coastlines are drawn in black. The plate boundaries are drawn in colors.

Appendix A

Resumen en castellano

Introducción

La Tectónica de Placas está basada en la división de la superficie terrestre en un grupo relativamente pequeño de placas en movimiento. Según su génesis y en consecuencia su composición y evolución, las placas se clasifican como continentales u oceánicas. Éstas últimas son las responsables de la dinámica del sistema: la litosfera oceánica es creada en las dorsales oceánicas, donde dos placas adyacentes se separan dando lugar a la generación de magmatismo. La nueva placa oceánica es generada por el material extruido una vez que éste se enfría y se vuelve rígido. Este proceso de creación de fondo oceánico está equilibrado con su destrucción en las zonas de subducción. De esta manera las placas oceánicas son creadas en las dorsales, se desplazan lateramente mientras se enfrían y se engrosan hasta que, en algún momento son consumidas en una zona de subducción. La Tectónica de Placas es capaz de asimilar una inmensa cantidad de evidencia geológica y geofísica proveniente de diversas ramas. Por ejemplo, la ubicación de los grandes arcos volcánicos y todos los terremotos profundos están relacionados con las zonas de subducción; las dorsales oceánicas producen vulcanismo y sismicidad moderada en la continua generación de la corteza oceánica; la batimetría, el flujo de calor y las señales gravimétricas del fondo oceánico están relacionados con el envejecimiento de la litosfera; prácticamente toda la deformación tectónica del planeta se produce en los bordes de las placas. A pesar del éxito de la Tectónica de Placas en predecir y explicar todos estas observaciones entre muchas otras, es una teoría puramente cualitativa, que brinda una explicación del funcionamiento del planeta, sin proponer los fundamentos físicos que la sostienen. De hecho, la dinámica de la Tierra y de los procesos descritos por la Tectónica de Placas aun hoy siguen sin ser comprendidos completamente. Algunos temas de investigación actual sobre la dinámica de la

litosfera y el manto son, por ejemplo, la causa de la estabilización de las litosferas oceánicas antiguas, las variables que controlan el régimen de deformación en las zonas de tras arco , las variables que controlan el ángulo conque subducen las placas, cómo comienza un proceso de subducción, etc. Entre las diferentes metodologías utilizadas para estudiar la litosfera y el manto terrestre encontramos observaciones indirectas, geológicas y geofísicas, por ejemplo el flujo de calor superficial, las señales gravimétricas o la signatura geoquímica de los volcanes, que nos permiten conocer el estado actual y los procesos activos. Los estudios de laboratorio brindan información sobre las propiedades físicas de los materiales que componen la Tierra. Y por último, de las ondas sísmicas que viajan por el interior del planeta podemos inferir datos importantes sobre composición, cambios de fase mineralógicos, grado de fusión, etc. Sin embargo, la amplia mayoría de estas fuentes brindan información sobre el estado actual de la Tierra pero describen pobremente la dinámica de los procesos que actúan en ella. Es por esto que el modelado numérico es una herramienta útil a la hora de estudiar los procesos geodinámicos.

Modelado numérico

La complejidad de la dinámica, la cantidad y variedad de procesos concurrentes y los grandes contrastes de propiedades que se presentan en los modelos que describen el comportamiento terrestre, requiere de técnicas numéricas avanzadas para aproximar las ecuaciones físicas resultantes. Numéricamente los modelos de convección incluyendo placas rígidas han sido un desafío desde mediados de los años 80. Sin embargo, en muchos sentidos el desafío computacional es mayor hoy que hace dos décadas, principalmente debido a la complejidad creciente de las reologías involucradas. La manera en que se deformarán las rocas es altamente dependiente de la temperatura, la presión, el estado tensional y su composición. La tendencia a localizar la deformación debido al comportamiento no lineal de las ecuaciones constitutivas, los altos gradiente de temperatura y los cambios composicionales, todos producen cambios bruscos de propiedades materiales en pequeñas escalas espaciales comparadas con el tamaño del sistema. Modelos reológicos complejos son ya habituales, por ejemplo incluyendo visco–plasticidad (e.g. Tackley, 1998, 2000; Bercovici, 2003), dependencia del tamaño de grano (e.g. Solomatov, 2001) o el efecto de volátiles (e.g. van Keken et al., 2002; Arcay et al., 2005; Abers et al., 2006).

Objetivos

Esta tesis tiene dos objetivos principales: el primero el desarrollo de un herramienta informática para el estudio de modelos geodinámicos. ésta debe resolver las ecuaciones físicas que gobiernan el problema (conservación de masa, momento y energía) de manera eficiente y flexible, de tal manera que sea sencillo agregar procesos secundarios como por ejemplo cambios de fases mineralógicos, procesos de fusión, etc. Para contrastar las simulaciones con datos reales es necesario proveer de observables sintéticos calculados a partir de los resultados del modelo, por ejemplo topografía, flujo de calor, anomalías gravimétricas, etc. Los elementos finitos extendidos (X–FEM) son una herramienta de reciente desarrollo actualmente aplicada en problemas de ingeniería, entre otras cosas, a problemas de flujo multifase. Uno de los objetivos de este trabajo es estudiar la eficiencia de esta metodología aplicada a problemas geofísicos. El segundo objetivo de este trabajo en la aplicación de la herramienta generada para el estudio de diferentes aspectos de la dinámica de la litosfera oceánica.

Modelo físico

En este capítulo se describen las ecuaciones que gobiernan el comportamiento físico de la litosfera y del manto. El modelo está basado en dos problemas físicos: un problema de mecánica de fluidos y un problema térmico. Ambos están acoplados explícita e implícitamente, por ejemplo en el término convectivo de la ecuación térmica o en la dependencia de las propiedades físicas de la presión (solución del problema mecánico) y la temperatura (solución del problema físico).

Térmica

En el interior de la tierra actúan tres mecanismos de transferencia de calor: convección, conducción y radiación. éste último se vuelve apreciable a temperaturas superiores a 1500 K. La importancia relativa entre los diferentes mecanismos determina tres regímenes térmicos: las regiones con un gradiente térmico cercano al gradiente adiabático[1] donde el transporte advectivo es dominante. Este es el caso del manto superior y de la zona de transición. Las regiones donde la conducción es comparable a la advección, por ejemplo la litosfera oceánica. Y por último las regiones en donde el transporte conductivo es dominante, por ejemplo en la litosfera continental. La ecuación (2.6) gobierna el balance de energía. El último

[1] el gradiente provocado por la compresión adiabática de los materiales

término de ésta incluye distintas fuentes de calor: un término constante debido a la desintegración de elementos radioactivos, un término fuente por disipación viscosa de calor (*shear heating*) descrito por la ecuación (2.7) y un término adiabático debido a la compresión y descompresión adiabática de materiales descrito en la ecuación (2.8). El manto superior está dominado por celdas convectivas en donde la convección térmica es dominante. Este proceso tiende a homogeneizar las temperaturas dando lugar a un gradiente casi adiabático. El régimen térmico de las placas oceánicas es más controversial; durante los primeros 70 Ma no hay dudas en que la placa sufre principalmente un enfriamiento conductivo (McKenzie, 1967; Parsons and Sclater, 1977). Este enfriamiento se ve reflejado en la batimetría y en el flujo superficial de calor: ambos son funciones de la edad de la placa. Sin embargo, una vez superada esa edad estos observables cambian su tendencia y su señal se hace casi constante indicando un estancamiento del enfriamiento de la placa (Parsons and Sclater, 1977; Schroeder, 1984; Stein and Stein, 1992). Este comportamiento es reproducido por un modelo empírico llamado "modelo de placa" que es capaz de predecir los valores observados pero no aporta ninguna explicación física del porqué se rompe la tendencia puramente conductiva. En las aplicaciones de este trabajo se tratará con más detalles la evolución en el tiempo de la litosfera oceánica.

Mecánica

A pesar de que el manto superior está compuesto en su 99% por rocas en estado sólido, su comportamiento mecánico a escalas de tiempo geológicas ($> 10^4$ años) es fluido. La deformación en estado sólido ocurre debido a procesos de movimiento de átomos dentro de la estructura cristalina (Ranalli, 1995). El comportamiento del manto es usualmente modelado como un fluido cuasi estático gobernado por la ecuación de Stokes (Busse, 1989; Schubert et al., 2001). El uso de esta ecuación asume: i) que las rocas con casi incompresibles, ii) dado que el numero de Prandtl del manto es prácticamente infinito, los términos inerciales son despreciados, y iii) dado que el numero de Rayleigh que caracteriza la convección del manto no es excesivamente grande, se desprecia el régimen de convección turbulenta. Teniendo en cuenta las asunciones anteriores y asumiendo la aproximación de Boussinesq extendida, el problema mecánico queda gobernado por la ecuación de conservación de masa (2.10) y de conservación de momento (2.15).

Viscosidad

El comportamiento mecánico de un fluido está caracterizado por su viscosidad. Ésta relaciona los esfuerzos que actúan sobre el fluido con la velocidad de deformación. La viscosidad del manto ha sido estimada usando observaciones geofísicas y estudios de laboratorio. La deformación de los minerales del manto en condiciones del manto suele seguir una ley exponencial en la cual la velocidad de deformación depende de una potencia de los esfuerzos no isótropos. Dos procesos a nivel atómico se consideran responsables de la mayor parte de la deformación del manto: la deformación por difusión y la deformación por dislocaciones (Kirby, 1983; Ranalli, 1995). Trabajos teóricos y experimentales indican que la ecuación constitutiva de las rocas del manto dependiendo de la temperatura, la presión y el estado tensional sigue una ley como la expresada en la ecuación (2.17). Usando la definición de viscosidad (2.18), se obtiene la fórmula explícita para la viscosidad (2.19). Las propiedades involucradas en esta ecuación son el parámetro pre exponencial A_D, la potencia n, la energía de activación E, el volumen de activación V y la constante de gases R. A proceso de deformación le corresponde un juego de estos parámetros. A bajas temperaturas, (< 700 K) la deformación ocurre mayormente en forma frágil. Para incluir este comportamiento se utiliza una ley simplificada de Mohr–Coulomb como la descrita en la ecuación (2.21) (Ranalli, 1995; Brace and Kohlstedt, 1980).

Cambios de fases minerales

Los minerales del manto son estables dentro de un rango de presión y temperatura, una vez fuera de sus límites se transforman en la fase más estable a las nuevas condiciones. Estas variaciones mineralógicas son las responsables de la mayor parte de las variaciones de las propiedades físicas de las rocas. En el manto superior las transformaciones que más influyen son: plagioclasa–espinela–granate que ocurre entre 40 y 80 km de profundidad, la olivina que se transforma sucesivamente en wadsleita y luego en ringwoodita a 410 y 510 km de profundidad respectivamente. A mayores presiones lo hace en magnesiowustita y ferropericlasa luego de los 660 km. Para incluir en el modelo la influencia de la mineralogía estable en las propiedades físicas se definieron cuatro dominios minerales separados por las transformaciones descritas. Cada uno de estos dominios representa la mineralogía estable a 200, 420, 600 y 750 km de profundidad. La composición mineralógica de estos dominios fue tomada del trabajo de Stixrude and Lithgow-Bertelloni (2007) y se muestra en la Figura 2.1 y en la Tabla 2.4. Para determinar qué dominio corresponde a una determinada presión y temperatura se utilizan las curvas de Clapeyron, aproximadas

por rectas como se muestra en la Figura 2.2.

Coeficiente de expansión térmica

Para aproximar esta propiedad se utiliza la fórmula de Schutt and Lesher (2006) junto con los datos de Fei (1995) que definen la variación del coeficiente para cada mineral. Ponderando luego estos valores con la cantidad presente de cada mineral se consiguen los parámetros correspondientes a cada dominio mineral descrito en la sección anterior. La dependencia de la presión se hace siguiendo a Chopelas (2000) y a Afonso et al. (2005).

Conductividad térmica

La conductividad térmica de los cristales suele ser no isótropa, sin embargo dada la distribución aleatoria de los minerales en las rocas, es válido considerar la conductividad de las rocas como isótropa. Ya que las medidas experimentales de conductividad incluyen el efecto de la radiación, los coeficientes obtenidos incluyen el efecto de ambas. En este trabajo se han utilizado dos leyes empíricas para modelar las variaciones de conductividad térmica con la presión y la temperatura: la fórmula empírica de (Clauser and Huenges, 1995) con los datos de (Gerya et al., 2004) y el modelo propuesto por (Hofmeister, 1999) (ecuaciones (2.24) y (2.25)). La variación de la conductividad con la profundidad para ambos modelos se muestra en la Figura 2.3.

Modelo numérico

Los problemas mecánico y térmico descritos en el capítulo anterior no disponen de soluciones analíticas. Por lo tanto es necesario utilizar métodos numéricos para aproximar las ecuaciones en derivadas parciales que los gobiernan. En este trabajo se utiliza el método de los elementos finitos para resolver dichas ecuaciones. El contenido de este Capítulo está descrito en dos artículos originales (Zlotnik et al., 2007a,b).

Problema mecánico

Para resolver el problema mecánico descrito por las ecuaciones (2.15) y (2.10) se utilizan elementos finitos mixtos, llamados de esta manera debido a que trabajan con dos tipos de incógnitas: las de velocidad y las de presión. Cada una debe

ser discretizada de manera diferente. Para asegurar que el sistema de ecuaciones generado es resoluble estas discretizaciones deben ser distintas y mantener una cierta relación. En este trabajo se utiliza el elemento *mini* mostrado en la Figura 3.1, que garantiza la no singularidad del sistema. Nótese que el planteo del problema mecánico descrito por estas ecuaciones no contempla la existencia de distintos materiales. El método de los elementos finitos se basa en una formulación débil de las ecuaciones y en una discretización del dominio. El problema, escrito en su forma fuerte en la ecuación (3.3), queda completamente definido cuando se incorporan las condiciones de contorno. La formulación débil equivalente queda definida como se expresa en las ecuaciones (3.10).

Problemas multifase y la técnica de *Level Sets*

Los problemas de flujo están definidos naturalmente con una descripción *Euleriana*, donde la malla computacional está fija en el espacio y el fluido se mueve con respecto a ella. Esta descripción cinemática facilita la descripción de las grandes deformaciones que sufre un fluido. Sin embargo, la descripción Euleriana tiene el inconveniente de complicar la descripción de interfaces móviles entre diferentes materiales. La técnica de *level sets*, inicialmente propuesta por Osher and Sethian (1988), permite describir la posición de dichas interfaces en el espacio y en el tiempo de una manera computacionalmente eficiente. La posición de la interface entre dos materiales queda determinada por una función ϕ, llamada función *level set*, definida en todo el dominio del problema. Su signo genera una partición del dominio siguiendo la convención definida en la ecuación (3.12). Es usual utilizar la función "distancia a la interface" como aproximación inicial de ϕ, usando valores positivos para un material y valores negativos para el otro. De esta manera la interface entre materiales queda definida por la curva en donde la función *level set* se anula. En la Figura 3.2 se muestran las fases, la interface y la función *level set*. En la práctica la función ϕ es discretizada sobre la misma malla de velocidades de los elementos finitos. Su actualización en el tiempo se realiza resolviendo la ecuación de convección pura (3.13), donde la velocidad $\mathbf{u}$ es la solución del problema de mecánico de *Stokes*.

Discretización en el espacio y soluciones enriquecidas

Como las propiedades físicas de los materiales cambian a un lado y al otro de la interface, es razonable esperar una solución con gradiente discontinuo a través de la interface. Sin embargo dentro de cada elemento, el gradiente de la solución brindado por el método de los elementos finitos es continuo. Como la técnica de los *level*

sets permite describir interfaces que corten los elementos, es usual enriquecer la solución para permitirle un gradiente discontinuo allí donde se encuentre la interface. La combinación de estás dos técnicas, *level sets* y una solución enriquecida, con el Método de los Elementos Finitos se suele llamar en la literatura Elementos Finitos eXtendidos o X–FEM. Las discretizaciones espaciales de la velocidad, la presión y la función *level set* se describen en las ecuaciones (3.15), (3.14) y (3.16) respectivamente. Usando la función *ridge* definida en la ecuación (3.17) para construir las funciones de interpolación M asociadas a los grados de libertad enriquecidos, las discretizaciones de la velocidad y de la presión enriquecidas quedan descritas en la ecuaciones (3.18) y (3.19). Usando la formulación de Galerkin el problema (3.10) discretizado en el espacio queda formulado de forma matricial como (3.23), con las matrices definidas de la manera indicada. Dado el carácter cuasi estático del problema mecánico, es decir dado que el número de *Prandtl* se puede considerar infinito y los términos inerciales son despreciables, éste no necesita discretización en el tiempo; su evolución se debe exclusivamente a los cambios en el campo térmico y en la posición de los materiales.

Problema térmico

El problema térmico (2.6) debe ser discretizado en el espacio y en el tiempo. La parte espacial es tratada de manera similar a la descrita para la ecuación de Stokes, la parte temporal se hace utilizando el algoritmo de *Padé*. La ecuación térmica se vuelve no lineal debido a la dependencia de la densidad y la conductividad térmica de la propia temperatura. Sin embargo, como se esperan grandes cambios en la temperatura entre dos pasos de tiempo consecutivos, las propiedades materiales con calculadas a partir del campo térmico del paso anterior. Las formas fuerte y débil del problema se brindan en las ecuaciones (3.24) y (3.25). Su discretización resulta en el sistema lineal (3.27). La discretización temporal se realiza usando el algoritmo de *Padé* descrito en (3.28) que, en la práctica, resulta en a resolución de una serie de sistemas lineales definidos por la ecuación (3.29). La función *level set* se discretiza como (3.30) en el espacio. En el tiempo se utiliza el método de *Taylor–Galerkin* de dos pasos y orden tres, descrito en (3.32b). Al aplicar este algoritmo a la ecuación (3.13) resultan los sistemas de ecuaciones (3.34). Para asegurar la estabilidad el incremento del tiempo Δt de un paso a otro debe cumplir que el número de *Courant* satisfaga la ecuación (3.34). Este criterio se combina con el criterio (3.36) que asegura la estabilidad de la parte difusiva del problema térmico.

Métodos numéricos avanzados

En este capítulo se describen los aportes originales numéricos que se han desarrollado en esta tesis. La Sección 4.1 propone una extensión de X–FEM para X–FEM para incluir cualquier número de materiales. El Seccion forma parte de un artículo enviado a *Computational Methods in Applied Mechanics and Engineering* (Zlotnik and Díez, 2008). La Sección 4.2 describe un esquema adaptativo de remallado para incrementar la precisión en la descripción de la posición de las interfases. La Sección 4.3 describe algunos aspectos computacionales de la implementación de nuestro modelo. Una tarea que requiere una cantidad no despreciable de capacidad de cálculo es el ensamblado de matrices ralas[2]. Para realizar esta tarea se propone un nuevo algoritmo que reduce tanto las operaciones de memoria necesarias, como el tiempo de ensamblado. El contenido de esta Sección fue enviado a *Communications in Numerical Methods in Engineering* para ser publicado (Zlotnik and Díez, 2007).

X–FEM jerárquico para modelos de flujo con n–fases

El Método de los Elementos Finitos eXtendidos es usualmente usado para el modelado de flujo con dos materiales. Esta restricción sobre el número de materiales está impuesta por el uso del signo de la función *leve set* para describir la ubicación de los mismos. Diferentes metodologías han sido propuestas para incrementar este número basadas en el uso de varias funciones *leve set*. Sin embargo todas ellas sufren de la posibilidad de generar regiones donde no se puede asignar ningún material, ya sea porque no se dispone de información o porque la información es contradictoria. En esta Sección se describe una metodología basada en un ordenamiento jerárquico de las funciones *level set* que evita de manera natural dichos problemas. La metodología se describe en el contexto de un problema de flujo multifase, pero es posible utilizarla en cualquier contexto donde X–FEM sea aplicable.

Ubicación de n materiales mediante *level sets* jerárquicos

En modelos de dos materiales, la ubicación de los mismos queda determinada por el signo de una función *level set* como se indica en la ecuación (4.2). Para ser capaces de describir la posición de cualquier número de fases materiales se propone incrementar el número de funciones *level set* asignando una jerarquía entre ellas. La primer fase material quedará definida por la parte positiva de la primera función *level set*, $\phi^{(1)}$, como se indica en la ecuación (4.3). La parte del dominio en donde la primer

[2] *sparse matrices*

función (4.3) sea negativa quedará determinada por el resto de las funciones *level set*. De esta manera la segunda función *level set*, $\phi^{(2)}$, determina la posición de la segunda fase en la región del dominio en donde $\phi^{(1)}$ toma un valor negativo como se indica en la ecuación (4.4). La región donde el *level set* con menor jerarquía toma un valor negativo representa la posición del último de los materiales. Esta idea de jerarquía puede extenderse a cualquier número de materiales como se muestra en las equaciones (4.5) y (4.6). En la Figura 4.3 se muestra un ejemplo de partición del domino en cuatro materiales con tres *level sets*.

Enriquecimiento de elementos con varios materiales

La jerarquía de *level sets* recién descrita permite que algunos elementos sean cortados por varias interfaces y contengan en su interior varios materiales. En este caso el enriquecimiento de la solución debe tener en cuenta cada una de las interfaces y la jerarquía entre ellas. La interpolación de la velocidad $\mathbf{u}$ está compuesta por una parte standard de los elementos finitos mas la parte enriquecida según la ecuación (4.7), donde los grados de libertad enriquecidos $\mathbf{a}_j$ son interpolados con las funciones de forma M_j. Éstas últimas se consiguen multiplicando las funciones de forma standard N por una función *ridge*, R, que posee derivada discontinua sobre la interfase entre materiales como se muestra en la Figura 4.5. En el caso de problemas que involucran dos materiales la función *ridge* se define como (4.9) (Moës et al., 2003). La extensión de la función *ridge* a problemas de varios materiales se realiza de la siguiente manera. Se define el *ridge* asociado al *level set* k–ésimo como (4.10). De esta manera los elementos cruzados por sólo la interfase k–ésima, utilizan el *ridge* $R = r^{(k)}$. En elementos multifase, que tienen varias interfases en su interior, la función *ridge* se construye usando los *ridges* de cada una de ellas, como se describe en la ecuación (4.11). La función $C^{(1)}$ introduce la jerarquía entre las interfaces y está definida en la ecuación (4.12). El *ridge* normalizado, $r^{(1)}_{\text{norm}}$, tiene la propiedad que su cresta tiene un valor constante igual a uno. Su definición se encuentra en la ecuación (4.13). En la Figura 4.6 se ilustra el proceso de construcción de un *ridge* para el caso de un elemento triangular con tres materiales en un interior.

Integración en elementos con varios materiales

El Método de los Elementos Finitos requiere resolver integrales dentro de cada elemento. Las cuadraturas tradicionales, por ejemplo las de Gauss, están diseñadas para integrar polinomios y funciones regulares, pero no garantizan un buen resultado sobre funciones discontinuas como las generadas dentro de los elementos enriquecidos. La integración en un elemento cortado por una única interfase se

suele realizar partiendo éste en dos subdominios, cada uno con un único material en su interior. Por lo tanto cada subdominio contendrá funciones continuas bien condicionadas para la integración. En el caso de elementos triangulares el cálculo de los subdominios es trivial. A medida que los elementos se vuelven más complejos o que las dimensiones del problema aumentan, la determinación de los subdominios se vuelve más cara y algorítmicamente más compleja. Cuando además existe la posibilidad de la existencia de varias interfaces dentro de un elemento, como en el caso aquí propuesto, los subdominios generados pueden tener cualquier forma poligonal aumentando aun más el costo de su determinación. En este contexto la idea de una cuadratura que no requiera del cálculo explícito de los subdominios materiales resulta atractiva. Por lo tanto aquí se propone una cuadratura adaptativa que, teniendo en cuenta las interfases entre materiales y su jerarquía, permite integrar en el elemento entero sin realizar particiones. La distribución de los puntos de integración se basa en la posición de las interfases, incrementando su densidad cerca de las mismas. A pesar de que el costo computacional de dicha cuadratura puede resultar alto, ésta solo se aplicará a muy pocos elementos del dominio, por lo cual se espera que su influencia en el costo total sea despreciable. El Algoritmo 2 determina la cuadratura propuesta basada en una subdivisión recursiva del elemento como la mostrada en la Figura 4.8.

Ejemplos numéricos

El método descrito en las secciones anteriores es aplicado aquí a un problema de inestabilidad gravitacional incluyendo varios materiales en dos y tres dimensiones.

Ejemplo 1: Inestabilidades en 2D. La disposición inicial de los materiales es la mostrada en la Figura 4.10. El material superior es más denso que los inferiores y, por lo tanto, se forma una inestabilidad gravitacional. Los dos materiales inferiores tienen distinta viscosidad y por lo tanto la inestabilidad generada es asimétrica horizontalmente. En la Figura 4.12 se muestra la evolución del modelo para cuatro diferentes configuraciones de viscosidad. La fila (a) corresponde a tres materiales con idéntica viscosidad y por lo tanto se comporta de forma isótropa. En el modelo de la columna (b) el material blanco es cinco veces más viscoso que el resto. A medida que el contraste de viscosidades aumenta en los casos (c) y (d), con contrastes de 10 y 100 respectivamente, la inestabilidad generada es cada vez más asimétrica. Este ejemplo cualitativo nos permite mostrar como el comportamiento complejo del sistema es reproducido por el modelo.

Ejemplo 2: Inestabilidades en 3D. Dos ejemplos de inestabilidades en tres dimensiones nos permiten analizar el comportamiento del modelo en dos situaciones distintas. Primero, una configuración similar a la del caso anterior en 2D muestra como el mismo efecto observado se obtiene también en tres dimensiones. El segundo ejemplo está compuesto por estratos horizontales. Ambos dominios son cubos. La configuración del primer ejemplo es similar a la del caso anterior, el material superior es mas denso que los inferiores, que tienen distinta viscosidad entre si. La interfase inicial entre el material superior y los dos inferiores tiene una perturbación sinusoidal para inducir la inestabilidad en el centro horizontal del dominio. La Figura 4.13 muestra la disposición de los materiales durante la evolución del modelo. Debido a la jerarquía entre los *level sets*, la interfase vertical sólo afecta debajo de la superficie roja. En el panel (b) se muestra el mismo momento desde una perspectiva distinta para facilitar su comparación con el modelo en dos dimensiones (c) con las mismas viscosidades. El segundo ejemplo involucra cinco materiales distintos. Las propiedades físicas de los mismos se describe en la Tabla 4.2. La configuración inicial y dos estados intermedios durante la evolución se muestra en la Figura 4.14. En este caso el material inferior, con menor densidad, induce la deformación de las capas superiores. Las secciones verticales del modelo muestran la evolución de la deformación. Estos dos ejemplos en 3D muestran como el flujo se resuelve cuando i) existen puntos triples, donde dos interfases se juntan dentro de un elemento y ii) cuando varias interfaces son paralelas dentro de un elemento y son transportadas manteniendo el paralelismo. Ambos casos se comportan consistentemente.

Adaptatividad de la malla

La precisión de la solución obtenida está relacionada con la discretización del dominio (la malla) utilizada. En problemas geodinámicos es común que alguna cantidad de interés tenga un tamaño pequeño con respecto al tamaño del dominio. Además, la ubicación de la cantidad de interés puede variar con el tiempo. Como la descripción del modelo es Euleriana, o bien se refina la malla por donde se espera que se necesite mayor detalle o se adopta un esquema dinámico que modifique la malla de acuerdo con las necesidades en cada momento. La primera opción es estática, la misma malla será utilizada durante toda la simulación, mientras que la segunda es dinámica en el sentido que la malla será modificada en cada momento para tener más detalle allí donde sea necesario. En este trabajo se ha desarrollado un esquema simple pero efectivo de adaptación de la malla basado en las funciones *level set* utilizadas para describir las interfaces entre elementos. El algoritmo se basa en una malla grosera inicial, que se irá refinando en cada paso solamente en los elementos cortados por

las interfases. Este procedimiento se repite en forma recursiva una cantidad fija de veces, llamado nivel de refinamiento d. El tamaño aproximado de elemento en las regiones finas de la malla será el del elemento de la malla base dividido por 4^d. El pseudo código del algoritmo de refinamiento está descrito en el Algoritmo 3. En la Figura 4.15 se puede ver como la parte fina de la malla sigue fielmente la posición de las interfases entre materiales. En este caso se utiliza un nivel de refinamiento $d = 3$. En la Figura 4.16 se comparan distintos niveles de refinamiento de la malla desde $d = 0$ hasta $d = 5$. Se puede observar como la jerarquía entre interfaces es respetada por el esquema de refinamiento. Por último, en la Figura 4.17 se compara un estado intermedio en la simulación de cuatro modelos con distinto nivel de refinamiento. La suavidad y precisión de las interfaces generadas se incrementan con el nivel de refinamiento. Pero las mejoras no se restringen a eso, sino que también se mejora la evolución de las interfaces: en la parte inferior izquierda de los paneles (a) y (b) de la Figura 4.17 el material verde desapareció. Esto no se debe a que la malla no es capaz de describirlo, los elementos gruesos pueden definir la posición de la interfaz, sino que está relacionado con la precisión de la solución mécanica obtenida.

Ensamblado de matrices ralas

El ensamblado de matrices ralas es una operación crucial dentro del ambiente de los Elementos Finitos. Esta operación puede resultar un cuello de botella, deteriorando el tiempo de ejecución si las condiciones son desfavorables. Un escenario donde el ensamblado resulta costoso es, por ejemplo, un problema de flujo multifase. En éste, varias matrices deben ser ensambladas en cada paso pero, debido a los grados de libertad enriquecidos que se crean y destruyen dinámicamente, la estructura de la matriz varía en cada paso. En esta sección se analiza el procedimiento de ensamblado de matrices en Matlab. Además se propone un algoritmo que presenta mejores resultados que la función propia de Matlab tanto en número de accesos a memoria como en tiempo de ejecución.

Almacenamiento de matrices ralas

En Matlab las matrices ralas se almacenan en el formato comprimido por columas[3] (Mathworks, 2006). Este formato está basado en tres vectores `pr`, `ir`, y `jc`. Una matriz K compuesta de m filas y n columnas, con `nnz` coeficientes distintos de cero es almacenada de la siguiente manera: 1) el vector de reales `pr` de longitud `nnz` contiene el valor de los coeficientes no nulos a_{ij} ordenados por columnas; 2) el

[3]Compressed Sparse Row format (CSR)

vector de enteros `ir` con longitud `nnz` contiene las filas de lada elemento de `pr` y, 3) el vector de enteros `jc` con longitud $n+1$ contiene punteros al comienzo de cada columna en `pr` y `ir`. La última posición de `jc` contiene el número de elementos no nulos `nnz`. Este esquema de almacenamiento requiere que, al insertar un nuevo coeficiente, se respete su posición en `pr`. Si la posición correspondiente se encuentra al comienzo de `pr`, será necesario mover grandes bloques de memoria para obtener el espacio en donde se debe realizar la inserción. En este contexto se define el *Costo* de una inserción como la cantidad de coeficientes que se deben mover para realizar una inserción.

Influencia de la numeración de los nodos

El Costo del ensamblado de una matriz depende del orden en el que se agreguen los coeficientes. Por lo tanto la numeración de los nodos y de los elementos tendrá gran influencia en el Costo total del ensamblado. Diferentes algoritmos han sido propuestos para minimizar el ancho de banda de una matriz (por ejemplo Akhras, 1987; Boutora et al., 2007; Cuthill and McKee, 1969; Kaveh, 1993; Lai, 1998). Estos mismos algoritmos mejoran Costo de ensamblado. En este trabajo se utilizará el clásico algoritmo de Cuthill–McKee (RCM) como herramienta para estudiar la influencia de la numeración en el ensamblado. Se considera el siguiente código Matlab

```
for e = 1:numberOfElements
   Te = T(e,:);
   Ke = calculateElementalMatrix( e );
   K(Te,Te) = K(Te,Te) + Ke;
end
```

donde `Ke` es la matriz elemental, `K` la matriz global, `T` el vector de conectividades y `Te` contiene la numeración global de los nodos del elemento `e`. La influencia de la numeración es evaluada calculando el Costo de ensamblado de matrices generadas por distintas mallas. La Figura 4.18 muestra el costo de la inserción de cada matriz elemental durante el proceso de ensamblado de una matriz global. El panel (a) corresponde al caso donde no se ha aplicado el algoritmo de ordenación. En este caso, ordenando los nodos mediante el algoritmo RCM la cantidad de movimientos de memoria requeridos durante el ensamblado se redujo en un factor de 7. En la Tabla 4.3 se compara el Costo de ensamblado de distintas mallas con y sin renumerado de nodos.

Inserción por paquetes

Llamamos inserción por paquetes a una estrategia en donde varios coeficientes son insertados en una única operación de alto nivel. Esto permite ubicar simultáneamente la posición de varios coeficientes en el vector `pr` y así reducir el número de movimientos en memoria. Un agrupamiento natural en la implementación del Método de Elementos Finitos está definido por las matrices elementales ya que los elementos son procesados uno a uno. Llamamos inserción elemento a elemento o EbE al algoritmo que contempla este nivel de agrupamiento. La idea es ubicar todas las posiciones necesarias para la inserción de todos los coeficientes del elemento y luego con esta información, minimizar los movimientos en memoria necesarios. El pseudo código del algoritmo EbE se muestra en el Algoritmo 4.

Ejemplos de ensamblado

En esta sección se analizan las propiedades del algoritmo propuesto en la sección anterior, comparándolo con el algoritmo de inserción simple de Matlab. En la Figura 4.19 se comparan los costos de ambos algoritmos para distintas mallas. En todos los casos se elige la mejor numeración de elementos y nodos disponible. El Costo de ensamblado usando el algoritmo EbE es menor en todos los casos probados, en algunos casos llegando a reducir más de 20 veces el Costo generado. Ya que la finalidad de este análisis es reducir los tiempos de ejecución, además de analizar Costos, se compara los tiempos de cálculo que lleva ensamblar matrices con ambos algoritmos. En la Figura 4.20 se muestra el tiempo de cada inserción elemental durante el proceso de ensamblado. El tiempo total de ensamblado está representado por el área bajo la curva. Al igual que con el Costo, el tiempo de ensamblado es menor con el algoritmo EbE en todos los casos.

Evolución de la litosfera oceánica

La litosfera oceánica es creada continuamente en las dorsales oceánicas, donde dos placas se mueve lateralmente, alejándose de la dorsal. A medida que la distancia a la dorsal aumenta, la litosfera se enfría y se hace más densa debido a la contracción térmica. Este enfriamiento se refleja en la dependencia de la batimetría y de flujo de calor superficial en la edad de la litosfera (McKenzie, 1967; Parsons and Sclater, 1977). Para placas con edad menor que 70 Ma ambas señales decrecen linealmente con $\sqrt{t}$, consistentemente con las predicciones del modelo *Half–Space Cooling* (HSC) (Turcotte and Oxburgh, 1967). Este modelo se basa en un enfriamiento puramente

conductivo en una placa rígida de longitud infinita. Sin embargo, cuando las placas oceánicas superan la edad de 70 Ma, la relación de los observables con la edad se interrumpe y ambas señales toman valores prácticamente constantes (Parsons and Sclater, 1977; Schroeder, 1984; Stein and Stein, 1992). Como estas señales reflejan el enfriamiento litosférico, sus valores constantes implican un comportamiento similar en la estructura térmica de la placa. El *modelo de placa* (McKenzie, 1967) es capaz de reproducir este comportamiento, sin embargo no brinda ninguna explicación física al hecho de que la placa oceánica deje de enfriarse. Una de las propuestas que intentan explicar de dónde proviene el calor extra necesario para evitar el enfriamiento es la existencia de pequeñas celdas convectivas actuando en la base de la litosfera (Parsons and Sclater, 1977; Parsons and McKenzie, 1978; Yuen and Fleitout, 1985). En este capítulo se estudiara este proceso de convección en pequeña escala y la influencia parámetros reológicos y físicos sobre él. Se prestará especial importancia en i) las señales de batimetría y flujo de calor superficial generadas, ii) el uso de valores para los parámetros físicos compatibles con los valores brindados por estudios de laboratorio.

Modelo físico

El modelo utilizado es el descrito en el Capitulo 2. El modelo se complementa con un modelo de fusión parcial de las rocas en la dorsal y un modelo de deshidratación. Ésta genera diferentes dominios químicos dentro de la litosfera oceánica de acuerdo con el contenido de agua. El dominio "seco" posee una viscosidad uno o dos órdenes de magnitud mayor que el dominio "húmedo". El modelo de fusión parcial está determinado en la ecuación (5.3). Asumiendo un decrecimiento lineal del contenido de agua con el grado de fusión, el primero queda determinado según la ecuación (5.4).

Observables geofísicos

Batimetría. Las estimaciones de batimetría son realizadas asumiendo un modelo de isostasia local, es decir, la masa por unidad de área de una columna vertical se compara con un valor de referencia, usualmente tomado en la dorsal. El cálculo de la isostasia local se realiza según Jarvis and Peltier (1982), como se indica en la ecuación (5.6).

Topografía dinámica. La componente vertical del flujo en el manto puede generar variaciones en la topografía, llamadas topografía dinámica para distinguirlas de la topografía generada por compensación isostática. De la misma manera que

McKenzie (1977), la topografía dinámica se estima según la ecuación (5.7).

Velocidades sísmicas El cáclulo de las velocidades sísmicas [$V_p^2\rho = K_S + 4/3G$ and $V_s^2\rho = G$] se basa en el modulo elástico de cada fase mineral estable, en la densidad de la roca a la temperatura y presión de interés, y en estimaciones del componente de atenuación anelastico. El cálculo de estas propiedades se realiza mediante el proceso de minimización de la energía libre utilizando el método propuesto por Connolly (2005). Los efectos anelásticos son calculados usando las ecuaciones (5.8) y (5.9) según Karato (1993); Afonso et al. (2008).

Model setup and boundary conditions

El dominio del modelo es un rectángulo que representa un plano vertical paralelo al movimiento de la placa como se muestra en la Figura 5.2a. La malla compuesta de aproximadamente 13000 elementos representa una sección de 660 km de profundidad. La corteza oceánica no juega ningún papel en el proceso de convección de pequeña escala y por lo tanto no está incluida en el modelo. La temperatura está impuesta en los lados superior e inferior del modelo, mientras que en los laterales se impone flujo cero. El campo térmico inicial se calcula usando el modelo HSC según la ecuación (5.10) (Schubert et al., 2001).

Resultados

Esta sección está dividida en dos partes, en la primera se describe las características principales de la convección de pequeña escala y sus efectos en la estructura térmica de la litosfera y el manto superior. En la segunda parte se estudia la influencia de los principales parámetros y procesos físicos en la evolución de dicha convección.

Características generales. En esta sección se muestra un ejemplo sencillo donde la convección de pequeña escala está bien desarrollada. La velocidad superficial está impuesta a 3.5 cm yr^{-1} comparable con las brindadas por Gripp and Gordon (2002) para algunas placas oceánicas. Este primer ejemplo incluye como única fuente de calor la componente adiabática y su reología está basada en el mecanismo de deformación por difusión (Newtoniano) sin tener en cuenta el contenido de agua de las rocas. Los parámetros reológicos utilizados son una energía de activación $E = 120$ kJ mol^{-1}, un volumen de activación $V = 4 \times 10^{-6}$ m^3 mol^{-1}, y un factor pre exponencial $A_D = 7.6 \times 10^{-16}$ Pa^{-1} s^{-1}. Valores similares a estos han sido utilizados en trabajos previos (van Hunen et al., 2003; Huang and Zhong, 2005; van

Hunen et al., 2005; Huang et al., 2003), lo que nos permite realizar comparaciones cuantitativas de los resultados. Sin embargo estos valores están fuera de los rangos estimados en estudios de laboratorio (Karato and Wu, 1993; Hirth and Kohlstedt, 2003).

En la Figura 5.3a se muestra la estructura térmica obtenida luego de alcanzar un estado estadísticamente estacionario. Las inestabilidades se forman en la parte inferior de la litosfera oceánica cuando ésta llega a aproximadamente los 60 Ma de edad. A edades más tempranas, la evolución térmica sigue el enfriamiento conductivo inicial. El campo de viscosidad asociado al campo térmico se muestra en la Figura 5.3b. Para que las inestabilidades se produzcan es necesario que la viscosidad en el manto sublitosférico sea menor a 10^{20} Pa s. Valores similares han sido obtenidos por Korenaga (2002); Huang and Zhong (2005); van Hunen et al. (2005). La convección de pequeña escala reduce la velocidad de enfriamiento litosférico cuando ésta se compara con la predicha por el modelo HSC. El mismo proceso enfría el manto sublitsférico como se ilustra en la Figura 5.4, donde se comparan distintos perfiles de temperatura durante la evolución del sistema. Durante la simulación se remueven aproximadamente 50 km de material inestable de la base de la litosfera. El enfriamiento del manto superior, de aproximadamente 200 K, no debe ser tomado como valor de referencia, ya que nuestro modelo no incluye el efecto del calor latente relacionado con los cambios de fase mineralógico.

Influencia de los parámetros físicos. Primero se estudia la influencia de la generación de calor por desintegración de elementos radioactivos y por difusión viscosa. Para esto se ejecutan cuatro modelos con idénticos parámetros según la Tabla 5.1. Los grosores litosféricos obtenidos son estimados usando la isoterma de 1603 K. En la Figura 5.5, donde se muestra el resultado de los cuatro modelos, se puede observar que el calor radiogénico ejerce una gran influencia en la evolución litosférica, mientras que el calor por difusión es despreciable.

Trabajos anteriores han encontrado una correlación entre la edad en donde comienzan las inestabilidades y la velocidad de la placa (Houseman, 1983; Huang et al., 2003; van Hunen et al., 2003). Para probar esta hipótesis, hemos hecho cinco modelos variando la velocidad en 2, 4, 6, 8, y 10 cm yr^{-1}. La primer inestabilidad se produjo a las edades 28, 43, 70, 72, y 80 My respectivamente. Estas observaciones son similares a las obtenidas por van Hunen et al. (2003) y Houseman (1983).

Teniendo en cuenta el efecto reológico de la deshidratación de las rocas en la dorsal, la batimetría y la producción de calor superficial reproducen fielmente la asíntota a valores constantes cuando la litosferas alcanza la edad de 70 Ma,

como se muestra en la Figura 5.10. Variando la profundidad a la que comienza la fusión parcial se obtienen distintos grosores litosféricos. Los perfiles de viscosidad obtenidos en cada caso se muestran en la Figura 5.10. Las transiciones mineralógical relacionadas con los minerales ricos en aluminio (plagioclasa–espinela–granate) no afectan la evolución del modelo.

Conclusiones

Se ha realizado un estudio de la evolución de la litosfera oceánica y su relación con la convección de pequeña escala. Nuestros resultados se resumen en los siguientes puntos:

- Se estudió la influencia de tres fuentes de calor. El calor por difusión viscosa no tiene influencia sobre la generación de celdas convectivas. En cambio el calor de origen radiogénico favorece el desarrollo de las celdas disminuyendo drásticamente el grosor litosférico. El efecto del calor adiabático es el de disminuir contrastes térmicos y en consecuencia, reducir la efectividad de celdas convectivas para erosionar la litosfera.

- Para la generación de celdas convectivas de pequeña escala es necesaria una región de baja viscosidad ($< 10^{20}$ Pa s) bajo la litosfera.

- Las celdas convectivas pueden ser generadas usando parámetros reológicos compatibles con los experimentos de laboratorio. Sin embargo la activación de la convección de pequeña escala no implica que las señales superficiales lleguen a tener valores constantes.

- Los transisiones mineralógicas de los minerales ricos en aluminio no parecen afectar a la evolución de la litosfera oceánica.

- La deshidratación de las rocas del manto, debido a la fusión parcial sufrida en las dorsales parece ser la responsable de la caída de la batimetría y el flujo de calor a valores constantes.

Desprendimiento de un *slab* y ángulo de subducción

Desprendimiento de un *slab*

El desprendimiento de la litosfera oceánica subducida (*slab*) ha sido propuesto por numerosos autores para explicar la falta de sismicidad a profundidades intermedias en algunas zonas de subducción (e.g. Fuchs et al., 1979; Xu et al., 2000; Blanckenburg and Davies, 1995; Ioane and Lillie, 2004). Se espera que este proceso tenga consecuencias superficiales tales como un aumento en la elevación (e.g. Westaway, 1993; Buiter et al., 2002; Gerya et al., 2004), magmatismo, metamorfismo (Blanckenburg and Davies, 1995; Davies and von Blanckenburg, 1995), etc. En esta sección se presenta un estudio numérico del proceso de desprendimiento. Se estudia la influencia de distintos parámetros en el proceso y se predicen consecuencias superficiales. La configuración inicial del modelo es la mostrada en la Figura 6.1b, ésta corresponde a una zona de subducción donde el slab alcanza los 400 km de profundidad. Se supone que el proceso de desprendimiento comienza una vez que la convergencia se detiene, por lo tanto se impone una velocidad superficial nula.

Resultados

La influencia de los distintos parámetros es estudiada comparando cada modelo de la Tabla 6.1 con un modelo de referencia. La evolución del modelo de referencia se muestra en la Figura 6.3. El desprendimiento del *slab* tiene una primera etapa de difusión térmica en donde éste incrementa su ángulo. Luego, un rápido proceso de estrechamiento en la litosfera subducida termina con su desprendimiento mecánico. Este período está caracterizado por una alta velocidad de deformación y un alto calentamiento viscoso. Los valores máximos obtenidos en cada modelo de velocidad de deformación se muestran en la Tabla 6.2. La evolución de la topografía generada por el desprendimiento se muestra en la Figura 6.4. Se alcanza un máximo de 1.5 km de elevación en un área localizada de unos 300 km de extensión. El calentamiento por difusión viscosa ejerce un gran efecto sobre el proceso de desprendimiento, ya que favorece la concentración de esfuerzos. Si este término no es tenido en cuenta el desprendimiento se retarda en un 50%. El calentamiento adiabático tiene el mismo efecto que el explicado anteriormente: actúa como estabilizador, decreciendo los contrastes térmicos.

Discusión

El desprendimiento de la litosfera subducida a sido propuesto en varios trabajos para explicar un adelgazamiento litosférico en una zona de colisión continente–continente (Molinaro et al., 2005; Ioane and Lillie, 2004; Schoonmaker et al., 2005). Nuestros resultados, y otros trabajos similares, no soportan esa hipótesis ya que los grosores litosféricos resultantes luego del desprendimiento siempre se incrementan. En la Figura 6.6 se muestran las dos evoluciones propuestas para el desprendimiento. Es posible que el resultado de los modelos se vea afectado por una reología demasiado simplificada (viscosa pura) o por la ausencia de la falla entre placas. Es necesario realizar nuevos estudios para investigar la influencia de estos elementos.

Conclusiones

En esta tesis se describe todo el proceso de modelado de la litosfera oceánica y el manto. Se expone la física que gobierna el problema, las ecuaciones que describen su comportamiento y los métodos numéricos utilizados para resolver estas ecuaciones. Además se brinda una implementación computacional de estos métodos. La herramienta generada es utilizada para estudia distintos aspectos de la dinámica de la litosfera oceánica: su estabilidad a lo largo del tiempo, la relación entre la velocidad de convergencia y la geometría de las zonas de subducción y la influencia de distintos parámetros en el desprendimiento de la litosfera subducida.

El modelo físico propuesto está basado en las ecuaciones de conservación de energía, masa y momento. Éste incluye comportamiento reológicos no lineales basados en los mecanismos de deformación que actúan en el manto. Las propiedades físicas de las rocas se calculan en función de la temperatura y la presión. Las transformaciones minerales más importantes están incluidas en el modelo, así como las tres fuentes de calor principales.

Para la resolución de las ecuaciones se han utilizado diversas técnicas numéricas. La base de nuestro modelo es el Método de los Elementos Finitos eXtendido (X–FEM), usado por primera vez en aplicaciones geofísicas. El método permite describir la ubicación de fases materiales en un entorno Euleriano, agregando dos nuevos ingredientes a los Elementos Finitos tradicionales: *level sets* y un enriquecimiento de la solución. La aplicación de *level sets* a problemas geofísicos a sido propuesta por dos trabajos simultáneos (Zlotnik et al., 2007a; Gross et al., 2007).

Para tratar con determinados aspectos de nuestro modelo se han desarrollado o extendido algunas técnicas numéricas. El Método de los Elementos Finitos

eXtendido en su versión standard es capaz de tratar con dos materiales distintos. Como parte de esta tesis, se ha propuesto una mejora del método que permite tratar cualquier número de materiales. Por otro lado, en modelos transitorios en donde en cada paso temporal es necesario el ensamblado de varias matrices, el algoritmo de ensamblado repercute en el tiempo total de ejecución. Aquí se presenta un estudio de los parámetros que afectan al ensamblado y se propone un algoritmo que mejora la cantidad de operaciones de memoria y el tiempo de ensamblado con respecto a las funciones brindadas por Matlab. Con este procedimiento el tiempo de ejecución de nuestro modelo se redujo en un 60% y el tiempo de ensamblado se redujo a la mitad.

Usando la herramienta desarrollada hemos estudiado la evolución de la litosfera oceánica en el tiempo y su relación con la convección de pequeña escala. Usando parámetros físicos y reológicos compatibles con los estudios de laboratorio, hemos reproducido los observables geofísicos superficiales (batimetría y flujo de calor) y profundos (velocidades sísmicas). Nuestros resultados muestran que la caída de la batimetría y flujo de calor a valores constantes está relacionada con la estratificación de la litosfera oceánica debida a la deshidratación de las rocas en las dorsales.

Los estudios de desprendimiento de la placa oceánica subducida muestran que el proceso es factible físicamente y que sus respuestas superficiales son apreciables geológicamente. Se destaca la importancia del calor por disipación viscosa que acelera el proceso de desprendimiento y de hundimiento de la placa. A pesar de que varios autores han usado este proceso para explicar un adelgazamiento litosférico, nuestros modelos predicen un engrosamiento. Esta diferencia puede deberse a la reología simplificada de nuestro modelos o a la falta de un buen modelo para la falla entre las placas.

Para mostrar la flexibilidad de nuestra implementación, presentamos dos modelos en tres dimensiones. Primero, inestabilidades gravitacionales nos permiten mostrar que los Elementos Finitos eXtendidos pueden ser fácilmente usados en 3D. Luego un modelo simple de manto global nos permite mostrar un dominio esférico en donde se imponen condiciones de contorno complejas. Los resultados de estos dos modelos se muestran en las Figuras 7.1, 7.2 y 7.3.

Trabajo futuro

Los ejemplos previos nos muestran que el desarrollo de un código completo en tres dimensiones es una interesante línea de trabajo. Otra posibilidad es la extensión de el modelo físico para incorporar la compresibilidad de los materiales. En las

condiciones del manto terrestre la presión es suficiente como para considerar a las rocas como compresibles. Una tercera continuaci'on interesante es la combinación de un código dinámico, como el que aquí se presenta, con un código petrológico como PerpleX (Connolly, 2005). Esto permitiría conocer las propiedades físicas de los materiales con una certeza mucho mayor. Cualquiera de las dos líneas de trabajo propuestas generará un código que demandará un gran poder computacional. Por lo tanto un requisito fundamental será un diseño que permita la ejecución en clusters o en máquinas paralelas.

Bibliography

G. A. Abers, P. E. van Keken, E. A. Kneller, A. Ferris, and J. C. Stachnik. The thermal structure of subduction zones constrained by seismic imaging: implications for slab dehydration and wedge flow. *Earth Planet. Sci. Lett.*, 241: 387–397, 2006.

J. C. Afonso, G. Ranalli, and M. Fernández. Thermal expansivity and elastic properties of the lithospheric mantle: results from mineral physics of composites. *Phys. Earth Planet. Inter.*, 149:279–306, 2005.

J. C. Afonso, G. Ranalli, and M. Fernàndez. Density structure and buoyancy of the oceanic lithosphere revisited. *Geophys. Res. Lett.*, 34:L10302, doi:10.1029/2007GL029515, 2007.

J. C. Afonso, M. Fernàndez, G. Ranalli, W. L. Griffin, and J. A. D. Connolly. Integrated geophysical-petrological modelling of the lithospheric-sublithospheric upper mantle: methodology and applications. *Geochem. Geophys. Geosyst.*, -:in press, 2008. doi: 10.1029/2007GC001834.

M. E. Akaogi, E. Ito, and A. Navrotsky. Olivine-modified spinel transitions in system Mg_2SiO_4-Fe_2SiO_4: calorimetric measurements, thermomechanical calculations, and geophysical implications. *J. Geophys. Res.*, 94:15671–15685, 1989.

G. Akhras. A new node renumbering algorithm for bandwidth reduction. *International Journal for Numerical Methods in Engineering*, 24(9):1823–1824, 1987.

O. L Anderson, H. Oda, and D. Isaak. A model for the computation of thermal expansivity at high compression and high temperatures: MgO as an example. *Geophys. Res. Lett.*, 19:1987–1990, 1992.

D. Arcay, E. Tric, and M. P. Doin. Numerical simulations of subduction zones. Effect of slab dehydration on the mantle wedge dynamics. *Phys. Earth Planet. Inter.*, 149(1–2):133–153, 2005.

G. D. Astis, P. D. Kempton, A. Peccerillo, and T. W. Wu. Trace element and isotopic variations from Mt. Vulture to Campanian volcanoes: constraints for slab detachment and mantle inflow beneath southern Italy. *Contrib. Mineral Petrol.*, 151:331–351, 2006.

I. Babuška. Error-bounds for finite element method. *Num. Math.*, 16:322–333, 1970.

G. K. Batchelor. *Fluid Dynamics*. Cambridge University Press, UK, 1967.

J. R. Baumgardner. Three–dimensional treatment of convective flow in the Earth's mantle. *J. Stat. Phys*, 39:501–511, 1985.

T. Belytschko and T. Black. Elastic crack growth in finite elements with minimal remeshing. *International Journal for Numerical Methods in Engineering*, 45(5): 601–620, 1999.

D. Bercovici. The generation of plate tectonics from mantle convection. *Earth Planet. Sci. Lett.*, 205:107–121, 2003.

F. Von Blanckenburg and J. H. Davies. Slab breakoff: a model for syncollisional magmatism and tectonics in the Alps. *Tectonics*, 14:120–131, 1995.

Y. Boutora, N. Takorabet, R. Ibtiouen, and Mezani S. A new method for minimizing the bandwidth and profile of square matrices for triangular finite elements mesh. *Ieee Transactions on Magnetics*, 43(4):1513–1516, 2007.

W. F. Brace and D. L. Kohlstedt. Limits on lithospheric stress imposed by laboratory experiments. *J. Geophys. Res.*, 85:6248–6252, 1980.

F. Brezzi. On the existence, uniqueness and approximation of saddle- point problems arising from lagrangian multipliers. *RAIRO Anal. Numér.*, 8(R–2):129–151, 1974.

F. Brezzi and M. Fortin. *Mixed and hybrid finite element methods*. Springer-Verlag, New York, second edition, 1991.

S. J. H. Buiter, R. Govers, and M. J. R. Wortel. Two–dimensional simulations of surface deformation caused by slab detachment. *Tectonophysycs*, 354:195–210, 2002.

F. H. Busse. Fundamentals of thermal convection. In W. R. Peltier, editor, *Mantle convection. Plate tectonics and global dynamics*, The fluid mechanics of astrophysics and geophysics, volume 2, pages 23–95. Gordon and breach science publishers, Montreux, Switzerland, 1989.

J. Chessa and T. Belytschko. An extended finite element method for two–phase fluids. *Transactions of the ASME*, pages 10–17, 2003.

A. Chopelas. Thermal expansivity of mantle relevant magnesium silicates derived from vibrational spectroscopy at high pressure. *Am. Miner.*, 85:270–278, 2000.

C. Clauser and E. Huenges. Thermal conductivity of rocks and minerals. In T. Ahren, editor, *Rock Physics and Phase Relations*, AGU Reference Shelf, part 3, pages 105–126. AGU, Washington DC, third edition, 1995.

R. E. Cohen. High–Performance Computing Requirements for the Computational Solid Earth Sciences. Technical report, Geophysical Laboratory, Carnegie Institution of Washington, 2005. 94 pp.

J. A. D. Connolly. Computation of phase equilibria by linear programming: A tool for geodynamic modeling and its application to subduction zone decarbonation. *Earth Planet. Sci. Lett.*, 236:524–541, 2005.

N. W. E. Curlet. Experimental and numerical modeling of three dimansional natural convection in an enclousure. *Phys. Earth Planet. Int.*, 125:45–64, 2001.

E. Cuthill and J. McKee. Reducing the bandwidth of sparse symmetric matrices. In *Proceedings of the 1969 24th national conference*, pages 157–172, New York, 1969. ACM Press.

G. F. Davies. Ocean bathymetry and mantle convection: 1. large scale flow and hotspots. *J. Geophys. Res.*, 93:10467–10480, 1988.

J. H. Davies and F. von Blanckenburg. Slab breakoff: a model of lithosphere detachment and its test in the magmatism and deformation of collisional orogens. *Earth Planet. Sci. Lett.*, 129:85–102, 1995.

N. L. Dobretsov and A. G. Kirdyashkin. *Deep–Level Geodynamics*. A.A.BALKEMA, 1998.

J. Donea and A. Huerta. *Finite Element Methods for Flow Problems*. Wiley, Chichester, West Sussex PO19 8SQ, England, 2002.

C. Dumoulin, M. P. Doin, and L. Fleitout. Numerical simulations of the cooling of an oceanic lithosphere above a convective mantle. *Phys. Earth Planet. Int.*, 125: 45–64, 2001.

C. Faccenna, O. Bellier, L. Martinod, C. Piromallo, and V. Regard. Slab detachment beneath eastern Anatolia: A possible cause for the formation of the North Anatolian fault. *Earth Planet. Sci. Lett.*, 242:85–97, 2006.

U. H. Faul and I. Jackson. The seismological signature of temperature and grain size variations in the upper mantle. *Earth Planet. Sci. Lett.*, 234:119–134, 2005.

Y. Fei. Thermal expansion. In T. Ahren, editor, *Rock Physics and Phase Relations*, AGU Reference Shelf, part 3, pages 29–44. AGU, Washington DC, third edition, 1995.

D. Forsyth and S. Uyeda. On the relative importance in the driving forces of plate motion. *J. Roy. Astron. Soc.*, 43:163–200, 1975.

K. Fuchs, K.-P. Bonjer, G. Bock, I. Cornea, C. Radu, D. Enescu, D. Jianu, A. Nourescu, G. Merkler, T.Moldoveanu, and G. Tudorache. The Romanian earthquake of March 4, 1977: II. Aftershocks and migration of seismic activity. *Tectonophysics*, 53:225–247, 1979.

K. P. Furlong, D. S. Chapman, and P. W. Alfeld. Thermal modeling of the geometry of subduction with implications for the tectonics of the overriding plate. *J. Geophys. Res.*, 87:1786–1802, 1982.

C. W. Gable, R. J. O'Connell, and B. J. Travis. Convection in three dimensions with surface plates: generation of toroidal flow. *J. Geophys. Res.*, 96:8391–8405, 1991.

A. Gerstenberger and W. A. Wall. An extended finite element method /lagrange multiplier based approach for fluid-structure interaction. *Computer Methods in Applied Mechanics and Engineering*, in press:(doi:10.1016/j.cma.2007.07.002), 2007.

T. V. Gerya and D. A. Yuen. Characteristics–based marker–in–cell method with conservative finite–differences schemes for modeling geological flows with strongly variable transport properties. *Phys. Earth Planet. Inter.*, 140(4):293–318, 2003.

T. V. Gerya and D. A. Yuen. Robust characteristics method for modelling multiphase visco-elasto-plastic thermo-mechanical problems. *Phys. Earth Planet. Inter.*, 163:83–105, 2007.

T. V. Gerya, D. A. Yuen, and W. V. Maresch. Thermomechanical modelling of slab detachment. *Earth Planet. Sci. Lett.*, 226:101–116, 2004.

W. Gorczyk, T. V. Gerya, J. A. D. Connolly, D. A. Yuen, and M. Rudolph. Large–scale rigid–body rotation in the mantle wedge and its implications for seismic tomography. *Geochem. Geophys. Geosyst.*, 7(5), 2006. doi:10.1029/2005GC001075.

J. C. De Gremaecker. Is the oceanic lithosphere elastic or viscous? *J. Geophys. Res.*, 82:2001–2004, 1977.

A. E. Gripp and R. G. Gordon. Young tracks of hotspots and current plate velocities. *Geophys. J. Int.*, 150:321–361, 2002.

L. Gross, L. Bourgouin, A. J. Hale, and H. Mühlhaus. Interface modeling in incompressible media using level sets in Escript. *Phys. Earth Planet. Inter.*, 163: 23–34, Aug 2007.

A. Guest, G. Schubert, and C. W. Gable. The phase–boundary between α-Mg_2SiO_4 and β-Mg_2SiO_4 determined by in–situ X–ray–observation. *Science*, 265:1202–1203, 1994.

A. Guest, G. Schubert, and C. W. Gable. Stresses along the metastable wedge of olivine in a subducting slab: possible explanation for the Tonga double seismic layer. *Phys. Earth Planet. Inter.*, 149:187–200, 2004.

M. Gurnis, C. Eloy, and S. Zhong. Free–surface formulation of mantle convection – II. implication for subduction–zone observables. *Geophys. J. Int.*, 127:719–727, 1996.

B. H. Hager and M. A. Richards. Long wavelength variations in Earth's geoid: physical models and dynamical implications. *Philos. Trans. R. Soc. Lond.*, 328: 309–327, 1989.

N. A. Haskell. The viscosity of the asthenosphere. *Am. J. Sci.*, 33:22–28, 1937.

A. Heuret and S. Lallemand. Plate motions, slab dynamics and back–arc deformation. *Phys. Earth Planet. Inter.*, 149:31–51, 2005.

G. Hirth and D. Kohlstedt. Water in the oceanic upper mantle: implications for rheology, melt extraction and the evolution of the lithosphere. *Earth Planet. Sci. Lett.*, 144:93–108, 1996.

G. Hirth and D. Kohlstedt. Rheology of the upper mantle and the mantle wedge: A view from the experimentalists. In J. Eiler, editor, *Inside the subduction factory, Geophys. Monograph 138, AGU*, pages 83–105. 2003.

A. M. Hofmeister. Mantle values of thermal conductivity and the geotherm from phonon lifetimes. *Science*, 283:1969–1706, 1999.

G. Houseman. Large aspect ratio convection cells in the upper mantle. *Geophys. J. R. Astron. Soc.*, 75:309–334, 1983.

J. Huang and S. Zhong. Sublithospheric small–scale convection and its implications for the residual topography at old ocean basins and the plate model. *J. Geophys. Res.*, 110, 2005. doi:10.1029/2004JB003153.

J. Huang, S. Zhong, and J. van Hunen. Controls on sublithospheric small–scale convection. *J. Geophys. Res.*, 108, 2003. doi:10.1029/2003JB002456.

T. J. R. Hughes. *The Finite Element Method. Linear Static and Dynamic Finite Element Analisis*. Prentice Hall, Englewood Cliffs, New Jersey, 2000.

B. Spernerand D. Ioane and R. J. Lillie. Slab behaviour and its surface expression: New insights from gravity modelling in the SE Carpathians. *Tectonophysics*, 382: 51–84, 2004.

B. Isacks and P. Molnar. Mantle earthquake mechanisms and the sinking of the lithosphere. *Nature*, 223:1121–1124, 1969.

E. Ito and E. Takahashi. Postspinel transformations in the system Mg_2SiO_4—Fe_2SiO_4 and some geophysical implications. *J. Geophys. Res.*, 94:10637–46, 1989.

I. Jackson, J. D. Fitz Gerald, U. H. Faul, and B. H. Tan. Grain-size-sensitive seismic wave attenuation in polycrystalline olivine. *J Geophys. Res.*, 107: NO.B12,1360,doi:10.1029/2001JB001225, 2002.

R. D. Jarrard. Relations among subduction parameters. *Rev. Geophys.*, 24:217–284, 1986.

G. T. Jarvis and W. R. Peltier. Mantle convection as a boundary layer phenomenon. *Geophys. J. R. Astron. Soc.*, 68:389–427, 1982.

C. Jaupart and B. Parsons. Convective instabilities in a varialbe viscosity fluid cooled from above. *Phys. Earth Planet. Inter.*, 39:14–32, 1985.

D.A. Yuen K. Regenauer-Lieb. Rapid conversion of elastic energy into plastic shear heating during incipient necking of the lithosphere. *Geophys. Res. Lett.*, 25:2737 2740, 1998.

M. Kameyama. Acuteman: A multigrid–based mantle convection simulation code and its optimization to the Earth Simulator. *Journal of the Earth Simulator*, 4, 2005.

S. Karato. Does partial melting reduce the creep strength of the upper mantle? *Nature*, 319:309–310, 1986.

S. I. Karato. Importance of anelasticity in the interpretation of seismic tomography. *Geophys. Res. Lett.*, 20:1623–1626, 1993.

S.-I. Karato and P. Wu. Rheology of the upper mantle: a synthesis. *Rev. Science*, 260:771–778, 1993.

T. Katsura and E. Ito. The system Mg_2SiO_4-Fe_2SiO_4 at high pressures and temperatures: Precise determination of stabilities of olivine, modified spinel, and spinel. *J. Geophys. Res.*, 94:15663–15670, 1989.

T. Katsura, H. Yamada, O. Nishikawa, M. Song, A. Kubo, T. Shinme, S. Yokoshi, Y. Aizawa, T. Yoshino, M. J. Walter, and E. Ito. Olivine-wadsleyite transition in the system $(Mg,Fe)_2SiO_4$. *J. Geophys. Res.*, 109, 2004. doi:10.1029/2003JB002438.

A. Kaveh. Bandwidth reduction of rectangular matrices. *Commun. Numer. Meth. Engrg.*, 9:259–267, 1993.

A. Kaveh and S. M. R. Behfar. Finite element nodal ordering algorithms. *Commun. Numer. Meth. Engrg.*, 11:995–1003, 1995.

S. D. King. Models of mantle viscosity. In T. Ahren, editor, *Rock Physics and Phase Relations*, AGU Reference Shelf, part 3, pages 105–126. AGU, Washington DC, third edition, 1995.

S. D. King, A. Raefsky, and B. H. Hager. ConMan: a vectorizing a finite element code for incompressible two–dimensional convection in the Earth's mantle. *Phys. Earth Planet. Inter.*, 59:195–2007, 1990.

S. H. Kirby. Rheology of the lithosphere. *Rev. Geophys*, 21:1458–1487, 1983.

P. Knupp. Updating meshes on deforming domains: An application of the target-matrix paradigm. *Commun. Numer. Meth. Engrg.*, 2007. In press.

J. Korenaga. On 'steady-state' heat flow and the rheology of oceanic mantle. *Geophys. Res. Lett.*, 29, 2002. doi:10.1029/2002GL016085.

J. Korenaga and T. H. Jordan. Physics of multiscale convection in Earth's mantle: evolution of sublithospheric convection. *J. Geophys. Res.*, 109: doi:10.1029/2003JB002464, 2004.

S. Labrosse and C. Jaupart. Thermal evolution of the Earth: Secular changes and fluctuations of plate characteristics. *Earth Planet. Sci. Lett.*, 260:465–481, 2007.

O. A. Ladyzhenskaya. *The mathematical theory of viscous incompressible flow.* Gordon and Breach Science, New York, 1969.

Y. C. Lai. A three-step renumbering procedure for high-order finite element analysis. *International Journal for Numerical Methods in Engineering*, 41(1):127–135, 1998.

S. Lallemand and A. Heuret. On the relationships between slab dip, back–arc stress, upper plate absolute motion, and crustal nature in subduction zones. *Geochem. Geophys. Geosyst.*, 6(9), 2005. doi:10.1029/2005GC000917.

C. A. Lee, A. Lenardic, C. M. Cooper, F Niu, and A. Levander. The role of chemical boundary layers in regulating the thickness of continental and oceanic thermal boundary layers. *Earth Planet. Sci. Lett.*, 230:379–395, 2005.

R. Lohner. Some useful renumbering strategies for unstructured grids. *International Journal for Numerical Methods in Engineering*, 36(19):3259–3270, 1993.

B. P. Luyendyc. Dips of downgoing lithospheric plates beneath island arcs. *Geological Society of America Bulletin*, 81:3411–3416, 1970.

P. Macera, D. Gasperini, G. Ranalli, and R. Mahatsente. Slab detachment and mantle plume upwelling in subduction zones: An example from the Italian South-Eastern Alps. *Journal of Geodynamics*, 45:32–48, 2008.

A. Maggi, E. Debayle, K. Priestly, and G. Barruol. Multimode surface waveform tomography of the Pacific Ocean: a closer look at the lithospheric cooling signature. *Geophys. J. Int.*, 166:1384–1397, 2006.

D. Mainprice, A. Tommasi, H. Couvy, P. Cordier, and D. J. Frost. Tpressure sensitivity of olivine slip systems and seismic anisotropy of earth's upper mantle. *Nature*, 433:731–733, 2005.

V. C. Manea and M. Gurnis. Subduction zone evolution and low viscosity wedges and channels. *Earth Planet. Sci. Lett.*, 264:22–45, 2007.

G. Marquart and H. Schmeling. Topography and geoid undulations caused by small-scale convection beneath continental lithosphere of variable elastic thickness. *Geophys. J.*, 97:511–527, 1989.

Mathworks. *MATLAB External Interfaces*. The MathWorks, 3 Apple Hill Drive, Natick, MA 01760-2098, release 2006b, for matlab 7.3 edition, September 2006.

R. McCaffrey, P. Molnar, S. Roecker, and Y. Joyodiwiryo. Microearthquake seismicity and fault plane solutions related to arc-continent collision in the eastern Sunda arc, Indonesia. *J. Geophys. Res.*, 90:4511–4528, 1985.

D. McKenzie, J. Jakson, and K. Priestely. Thermal structure of oceanic and continental lithosphere. *Earth Planet. Sci. Lett.*, 233:337–349, 2005.

D. P. McKenzie. Some remarks on heat flow and gravity anomalies. *J. Geophys. Res.*, 72:6261–6273, 1967.

D. P. McKenzie. Surface deformation, gravity anomalies and convection. *Geophys. J. Roy. Astron. Soc.*, 48:211–238, 1977.

D. P. McKenzie, J. M. Roberts, and N. O. Weiss. Convection in the mantle: Towards a numerical simulation. *J. Fluid Mech.*, 62:465–538, 1974.

P.Th. Meijer and M.J.R. Wortel. Temporal variations in the stress field of the aegean region. *Geophys. Res. Lett.*, 23:439–442, 1996.

H. J. Melosh and A. Raefsky. The dynamical origin of subduction zone topography. *Geophys. J. Roy. Astron. Soc.*, 60:333–354, 1980.

N. Moës, M. Cloirec, P. Cartaud, and J. F. Remacle. A computational approach to handle complex microstructure geometries. *Comput. Methods Appl. Mech. Engrg.*, 192:3163–3177, 2003.

M. Molinaro, H. Zeyen, and X. Laurencin. Lithospheric structure beneath the south–eastern Zagros mountains, Iran: recent slab break–off? *Terra Nova*, 17:1–6, 2005.

L. Moresi and V. S. Solomatov. Numerical investigations of 2d convection with large viscosity contrasts. *Phys. Fuids*, 7:2154–2162, 1995.

L. Moresi, S. Zhong, and M. Gurnis. The accuracy of finite element solutions of Stokes' flow with strongly varying viscosity. *Phys. Earth Planet. Inter.*, 97:83–94, 1996.

L. Moresi, S. Quenette, V. Lemiale, C. Mériaux, B. Appelbe, and H.-B. Mühlhaus. Computational approaches to studying non-linear dynamics of the crust and mantle. *Phys. Earth Planet. Inter.*, 163:69–82, 2007.

L. N. Moresi and M. Gurnis. Constraints on lateral strength of slabs from 3–D dynamic flow models. *Earth Planet. Sci. Lett.*, 138:15–28, 1996.

J. P Morgan. The generation of a compositional lithosphere by mid-ocean ridge melting and its effect on subsequent off-axis hotspot upwelling and melting. *Earth Planet. Sci. Lett.*, 146:213–232, 1997.

J. P Morgan and W. H. S. Smith. Flattening of the sea–floor depth–age curve as a response to asthenospheric flow. *Nature*, 359:524–527, 1992.

M. Nettles and A. M. Dziewonski. Radially anisotropic shear-velocity structure of the upper mantle globally and beneath norht america. *J. Geophys. Res.*, 113, 2008. doi: doi:10.1029/2006JB004819.

A. R. Oganov, J. P. Brodholt, and G. D. Price. Ab initio elasticity and thermal equation of state of $MgSiO_3$ perovskite. *Earth Planet. Sci. Lett.*, 184:555–560, 2001.

M.C. Oncescu, V. Burlacu, M. Anghel, and V. Smalbergher. Three-dimensional p-wave velocity image under the carpathian arc. *Tectonophysics*, 106:305–319, 1984.

C. O'Neill, L. Moresi, D. Müller, R. Albert, and F. Dufour. Ellipsis 3d: A particle–in–cell finite–element hybrid code for modelling mantle convection and lithospheric deformation. *Computers & Geosciencies*, 32:1769–1779, 2006.

S. Osher and R. Fedkiw. Level set methods: an overview and some recent results. *Journal of Computational Physics*, 169:463–502, 2001.

S. Osher and J. A. Sethian. Front propagating with curvature dependent speed: algorithms based on Hamilton-Jacobi formulations. *Journal of Computational Physics*, 79:12–49, 1988.

B. Parsons and D. McKenzie. Mantle convection and thermal structure of the plates. *J. Geophys. Res.*, 83:4485–4496, 1978.

B. Parsons and J. G. Sclater. An analysis of the variation of ocean floor bathymetry and heat flow with age. *J. Geophys. Res.*, 82:803–827, 1977.

G. Pascal, J. Dubois, M. Barazangi, B. L. Isacks, and J. Oliver. Seismic velocity anomalies beneath the New Hebrides island arc: evidence for a detached slab in the upper mantle. *Geophysics*, 78:6998–7004, 1973.

G. Ranalli. *Rheology of the Earth*. Chapman and Hall, 2–6 Boundary Row, London, second edition, 1995.

K. Regenauer-Lieb, B. Hobbs, D. A. Yuen, A. Ord, Y. Zhang, H. B. Mühlhaus, and G. Morra. From point defects to plate tectonic faults. *Philosophical Magazine*, 86:3373 – 3392, July 2006.

M. Ritzwoller, N. Shapiro, and S.-J. Zhong. Cooling history of the Pacific lithosphere. *Earth Planet. Sci. Lett.*, 226:69–84, 2004.

D. H. Roeder. Tectonic effects of dip changes on subduction zones. *Am. J. Sci.*, 275:252–264, 1975.

S. J. Ruuth. A diffusion–generated approach to multiphase motion. *Journal of Computational Physics*, 145:166–192, 1998.

H. Schmeling and G. Marquart. The influence of second-scale convection on the thickness of continental lithosphere and crust. *Tectonophysics*, 189:281–306, 1991.

A. Schoonmaker, W. S. F. Kidd, and D. C. Bradley. Foreland-forearc collisional granitoid and mafic magmatism caused by lower-plate lithospheric slab breakoff: The Acadian of Maine, and other orogens. *Geology*, 33:961964, 2005.

W. Schroeder. The empirical age–depth relation and depth anomalies in the Pacific ocean basin. *J. Geophys. Res.*, 89:9873–9883, 1984.

G. Schubert, D. L. Turcotte, and P. Olson. *Mantle Convection in Earth and Planets*. Cambridge University Press, UK, 2001.

D. L. Schutt and C. E. Lesher. Effects of melt depletion on the density and seismic velocity of garnet and spinel lherzolite. *J. Geophys. Res.*, 111, 2006. doi:10.1029/2003JB002950.

V. Selmin. Third–order finite element schemes for the solution of hyperbolic problems. Technical report, INRIA, 1987.

J. A. Sethian and P. Smereka. Level set methods for fluid interfaces. *Annual Review of Fluid Mechanics*, 35:341–372, 2003.

V. S. Solomatov. Grain size-dependent viscosity convection and the thermal evolution of the earth. *Earth Planet. Sci. Lett.*, 191:203–212, 2001.

W. Spakman. *Upper mantle delay time tomography with an application to the collision zone of Eurasian, African and Arabian plates.* PhD thesis, Univ. of Utrech, Utrech, The Netherlands, 1988.

C. A. Stein and S. Stein. A model for the global variation in oceanic depth and heat flow with lithospheric age. *Nature*, 129:123–129, 1992.

L. Stixrude and M. S. T. Bukowinski. Fundamental thermodynamic relations and silicate melting with implications for the constitution of d". *J. Geophys. Res.*, 95: 19311–19325, 1990.

L. Stixrude and C. Lithgow-Bertelloni. Mineralogy and elasticity of the oceanic upper mantle: Origin of the low-velocity zone. *J. Geophys. Res.*, 110:B03204, doi:10.1029/2004JB002965, 2005.

L. Stixrude and C. Lithgow-Bertelloni. Influence of phase transformations on lateral heterogeneity and dynamics in Earth's mantle. *Earth Planet. Sci. Lett.*, 263:45–55, 2007.

M. Stolarska, D. L. Chopp, N. Moës, and T. Belytschko. Modelling crack growth by level set in the extended finite element method. *International Journal for Numerical Methods in Engineering*, 51:943–960, 2001.

I. K. Suzuki, S. Okajima, and K. Seya. Thermal expansion of single–crystal manganosite. *J. Phys. Earth*, 27:63–69, 1979.

P. J. Tackley. Self–consistent generation of tectonic plates in three dimensional mantle convection. *Earth Planet. Sci. Lett.*, 157:9–22, 1998.

P. J. Tackley. Mantle convection and plate tectonics: Toward an integrated physical and chemical theory. *Science*, 288:2002–2007, 2000.

P. J. Tackley and S. Xie. Stag3d: A code for modeling thermo-chemical multiphase convection in Earth's mantle. In *Proc. of the Second MIT Conference on Computational Fluid and Solid Mechanics*, 2003.

L. Tan and N. Zabaras. A level set simulation of dendritic solidification of multi-component alloys. *Journal of Computational Physics*, 221:9–40, 2007.

A. Tovish and G. Schubert. Island arc curvature, velocity of convergence and angle of subduction. *Geophys. Res. Lett.*, 5:329–332, 1978.

D. L. Turcotte. Flexure. *Adv. Geophys.*, 21:51–86, 1979.

D. L. Turcotte and E. R. Oxburgh. Finite amplitude convective cells and continental drift. *J.Fluid Mech,*, 28:29–42, 1967.

J. van Hunen, J. Huang, and S. Zhong. The effect of shearing on the onset and vigor of small-scale convection in a newtonian rheology. *Geophys. Res. Lett.*, 30: doi:10.1029/2003GL018101, 2003.

J. van Hunen, A. P. van Den Berg, and N. J. Vlarr. Various mechanisms to induce present–day shallow flat subduction and implications for the younger Earth: a numerical parameter study. *Phys. Earth Planet. Inter.*, 146:179–194, 2004.

J. van Hunen, S. Zhong, N. M. Shapiro, and M. H. Ritzwoller. New evidence for dislocation creep from 3-d geodynamic modeling of the Pacific upper mantle structure. *Earth Planet. Sci. Lett.*, 238:146–155, 2005.

P. E. van Keken, S. D. King, H. Schmeling, U. R. Christensen, D. Numeister, and M.-P. Doin. A comparison of methods for the modeling of thermochemical convection. *J. Geophys. Res.*, 102(B10):22477–22495, 1997.

P. E. van Keken, B. Kiefer, and S. Peacock. High resolution models of subduction zones: Implications for mineral dehydration reactions and the transport of water into the deep mantle. *Geochem. Geophys. Geosyst.*, 10(3), 2002. doi:10.1029/2001GC000256.

M. S. Vassiliou and B. H. Hager. Subduction zone earthquakes and stress in slabs. *Pure Appl. Geophys.*, 128:547–624, 1988.

G. J. Wagner, N. Moës, W. K. Liu, and T. Belytschko. The extended finite element method for rigid particles in Stokes flow. *International Journal for Numerical Methods in Engineering*, 51(3):293–313, 2001.

R. Westaway. Quaternary uplift of Southern Italy. *J. Geophys. Res.*, 98:21741–21772, 1993.

B. J. Wood and D. A. Yuen. The role of lithospheric phase transitions on seafloor flattening at old ages. *Earth Planet. Sci. Lett.*, 66:303–314, 1983.

M. J. R. Wortel and W. Spakman. Structure and dynamics of subducted lithosphere in the Mediterranean region. In *Proc. Kon. Ned. Akad. Wetensch.*, volume 95, page 325347, 1992.

M. J. R. Wortel and W. Spakman. Subduction and slab detachment in the Mediterranean–Carpathian region. *Science*, 290:1910–1917, 2000.

P. F. Xu, R. M. Sun, F. T. Liu, Q. Wang, and B. Cong. Seismic tomography showing, subduction and slab breakoff of the Yangtze block beneath the Dabie—Sulu orogenic belt. *Chin. Sci. Bull*, 45:70–74, 2000.

S. Yoshioka and M. J. R. Wortel. Three–dimensional numerical modeling of detachment of subducted lithosphere. *J. Geophys. Res.*, 100(B10):20223–20244, October 1995.

D. A. Yuen and L. Fleitout. Thinning of the lithosphere by small–scale convective destabilization. *Nature*, 313:125–128, 1985.

D. A. Yuen, W. R. Peltier, and G. Schubert. On the existence of a second scale of convection in the upper mantle. *Geophys. J. Roy. Astron. Soc.*, 65:171–190, 1981.

S. E. Zaranek and E. M. Parmentier. Convective cooling of an initially stably stratified fluid with temperature-dependent viscosity: implications for the role of solid-state convection in planetary evolution. *J. Geophys. Res.*, 109: doi:10.1029/2003JB002462, 2004.

K. Zhang, B. H. Hager, and A. Raefsky. A critical assessment of viscous models of trench topography and corner flow. *Geophys. J. Roy. Astron. Soc.*, 83:451–475, 1985.

H.-K. Zhao, T. Chan, B. Merriman, and Osher. A variational level set approach to multiphase motion. *Journal of Computational Physics*, 127:179–195, 1996.

S. Zhong and M. Gurnis. Controls on the trench topography from dynamic models of subducted slabs. *J. Geophys. Res.*, 99:15683–15695, 1994.

O. C. Zienkiewicz and R. L. Taylor. *The Finite Element Method. Fluid Dynamics*, volume 3. Butterworth Heinemann, London, fifth edition, 2000.

S. Zlotnik and P. Díez. Assembling sparse matrices in MATLAB. *Commun. Numer. Meth. Engrg.*, 2007. Submitted.

S. Zlotnik and P. Díez. Hierarchical X–FEM for n–phase flow ($n > 2$). *Comput. Methods Appl. Mech. Engrg.*, 2008. Submitted.

S. Zlotnik, P. Díez, M. Fernández, and J. Vergés. Numerical modelling of tectonic plates subduction using X–FEM. *Comput. Methods Appl. Mech. Engrg.*, 196: 4283–4293, May 2007a.

S. Zlotnik, M. Fernández, P. Díez, and J. Vergés. Modelling gravitational instabilities: slab break–off and Rayleigh–Taylor diapirism. *Pure Appl. Geophys.*, 2007b. Submitted.